A Study on Enhanced Electrode Performance of Li and Na Secondary Batteries by Ionic Liquid Electrolytes

Jinkwang Hwang

2019

Table of Contents

Chapter 1

General Introduction

1.1 Energy Storage Systems

The global energy consumption has been rapidly increasing, and more than 80 % of the current energy is produced from fossil fuels, which emit carbon dioxide, which is a well-known greenhouse gas [1-3]. As a result, the United Nations Framework Convention on Climate Change (UNFCCC) have been firstly organized in 1995, and plan for the climate change has been determined in the UNFCCC of the Parties held in Kyoto, Japan on December 1997. The implementation plan so-called 'Kyoto Protocol' has been determined by the specific greenhouse gas reduction targets of developed countries [4]. In 2015, 196 state parties joined the Paris agreement within the UNFCCC to keep the rise in global temperature. Thus, fossil fuels are encouraged to be replaced with a new type of clean energy sources which produce fewer greenhouse gases and could be renewable.

A possible scenario is using renewable energy sources such as solar and wind powers. The main problem of these renewable energy sources is intermittent production and the variation of the demand levels on time. The energy storage system (ESS) is the most important technology to realize renewable energy sources to provide electricity to utilities and to establish large-scale power supply networks. The ESSs currently proposed for large-scale stationary applications, including pumped-storage hydroelectricity, flywheels, etc [5, 6]. For the ESS proposed to date, those using secondary battery systems are advantageous with respect to their high power and energy densities, pollution-free operation, high efficiency, simple maintenance, and versatility [7-10]. Another attracting technology is a smart grid with demand-side management (DSM). DSM is a management system to encourage the energy consumer to purchase an energy-efficient appliance or use less energy to move the time of energy use to off-peak times [11]. For example, the demand for electricity during nighttime is less than daytime, and the surplus electricity can be stored in energy storage systems during nighttime and be used during daytime [11, 12]. In a word, ESSs is also a key enabler for the DSM system.

1.2 Li and Na Secondary Batteries

So far, the most powerful battery is recognized as Li-ion battery (LIB) in terms of energy and power densities and cycleability [13-17]. Several devices adopting LIBs have been commercialized owing to their high performance, enabling their high share in the global rechargeable battery market for the past two decades. However, Li resources are not abundant and are unevenly distributed in the world, mainly in South America [18]. This lack of resource and utilizable reserve of Li is a big obstacle to establish economically feasible on large-scale batteries. In terms of economic feasibility, Na secondary battery is certainly a good candidate for large scale energy storage because Na resources are abundant and evenly distributed all over the world. Table 1-1 lists some information on Na and Li. The low standard redox potential ($E^{o}_{Na+/Na} = -2.71$ V vs. SHE; $E^{o}_{Li+/Li} = -3.04$ V vs. SHE), the second smallest ionic radius in the group 1 elements (1.02 Å for Na^+ and 0.76 Å for Li^+ in the case of 6-coordination [19]), and relatively similar chemical properties between Na and Li also make Na secondary batteries most reliable in a range of post lithium secondary batteries.

A secondary battery is mainly composed of a positive electrode, a negative electrode, and electrolyte. The positive and negative electrodes are oxidized and reduced, respectively, during charging. At the same time, Na^+ or Li^+ moves from the positive electrode to the negative electrode in the electrolyte. The mechanism of discharging is exactly opposed to that of charging above. The electrolyte is a pure ionic conductor that electronically separates negative and positive electrodes. In addition, the electrolyte forms solid electrolyte interphase (SEI) layers on the surface of electrodes, which is very important to stabilize battery performance and improve safety and efficiency. Thus, understanding of the physical and chemical properties of SEI layers is very important to optimize batteries.

1.3 Positive Electrode Materials Investigated in Ionic Liquid

Electrode materials for Na secondary batteries were developed firstly extracted Li^+ and inserted to Na^+ to the electrode material developed for Li secondary batteries. For example, Li^+ of $LiFePO_4$, $LiCoNiMnO_2$, and $Li_3V_2(PO_4)_3$ is chemically or electrochemically replaced with Na^+ to produce $NaFePO_4$, $NaCoNiMnO_2$, $Na_3V_2(PO_4)$. Here, positive electrode materials for Na secondary batteries investigated in IL electrolytes are mainly summarized. The prospective advantages of Na secondary batteries are their economic feasibility and their ability to act as sustainable energy sources for large-scale applications such as ESSs and electric vehicles. Thus, research into electrode materials for Na secondary batteries should comply with the principle of the utilization of earth-abundant elements [20-22]. Positive electrode materials have been widely studied as a means to maximize the performance of Na secondary batteries concerning power and energy densities, coulombic efficiency, cycleability, and safety.

Various polyanionic compounds, layered transition-metal oxides, and organic compounds have been reported as positive electrode materials for Na secondary batteries [22-26]. Several of them exhibit excellent performance in ILs, providing unique electrochemical results such as improved cycleability, high rate capability, and enhanced electrochemical activity at elevated operating temperatures [26-29]. These findings were enabled by exploiting the electrochemical and thermal stabilities of IL electrolytes.

Figure 1-1 summarizes the information of positive electrode materials applied in IL electrolytes. The gravimetric theoretical capacities (mAh g^{-1}) and working potentials (V vs. Na^+/Na) are illustrated in Figure 1-1a. Most of the studies on positive electrode materials utilizing IL electrolytes have been carried out using polyanionic compounds and O3- and P2-type layered transition-metal oxides. The “O3” and “P2” nomenclature developed by Delmas et al. [30] is used to indicate the Na-O coordination (O for octahedral and P for prismatic) and repeating stacking period in the unit cell (2 or 3). These materials are highly reversible based on Na-intercalation with limited volumetric change. The structural properties of selected representative polyanionic compounds ($Na_2FeP_2O_7$ and $Na_3V_2(PO_4)_3$) and O3- and P2-type layered transition-metal oxides are shown in Figure 1-1b. A comprehensive list of positive electrode materials tested in IL electrolytes is provided in Table 1-2 along with their structural and electrochemical properties. Electrochemical properties obtained with positive electrode materials in designated IL electrolytes under certain measurement conditions, including mass loading, operating temperature, Cut-off voltage, and current density, are shown in Table 1-3 (an abbreviation of some ions for ILs is also shown in Table 3-1). The following sections review the electrochemical properties of polyanionic compounds and layered oxide materials tested with IL electrolytes in Table 1-2, including their structural properties. Their performance in reported full-cell tests is also briefly described.

1.3.1 Polyanionic Compounds

In recent years, polyanionic compounds have been attracting considerable attention as high-performance positive electrode materials for Na secondary batteries. Polyanionic compounds build stable structural frameworks with $(XO_4)^{n-}$ or $(X_mO_{3m+1})^{n-}$ (X=S, P, Si, As, B, and so on) tetrahedral units and MO_6 (M= transition metal) octahedral units [31, 32]. These units are connected via oxygen bridging with the edges or corners of the polyhedra being shared, resulting in a variety of polyanionic compounds that exhibit one-, two-, and three-dimensional structural ordering for facile Na^+ diffusion paths [33-35]. For example, a three-dimensional $Na_3V_2(PO_4)_3$ crystal structure is formed by corner-sharing of octahedral VO_6 units and tetrahedral PO_4 units, and this material is well-known as a Na Super Ionic CONductor (NASICON) [36-39]. Polyanionic compounds usually exhibit high thermal stabilities owing to the strong X−O covalent bonds and strong resistance to natural oxidation [32, 40-42]. However, their poor electronic conductivity results in poor electrochemical performance, which can be overcome by surface modifications, carbon coating, and elevation of operating temperature using IL electrolytes, as reported in recent studies.

NASICON-type $Na_3V_2(PO_4)_3$, which crystallizes in the rhombohedral space group $R\bar{3}c$ [43, 44], is the polyanionic material that has been most extensively studied using IL electrolytes owing to its open structure for facile Na^+ transport, high thermal stability, and high energy density. $Na_3V_2(PO_4)_3$ can provide two types of redox reactions based on V^{4+}/V^{3+} and V^{3+}/V^{2+}. The V^{4+}/V^{3+} reaction is a two-electron reaction (for two V atoms) with a theoretical capacity of 117 mAh g^{-1}, showing an average potential of 3.4 V vs. Na^+/Na (Eq. 1). The V^{3+}/V^{2+} reaction is a one-electron reaction (for two V atom) with a theoretical capacity of 55 mAh g^{-1} showing an average potential of 1.6 V vs. Na^+/Na (Eq. 2) [36, 45]. This double-redox system enables the fabrication of a symmetric $Na_3V_2(PO_4)_3$ cell and is often used for testing new electrolytes.

$$Na_3V_2(PO_4)_3 \rightleftarrows NaV_2(PO_4)_3 + 2Na^+ + 2e^- \qquad (1)$$

$$Na_3V_2(PO_4)_3 + Na^+ + e^- \rightleftarrows Na_4V_2(PO_4)_3 \qquad (2)$$

The first study on the electrochemical performance of positive electrodes in Na secondary batteries with an IL electrolyte was performed using a $Na_3V_2(PO_4)_3$ symmetric cell. In this study, a $Na[BF_4]$-$[C_2C_1im][BF_4]$ ($C_2C_1im^+$ = 1-ethyl-3-methylimidazolium cation) IL electrolyte was incorporated [36]. The $Na_3V_2(PO_4)_3$ symmetric cell exhibited a lower discharge capacity with a $Na[BF_4]$-$[C_2C_1im][BF_4]$ IL than that in 1 mol dm^{-3} $Na[ClO_4]$-PC at 25 °C, but rate capability is improved at 80 °C [36]. The high viscosity and low conductivity of the IL and low electronic conductivity of $Na_3V_2(PO_4)_3$ at 298 K were identified as the obstacles to rate capability.

A study on $Na_3V_2(PO_4)_3$ revealed that $Na_3V_2(PO_4)_3$ with carbon-coating exhibits good rate capability in 1 mol dm^{-3} $Na[ClO_4]$-EC/PC electrolyte [46]. In this study, $Na_3V_2(PO_4)_3$ was prepared by the soft template method. The preparation method provided 6wt% carbon with $Na_3V_2(PO_4)_3$ materials. The composited exhibited a high rate capability of 92.2% of capacity at 1C was retained at 10 C. Nearly 80% and 54% of the capacity was retained at 20C and 40C, respectively (1C = 114 mAh g^{-1}). This improvement is owing to carbon-coating, which efficiently improved the electronic conductivity of $Na_3V_2(PO_4)_3$.

Owing to the high thermal, chemical, and electrochemical stabilities of $Na_3V_2(PO_4)_3$, it has become the standard material for assessing new IL electrolytes. For example, the protic IL, 0.3 mol dm^{-3} Na[TFSA]-$[C_4Hpyrr]$[TFSA], has been studied as an electrolyte for Na secondary batteries [47]. This protic IL electrolyte exhibits more stable cycleability with $Na_3V_2(PO_4)_3$ than that with a 0.3 mol dm^{-3} Na[TFSA]-$[C_4C_1pyrr]$[TFSA] aprotic IL. A gelled 0.8 mol kg^{-1} Na[FSA]-$[C_3C_1pyr]$[FSA]-PVdF-co-HFP ($C_3C_1pyrr^+$ = *N*-propyl-*N*-methylpyrrolidinium cation, PVdF-co-HFP = polyvinylidene fluoride-co-hexafluoropropylene) IL gel electrolyte showed good cycleability with 92% capacity retention and 99.9% Coulombic efficiency over 150 cycles [48]. Another study on $Na_3V_2(PO_4)_3$ with $Na[PF_6]$-$[C_4C_1im]$[TFSA] showed improved cycling performance over that achieved with an organic solvent electrolyte [49].

Olivine-type $LiFePO_4$ is one of the most well-studied materials for LIBs because of its cost-effective, facile synthesis, and a high theoretical capacity of 170 mAh g^{-1} [34, 50]. In the same manner, Fe-based phosphates ($NaFePO_4$) have been investigated as potential positive electrode materials using IL electrolytes. Olivine $NaFePO_4$, which has the highest theoretical capacity of 155 mAh g^{-1} among the Fe-based phosphates, has two polymorphs, i.e., triphylite and maricite phases, both of which crystallize in the orthorhombic space group *Pnma* [51]. However, the triphylite-phase of $NaFePO_4$ is not thermally stable and can only be prepared by electrochemical/chemical extraction of Li from $LiFePO_4$, followed substitution with Na [51]. Electrochemical behaviour of triphylite-$NaFePO_4$ was assessed using [C_4C_1pyrr][TFSA] IL electrolytes containing Na[BF_4], Na[ClO_4], Na[PF_6], or Na[TFSA] and a conventional 1 mol dm^{-3} Na[ClO_4]-EC/DEC (1:1, v/v) organic electrolyte at 298, 323, and 348 K [52, 53]. At 298 K, 1 mol dm^{-3} Na[ClO_4]-EC/DEC exhibited the highest rate capability and cycleability, but at the elevated temperature of 323 K, the cycleability became poorer. A significant improvement in reversible capacity, rate capability, and cycleability were observed in 1 mol dm^{-3} Na[BF_4]-[C_4C_1pyrr][TFSA]. The discharge capacity was further improved to 152 mAh g^{-1} (at 0.05 C) at 348 K in 1 mol dm^{-3} Na[BF_4]-[C_4C_1pyrr][TFSA] electrolyte [52, 53].

Recently, the cycleability improvement was reported for a 1 mol dm^{-3} Na[FSA]-[P_{111i4}][FSA] IL electrolyte with a capacity retention of 95% over 100 cycles (323 K, C/2) [54]. In this study, it was suggested that electrolyte conductivity is not the main factor for determining cell performance and is not significantly related to capacity. Above all, the SEI determines the cycle stability, as is discussed in more detail in the section on negative electrodes below. XPS measurements confirmed the existence of IL-derived decomposition products like NaOH, Na_2S, and NaF on the Na metal surface, which provided stable cycleability in a half-cell [54].

Maricite-$NaFePO_4$ can be prepared by the conventional solid-state method. It was previously believed that maricite-$NaFePO_4$ was electrochemically inactive [51, 55]. However, nano-sized maricite-$NaFePO_4$ transforms into an amorphous $FePO_4$ phase during the first charge (desoditation) and shows unexpected charge-discharge performance [56]. This material is selected for my research to investigate elevation operating temperature by ILs should show reversible (de)sodiation properties.

Pyrophosphate compounds such as $Na_2FeP_2O_7$, $Na_{1.56}Fe_{1.22}P_2O_7$, and $Na_4Fe(PO_4)_2P_2O_7$, offer stable three-dimensional diffusion paths for Na ions composed of corner-sharing FeO_6 units [57]. $Na_2FeP_2O_7$ crystallizes in the triclinic space group $P\bar{1}$ [58, 59]. Its theoretical capacity is estimated from the one-electron reaction based on the Fe^{2+}/Fe^{3+} redox reaction (Eq. 3) [59].

$$Na_2FeP_2O_7 \rightleftarrows NaFeP_2O_7 + Na^+ + e^- \qquad (3)$$

$Na_2FeP_2O_7$ in Na[FSA]-[C_2C_1im][FSA] with various salt concentrations at 298 to 363 K and 56 mol% Na[FSA]-K[FSA] at 363 K show adequate reversible capacities [29, 60]. In particular, $Na_2FeP_2O_7$ in a 30 mol% Na[FSA]-[C_2C_1im][FSA] IL electrolyte shows the excellent rate capability of 83 mAh g^{-1} at 2000 mA g^{-1} at 363 K but only 17 mAh g^{-1} at 298 K [29, 60].

$Na_{2-x}Fe_{1+x/2}P_2O_7$ compounds (where $0 < x < 0.44$) were prepared by a solid-state method and evaluated in IL. Among them, $Na_{1.56}Fe_{1.22}P_2O_7$, (where $x = 0.44$) is introduced here, as it showed the highest theoretical capacity (118 mAh g^{-1}) of the $Na_{2-x}Fe_{1+x/2}P_2O_7$ compounds

[61, 62]. Notably, the theoretical capacity of $Na_2FeP_2O_7$ (~20 mAh g^{-1}) was increased by the substitution of Na with Fe to form $Na_{1.56}Fe_{1.22}P_2O_7$, and it is estimated that 1.22 equivalents of Na are reversibly (de)sodiated based on the Fe^{2+}/Fe^{3+} redox couple reaction (Eq. 4) [61, 62].

$$Na_{1.56}Fe_{1.22}P_2O_7 \rightleftarrows Na_{0.34}Fe_{1.22}P_2O_7 + 1.22Na^+ + e^- \qquad (4)$$

However, the actual reversible capacity of $Na_{1.56}Fe_{1.22}P_2O_7$ was limited to 85 mAh g^{-1} in an organic electrolyte. Using 20 mol% Na[FSA]-[C_3C_1pyrr][FSA] IL electrolyte at 363 K, a reversible capacity of 108 mAh g^{-1} was obtained, which is more than that obtained in the organic electrolyte by approximately 15% under the same conditions [63]. Furthermore, superior cycleability was reported with this IL electrolyte at 298, 323, and 363 K. This improvement was achieved owing to the high cycleability of the Na metal counter electrode in the IL electrolyte and the small volume change of $Na_{1.56}Fe_{1.22}P_2O_7$ during (de)sodiation (only 1.9%) as compared to those of the triphylite-$NaFePO_4$ (17.6%), $Na_3V_2(PO_4)_3$ (8.3%), and $Na_2FeP_2O_7$ (2.6%) [51, 58, 62-64].

Na_2MnSiO_4 is a low-cost and environmentally benign material composed of only earth-abundant elements. In a recent study, carbon-coated Na_2MnSiO_4 was prepared by a sol-gel method and assessed in a 20 mol% Na[FSA]-[C_3C_1pyrr][FSA] IL [65]. This material has theoretical capacities of 278 mAh g^{-1} and 125 mAh g^{-1} based on a two-electron and one-electron reaction, respectively [65, 66]. However, the obtained reversible capacities of 70, 94, and 125 mAh g^{-1} at 298, 323, and 363 K, respectively, suggested that the redox activity is derived only from the one-electron reaction, which corresponds to the Mn^{3+}/Mn^{2+} redox reaction.

Vanadium-based phosphate ($NaVOPO_4$) crystallizes in the monoclinic space group $P2_1/c$. $NaVOPO_4$ has a high operating potential of 3.6 V vs. Na^+/Na with a large theoretical capacity of 145 mAh g^{-1} based on the V^{5+}/V^{4+} redox couple reaction [67]. The charge-discharge behavior of $NaVOPO_4$ was investigated using 20 mol% Na[FSA]-[C_3C_1pyrr][FSA] IL electrolytes at 298 and 363 K. Reversible capacities of 60 and 101 mAh g^{-1} were obtained at 298 and 363 K, respectively [68].

1.3.2 Transition-metal Oxides

LIB usage has been promoted by the intensive utilization of transition-metal oxides such as Li_xMO_2 (M = Co, Ni, and Mn) [69-74]. Such transition-metal oxides as positive electrode materials exhibit excellent performance in terms of high capacity, energy density, and cycleability [70, 73, 74]. Accordingly, a number of transition-metal oxides for Na secondary batteries have been explored [24, 26, 75-79]. In this section, representative transition-metal oxide compounds that have been investigated with IL electrolytes are discussed, including O3- and P2-type layered transition-metal oxides. $Na_{0.44}MnO_2$ with an S-shaped tunnel structure will also be discussed.

The structures of O3- and P2-type layered transition-metal oxides are shown in Figures 1-1d and 1-1e, respectively. Despite the success of layered transition metal oxides as positive electrode materials in LIBs, the number of studies on their use in IL electrolytes for Na secondary batteries is still limited. In terms of cost and resource sustainability, Ni and Co layered transition-metal oxide are not particularly attractive materials for Na secondary batteries. Thus, the layered transition-metal oxides for Na secondary batteries investigated in IL electrolytes mostly contain Mn, Fe, and Cr elements instead of Co and Ni.

The first report on reversible Na insertion and extraction was reported for O3-type $NaCrO_2$ [80]. The theoretical capacity of this material is 125 mAh g^{-1} for the one-electron reaction based on the Cr^{4+}/Cr^{3+} redox couple [81]. O3-type $NaCrO_2$ exhibits numerous two-phase regions in its charge-discharge plateaus up to 3.5 V. The upper Cut-off voltage was 3.6 V because further desodiation causes an irreversible phase transition. The material was assessed with IL electrolytes comprising 56 mol% Na[FSA]-K[FSA] at 353 K. The Na/Na[FSA]-K[FSA]/$NaCrO_2$ cell exhibited a specific discharge capacity of 77.3 mAh g^{-1} [82]. This capacity was improved to 101.4 mAh g^{-1} at 423 K using 10 mol% Na[TFSA]-Cs[TFSA] [83]. Furthermore, the use of $NaCrO_2$ in a wide temperature range (253 to 363 K) with 20 mol% Na[FSA]-[C_3C_1pyrr][FSA] IL electrolyte has been reported [84].

Recently, binary and ternary mixed transition metal oxides have been investigated using IL electrolytes. O3- and P2-type $NaFe_{1-x}Mn_xO_2$ consisted of earth-abundant elements and was expected to deliver a high reversible capacity. O3- and P2-type $Na_{2/3}Fe_{2/3}Mn_{1/3}O_2$ was assessed in a 0.5 mol dm^{-3} Na[PF_6]-EC/DMC organic solvent electrolyte. The P2-type $Na_{2/3}Fe_{2/3}Mn_{1/3}O_2$ and O3-type $Na_{2/3}Fe_{2/3}Mn_{1/3}O_2$ delivered the first discharge capacities of 151 and 157 mAh g^{-1}, respectively, over the voltage range 4.2–1.5 V at C/10. However, the capacity of both P2- and O3-$Na_{2/3}Fe_{2/3}Mn_{1/3}O_2$ faded within 10 cycles [85]. Interestingly, the capacity and cycleability were improved in measurements using 2.3 mol dm^{-3} Na[FSA]-[P_{111i4}][FSA][86] only for O3-type $Na_{2/3}Fe_{2/3}Mn_{1/3}O_2$, which exhibited excellent performance using the IL electrolyte at 323 K. The capacity of O3-type $Na_{2/3}Fe_{2/3}Mn_{1/3}O_2$ was improved to 184 mAh g^{-1} over the voltage range of 4.0–1.75 V, while P2-type $Na_{2/3}Fe_{2/3}Mn_{1/3}O_2$ provided a capacity of 130 mAh g^{-1} because a narrower voltage range was applied. The rate capability and cycleability were improved for both P2-type and O3-type $Na_{2/3}Fe_{2/3}Mn_{1/3}O_2$ upon using IL electrolytes [86].

A material with a different Fe/Mn ratio, P2-$Na_{2/3}Fe_{1/3}Mn_{2/3}O_2$, was investigated in a Na[FSA]-[C_3C_1pyrr][FSA] IL electrolyte, and showed the high discharge capacity of 227 mAh g^{-1} at a current density of 20 mA g^{-1} over the voltage range 2.0–4.3 V. With a wider Cut-off voltage of 1.5–4.2 V, P2-$Na_{2/3}Fe_{1/3}Mn_{2/3}O_2$ exhibited the very high discharge capacity of 317 mAh g^{-1} in the IL, but this capacity exceeds its theoretical capacity of 261 mAh g^{-1}, indicating unfavorable side reactions [87].

A recent report on P2-$Na_{2/3}Ni_{1/3}Mn_{2/3}O_2$ revealed stable cycling involving an O redox reaction in 1 mol dm^{-3} Na[TFSA]-[C_4C_1pyrr][TFSA] IL electrolyte. The discharge capacity of 220 mAh g^{-1} fell to 200 mAh g^{-1} after 14 cycles in the IL electrolyte at 333 K, whereas it decreased to 160 mAh g^{-1} after 14 cycles in 1 mol dm^{-3} Na[PF_6]-EC/DMC at 298 K [88].

The ternary transition metal oxide P2-$Na_{0.45}Ni_{0.22}Co_{0.11}Mn_{0.66}O_2$ provides a good example of the superiority of IL electrolytes. Compared to the case in an organic electrolyte, a higher reversibility of the P2–O2 phase transition was observed for P2-$Na_{0.45}Ni_{0.22}Co_{0.11}Mn_{0.66}O_2$ using 10 mol% Na[TFSA]-[C_4C_1pyrr][FSA] above 4.2 V, which is attributable to the wide electrochemical window of the IL. The cell exhibited a capacity of approximately 220 mAh g^{-1} at 12 mA g^{-1} at 20 °C. This is because the electrochemical stability of the IL electrolyte is higher than that of the organic electrolyte. Furthermore, the low solubility of Mn in the IL electrolyte at potentials below 2.2 V helps to maintain its good cycleability [27]. A discussion of the cycleability of the materials is presented in the relevant section. P2-$Na_{2/3}Ni_{0.30}Co_{0.15}Mn_{0.55}O_2$, which has a similar composition, was investigated using [$Na(L)_n$][FSA] (with L = G1, G2, or G3, n = 1, 2, or 3) IL, and exhibited stable performance over 100 cycles with [$Na(G1)_3$][FSA] [89].

$Na_{0.44}MnO_2$ is an attractive material for Na secondary batteries in terms of the low cost and earth-abundance of its constituent elements. It crystallizes in the orthorhombic space group

Pbam and has wide tunnels for Na^+ diffusion [90]. The initial charge desodiates 0.26 equivalents of Na^+ from $Na_{0.44}MnO_2$ (Eq. 5). After the initial charge, the charge-discharge reaction is based on (de)sodiation with 0.46 equivalents Na^+ (Eq. 6). The theoretical capacity is calculated to be 127 mAh g^{-1} based on the Mn^{4+}/Mn^{3+} redox couple reaction.

$$Na_{0.44}MnO_2 \rightarrow Na_{0.18}MnO_2 + 0.26Na^+ + 0.26e^- \qquad (5)$$

$$Na_{0.18}MnO_2 + 0.46Na^+ + 0.46e^- \rightleftarrows Na_{0.64}MnO_2 \qquad (6)$$

Electrochemical measurements of $Na_{0.44}MnO_2$ were performed using a Na/[Na(G5)][TFSA]/$Na_{0.44}MnO_2$ cell. The cell showed a reversible charge-discharge capacity of 110 mAh g^{-1} over a voltage range of 2.0–4.0 V at 333 K [91]. This electrochemical performance was improved using [Na(G5)][FSA] mixed with the molecular solvent hydrofluoroether (HFE). As a consequence, $Na_{0.44}MnO_2$ in [(NaG5)][FSA] with HFE showed a reversible charge-discharge capacity of 113 mAh g^{-1} at 303 K and was stable for 50 cycles (Coulombic efficiency of 99%) without significant capacity degradation [92].

1.3.3 Others

Vanadium-based fluoride phosphates ("fluorophosphate" is the wrong nomenclature because there are no P−F bonds) such as $Na_3V_2(PO_4)_2F_3$ and $NaVPO_4F$ are good candidates in terms of high energy density and have been vigorously studied in organic solvents, but not in IL electrolytes. Fe- and Mn-based materials are excellent candidates in terms of economic and resource considerations. Na_2FePO_4F has a high theoretical capacity of 124 mAh g^{-1} and a high operating voltage of 3.5 V, as does Na_2MnPO_4F [93, 94]. Thus, these materials would be promising if their cycleabilities and rate capacities could be improved.

Prussian blue analogs have not yet been tested using IL electrolytes. For example, $Na_4Fe(CN)_6$, which is made from naturally abundant resources, could be an interesting material that simultaneously achieves high capacity and moderate working potential [95].

Finally, organic compounds are very attractive materials for Na secondary batteries in terms of sustainability and diversity [96]. One of the most important advantages of organic compounds is their tunable functionality. Thus, various redox-active organic electrodes are currently known. Nevertheless, organic electrode materials for Na secondary batteries have not been well investigated in IL electrolytes. A study on the organic electrode material poly(3,4)-ethylenedioxythiophene)biopolymer in 20 mol% Na[TFSA]-[C_4C_1pyrr][TFSA] and Na[FSA]-[C_2C_1im][FSA] IL electrolytes indicated their stable electrochemical performance [97]. In another recent study, calix[4]quinone and 5,7,12,14-pentacenetetrone organic-based positive electrode materials were investigated in a 0.3 mol dm^{-3} Na[TFSA]-[C_3C_1pyrr][TFSA] IL electrolyte [98]. A Na/Calix[4]quinone half cell exhibited a very high reversible capacity of 406 mAh g^{-1} at 20 mA g^{-1} and excellent cycleability with a stable capacity retention of 99.7% after 300 cycles. A Na/5,7,12,14-pentacenetetrone half cell with a 0.3 mol dm^{-3} Na[TFSA]-[C_3C_1pyrr][TFSA] IL electrolyte exhibited similarly high performance with a capacity of 245 at 30 mA g^{-1}. The authors insisted that these improvements were achieved using the IL electrolyte because it overcame problems associated with the poor dissolution of quinone compounds [98]. Thus, IL electrolytes may be useful to overcome problems associated with organic compounds such as suppressing the dissolution of active materials that typically occurs in aprotic solvents and ameliorating the low intrinsic electronic conductivity by elevated temperature operating [96, 99-101].

1.4 Ionic Liquid Electrolytes

Electrolytes play very important roles in achieving high-performance and safe batteries. An electrolyte must meet high ionic conductivity ($\sigma > \sim 1$ mS cm^{-1}), physical and chemical compatibility with the electrodes, and provide a stable interface in order to deliver the expected performance[102, 103]. Organic electrolytes such as ethylene carbonate (EC), propylene carbonate (PC), diethylene carbonate (DEC), dimethyl carbonate (DMC), and 1,2-dimethoxyethane (DME) coupled with the Na salts, Na[ClO_4] and Na[PF_6], are routinely used for Na secondary battery studies and achieve good performance. However, the safety issues surrounding secondary batteries are mostly concerned with the volatility and flammability of organic electrolytes [104-106].

As Na secondary batteries are mainly intended as large-scale batteries for ESSs and electric vehicles, the safety problems become more significant as the battery size increases. As well as safety benefits, recent studies have revealed that ILs bring excellent cycleability and superior rate capability. This is because IL electrolytes can form more stable SEIs that enable more facile Na diffusion and can also form a stable passivation layer on Al current collectors, preventing Al corrosion [107]. Furthermore, ILs enable operation at elevated temperatures, which can facilitate Na diffusion in the electrode and electrolyte as well as electrode reactions. ILs are entirely composed of cations and anions. This chemical feature brings great advantages to ILs as electrolytes owing to their nonflammability, non-detectable vapor pressure, good chemical, electrochemical, and thermal stabilities [108, 109]. Passerini *et al.* and Hagiwara *et al.* have investigated the Na[FSA]-[C_3C_1pyrr][FSA] IL [110-112] and Na[FSA]-[C_2C_1im][FSA] IL [113] as electrolytes for Na secondary battery at intermediate-temperatures. Those IL electrolytes exhibit wide electrochemical window and ionic conductivity (e.g. ionic conductivity: 17 mS cm^{-1} at 363 K for 30 mol% Na[FSA]-[C_3C_1pyrr][FSA] and 31 mS cm^{-1} at

363 K for 30 mol% Na[FSA]-[C_2C_1im][FSA] [111, 113] (see Table 1-4 as well). The structures of FSA anion, C_3C_1pyrr cation, and C_2C_1im cation are shown in Figs. 1-2, 1-3, and 1-4, respectively.

1.4.1 High Thermal and Electrochemical Stability

The use of ILs extends the temperature limits and Cut-off voltage range upon electrochemical measurement. This flexibility in testing conditions is advantageous not only for evaluating well-developed materials in comprehensive conditions but also for identifying the optimal working environments for new materials.

$Na_3V_2(PO_4)_3$ and $NaCrO_2$ were evaluated in the wide temperature range 243–363 K using 20 mol% Na[FSA]-[C_2C_1im][FSA] and Na[FSA]-[C_3C_1pyrr][FSA] IL electrolytes [84]. The $Na_3V_2(PO_4)_3$ cells provided stable reversible performance across the whole temperature range and achieved capacities of 100.8, 78.1, and 57.6 mAh g^{-1} at 298, 263, and 253 K . Charge-discharge testing of the $NaCrO_2$ cell was performed between 298 and 363 K, and it also exhibited very stable reversible capacities. With a decrease in temperature, the polarisation of the cell increases, and the reversible capacity decreases as a consequence of the increase in internal cell resistance, which is due to the reduced ionic conductivity of the electrolyte, retarded Na diffusion in the electrode, and higher charge transfer resistance. Nonetheless, IL electrolytes achieve the broadest operating temperature for Na secondary batteries.

The Ni-based polyanionic compound $Na_4Ni_3(PO_4)_2(P_2O_7)$/C was expected to exhibit a high operating voltage based on its Ni^{3+}/Ni^{2+} redox activity. Unfortunately, when a 1 mol dm^{-3} Na[PF_6]-EC/DEC organic solvent electrolyte was used, the cell could only be charged to 4.9 V. The first charge capacity was approximately 97 mAh g^{-1}, which involves 2.3 equivalents of Na based on the capacity during the desodiation process [28]. However, only 0.9 equivalents of Na were reversibly sodiated into the composite, corresponding to a Coulombic efficiency for the first cycle of about 40%. This may indicate electrolyte decomposition at such a high potential. Conversely, this material could be charged up to 5.1 V in 10 mol% Na[TFSA]-[C_3C_1pyrr][FSA] IL and the composite was able to (de)sodiate more [27]; 2.7 and 1.3 equivalents of Na were desodiated and sodiated, respectively, during the first cycle. The *ex-situ* XRD patterns indicate that neither phase change nor irreversible structural reorganization occurred during the charge-discharge process, confirming the robustness of this material. Although $Na_4Ni_3(PO_4)_2(P_2O_7)$/C may appear to be less appealing for practical use owing to the limited achievable capacity, these studies highlight the possibility of using IL electrolytes for electrode studies with new materials.

1.4.2 Improved Performance

Rate capability and power density are significantly improved by the elevated temperature operation available by using ILs owing to the improved interfacial process between electrodes and electrolytes as well as ionic conductivity, as mentioned above.

Numerous studies have reported that IL electrolytes exhibit improved cycling performance over a wide temperature range [27, 29, 49, 53]. It is widely acknowledged that IL electrolytes can provide a uniform and robust SEI layer on reactive Na metal. Cycling testing of a Na/$NaFePO_4$ cell initially confirmed the better cycleability using a Na[TFSA]-[C_4C_1pyrr][TFSA] IL (Na[TFSA] = 0.1, 0.5, and 1mol dm^{-3}) electrolyte than that using a 1 mol dm^{-3} Na[ClO_4]-EC/DEC organic electrolyte at 323 K [53]. The capacity retentions after 100 cycles were 62% and 87% with the organic and IL electrolyte, respectively. Furthermore, Na[TFSA]-[C_4C_1pyrr][TFSA] IL electrolyte containing 0.5 mol dm^{-3} Na[TFSA] salt gave better cycleability than that with 0.1 and 1 mol dm^{-3} Na[TFSA] [53]. The authors reported that the organic electrolyte at 323 K presented undesirable electrode-electrolyte interactions and evaporation of the electrolyte, whereas the thermally stable IL electrolyte provided higher Na^+ supply as the temperature increased without the above-mentioned drawbacks [53].

Another study on $Na_{0.45}Ni_{0.22}Co_{0.11}Mn_{0.66}O_2$ reported that the cycleability with an IL electrolyte was superior to that with an organic solvent electrolyte at 20 °C, [27] which clearly indicates that IL electrolytes present more stable cycling behavior, not only at elevated temperature but also at room temperature, than that with the organic solvent electrolyte. Cycling of $Na_{0.45}Ni_{0.22}Co_{0.11}Mn_{0.66}O_2$ in 0.5 mol dm^{-3} $Na[PF_6]$-PC/ and 10 mol% Na[TFSA][C_4C_1pyrr][FSA] at 12 mA g^{-1} also revealed improved cycleability and Coulombic efficiency with the IL electrolyte [27]. The initial poor Coulombic efficiency was improved after several cycles for both cells. The $Na_{0.45}Ni_{0.22}Co_{0.11}Mn_{0.66}O_2$ cell with the organic solvent electrolyte exhibited a capacity retention of only 40% (approximately 90 mAh g^{-1}) after 100 cycles with an average Coulombic efficiency of 97.8%, whereas the cell with the IL electrolyte showed 80% capacity retention (discharge capacity of 177 mAh g^{-1}) after 100 cycles with a Coulombic efficiency of 98.7%. The authors claimed that the rapid capacity fading in both electrolytes was due to the irreversibility of the P2–O2 phase transition of $Na_{0.45}Ni_{0.22}Co_{0.11}Mn_{0.66}O_2$. However, the dissolution of Mn ions in the IL electrolyte is restricted, making the $Na_{0.45}Ni_{0.22}Co_{0.11}Mn_{0.66}O_2$ with IL much more electrochemically reversible and stable [27].

The extended cycleability of a Na/Na[FSA]-[C_2C_1im][FSA]/$Na_2FeP_2O_7$ cell was assessed at 363 K [29]. The high capacity retention of 93 % was attained for 1,500 cycles in this cell with an average Coulombic efficiency of 99.9%. Another study using $Na_3V_2(PO_4)_3$ with the same IL electrolyte also revealed very stable cycleability. The capacity retention was 99.9% after 300 cycles at 298 and 363 K at 1C (117 mA g^{-1}). Furthermore, a faster current cycle test at 20C and the elevated temperature of 363 K revealed capacity retention of 89.2%, even after 5000 cycles . This extremely good cycleability was due to the combination of the superior performance of this positive electrode material and stable Na metal deposition-dissolution at the counter electrode in the IL electrolyte at 363 K [114].

A study on $Na_3V_2(PO_4)_3$ in Na[PF_6]-[C_4C_1im][TFSA] (Na[PF_6] = 0.1, 0.25, 0.5, and 0.75 mol dm^{-3}) IL electrolytes indicated that optimising the salt concentration of the IL electrolyte could improve capacity and cycleability at the same time [49]. IL of 0.25 mol dm^{-3} Na[PF_6]-[C_4C_1im][TFSA] exhibited a discharge capacity of 107.2 mAh g^{-1} and retained 104 mAh g^{-1} after 40 cycles at the current density of 50 mA g^{-1} [49]. The discharge capacity and capacity retention with the IL were superior to those with 1 mol dm^{-3} Na[PF_6]-PC. The authors suggested that IL electrolyte formed a better SEI on $Na_3V_2(PO_4)_3$ than the organic solvent electrolyte and demonstrated that the concentration of Na[PF_6] is an important parameter for electrochemical performance [49]. It should be noted that the (de)sodiation process can be promoted by supplying a sufficient amount of $Na^{+,}$ while excessive Na^+ can negatively affect electrochemical performance owing to the decreased ionic conductivity of the electrolyte.

1.5 Aims of Study

The greatest challenge for secondary batteries systems are safe, cycleability (life-span), energy and power densities and are of reasonable cost. Therefore, the present study aims at i) development of economic positive electrode materials, ii) development of high energy and power densities electrode material, iii) wide temperature operable batteries, iv) establishment of analytical tools using electrical impedance spectroscopy, and v) launch of safe Li metal secondary batteries. The aim of each chapter is provided below.

Chapter 2 describes experimental details generally required for this thesis.

In Chapter 3, the charge-discharge behavior and long term cycleability of maricite-

$NaFePO_4$ were evaluated at 298 K and 363 K using the Na[FSA]-[C_3C_1pyrr]FSA (30:70 molar ratio) IL electrolytes. The purpose of this chapter is to evaluate the capacity impro vement through the elevating operating temperature.

In Chapter 4, the electrochemical properties of the as-synthesized maricite-$NaFePO_4$, the ball-milled maricite-$NaFePO_4$, and the re-calcined maricite-$NaFePO_4$ electrodes are investigated in the Na[FSA]-[C_2C_1im][FSA] IL electrolyte at 298 and 363 K to verify the effects of temperature and crystallite size on electrochemical performance. The structural variation of maricite-$NaFePO_4$ by sodiation/desodiation was studied by *ex-situ* XRD analysis.

In Chapters 5, the charge-discharge behavior of carbon-coated $Na_3V_2(PO_4)_3$ is investigated in the Na[FSA]-[C_2C_1im][FSA] IL at 243–363 K to evaluate the operability of the IL electrolyte for wide-temperature Na secondary battery applications. The temperature and salt concentration dependence of the rate capability and cycleability was also examined.

In Chapter 6, carbon nanofibers (CNFs) are incorporated as a conductive material along with glucose for carbon coating and fixing CNF frames to $Na_3V_2(PO_4)_3$. Electrochemical measurements using a high mass loading electrode ~8.5 mg-active material cm^{-2} with the Na[FSA]-[C_2C_1im][FSA] IL were carried out to evaluate true rate capability improvement through fabricating electrode materials and elevated operating temperature.

In Chapter 7, symmetric cell electrochemical impedance spectroscopy (SCEIS) is employed to investigate the electrochemical performance of the $Na_2FeP_2O_7$ positive electrode for Na secondary batteries operating at temperatures ranging from room to intermediate temperatures using Na[FSA]-[C_2C_1im][FSA] with various Na[FSA] concentration. Furthermore, high-frequency and charge-transfer resistance and activation energies were discussed with various electrode conditions to provide detailed interpretation methods using those for other materials.

In Chapter 8, Li mental dendrite growth in Li[FSA]-[C_2C_1im][FSA] and dead Li accumulation behavior were investigated. The electrochemical and optical analysis using Li/Li cycling test, XPS, SEM, and EIS on Li metal was investigated to be used as a negative electrode for Li metal secondary batteries

Table 1-1 Comparison of selected information on Na and Li [23, 25, 115].

	Na	Li
E^0 (vs. SHE)	–2.71 V	–3.04 V
Ionic radius	1.02 Å	0.76 Å
Melting point	371 K	454 K
Price (Carbonate)	150 USD T^{-1}	<5000 USD T^{-1}
Capacity, (metal)	1165 mAh g^{-1}	3829 mAh g^{-1}
Distribution	Evenly worldwide	70% in South America

Table 1-2 Structural information and electrochemical properties of positive electrode materials tested in Na secondary batteries using IL electrolytes.

Positive electrode	Lattice system	Space group	Redox couple	Average potential / V	Theoretical capacity / mAh g^{-1}	Ref.
$Na_2FeP_2O_7$	Triclinic	$P\bar{1}$	Fe^{3+}/Fe^{2+}	2.9	97	[116]
$Na_{1.56}Fe_{1.22}P_2O_7$	Triclinic	$P\bar{1}$	Fe^{3+}/Fe^{2+}	3.0	118	[61-63]
$NaFePO_4$ (maricite)	Orthorhombic	*Pnma*	Fe^{4+}/Fe^{3+}	2.6	155	[51]
$NaFePO_4$ (tryphylite)	Orthorhombic	*Pnma*	Fe^{4+}/Fe^{3+}	2.7	155	[51]
$NaVOPO_4$	Monoclinic	$P2_1/c$	V^{5+}/V^{4+}	3.6	145	[67]
$Na_3V_2(PO_4)_3$	Rhombohedral	$R\bar{3}c$	V^{3+}/V^{2+}	3.4	117	[117]
$Na_4Ni_3(PO_4)_2(P_2O_7)$	Orthorhombic	$Pn2_1a$	Ni^{3+}/Ni^{2+}	4.8	127	[28]
Na_2MnSiO_4	Monoclinic	*P*n	Mn^{4+}/Mn^{2+}	3.3	278 (two-electron) 125 (one-electron)	[65, 66]
$Na_{0.44}MnO_2$	Orthorhombic	*Pbam*	Mn^{4+}/Mn^{3+}	3.0	127	[90, 118]
O3-$NaCrO_2$	Monoclinic	$R\bar{3}m$	Cr^{4+}/Cr^{3}	2.9	125	[119]
O3-$Na_{2/3}Fe_{2/3}Mn_{1/3}O_2$	Rhombohedral	$R\bar{3}m$	Me^{3+}/Me^{4+} (Me = $Fe_{2/3}Mn_{1/3}$)	2.7	174	[85, 120]
P2-$Na_{2/3}Fe_{2/3}Mn_{1/3}O_2$	Hexagonal	$P6_3/mmc$	Me^{3+}/Me^{4+} (Me = $Fe_{2/3}Mn_{1/3}$)	2.5	174	[85, 120]
P2-$Na_{0.6}Mn_{0.9}Co_{0.1}O_2$	Hexagonal	$P6_3/mmc$	Me^{3+}/Me^{4+} (Me = $Mn_{0.9}Co_{0.1}$)	2.2	159	[121]
P2-$Na_{2/3}Ni_{1/3}Mn_{2/3}O_2$	Hexagonal	$P6_3/mmc$	Ni^{4+}/Ni^{2+}	3.5	172	[88]
P2-$Na_{2/3}Fe_{1/3}Mn_{2/3}O_2$	Hexagonal	$P6_3/mmc$	Me^{3+}/Me^{4+} (Me = $Fe_{1/3}Mn_{2/3}$)	2.0	261	[87]
P2-$Na_{2/3}Ni_{0.30}Co_{0.15}$ $Mn_{0.55}O_2$	Hexagonal	$P6_3/mmc$	Ni^{4+}/Ni^{2+} Mn^{4+}/Mn^{3+} Co^{4+}/Co^{3+}	1.8	120	[89, 122]
P2-$Na_{0.45}Ni_{0.22}Co_{0.11}Mn_{0.66}O_2$	Hexagonal	$P6_3/mmc$	Ni^{4+}/Ni^{2+} Mn^{4+}/Mn^{3+} Co^{4+}/Co^{3+}	2.7	123	[123]
P2-$Na_{0.45}Ni_{0.22}Co_{0.11}Mn_{0.66}O_2$	Hexagonal	$P6_3/mmc$	Ni^{4+}/Ni^{2+}		~230*	[27]
P2-$Na_{0.6}Ni_{0.22}Fe_{0.11}Mn_{0.66}O_2$	Hexagonal	$P6_3/mmc$	Mn^{4+}/Mn^{3+} Co^{4+}/Co^{3+} Ni^{4+}/Ni^{2+} Fe^{3+}/Fe^{2+}	3.1	~150*	[77, 124]
P2-$Na_{2/3}Ti_{0.1}Fe_{0.1}Mn_{0.8}O_2$	Hexagonal	$P6_3/mmc$	Mn^{4+}/Mn^{3+}	2.8	176	[120, 125]

* Specific discharge capacity

Table 1-3 Specifications of positive electrode materials in IL electrolytes.^{a}

Cell configuration	Electrolyte	Mass loading / mg cm^{-2}	Temp. / K	Discharge capacity / mAh g^{-1} @ mA g^{-1}	Rate capability / mAh g^{-1} @ mA g^{-1}	Cycleability	Ref.
Na/Na$_2$FeP$_2$O$_7$	56 mol% Na[FSA]-K[FSA]	–	363	91 @ 10	59 @ 2000	91% after 1000 cycles	[60]
Na/Na$_2$FeP$_2$O$_7$	30 mol% Na[FSA]-[C$_2$C$_1$im][FSA]	–	298	89 @ 1	17 @ 2000	97% after 300 cycles	[29]
Na/Na$_2$FeP$_2$O$_7$	30 mol% Na[FSA]-[C$_2$C$_1$im][FSA]	–	363	93 @ 10	83 @ 2000	93% after 1500 cycles	[29]
Na/Na$_{1.56}$Fe$_{1.22}$P$_2$O$_7$	20 mol% Na[FSA]-[C$_3$C$_1$pyrr][FSA]	2	298	363 @ 11.8	47 @ 1180	98.5% after 300 cycles	[63]
Na/Na$_{1.56}$Fe$_{1.22}$P$_2$O$_7$	20 mol% Na[FSA]-[C$_3$C$_1$pyrr][FSA]	2	363	0	64 @ 4720	71% after 3000 cycle	[63]
Na/Na$_4$Ni$_3$(PO$_4$)$_2$(P$_2$O$_7$)	10 mol% Na[TFSA]-[C$_4$C$_1$pyrr][FSA]	2.8	293	63 @ 10	–	–	[28]
Na$_3$V$_2$(PO$_4$)$_3$/Na$_3$V$_2$(PO$_4$)$_3$	0.4 mol dm^{-3} Na[BF$_4$]-[C$_2$C$_1$im][BF$_4$]	–	298	63 @ 0.1	~15 @ 2.0	–	[36]
Na$_3$V$_2$(PO$_4$)$_3$/Na$_3$V$_2$(PO$_4$)$_3$	0.4 mol dm^{-3} Na[BF$_4$]-[C$_2$C$_1$im][BF$_4$]	–	353	83 @ 0.1	~25 @ 2.0	–	[36]
AC*/Na$_3$V$_2$(PO$_4$)$_3$	0.3 mol dm^{-3} Na[TFSA]-[C$_4$Hpyrr][TFSA]	1.6	313	70 @ 118	~25 @ 1180	93 mAh g^{-1} after 100 cycles	[47]
HC**//Na$_3$V$_2$(PO$_4$)$_3$	1 mol dm^{-3} Na[FSA]-[C$_3$C$_1$pyrr][FSA]	–	298	85 @ 11.7	60 @ 234	75 % after	[126]
Na/Na$_3$V$_2$(PO$_4$)$_3$@C	0.25 mol dm^{-3} Na[PF$_6$]-[C$_4$C$_1$im][TFSA]	–	298	107 @ 50	–	104 mAh g^{-1} after 50 cycles	[49]
Na/*t*-NaFePO$_4$	0.5 mol dm^{-3} Na[TFSA]-[C$_4$C$_1$pyrr][TFSA]	–	323	125 @ 7.8	75 @ 155	83% after 100 cycles	[53]
Na/*t*-NaFePO$_4$	1 mol dm^{-3} Na[BF$_4$]-[C$_4$C$_1$pyrr][TFSA]	2.5	348	152 @ 7.8	91 @ 155	363% after 100 cycles	[52]
Na/*t*-NaFePO$_4$	42 mol% Na[FSA]-[N$_{2(20201)3}$][FSA]	–	323	97 @ 15.5	66 @ 155	71% after 100 cycles	[54]
Na/*t*-NaFePO$_4$	45 mol% Na[FSA]-[P$_{1i4i4i4}$][FSA]	–	323	113 @ 15.5	88 @ 155	12% after 100 cycles	[54]
Na/*t*-NaFePO$_4$	55 mol% Na[FSA]-[P$_{111i4}$][FSA]	–	323	107 @ 15.5	84 @ 155	95% after 100 cycles	[54]
Na/NaVOPO$_4$-AB-8h	20 mol% Na[FSA]-[C$_3$C$_1$pyrr][FSA]	2	298	60 @ 5	–	–	[68]
Na/NaVOPO$_4$-AB-8h	20 mol% Na[FSA]-[C$_3$C$_1$pyrr][FSA]	2	363	101 @ 5	77 @ 725	76% after 300 cycles	[68]
Na/NaCrO$_2$	56 mol% Na[FSA]-K[FSA]	–	353	77 @ 15	58 @ 150	89% after 100 cycles	[82]
Na/NaCrO$_2$	10 mol % Na[TFSA]-Cs[TFSA]	–	423	94 @ 10	66.4 @ 100	83.4 mAh g^{-1} after 10 cycles	[83]
Na/NaCrO$_2$	20 mol% Na[FSA]-[C$_3$C$_1$pyrr][FSA]	–	298	92 @ 20	–	–	[127]
Na/NaCrO$_2$	20 mol% Na[FSA]-[C$_3$C$_1$pyrr][FSA]	–	353	106 @ 20	62 @ 500	–	[127]
HC**/NaCrO$_2$	20 mol% Na[FSA]-[C$_3$C$_1$pyrr][FSA]	13.5 (HC 5.2)	298	27 Ah @ 2.7 A	26 Ah @ 10.8 A	–	[128]
HC**/NaCrO$_2$	20 mol% Na[FSA]-[C$_3$C$_1$pyrr][FSA]	13.5 (HC 5.2)	333	28 Ah @ 2.7 A	27 Ah @ 10.8 A	87% after 500 cycels	[128]
HC**/NaCrO$_2$	20 mol% Na[FSA]-[C$_3$C$_1$pyrr][FSA]	13.5 (HC 5.2)	363	28 Ah @ 2.7 A	27 Ah @ 10.8 A	–	[128]
Na/NaMnO$_2$	10 mol% Na[TFSA]-[C$_4$C$_1$pyrr][TFSA]	2-4	298	130 @ 9.7	–	81% after 10 cycles	[129]
Na/Na$_{0.44}$MnO$_2$	[Na(G5)$_1$][TFSA]	–	333	110 @ 12.7	–	95% after 30 cycles	[91]
Na/Na$_{0.44}$MnO$_2$	1 mol dm^{-3} Na[ClO$_4$]-[C$_4$C$_1$pyrr][TFSA]	–	323	109 @ 6.4	82 @ 127	80% after 100 cycles	[118]
HC**//Na$_{0.44}$MnO$_2$	1 mol dm^{-3} Na[FSA]-[C$_3$C$_1$pyrr][FSA]	1.5	298	120 @ 30	70 @ 1000	97% after 100 cycles	[130]
Na/P2-Na$_{2/3}$Fe$_{1/3}$Mn$_{2/3}$O$_2$	20 mol% Na[FSA]-[C$_3$C$_1$pyrr][FSA]	–	363	227 @ 20	65 @ 500	64% after 200 cycles	[87]
Na/P2-Na$_{2/3}$Fe$_{2/3}$Mn$_{1/3}$O$_2$	2.3 mol dm^{-3} Na[FSA]-[P$_{111i4}$][FSA]	–	323	130 @ 17.4	110 @ 34.8	–	[86]
Na/O3-Na$_{2/3}$Fe$_{2/3}$Mn$_{1/3}$O$_2$	2.3 mol dm^{-3} Na[FSA]-[P$_{111i4}$][FSA]	–	323	167 @ 17.4	130 @ 34.8	57% after 100 cycles	[86]
Na/P2-Na$_{2/3}$Ni$_{1/3}$Mn$_{2/3}$O$_2$	1 mol dm^{-3} Na[TFSA]-[C$_4$C$_1$pyrr][TFSA]	3	333	220 @ 10	–	200 mAh g^{-1} after 14 cycles	[88]
Na/Na$_{0.6}$Mn$_{0.9}$Co$_{0.1}$O$_2$	0.5 mol dm^{-3} Na[FSA]-DEME-[TFSA]	–	298	205 @ 20	68 @ 400	70% after 350 cycles	[131]
Na/Na$_{0.6}$Mn$_{0.9}$Co$_{0.1}$O$_2$	0.5 mol dm^{-3} Na[FSA]-MOEMPIP-[TFSA]	–	298	117 @ 20	20 @ 400	80% after 350 cycles	[131]
Na/P2-NaNa$_{0.6}$Ni$_{0.22}$Fe$_{0.11}$Mn$_{0.66}$O$_2$	0.2 mol dm^{-3} Na[TFSA]-[C$_4$C$_1$pyrr][TFSA]	1	298	150 @ 10	–	–	[124]
Na$_x$SB-C/P2-NaNa$_{0.6}$Ni$_{0.22}$Fe$_{0.11}$Mn$_{0.66}$O$_2$	0.2 mol dm^{-3} Na[TFSA]-[C$_4$C$_1$pyrr][TFSA]	1 (Na$_x$SB-C 1.9)	298	120 @ 10	–	–	[124]

AC*/$Na_{0.67}Mn_{0.89}Mg_{0.11}O_2$	0.3 mol dm^{-3} Na[TFSA]-[C_4C_1pyrr][TFSA]	2.1	313	57 @ 100	–	59 mAh g^{-1} after 100 cycles	[47]
$Na_{2.55}V_6O_{16}$/$Na_{0.6}Co_{0.1}Mn_{0.9}O_2$	0.5 mol dm^{-3} Na[FSA]-[C_4C_1pyrr][TFSA]	1.75 ($Na_{2.55}V_6O_{16}$0.65)	298	125 @ 50	60 @ 600	76% after 100 cycles	[132]
Na/P2-$Na_{0.45}Ni_{0.22}Co_{0.11}Mn_{0.66}O_2$	0.4 mol dm^{-3} Na[TFSA]-[C_4C_1pyrr][TFSA]	2.5	293	210 @ 23	–	80% after 100 cycles	[27]
Na/P2-$Na_{2/3}Mn_{0.55}Ni_{0.30}Co_{0.15}O_2$	[Na(G1)$_3$][FSA]	6	298	120 @ 12	84 @ 120	88% after 100 cycles	[89]
Na/P2-$Na_{2/3}Mn_{0.8}Fe_{0.1}Ti_{0.1}$O2	2.3 mol dm^{-3} Na[FSA]-[P_{111i4}][FSA]	–	323	176 @ 17.6	125 @ 88	92% after 50 cycles	[120]
Na/P2-$Na_{2/3}Mn_{0.8}Fe_{0.1}Ti_{0.1}$O2	45 mol% Na[FSA][$P_{1i4i4i4}$][FSA]	–	323	101 @ 17.6	60 @ 88	28% after 50 cycles	[120]
Na/P2-$Na_{2/3}Mn_{0.8}Fe_{0.1}Ti_{0.1}$O2	55 mol% Na[FSA][$N_{2(2O2O1)3}$][FSA]	–	323	153 @ 17.6	30 @ 88	58% after 50 cycles	[120]
Na/Calix[4]quinone	0.3 mol dm^{-3} Na[TFSA]-[C_3C_1pyrr][TFSA]	0.58	298	406 @ 20	–	99.7 after 300 cycles	[98]
Na/5,7,12,14-pentacenetetrone	0.3 mol dm^{-3} Na[TFSA]-[C_3C_1pyrr][TFSA]	0.58	298	245 @ 30	–	–	[98]

*AC = activated carbon, ** HC = hard carbon, *** CNF = carbon nanofiber **** Na2TP = diNa terephthalate, TFSA = TFSI = bis(trifluoromethylsulfonyl)amide, FSA = FSI = bis(fluorosulfonyl)amide), C_2C_1im = EMI = 1-ethyl-3-methylimidazolium, C_3C_1pyrr = *N*-methyl-*N*-propylpyrrolidinium, C_4C_1pyrr =Py_{14} = BMP = pyr_{14} = *N*-butyl-*N*-methyl-pyrrolidinium, Pyr_{H4} N-butyl-pyrrolidinium, G1 = monoglyme, G5 = pentaglyme, P_{111i4} = trimethyl-iso-butyl phosphonium, $P_{1i4i4i4}$ = methyl-tri-isobutyl, $N_{2(2O2O1)3}$FSA = N-ethyl-2-(2-methoxyethoxy)-N,N-bis(2-(2-methoxyethoxy)ethyl)ethan-1-ammonium, MOEMPIP = 1-(2-methoxyethyl)-1-methylpiperidinium, DEME = N,N-diethyl-2-methoxy-N-methylethanamonium

Table 1-4. Comparison of ionic conductivity for organic and ionic liquid electrolytes [111, 113, 133].

	Ionic conductivity / mS cm^{-1}
1 mol dm^{-3} NaClO$_4$-PC [133]	6 (298 K)
30 mol% Na[FSA]-[C$_3$C$_1$pyrr][FSA] [111]	5 (298 K) 17 (363 K)
30 mol% Na[FSA]-[C$_2$C$_1$im][FSA] [113]	5 (298 K) 31 (363 K)

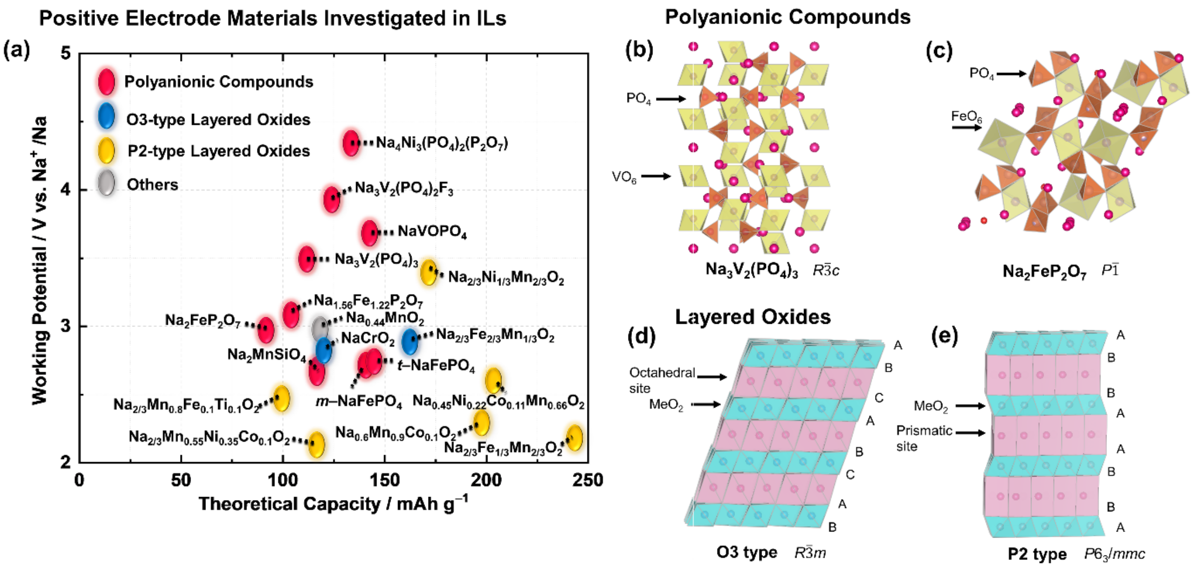

Figure 1-1 Positive electrode materials for Na secondary batteries investigated in IL electrolytes. (a) The relationship between theoretical capacity and working potential. Crystal structures of selected polyanionic compounds: (b) $Na_3V_2(PO_4)_3$, (c) $Na_2FeP_2O_7$, (d) O3-type layered oxide, and (e) a P2-type layered oxide.

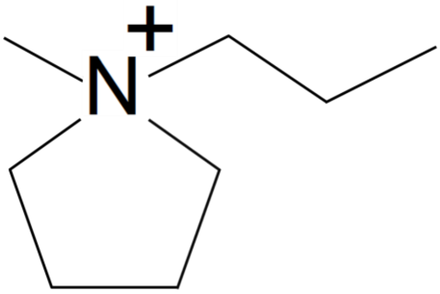

Figure 1-2 Structure of *N*-methyl-*N*-propylpyrrolidinium cation ($C_3C_1pyrr^+$).

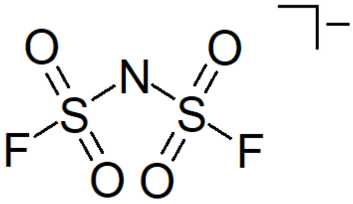

Figure 1-3 Structure of bis(fluorosulfonyl)amide anion (FSA^-).

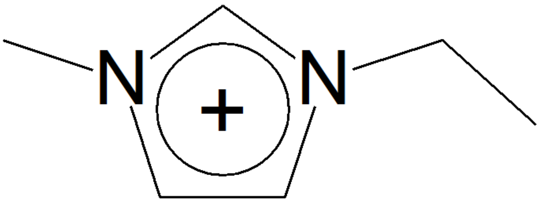

Figure 1-4 Structure of 1-ethyl-3-methylimidazolium cation ($C_2C_1im^+$).

References

[1] P. J. Meier, P. P. H. Wilson, G. L. Kulcinski, and P. L. Denholm, Energy Policy, 33 (2005) 1099.

[2] Z. Yang, J. Zhang, M. C. W. Kintner-Meyer, X. Lu, D. Choi, J. P. Lemmon, and J. Liu, Chem. Rev., 111 (2011) 3577.

[3] Climate Change Indicators in the United States, 4th Edn., USEPA (2016).

[4] Kyoto Protocol to the United Nations Framework Convention on Climate Change, UN (1998).

[5] B. Dunn, H. Kamath, and J.-M. Tarascon, Science, 334 (2011) 928.

[6] J. Liu, J.-G. Zhang, Z. Yang, J. P. Lemmon, C. Imhoff, G. L. Graff, L. Li, J. Hu, C. Wang, J. Xiao, G. Xia, V. V. Viswanathan, S. Baskaran, V. Sprenkle, X. Li, Y. Shao, and B. Schwenzer, Adv. Funct. Mater., 23 (2013) 929.

[7] B. Dunn, H. Kamath, and J. M. Tarascon, Science, 334 (2011) 928.

[8] G. L. Soloveichik, Annu. Rev. Chem. Biomol. Eng., 2 (2011) 503.

[9] J. B. Goodenough, and K. S. Park, J. Am. Chem. Soc., 135 (2013) 1167.

[10] L. Chen, M. Fiore, J. E. Wang, R. Ruffo, D.-K. Kim, and G. Longoni, Adv. Sustainable Syst., 2 (2018) 1700153.

[11] S. L. David, and K. Jonathan, Energy J., 25 (2004) 19.

[12] M. Wolsink, Renew. Sustain. Energy Rev., 16 (2012) 822.

[13] G. L. Soloveichik, Annual. Rev. Chem. Biom. Eng., 2 (2011) 503.

[14] V. Etacheri, R. Marom, R. Elazari, G. Salitra, and D. Aurbach, Energy Environ. Sci., 4 (2011) 3243.

[15] J. B. Goodenough, and Y. Kim, Chem. Mater., 22 (2010) 587.

[16] J. M. Tarascon, and M. Armand, Nature, 414 (2001) 359.

[17] B. Scrosati, J. Hassoun, and Y.-K. Sun, Energy Environ. Sci., 4 (2011) 3287.

[18] J.-M. Tarascon, Nat. Chem., 2 (2010) 510.

[19] R. Shannon, Acta Crystallogr A, 32 (1976) 751.

[20] D. Wu, X. Li, B. Xu, N. Twu, L. Liu, and G. Ceder, Energy Environ. Sci., 8 (2015) 195.

[21] P. Barpanda, G. Oyama, S.-i. Nishimura, S.-C. Chung, and A. Yamada, Nat. Commun., 5 (2014) 4358.

[22] V. Palomares, P. Serras, I. Villaluenga, K. B. Hueso, J. Carretero-González, and T. Rojo, Energy Environ. Sci., 5 (2012) 5884.

[23] S.-W. Kim, D.-H. Seo, X. Ma, G. Ceder, and K. Kang, Adv. Energy. Mater., 2 (2012) 710.

[24] N. Yabuuchi, K. Kubota, M. Dahbi, and S. Komaba, Chem. Rev., 114 (2014) 11636.

[25] M. D. Slater, D. Kim, E. Lee, and C. S. Johnson, Adv. Funct. Mater., 23 (2013) 947.

[26] H. Kim, H. Kim, Z. Ding, M. H. Lee, K. Lim, G. Yoon, and K. Kang, Adv. Energy. Mater., 6 (2016) 1600943.

[27] L. G. Chagas, D. Buchholz, L. Wu, B. Vortmann, and S. Passerini, J. Power Sources, 247 (2014) 377.

[28] H. Zhang, I. Hasa, D. Buchholz, B. Qin, D. Geiger, S. Jeong, U. Kaiser, and S. Passerini, NPG Asia Mater., 9 (2017) e370.

[29] C.-Y. Chen, T. Kiko, T. Hosokawa, K. Matsumoto, T. Nohira, and R. Hagiwara, J. Power Sources, 332 (2016) 51.

[30] C. Delmas, C. Fouassier, and P. Hagenmuller, Physica B+C, 99 (1980) 81.

[31] Z. Gong, and Y. Yang, Energy Environ. Sci., 4 (2011) 3223.

[32] C. Masquelier, and L. Croguennec, Chem. Rev., 113 (2013) 6552.

[33] M. Dutreilh, C. Chevalier, M. El-Ghozzi, D. Avignant, and J. M. Montel, J. Solid State Chem., 142 (1999) 1.

[34] A. K. Padhi, K. S. Nanjundaswamy, and J. B. Goodenough, J. Electrochem. Soc., 144 (1997) 1188.

[35] J. M. Clark, S.-i. Nishimura, A. Yamada, and M. S. Islam, Angew. Chem. Int. Ed., 51 (2012) 13149.

[36] L. S. Plashnitsa, E. Kobayashi, Y. Noguchi, S. Okada, and J.-i. Yamaki, J. Electrochem. Soc., 157 (2010) A536.

[37] W. Song, X. Ji, Z. Wu, Y. Zhu, Y. Yang, J. Chen, M. Jing, F. Li, and C. E. Banks, J. Mater. Chem. A, 2 (2014) 5358.

[38] Z. Jian, Y.-S. Hu, X. Ji, and W. Chen, Adv. Mater., 29 (2017) 1601925.

[39] J. Gaubicher, C. Wurm, G. Goward, C. Masquelier, and L. Nazar, Chem. Mater., 12 (2000) 3240.

[40] P. Barpanda, L. Lander, S.-i. Nishimura, and A. Yamada, Adv. Energy. Mater., 8 (2018) 1703055.

[41] B. Senthilkumar, C. Murugesan, L. Sharma, S. Lochab, and P. Barpanda, Small Methods, 3 (2019) 1800253.

[42] S.-P. Guo, J.-C. Li, Q.-T. Xu, Z. Ma, and H.-G. Xue, J. Power Sources, 361 (2017) 285.

[43] I. Zatovsky, Acta Cryst. E, 66 (2010) i12.

[44] B. L. Cushing, and J. B. Goodenough, J. Solid State Chem., 162 (2001) 176.

[45] W. Duan, Z. Zhu, H. Li, Z. Hu, K. Zhang, F. Cheng, and J. Chen, J. Mater. Chem. A, 2 (2014) 8668.

[46] K. Saravanan, C. W. Mason, A. Rudola, K. H. Wong, and P. Balaya, Adv. Energy. Mater., 3 (2013) 444.

[47] T. Vogl, C. Vaalma, D. Buchholz, M. Secchiaroli, R. Marassi, S. Passerini, and A. Balducci, J. Mater. Chem. A, 4 (2016) 10472.

[48] T. C. Mendes, X. Zhang, Y. Wu, P. C. Howlett, M. Forsyth, and D. R. Macfarlane, ACS Sustainable Chem. Eng., 7 (2019) 3722.

[49] F. Wu, N. Zhu, Y. Bai, Y. Li, Z. Wang, Q. Ni, H. Wang, and C. Wu, Nano Energy, 51 (2018) 524.

[50] J. Wang, and X. Sun, Energy Environ. Sci., 8 (2015) 1110.

[51] M. Avdeev, Z. Mohamed, C. D. Ling, J. Lu, M. Tamaru, A. Yamada, and P. Barpanda, Inorg. Chem., 52 (2013) 8685.

[52] N. Wongittharom, C.-H. Wang, Y.-C. Wang, C.-H. Yang, and J.-K. Chang, ACS Appl. Mater. Interfaces, 6 (2014) 17564.

[53] N. Wongittharom, T.-C. Lee, C.-H. Wang, Y.-C. Wang, and J.-K. Chang, J. Mater. Chem. A, 2 (2014) 5655.

[54] M. Hilder, P. C. Howlett, D. Saurel, H. Anne, M. Casas-Cabanas, M. Armand, T. Rojo, D. R. MacFarlane, and M. Forsyth, J. Power Sources, 406 (2018) 70.

[55] S. P. Ong, V. L. Chevrier, G. Hautier, A. Jain, C. Moore, S. Kim, X. Ma, and G. Ceder, Energy Environ. Sci., 4 (2011) 3680.

[56] J. Kim, D.-H. Seo, H. Kim, I. Park, J.-K. Yoo, S.-K. Jung, Y.-U. Park, W. A. Goddard Iii, and K. Kang, Energy Environ. Sci., 8 (2015) 540.

[57] Y. Niu, Y. Zhang, and M. Xu, J. Mater. Chem. A (2019).

[58] P. Barpanda, G. Liu, C. D. Ling, M. Tamaru, M. Avdeev, S.-C. Chung, Y. Yamada, and A. Yamada, Chem. Mater., 25 (2013) 3480.

[59] T. Honma, T. Togashi, N. Ito, and T. Komatsu, J. Ceram. Soc. Jpn., 120 (2012) 344.

[60] C.-Y. Chen, K. Matsumoto, T. Nohira, R. Hagiwara, Y. Orikasa, and Y. Uchimoto, J. Power Sources, 246 (2014) 783.

[61] T. Honma, N. Ito, T. Togashi, A. Sato, and T. Komatsu, J. Power Sources, 227 (2013) 31.

[62] K.-H. Ha, S. H. Woo, D. Mok, N.-S. Choi, Y. Park, S. M. Oh, Y. Kim, J. Kim, J. Lee, L. F. Nazar, and K. T. Lee, Adv. Energy. Mater., 3 (2013) 770.

[63] C.-Y. Chen, K. Matsumoto, T. Nohira, and R. Hagiwara, J. Electrochem. Soc., 162 (2015) A176.

[64] Z. Jian, W. Han, X. Lu, H. Yang, Y.-S. Hu, J. Zhou, Z. Zhou, J. Li, W. Chen, D. Chen, and L. Chen, Adv. Energy. Mater., 3 (2013) 156.

[65] C.-Y. Chen, K. Matsumoto, T. Nohira, and R. Hagiwara, Electrochem. Commun., 45 (2014) 63.

[66] M. Law, V. Ramar, and P. Balaya, J. Power Sources, 359 (2017) 277.

[67] J. Song, M. Xu, L. Wang, and J. B. Goodenough, Chem. Commun., 49 (2013) 5280.

[68] C.-Y. Chen, K. Matsumoto, T. Nohira, and R. Hagiwara, J. Electrochem. Soc., 162 (2015) A2093.

[69] M. Armand, and J. M. Tarascon, Nature, 451 (2008) 652.

[70] K. Kang, Y. S. Meng, J. Bréger, C. P. Grey, and G. Ceder, Science, 311 (2006) 977.

[71] T. Ohzuku, and A. Ueda, Solid State Ionics, 69 (1994) 201.

[72] K. Takada, N. Aotani, K. Iwamoto, and S. Kondo, Solid State Ionics, 79 (1995) 284.

[73] P. He, H. Yu, D. Li, and H. Zhou, J. Mater. Chem., 22 (2012) 3680.

[74] W. Liu, P. Oh, X. Liu, M.-J. Lee, W. Cho, S. Chae, Y. Kim, and J. Cho, Angew. Chem. Int. Ed., 54 (2015) 4440.

[75] S. Okada, Y. Takahashi, T. Kiyabu, T. Doi, J.-I. Yamaki, and T. Nishida, Meeting Abstracts, MA2006-02 (2006) 201.

[76] B. L. Ellis, and L. F. Nazar, Curr. Opin. Solid State Mater. Sci., 16 (2012) 168.

[77] I. Hasa, D. Buchholz, S. Passerini, and J. Hassoun, ACS Appl. Mater. Interfaces, 7 (2015) 5206.

[78] M. H. Han, E. Gonzalo, G. Singh, and T. Rojo, Energy Environ. Sci., 8 (2015) 81.

[79] K. Kubota, and S. Komaba, J. Electrochem. Soc., 162 (2015) A2538.

[80] J. J. Braconnier, C. Delmas, and P. Hagenmuller, Mater. Res. Bull., 17 (1982) 993.

[81] S. Komaba, C. Takei, T. Nakayama, A. Ogata, and N. Yabuuchi, Electrochem. Commun., 12 (2010) 355.

[82] A. Fukunaga, T. Nohira, Y. Kozawa, R. Hagiwara, S. Sakai, K. Nitta, and S. Inazawa, J. Power Sources, 209 (2012) 52.

[83] T. Nohira, T. Ishibashi, and R. Hagiwara, J. Power Sources, 205 (2012) 506.

[84] C. Ding, T. Nohira, A. Fukunaga, and R. Hagiwaraa, Electrochemistry, 83 (2015) 91.

[85] E. Gonzalo, M. H. Han, J. M. López del Amo, B. Acebedo, M. Casas-Cabanas, and T. Rojo, J. Mater. Chem. A, 2 (2014) 18523.

[86] M. Hilder, P. C. Howlett, D. Saurel, E. Gonzalo, M. Armand, T. Rojo, D. R. MacFarlane, and M. Forsyth, J. Power Sources, 349 (2017) 45.

[87] C. Ding, T. Nohira, and R. Hagiwara, Electrochim. Acta, 231 (2017) 412.

[88] T. Risthaus, D. Zhou, X. Cao, X. He, B. Qiu, J. Wang, L. Zhang, Z. Liu, E. Paillard, G. Schumacher, M. Winter, and J. Li, J. Power Sources, 395 (2018) 16.

[89] P. Geysens, V. S. Rangasamy, S. Thayumanasundaram, K. Robeyns, L. Van Meervelt, J.-P. Locquet, J. Fransaer, and K. Binnemans, J. Phys. Chem. B, 122 (2018) 275.

[90] F. Sauvage, L. Laffont, J. M. Tarascon, and E. Baudrin, Inorg. Chem., 46 (2007) 3289.

[91] S. Terada, T. Mandai, R. Nozawa, K. Yoshida, K. Ueno, S. Tsuzuki, K. Dokko, and M. Watanabe, Phys. Chem. Chem. Phys., 16 (2014) 11737.

[92] S. Terada, H. Susa, S. Tsuzuki, T. Mandai, K. Ueno, K. Dokko, and M. Watanabe, J. Phys. Chem. C, 122 (2018) 16589.

[93] Y. Kawabe, N. Yabuuchi, M. Kajiyama, N. Fukuhara, T. Inamasu, R. Okuyama, I. Nakai, and S. Komaba, Electrochem. Commun., 13 (2011) 1225.

[94] X. Lin, X. Hou, X. Wu, S. Wang, M. Gao, and Y. Yang, RSC Advances, 4 (2014) 40985.

[95] J. Qian, M. Zhou, Y. Cao, X. Ai, and H. Yang, Adv. Energy. Mater., 2 (2012) 410.

[96] H. Kim, J. E. Kwon, B. Lee, J. Hong, M. Lee, S. Y. Park, and K. Kang, Chem. Mater., 27 (2015) 7258.

[97] N. Casado, M. Hilder, C. Pozo-Gonzalo, M. Forsyth, and D. Mecerreyes, ChemSusChem, 10 (2017) 1783.

[98] X. Wang, Z. Shang, A. Yang, Q. Zhang, F. Cheng, D. Jia, and J. Chen, Chem, 5 (2019) 364.

[99] H.-g. Wang, and X.-b. Zhang, Chem.: Eur. J., 24 (2018) 18235.

[100] Y. Xu, M. Zhou, and Y. Lei, Mater. Today, 21 (2018) 60.

[101] S. Wu, W. Wang, M. Li, L. Cao, F. Lyu, M. Yang, Z. Wang, Y. Shi, B. Nan, S. Yu, Z. Sun, Y. Liu, and Z. Lu, Nat. Commun., 7 (2016) 13318.

[102] D. Yaakov, Y. Gofer, D. Aurbach, and I. C. Halalay, J. Electrochem. Soc., 157 (2010) A1383.

[103] K. Xu, Chem. Rev., 104 (2004) 4303.

[104] Y. Negishi, W. Kurashige, Y. Niihori, and K. Nobusada, Phys. Chem. Chem. Phys., 15 (2013) 18736.

[105] S. Wilken, P. Johansson, and P. Jacobsson, Solid State Ionics, 225 (2012) 608.

[106] S. Wilken, M. Treskow, J. Scheers, P. Johansson, and P. Jacobsson, RSC Advances, 3 (2013) 16359.

[107] R.-S. Kühnel, M. Lübke, M. Winter, S. Passerini, and A. Balducci, J. Power Sources, 214 (2012) 178.

[108] M. Armand, F. Endres, D. R. MacFarlane, H. Ohno, and B. Scrosati, Nat. Mater., 8 (2009) 621.

[109] V. Acosta, and P. Hemmer, MRS Bulletin, 38 (2013) 127.

[110] Q. Zhou, W. A. Henderson, G. B. Appetecchi, M. Montanino, and S. Passerini, J. Phys. Chem. B, 112 (2008) 13577.

[111] K. Matsumoto, Y. Okamoto, T. Nohira, and R. Hagiwara, J. Phys. Chem. C, 119 (2015) 7648.

[112] C. Ding, T. Nohira, R. Hagiwara, K. Matsumoto, Y. Okamoto, A. Fukunaga, S. Sakai, K. Nitta, and S. Inazawa, J. Power Sources, 269 (2014) 124.

[113] K. Matsumoto, T. Hosokawa, T. Nohira, R. Hagiwara, A. Fukunaga, K. Numata, E. Itani, S. Sakai, K. Nitta, and S. Inazawa, J. Power Sources, 265 (2014) 36.

[114] T. Nohira. T. Hosokawa, K. Matsumoto, and R. Hagiwara, Denki Kagaku, 86 (2018) 293.

[115] H. Pan, Y.-S. Hu, and L. Chen, Energy Environ. Sci., 6 (2013) 2338.

[116] P. Barpanda, T. Ye, S.-i. Nishimura, S.-C. Chung, Y. Yamada, M. Okubo, H. Zhou, and A. Yamada, Electrochem. Commun., 24 (2012) 116.

[117] Z. Jian, L. Zhao, H. Pan, Y.-S. Hu, H. Li, W. Chen, and L. Chen, Electrochem. Commun., 14 (2012) 86.

[118] C.-H. Wang, Y.-W. Yeh, N. Wongittharom, Y.-C. Wang, C.-J. Tseng, S.-W. Lee, W.-S. Chang, and J.-K. Chang, J. Power Sources, 274 (2015) 1016.

[119] C.-Y. Chen, K. Matsumoto, T. Nohira, R. Hagiwara, A. Fukunaga, S. Sakai, K. Nitta, and S. Inazawa, J. Power Sources, 237 (2013) 52.

[120] M. Hilder, P. C. Howlett, D. Saurel, E. Gonzalo, A. Basile, M. Armand, T. Rojo, M. Kar, D. R. MacFarlane, and M. Forsyth, Electrochim. Acta, 268 (2018) 94.

[121] N. Bucher, S. Hartung, J. B. Franklin, A. M. Wise, L. Y. Lim, H.-Y. Chen, J. N. Weker, M. F. Toney, and M. Srinivasan, Chem. Mater., 28 (2016) 2041.

[122] V. S. Rangasamy, L. Zhang, J. W. Seo, J.-P. Locquet, and S. Thayumanasundaram, Electrochim. Acta, 237 (2017) 29.

[123] D. Buchholz, A. Moretti, R. Kloepsch, S. Nowak, V. Siozios, M. Winter, and S. Passerini, Chem. Mater., 25 (2013) 142.

[124] I. Hasa, S. Passerini, and J. Hassoun, J. Power Sources, 303 (2016) 203.

[125] M. H. Han, E. Gonzalo, N. Sharma, J. M. López del Amo, M. Armand, M. Avdeev, J. J. Saiz Garitaonandia, and T. Rojo, Chem. Mater., 28 (2016) 106.

[126] C. V. Manohar, T. C. Mendes, M. Kar, D. wang, C. Xiao, M. Forsyth, S. Mitra, and D. R. MacFarlane, Chem. Commun., 54 (2018) 3500.

[127] C. Ding, T. Nohira, K. Kuroda, R. Hagiwara, A. Fukunaga, S. Sakai, K. Nitta, and S. Inazawa, J. Power Sources, 238 (2013) 296.

[128] A. Fukunaga, T. Nohira, R. Hagiwara, K. Numata, E. Itani, S. Sakai, and K. Nitta, J. Appl. Electrochem., 46 (2016) 487.

[129] S. Brutti, M. A. Navarra, G. Maresca, S. Panero, J. Manzi, E. Simonetti, and G. B. Appetecchi, Electrochim. Acta, 306 (2019) 317.

[130] C.-H. Wang, C.-H. Yang, and J.-K. Chang, Chem. Commun., 52 (2016) 10890.

[131] P. J. Fischer, M. P. Do, R. M. Reich, A. Nagasubramanian, M. Srinivasan, and F. E. Kuehn, Phys. Chem. Chem. Phys., 20 (2018) 29412.

[132] M. P. Do, P. J. Fischer, A. Nagasubramanian, J. Geder, F. E. Kühn, and M. Srinivasan, J. Electrochem. Soc., 166 (2019) A944.

[133] K. Kuratani, N. Uemura, H. Senoh, H. T. Takeshita, and T. Kiyobayashi, J. Power Sources, 223 (2013) 175.

Chapter 2

Experimental

2.1 Apparatus and Material Handling

All the experimental tools were washed with deionized water, acetone, and ethanol, and were completely dried in an oven at 363 K before use. The electrode materials and test cell assembly were handled in a glove box (Miwa Manufacturing Co., Ltd. DBO-2LKH-HNBR) under dried and deoxygenated argon gas (99.995%) with a gas-refining instrument (Miwa Manufacturing Co., Ltd., MS3-P60S-N). The dew point (ca. 163 K) and concentration of oxygen (ca. 0.5 ppm) were monitored during the experiment. The weight of electrodes, ionic liquids (ILs), and samples were measured in the glovebox using electric balances (CPA225D, Sartorius; WMC25-SH, Mettler Toledo).

Synthesized products were dried with a vacuum line and preserved in the Ar atmosphere. The schematic drawings of the vacuum line and drying vessel are shown in Figures 2-1 and 2-2, respectively, which were used to dry the materials and impregnate ILs into separators and electrodes. The vacuum line was made of corrosion-resistant stainless steel pipes (SUS316, 1/2 inch o.d.) connected by the stainless unions and valves with a Kel-F (polychlorotrifluoroethylene) tip (Swagelok Co.). Metal and PFA (tetrafluoroethylene-perfluoroalkyl vinyl ether copolymer) tube (1/4 inch o.d.) were used as the connecting parts to a vacuum vessel. The line was connected to a rotary vacuum pump through a Pyrex glass cold trap. The cold glass trap was cooled down using liquid nitrogen. The pressure was monitored by Pirani gauges. The degree of vacuum was about 1 Pa in this system.

2.2 Synthesis and Fabrication of Electrode Materials

Each chapter will provide details about the preparation and synthetic method of electrode materials. For the ball milling process (Pulverisette 7 Premium Line, Fritsch), specific precursors were thoroughly mixed in the zirconia grinding chamber (Figure 2-3) with balls (diameter = 3 mm). The ball-to-powder volume ratio was 1:2. For the heating treatment, a tube furnace (KTF045N1, Koyo) was used under a steady Ar flow. The heating and cooling rates were 5 and 2 K min^{-1}, respectively. The schematic illustration of the tube furnace is shown in Figure 2-4. The detailed procedures are described in each chapter.

2.3 Material Characterization

2.3.1 X-ray Diffraction (XRD)

The structures of $NaFePO_4$, $Na_3V_2(PO_4)_3$, $NaCrO_4$ and $Na_2FeP_2O_7$ were characterized by XRD using a Rigaku SmartLab diffractometer with Ni-filtered Cu-$K\alpha$ radiation (40 kV and 30 mA) and a silicon strip high-speed detector (Rigaku D/teX Ultra 250). Rietveld refinement was performed by the FullProf software [1]. The crystal structures were visualized using crystallographic data from the Rietveld refinement and the VESTA program [2]. Sodiation/desodiation mechanisms of materials were revealed by *ex-situ* or *in-situ* X-ray diffraction analysis during the charge-discharge test. The samples of *ex-situ* XRD were rinsed with dehydrated tetrahydrofuran (THF; Wako, water content < 10 ppm, oxygen content < 1 ppm) to remove the electrolyte and placed in an air-tight cell with Be windows to avoid exposure to the air. XRD patterns were recorded under an Ar atmosphere at room temperature.

2.3.2 Field Emission Scanning Electron Microscopy (SEM) and Energy Dispersive X-ray Analysis (EDS)

The morphology of samples was observed with a field emission scanning electron microscope (FE-SEM, Hitachi SU-8020) operating at 0.5-10 kV. EDS mapping was performed using an EDS analyzer (Horiba EMAXEvolution X-max) attached to the SEM

2.3.3 Nitrogen Adsorption Measurement

The specific surface area was tested by a nitrogen adsorption/desorption measurement by a Micromeritics TriStar II 3020 analyzer at 77 K and calculated by the Brunauer Emmett and Teller (BET) model [3]. Since the BET theory ignores inhomogeneity of the surface and lateral adsorbate-adsorbate interactions, high energy sites at lower relative pressures ($P/P_0 < 0.05$) may cause the nonlinearity of BET plots. Thus, relative pressure near-completed monolayers ($0.05 < P/P_0 < 0.50$) was used for the surface area determination.

2.3.4 X-ray Photoelectron Spectroscopy (XPS)

The elemental compositions and chemical states of the SEI layer on the Li metal electrode were investigated by X-ray photoelectron spectroscopy (XPS; JEOL, JPS-36310, Mg Kα source). Depth profiles of these electrodes were obtained by a combination with the argon-ion etching apparatus. The accelerating voltage and current of etching were fixed at 800 V and 19.0 mA, respectively.

2.4 Electrochemical Measurement

2.4.1. Electrode and Cell Preparation

The positive electrodes were prepared with two different binders of polytetrafluoroethylene (PTFE) and polyvinylidene fluoride (PVDF). The PTFE electrode, which is schematically shown in Figure 2-5, was prepared by mixing active materials (with several fabricated version, the fabrication conditions were described in each chapter.), carbon black as a conductive additive, and PTFE with a pestle and mortar, and pasted on an Al mesh. The PVDF electrode was prepared by casting the slurry (active materials, carbon black, PVDF, and *N*-methylpyrrolidone (NMP)) on Al foil, followed by drying, as shown in Figure 2-6. Metallic Na discs (Aldrich, purity 99.95%) pressed onto Al disk were used as reference and counter electrodes. Borosilicate glass microfiber filters (Whatman GF/A, the thickness of 260 μm) were used as the separators. The separators were impregnated with Na[FSA]-[C_3C_1pyrr][FSA] and Na[FSA]-[C_2C_1im][FSA] under vacuum at 363 K for 1 day and used as electrolytes. A schematic drawing of the coin cell and symmetric cell with two positive electrodes for EIS is shown in Figures 2-7 and 2-8. For the symmetric cell, another positive electrode was used instead of a Na metal counter electrode. All cells were assembled in the Ar-filled glove box.

2.4.2 Charge-discharge Test

The specific capacity of the electrode materials was evaluated by galvanostatic charge-discharge test. Bio-Logic VSP potentiostat/galvanostat or a charge-discharge unit (HJ1001SD8, Hokuto Denko) was used for controlling the system. The current densities are provided in each chapter. The operating temperature was controlled by an ESPEC SU221 Environmental Test Chamber, and the measurement was normally started after 3 h temperature adjustment.

2.4.3. Electrochemical Impedance Spectroscopy

Electrochemical impedance spectroscopy (EIS) measurements were carried out using a Bio-Logic VSP (Bio-Logic) over a frequency range from 500 kHz to 1 mHz with an AC perturbation voltage of 10 mV.

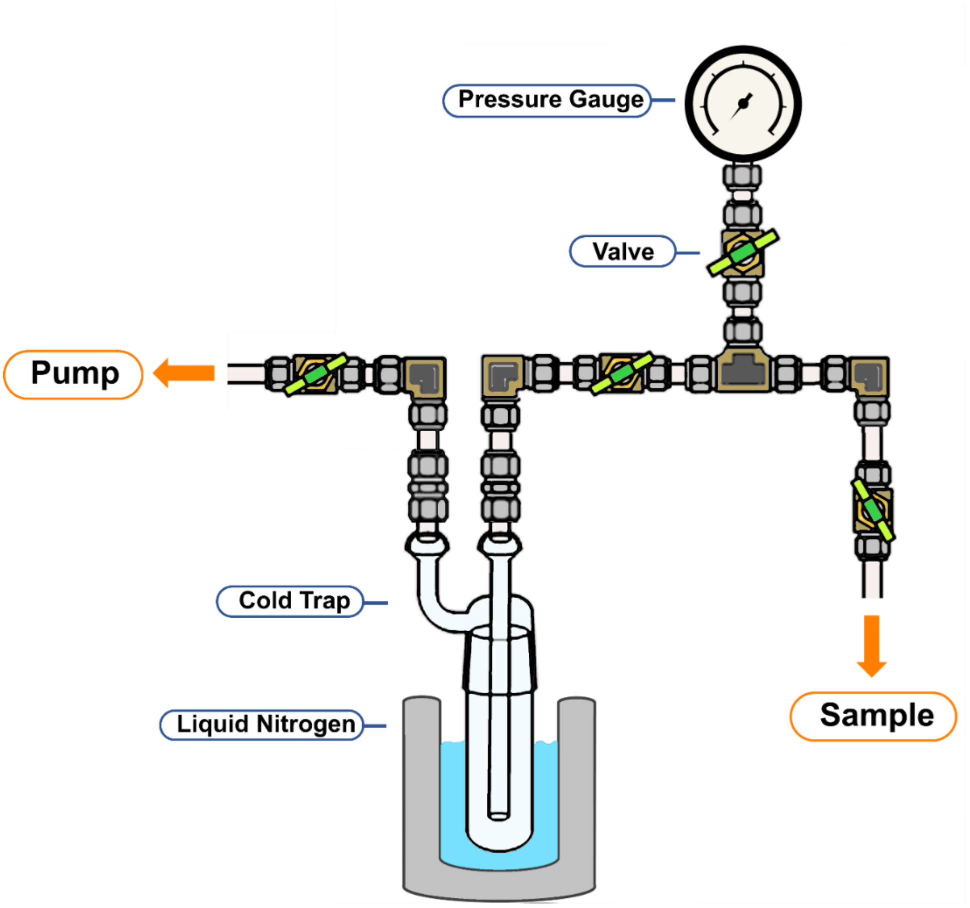

Figure 2-1 A schematic illustration of a vacuum line.

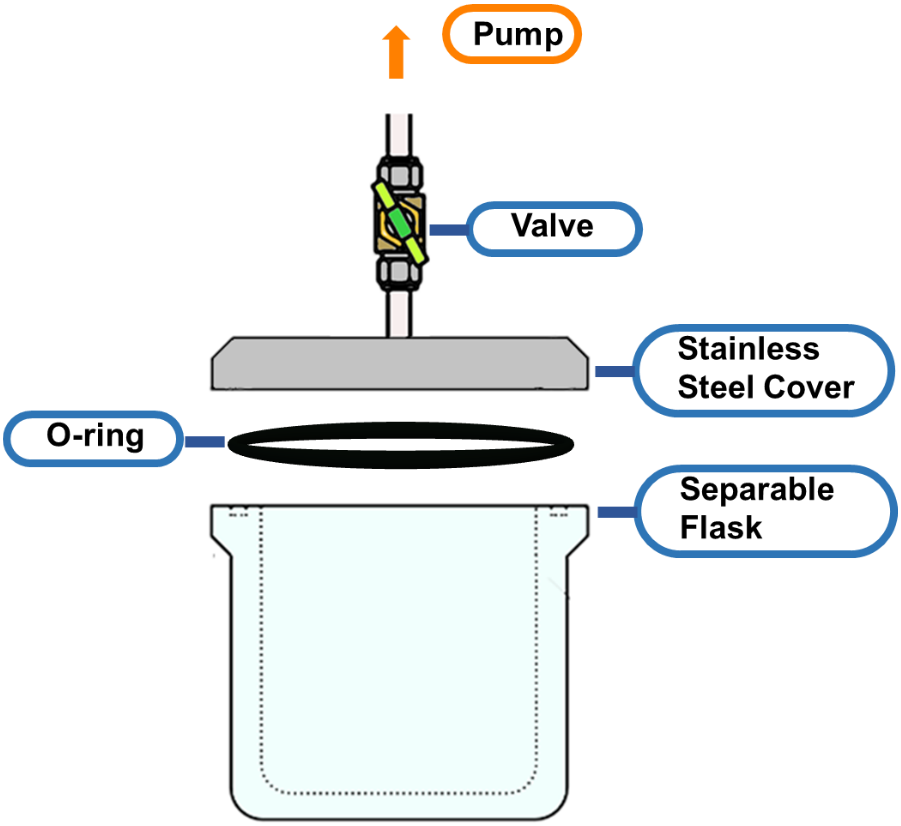

Figure 2-2 A schematic illustration of a vessel for vacuum drying.

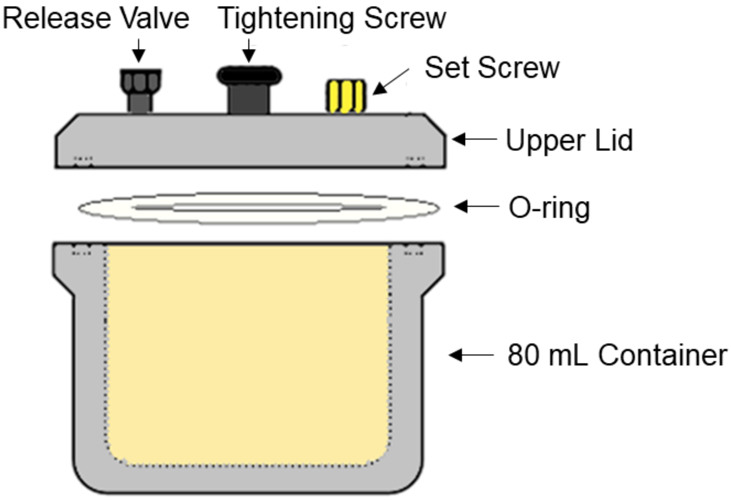

Figure 2-3 A schematic illustration of the ball-milling chamber.

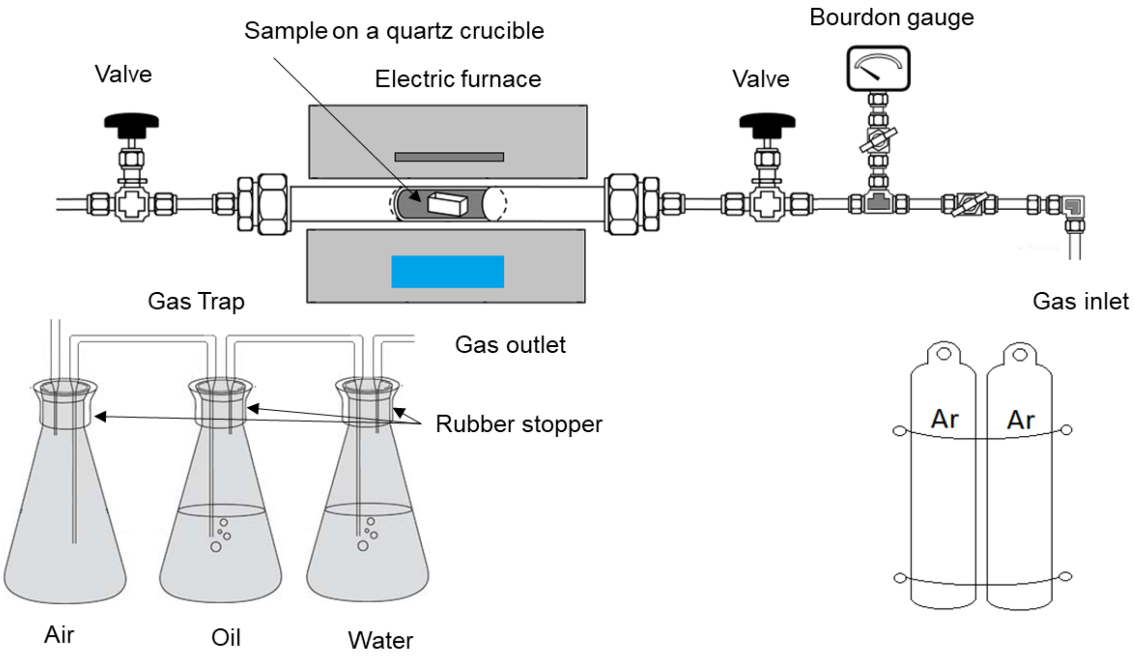

Figure 2-4 A schematic illustration of a tube furnace.

Figure 2-5 An image of the electrode with a PTFE binder attached to Al mesh.

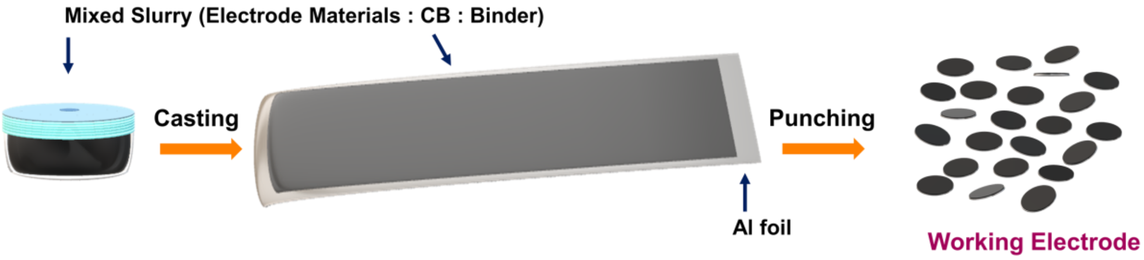

Figure 2-6 A schematic illustration of electrode preparation using PVDF binder.

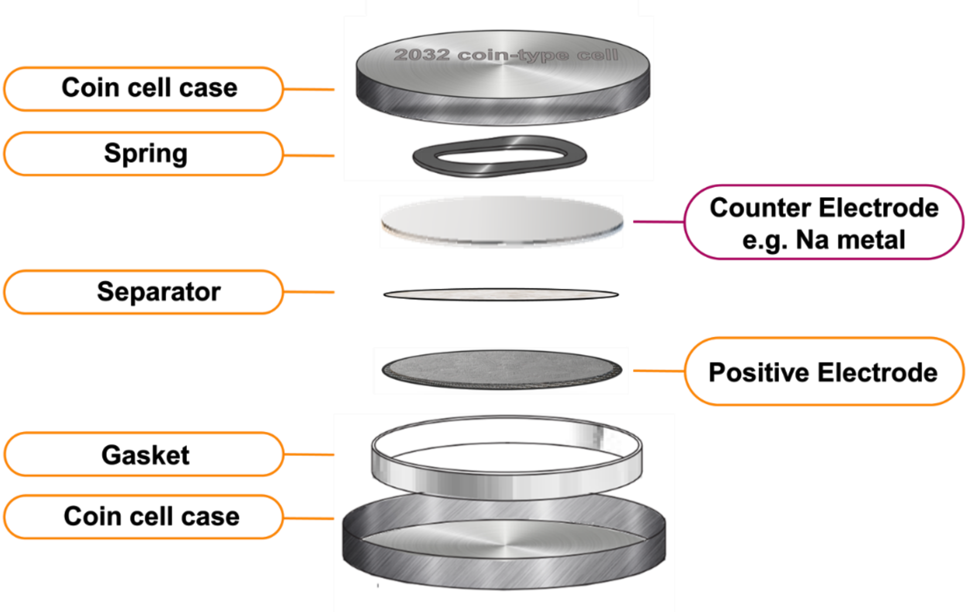

Figure 2-7 A schematic illustration of the coin cell.

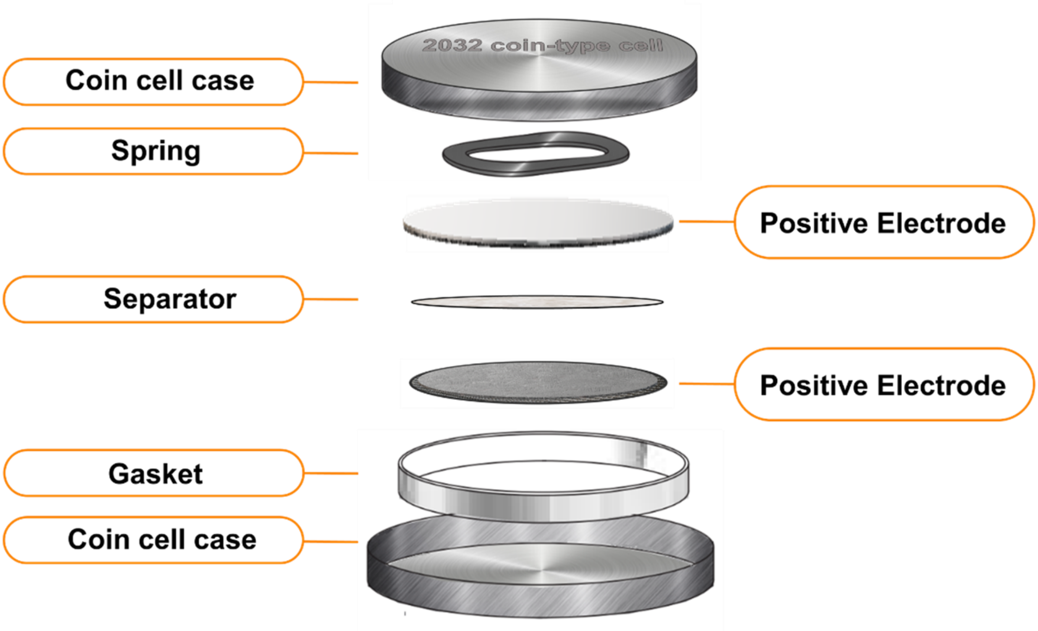

Figure 2-8 A schematic drawing of the symmetric cell with two positive electrodes for EIS.

References

[1] J. Rodríguez-Carvajal, *Phys. B*, **192** (1993) 55.

[2] K. Momma, and F. Izumi, *J. Appl. Crystallogr.*, **41** (2008) 653.

[3] S. Brunauer, P. H. Emmett, and E. Teller, *J. Am. Chem. Soc.,* **60** (1938) 309.

Chapter 3

Electrochemical Sodiation-desodiation of Maricite-$NaFePO_4$ Positive Electrode

3.1 Introduction

Positive electrode materials based on Fe^{3+}/Fe^{2+} redox have enormous merits for Na secondary batteries because of their natural abundance and low cost. In particular, $NaFePO_4$ is composed of abundant elements and has the highest theoretical capacity of 155 mAh g^{-1} in the iron-based phosphate family (e.g. Na_2FePO_4F = 120 mAh g^{-1}, $Na_2FeP_2O_7$ = 97 mAh g^{-1}, and $Na_4Fe(PO_4)_2P_2O_7$ = 130 mAh g^{-1}) [1-6]. Olivine $NaFePO_4$ is known to have two polymorphs (triphylite and maricite) [7]. Triphylite $NaFePO_4$ is commonly called olivine, which is isostructural to olivine $LiFePO_4$. This material was prepared by a chemical and electrochemical Li-Na exchange process (delithiation of $LiFePO_4$ and sodiation of $FePO_4$) [8, 9]. Triphylite $NaFePO_4$ delivers a practical reversible capacity of 120 mAh g^{-1} based on Fe^{3+}/Fe^{2+} redox activity [8]. Maricite $NaFePO_4$ (m-$NaFePO_4$) is a thermodynamically stable phase and is synthesized by a conventional solid-state method [8]. This polymorph was previously believed to be electrochemically inactive as a positive electrode material for Na secondary batteries because of the network of FeO_6-FeO_6 (edge-sharing) and PO_4-FeO_6 (corner-sharing) units hinder effective diffusion of Na^+ [1, 8-10]. A recent report, however, revealed that nano-sized m-$NaFePO_4$ could be used as a positive electrode material [9]. This finding was related to the transformation of the m-$NaFePO_4$ phase into an amorphous structure during the first charge. Although two preferable pathways for Na^+ diffusion were proposed, the activation barriers in the maricite structure along the diffusion paths are too high to overcome at room temperature; therefore, amorphization is required for Na^+ diffusion [9].

Despite recently highlighted safety issues, most of the research on Na secondary batteries are still conducted using organic electrolytes [11, 12]. Organic electrolytes, however, can only be used in a limited temperature range (<363 K) owing to their flammability and volatility [13-15]. On the other hand, ionic liquids (ILs) consist of only cations and anions and have several benefits, including low flammability, negligible vapor pressure, high thermal stability, and a wide electrochemical window as electrolytes [16-19]. Thermally and chemically stable IL electrolytes facilitate the operating of Na secondary batteries at elevated temperatures. Operating of batteries at elevated temperatures can be realized in environments at intermediate temperatures, which exist not only near industrial surroundings but also residential areas, where the latent heat from machines, automobile engines, and domestic boilers can be exploited. Moreover, the elevated operating temperatures of IL electrolytes have been reported to be very effective for improving the charge-discharge performance of $NaCrO_2$ positive electrodes, and hard carbon and Sn alloy negative electrodes [20-26]. In the case of a $Na/Na_2FeP_2O_7$ cell using IL electrolytes, high rate capability, and outstanding cycleability have been achieved at 363 K [27, 28].

In this chapter, the charge-discharge behavior of m-$NaFePO_4$ positive electrode in Na[FSA]-[C_3C_1pyrr][FSA] electrolyte is investigated at intermediate-temperatures (e.g. ionic conductivity is 17.3 mS cm^{-1} at 363 K for 30 mol% Na[FSA]-[C_3C_1pyrr][FSA] [19]). Elevating the operating temperature up to 363 K is expected to improve Na^+ diffusion in the solid-state and in the electrolyte, and enhance the electrode reaction, thus converting an electrochemically inactive m-$NaFePO_4$ to active material.

3.2 Experimental

The powdery sample of m-$NaFePO_4$ was synthesized by a conventional solid-state method [14]. Stoichiometric amounts of Na_2CO_3 (Wako Pure Chemical Industries, purity 99.8%), $FeC_2O_4 \cdot 2H_2O$ (Wako Pure Chemical Industries, purity 99%) and $(NH_4)_2HPO_4$ (Wako Pure Chemical Industries, purity > 99%) were used without further purification and thoroughly mixed by wet planetary ball milling in acetone for 12 h(600 rpm). The ball-milled mixture was collected by flushing with acetone, followed by drying for 24 h at 393 K. The mixture was well ground using a mortar and pestle after the drying procedure. The precursor mixture was then calcined at 623 K for 3 h and then baked at 873 K for 12h under Ar atmosphere.

The pure phase of m-$NaFePO_4$ was confirmed by XRD using a Rigaku Smart Lab diffractometer with Cu-*Ka* radiation (40 kV and 30 mA), and Rietveld refinement was performed using the FullProf software [29]. The morphology of the as-prepared m-$NaFePO_4$ and the ball-milled sample was observed by field-emission scanning electron microscopy (FE-SEM, Hitachi SU-8020). *Ex-situ* XRD measurements were performed using an airtight XRD sample holder by the Rigaku Smart Lab. After electrochemical measurements, cells were disassembled in an Ar-filled glovebox, and the m-$NaFePO_4$ electrodes were washed three times with super dehydrated tetrahydrofuran (Wako Pure Chemical Industries, water content ≤ 10 ppm) in the glovebox. Each dried electrode was loaded onto the airtight XRD sample holder for the measurement.

The electrochemical studies of m-$NaFePO_4$ were performed with 2032-type coin cells at 298, and 363 K. The prepared m-$NaFePO_4$ and Super C65 carbon were mixed by planetary ball milling (Fritsch Pulverisette 7 Premium Line) at a ratio of 80:20 wt% for 6 h under Ar atmosphere. The materials were loaded into a ball-milling container and capped in an Ar-filled glove box to avoid contact with moisture and oxygen. The ball-milled mixture, Super C65, and PTFE (80:10:10 wt%) were mixed using a mortar and pestle in the glovebox. Approximately 4 mg cm^{-2} of the mixed material was pressed on Al mesh and used as a positive electrode. Metallic Na (Aldrich, purity 99.95%) was cut into a disk with a diameter of 16 mm and used as an electrode. The salts, Na[FSA] (Mitsubishi Materials Electronic Chemicals purity >99%) and [C_3C_1pyrr][FSA] (Kanto Chemical, purity >99.9%), were dried under vacuum for 24 h at 353 K. The 30 mol% Na[FSA]-[C_3C_1pyrr][FSA] ionic liquid was used as the electrolyte [19]. For comparison, an organic electrolyte, 1 mol dm^{-3} Na[PF_6]-EC/DMC (1:1 vol) was used in the charge-discharge tests at 298 K. Glass microfiber filter (Whatman GF/A) was impregnated with the electrolyte at 333 K under vacuum for 1 day prior to the test.

Charge-discharge tests were measured by a Hokuto Denko HJ1001SD8 charge-discharge test device. All the electrochemical measurements were conducted at least three hours after temperature adjustment in an ESPEC Environmental Test Chamber.

3.3 Results and Discussion

Figure 3-1 shows the results of Rietveld refinement for the XRD patterns of the synthesized m-$NaFePO_4$. Table 3-1 summarizes the corresponding crystallographic data. The refinement revealed a pure single phase of m-$NaFePO_4$, belonging to the *Pnma* space group, which agrees with previously reported data [8]. The prepared m-$NaFePO_4$ and Super C65 were thoroughly mixed by ball milling. Figure 3-2 shows the comparison of the XRD patterns for the m-$NaFePO_4$ before and after ball milling with Super C65. The XRD measurements confirm that the ball-milled m-$NaFePO_4$ was pure and that peak broadening was characterized by reduction of the crystallite size during milling. Figure 3-3 shows SEM images of the as-synthesized m-

$NaFePO_4$, Super C65, and the mixture of m-$NaFePO_4$ and Super C65 after planetary ball milling, respectively. The size of the synthesized m-$NaFePO_4$ particles ranged from 500 to 250 nm. The particle size was reduced to 200 to 100 nm by ball milling. Super C65 with a particle size smaller than 50 nm was well distributed among the m-$NaFePO_4$ particles.

Figure 3-4 shows the results of galvanostatic charge-discharge tests for the Na/m-$NaFePO_4$ cell at 298 and 363 K with the 30 mol% Na[FSA]-[C_3C_1pyrr][FSA] IL electrolyte, and at 298 K with the 1 mol dm^{-3} Na[PF_6]-EC/DMC (1:1) organic electrolyte. Under the Cut-off voltage of 1.5-4.5 V, the m-$NaFePO_4$ electrode exhibited a reversible capacity of 38 mAh g^{-1} and 40 mAh g^{-1} at a rate of C/20 (1C = 155 mA g^{-1}) at 298 K using 30 mol% Na[FSA]-[C_3C_1pyrr][FSA] and 1 mol dm^{-3} Na[PF_6]-EC/DMC, respectively (Figure 3-4a and 3-4b) in the 2nd cycle. Although the practical capacity was quite limited at 298 K, stable reversibility was observed during successive cycles. The charge-discharge test at 363 K in 30 mol% Na[FSA]-[C_3C_1pyrr][FSA] delivered a reversible capacity of 80 mAh g^{-1} in the initial discharge at a rate of C/20 (Figure 3-4c) under a Cut-off voltage of 2.0-4.0 V. The discharge capacity was doubled by merely elevating the operating temperature from 298 to 363 K. However, an irreversible capacity emerged from the 3th discharge, despite the narrower voltage region as compared to that in the tests conducted at 298 K. This irreversible capacity probably results from the decomposition of the IL electrolyte, which is accelerated at elevated temperatures, particularly on nanosized materials, including carbon black [30]. The irreversible capacity fades upon further limiting the lower Cut-off voltage from 2.0 to 2.2 V at a current density of C/5. After this adjustment, the material exhibited stable cycleability with a reversible capacity of 80 mAh g^{-1} by the 20th cycle (Figure 3-4d).

Galvanostatic charge-discharge tests on Super C65 were conducted to clarify the effects of Super C65 on the capacity at intermediated temperature. Super C65 powder was also planetary ball-milled for 6 hin Ar atmosphere, which was the same conditions used for the mixture of m-$NaFePO_4$ and Super C65 ball-milled. Figure 3-5 shows the charge-discharge curves of the Super C65 electrode at 298 and 363 K in the 30 mol% Na[FSA]-[C_3C_1pyrr][FSA] IL electrolyte. The working electrode composed of 50 wt% of Super C65and 50 wt% of PTFE, delivered 14.4 mAh g^{-1} at 298 K (Cut-off voltage: 1.5-4.5 V) and 4.5 mAh g^{-1} at 363 K (Cut-off voltage: 2.2-4.0 V). Little irreversible capacity was observed in this case because of the higher Cut-off voltage of 2.2 V. In the charge-discharge test for the m-$NaFePO_4$ electrode, each electrode contained 26 wt% of Super C65, and therefore the results proved that the influence of capacity by Super C65 was at most 3 mAh g^{-1}.

Figure 3-6 shows the cycling performance of the Na/30 mol% Na[FSA]-[C_3C_1pyrr][FSA]/m-$NaFePO_4$ cell at C/2 rate with a Cut-off voltage of 4.0 and 2.2 V. The discharge capacity was 58 mAh g^{-1} at the initial discharge, which continuously increased during subsequent cycles, reaching 100 mAh g^{-1} at the 120th cycle with nearly 100% Coulombic efficiency. Figure 3-7 shows the *ex-situ* XRD patterns of the m-$NaFePO_4$ electrode after the 1st, 10th, and 100th cycles. The XRD pattern before cycling is also shown for comparison. The maricite structure was maintained even after 100 cycles of charge and discharge as represented by diffraction peaks with indices 101 at 20.25°, 111 at 23.96°, 220 at 32.65°, and 301 at 34.67°. No significant peak broadening was observed, suggesting that amorphization or reduction of the crystallite diameter did not occur during the cycles. This is in contrast to the previous report, which claimed the phase transformation of m-$NaFePO_4$ to amorphous $NaFePO_4$ during charging [10]. Although the different fabrication methods and measurement conditions may affect the structural change along with electrochemical reactions, the present result may indicate the reversible redox activity of m-$NaFePO_4$ without loss of its crystallinity. The reason for the increase in capacity for m-$NaFePO_4$ is not clear in the current stage. A decrease in particle size followed by Na^+ extraction and insertion processes may provide effective Na^+ pathways since the crystallite size confirmed by XRD does not always agree with the particle size. Additionally, m-$NaMnPO_4$ was synthesized with the same synthetic method of m-$NaFePO_4$. Figure 3-8 shows the pure phase of m-$NaMnPO_4$ confirmed by XRD using a Rigaku Smart Lab diffractometer with Cu-*Ka* radiation (40 kV and 30 mA). The XRD patterns of m-$NaFePO_4$ and m-$NaMnPO_4$ are very similar to each other, but the peaks of m-$NaMnPO_4$ totally located at a lower angle than m-$NaFePO_4$ because the atomic radii of Mn are larger than Fe. Figure 3-9 show Galvanostatic charge-discharge test and cycle test on m-$NaMnPO_4$ at 363 K in 30 mol% Na[FSA]-[C_3C_1pyrr][FSA] at C/20. The reversible capacity was limited to only 27 mAh $g^{-1,}$ which is worse than m-$NaFePO_4$.

3.4 Conclusions

In summary, the potential activity of m-$NaFePO_4$ was demonstrated as a positive electrode material for Na secondary batteries using an IL electrolyte at an intermediate temperature. Nonflammable Na[FSA]-[C_3C_1pyrr][FSA] electrolyte is a key component that results in good performance of m-$NaFePO_4$ at intermediate temperature. This material delivers a reversible capacity of 100 mAh g^{-1} with C/2 after 100 charge and discharge cycles at 363 K. Although the practical capacity in the present study still does not reach the theoretical value, 155 mAh g^{-1}, improvements in fabrication techniques, including control of particle size and carbon coating, can further enhance the possibility of superior performance. The simple synthetic procedure, abundant constituent elements, and the highest theoretical capacity among Fe-based phosphates make m-$NaFePO_4$ an attractive positive electrode material for future Na secondary batteries. Further structural study on the redox activity of crystalline m-$NaFePO_4$ is now underway. This study also suggests that many other inactive materials can be converted into active materials by a combination of nano-sizing and intermediate-temperature operating.

Table 3-1 Crystallographic data of the prepared m-$NaFePO_4$ by Rietveld refinement.

Chemical formula $NaFePO_4$ (S.G. *Pnma*)

Refinement results

*Chi*2 = 1.67, R_p = 0.489%, R_{wp} = 0.632%

***a*/Å**	***b*/Å**	***c*/Å**	***V*/Å³**
8.981445(9)	6.86687(8)	5.0441(6)	311.089(6)

Atom	Wyckoff symbol	*x*	*y*	*z*	B_{iso}/Å^2	Occup.
Fe	4*a*	0	0	0	0.5	1.0
P	4*c*	0.1751(2)	0.25	0.4556(5)	0.5	1.0
Na	4*c*	0.3453(3)	0.25	0.9689(6)	0.5	1.0
O1	8*c*	0.1180(2)	0.06698(3)	0.3267(3)	0.5	1.0
O2	4*c*	0.3491(3)	0.25	0.4576(7)	0.5	1.0
O3	4*c*	0.1222(4)	0.25	0.7457(6)	0.5	1.0

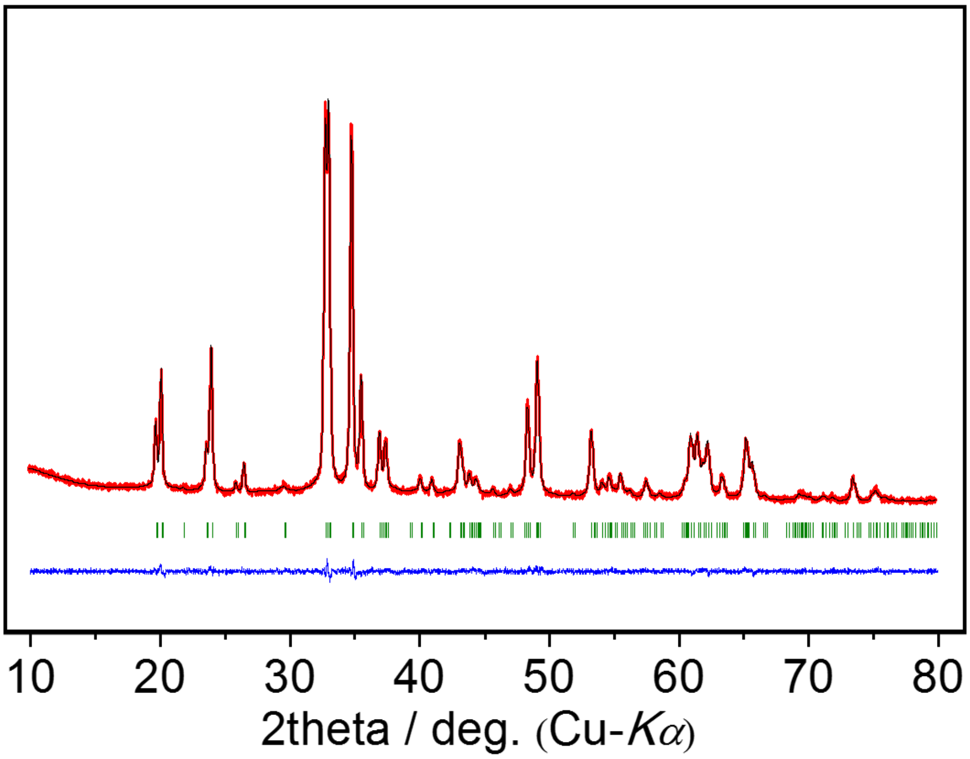

Figure 3-1 Rietveld refinement result for m-$NaFePO_4$ prepared by a solid-state method. The red line indicates the observed pattern, and the black line refers to the calculated pattern. The blue line is the difference between the red and black lines. The positions of the diffraction peaks are indicated by green marks.

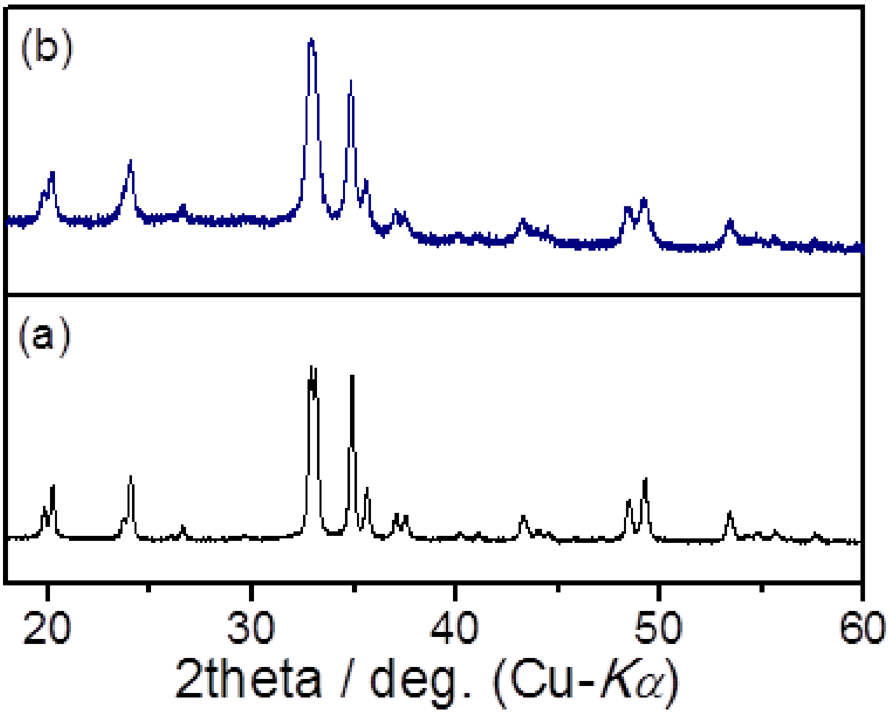

Figure 3-2 X-ray diffraction patterns of m-$NaFePO_{4a}$ as-synthesized and (b) after ball-milling with Super C65 for 12 h.

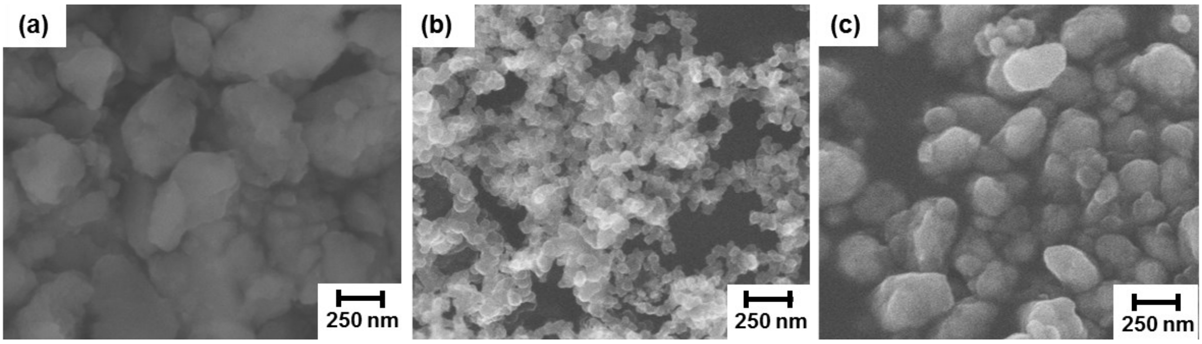

Figure 3-3 Field-emission SEM images (a) as prepared m-$NaFePO_4$, (b) Super C65, and (c) mixture of m-$NaFePO_4$ and Super C65 after ball-milling for 12 h.

.

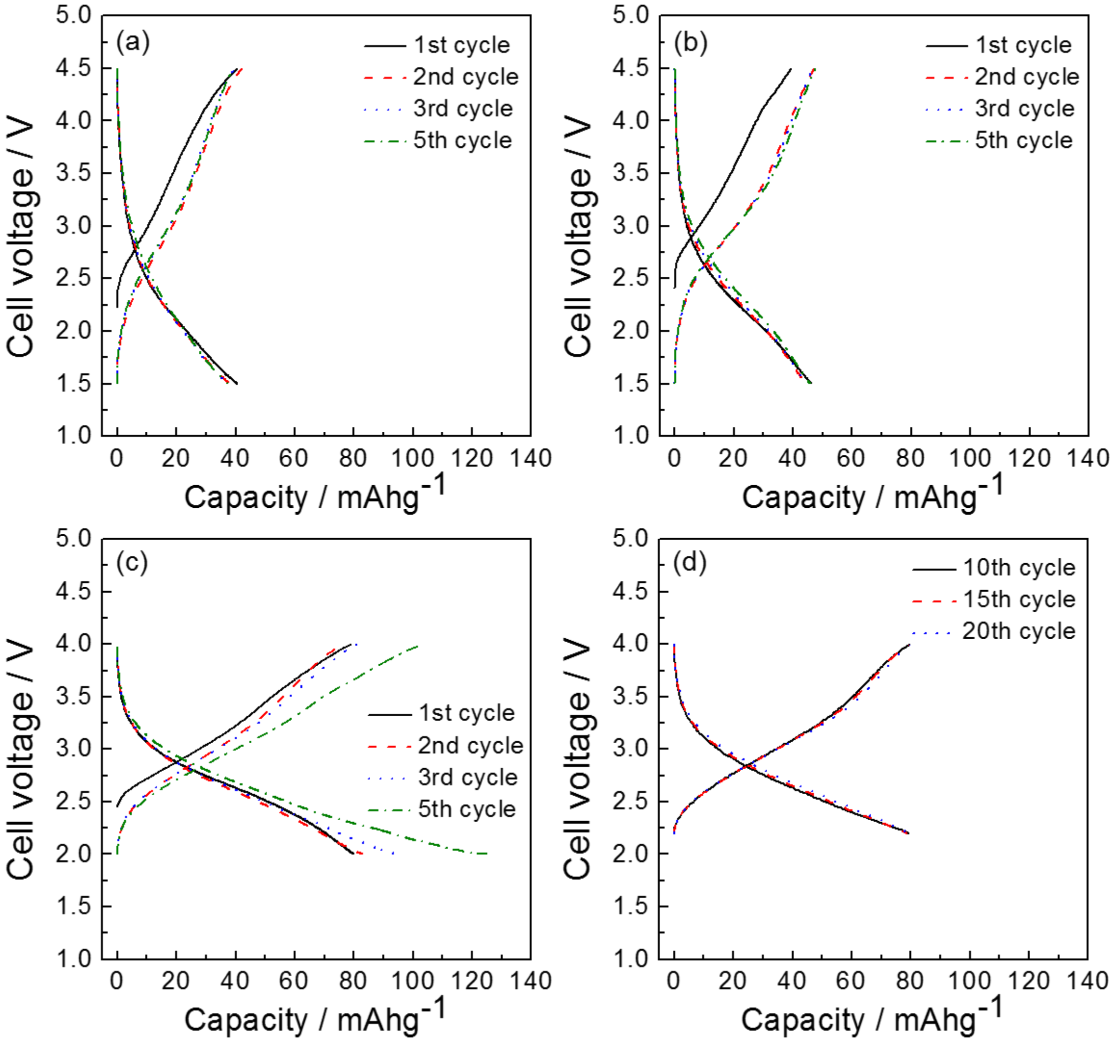

Figure 3-4 Charge-discharge curves of a Na/m-$NaFePO_4$ cell (a) at 298 K in Na[FSA]-[C_3C_1pyrr][FSA] at C/20 (Cut-off voltage: 1.5-4.5 V), (b) at 298 K in 1 mol dm^{-3} Na[PF_6]-EC-DMC (1:1) at C/20 (Cut-off voltage: 1.5-4.5 V), (c) at 363 K in Na[FSA]-[C_3C_1pyrr][FSA] at C/20 (Cut-off voltage: 1.5-4.5 V), and (d) in subsequent measurement of (c) after the 9th cycle at a higher current density of C/5 (Cut-off voltage: 2.2-4.0 V).

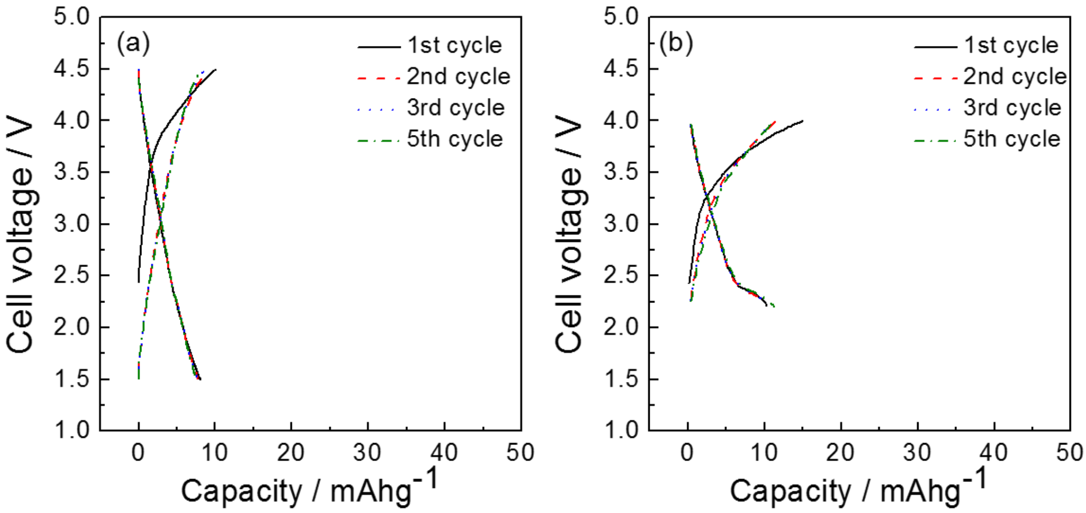

Figure 3-5 Charge-discharge curves of a Na/Super C65: PTFE (50:50 wt%) cell (a) at 298 K in Na[FSA]-[C_3C_1pyrr][FSA] at 10 mA g^{-1} with Cut-off voltage: 1.5-4.5 V, (b) at 363 K in Na[FSA]-[C_3C_1pyrr][FSA] at 10 mA g^{-1} with Cut-off voltage: 2.2-4.0 V.

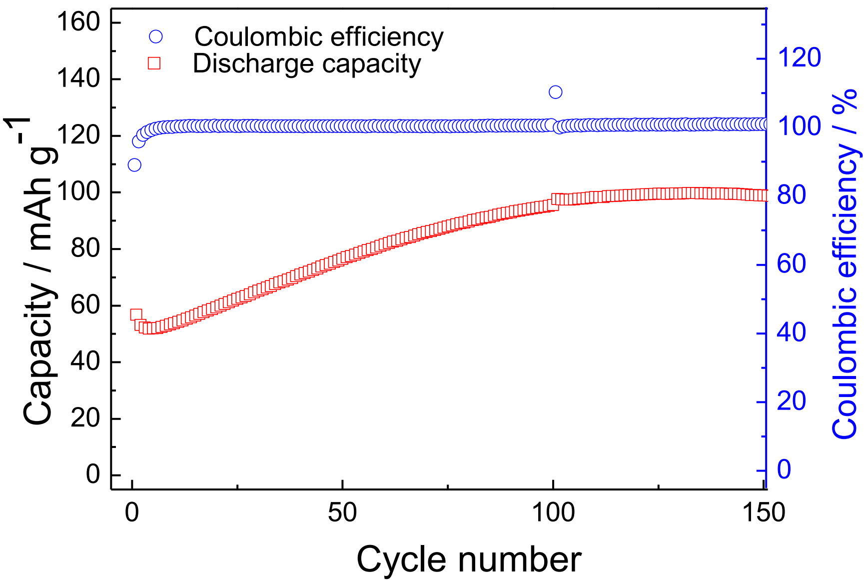

Figure 3-6 Cycling performance of m-$NaFePO_4$ at 363 K in Na[FSA]-[C_3C_1pyrr][FSA] at C/2 with Cut-off voltage: 2.2-4.0 V. Red and blue markers indicate discharge capacity and Coulombic efficiency, respectively, at each cycle. The measurement was interrupted at the 100th cycle only and then restarted to determine the effect of intermission.

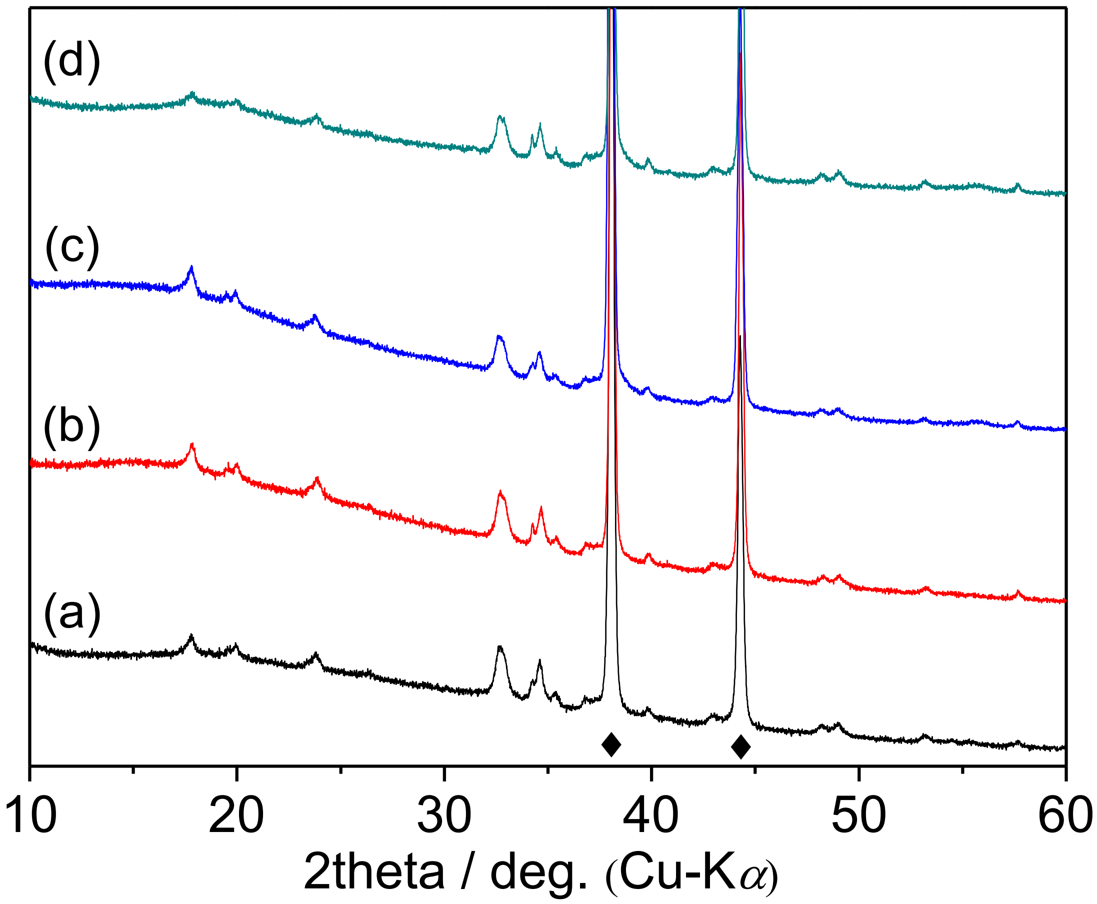

Figure 3-7 *Ex-situ* XRD patterns of the m-$NaFePO_4$ electrode (a) before the charge-discharge test, (b) after the 1st cycle, (c) after the 10th cycle, and (d) after the 100th cycle. The ♦ marks indicate the peaks of Al mesh. The diffraction peak at 18.1° is assigned to PTFE.

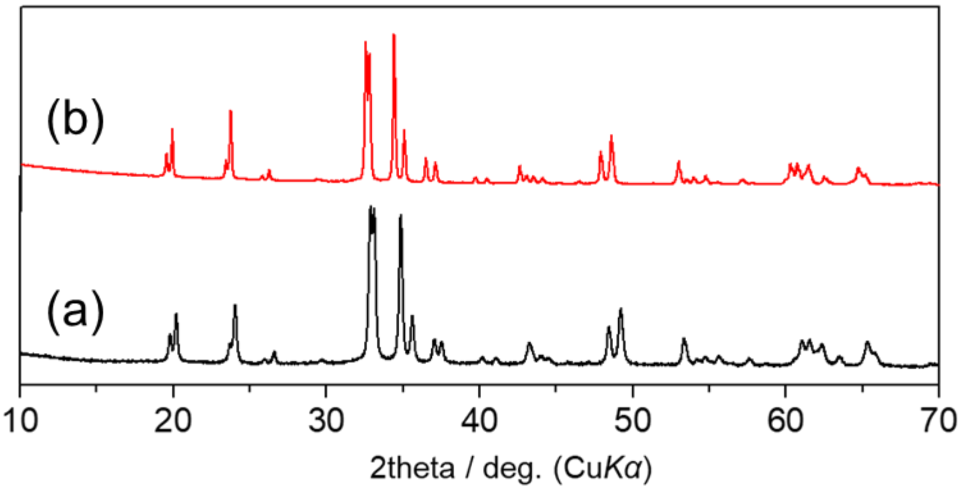

Figure 3-8 XRD of (a) m-$NaFePO_4$ and (b) m-$NaMnPO_4$.

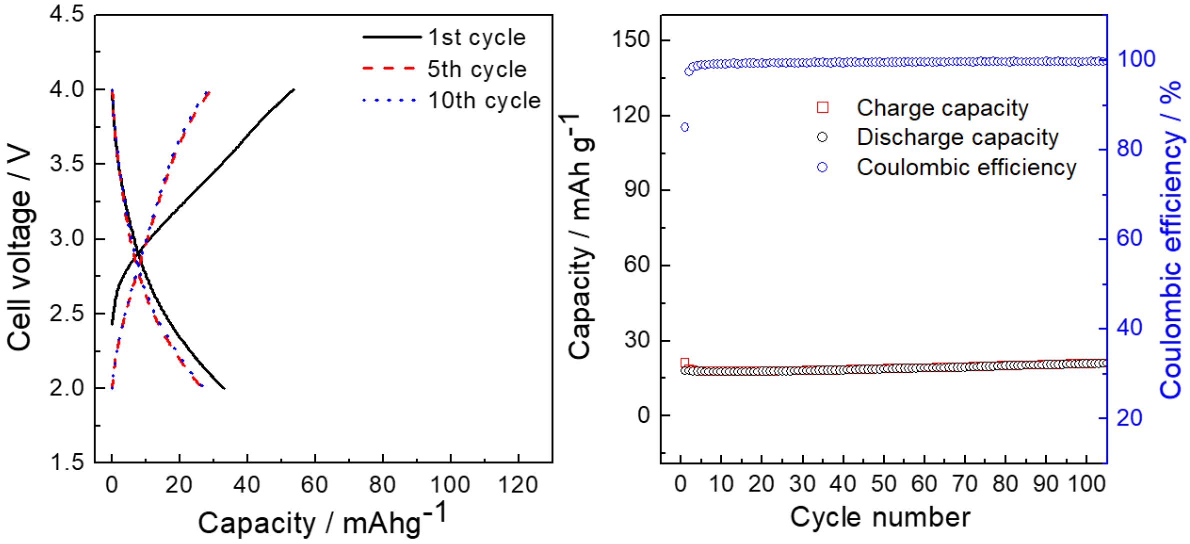

Figure 3-9 (left) charge-discharge curves of a Na/m-$NaMnPO_4$ at C/20 (Cut-off voltage: 2.0-4.0 V), and (right) Cycling performance of m-NaMnPO4 at C/2 at 363 K in Na[FSA]-[C_3C_1pyrr][FSA].

References

[1] A. Yamada, MRS Bull., 39 (2014) 423.

[2] Y. Zhu, Y. Xu, Y. Liu, C. Luo, and C. Wang, Nanoscale, 5 (2013) 780.

[3] C.Y. Chen, K. Matsumoto, T. Nohira, R. Hagiwara, and Y. Orikasa, Y. Uchimoto, J. Power Sources, 246 (2014) 783.

[4] P. Barpanda, T. Ye, S.-J. Chung, Y. Yamada, M. Okubo, H. Zhou, and A. Yamada, A. Electrochem. Commun., 24 (2012) 116.

[5] H. Kim, R.A. Shakoor, C. Park, S.Y. Kim, J.-S. Kim, Y.N. Jo, W. Cho, K. Miyasaka, R. Kahraman, Y. Jung, and J.W. Choi, Adv, Func. Mater., 23 (2013) 1147.

[6] P. Barpanda, G. Liu, C. D. Ling, M Tamaru, M. Avdeev, S.-C. Chungm, Y. Yamada, and A. Yamada, A. Chem. Mater., 25 (2013) 3480.

[7] M. Avdeev, Z. Mohamed, C. D. Ling, J. Lu, M. Tamaru, A. Yamada, and P. Barpanda, Inorg. Chem., 52 (2013) 8685.

[8] S.Oh, S.-T. Myung, J. Hassoun, B. Scrosati, and Y.-K. Sun, Electrochem. Commun., 22 (2012) 149.

[9] J. Kim, D. Seo, H. Kim, I, Park, J. Yoo, S. Jung, Y. Park, W. A. Goddard III, and K. Kang, Energy Environ. Sci., 8 (2015) 540.

[10] A. Sun, and J. Manivannan, ECS Trans., 35 (2011) 3.

[11] K. Kuratani, N. Uemura, H. Senoh, H.T. Takeshita, and T. Kiyobayashi, J. Power Sources, 223 (2013) 175.

[12] A. Ponrouch, R. Dedryvère, D. Monti, A.E. Demet, J.M. Ateba Mba, L. Croguennec, C. Masquelier, P. Johansson, and M.R. Palacín, Energy Environ. Sci., 6 (2013) 2361.

[13] G.G. Eshetu, S. Grugeon, S. Laruelle, S. Boyanov, A. Lecocq, J.-P. Bertrand, and G. Marlairl, Phys. Chem. Chem. Phys., 15 (2013) 9145.

[14] S. Wilken, P. Johansson, and P. Jacobsson, Solid State Ionics., 225 (2012) 608.

[15] S. Wilken, M. Treskow, J. Scheers, P. Johansson, and P. Jacobsson, RSC Adv., 3 (2013) 16359.

[16] M. Armand, F. Endres, D.R. MacFarlane, H. Ohno, and B. Scrosati, Nat. Mater., 8 (2009) 621.

[17] J.P. Hallett, and T. Welton, Chem. Rev., 111 (2011) 3508.

[18] D.R. MacFarlane, N. Tachikawa, M. Forsyth, J.M. Pringle, P.C. Howlett, G.D. Elliott, J.H. Davis, M. Watanabe, and P. Simon, C.A. Angell, Energy Environ. Sci., 7 (2014) 232.

[19] Matsumoto, Y. Okamoto, T. Nohira, and R. Hagiwara, J. Phys. Chem. C, 119 (2015) 7648.

[20] C. Chen, K. Matsumoto, T. Nohira, C. Ding, T. Yamamoto, and R. Hagiwara Electrochim. Acta, 133 (2014) 583.

[21] A. Fukunaga, T. Nohira, Y. Kozawa, R. Hagiwara, S. Sakai, K. Nitta, and S. Inazawa, J. Power Sources, 209 (2012) 52.

[22] C. Ding, T. Nohira, K. Kuroda, R. Hagiwara, A. Fukunaga, S. Sakai, K. Nitta, and S. Inazawa, J. Power Sources, 238 (2013) 296.

[23] C. Ding, T. Nohira, R. Hagiwara, K. Matsumoto, Y. Okamoto, A. Fukunaga, S. Sakai, K. Nitta, and S. Inazawa, J. Power Sources, 269 (2014) 124.

[24] C.-Y. Chen, K. Matsumoto, T. Nohira, and R. Hagiwara, J. Electrochem. Soc., 162 (2014) A176.

[25] C.-Y. Chen, K. Matsumoto, T. Nohira, C. Ding, T. Yamamoto, and R. Hagiwara, Electrochim. Acta, 133 (2014) 583.

[26] T. Yamamoto, T. Nohira, R. Hagiwara, A. Fukunaga, S. Sakai, and K. Nitta, Electrochim. Acta, 211 (2016) 234.

[27] C.-Y. Chen, T. Kiko, T. Hosokawa, K. Matsumoto, T. Nohira, and R. Hagiwara, J. Power Sources, 332 (2016) 51.

[28] K. Matsumoto, T. Hosokawa, T. Nohira, R. Hagiwara, A. Fukunaga, K. Numata, E. Itani, S. Sakai, K. Nitta, and S. Inazawa, J. Power Sources, 265 (2014) 36.

[29] J R.-Carvajal, Commission on powder diffraction (IUCr) Newsletter, 26 (2001) 12.

[30] C.-Y. Chen, K. Matsumoto, T. Nohira, and R. Hagiwara, J. Electrochem. Soc., 162 (2015) A2093.

Chapter 4

Charge-discharge Behavior of Crystalline Maricite-$NaFePO_4$ Positive Electrode

4.1 Introduction

According to our previous studies using ILs, elevating operating temperatures using IL electrolytes can enhance Na^+ diffusion in the solid-state and in an electrolyte, which effectively improves the electrochemical performance of positive electrodes and negative electrodes [1-6]. Thus, there is a possibility sodiation-de-sodiation can occur in the m-$NaFePO_4$ at elevated temperatures based on our previous results.

Particularly, the iron-based phosphate family such as Na_2FePO_4F, $Na_2FeP_2O_7$, and $Na_4Fe(PO_4)_2P_2O_7$ have been studied as potential positive electrodes for Na secondary batteries [7-12]. Although $NaFePO_4$ has the highest theoretical capacity of 155 mAh g^{-1} among them ($NaFePO_4$ is known as olivine structure with two polymorphs triphylite and maricite) [13]), it has not been deeply studied because of its difficult preparative method (triphylite) or electrochemical inactivity (maricite). Triphylite-$NaFePO_4$ (t-$NaFePO_4$) can be prepared by a chemical and electrochemical Li-Na exchange process (de-lithiation of $LiFePO_4$ and sodiation of $FePO_4$) [13, 14]. Thus, no one directly synthesizes t-$NaFePO_4$ for practical use even it delivers a reversible capacity of 120 mAh g^{-1} based on Fe^{3+}/Fe^{2+} redox activity [14]. Maricite $NaFePO_4$ (m-$NaFePO_4$) can be synthesized by a conventional solid-state method because it is the thermodynamically stable phase [13]. However, m-$NaFePO_4$ was considered to be electrochemically inactive for a long time until the recent report by Kang's group [15], where

Na^+ was proved to be de-sodiated from nano-sized m-$NaFePO_4$, and the maricite phase was transformed into the electrochemically active amorphous $FePO_4$ during the first charge. The phase exhibits a reversible capacity of 142 mA g^{-1} at room temperature [30]. Some other groups also have researched with m-$NaFePO_4$ [16-18], but the detailed reaction mechanism and improvement of performance to practical applications for m-$NaFePO_4$ have not sufficiently been done.

In Chapter 3, m-$NaFePO_4$ exhibits a reversible capacity of 80 mAh g^{-1} at C/5 in pyrrolidinium-based IL at 363 K. Although it did not directly show the electrochemical activity of m-$NaFePO_4$, *ex-situ* XRD measurements suggested some crystalline m-$NaFePO_4$ is preserved even after 100 cycles [19]. However, because capacity was not enough, the IL electrolyte is changed into the imidazolium-based one with higher ionic conductivity. The ball-milling condition is also changed to confirm its effects on electrochemical properties. Because another preliminary report using $Na_2FeP_2O_7$ suggested that the imidazolium-based ILs exhibited better rate capability owing to their higher conductivity than the pyrrolidinium-based ILs [5]. Here, m-$NaFePO_4$ electrodes were prepared in three different conditions (as-synthesized, ball-milled, and re-calcined), their charge-discharge profiles were examined at 298 and 363 K using the Na[FSA]-[C_2C_1im][FSA] IL electrolyte to examine the activation mechanism of m-$NaFePO_4$. Furthermore, the effects of temperature and ball-milling on activation of m-$NaFePO_4$ was investigated electrochemical impedance spectroscopy (EIS) using $NaFePO_4$/$NaFePO_4$ symmetric cells.

4.2 Experimental

The powdery sample of m-$NaFePO_4$ has synthesized a conventional solid-state method, as described in Chapter 3 [10]. The synthesized m-$NaFePO_4$ was fabricated under two different conditions of ball-milled m-$NaFePO_4$, and re-calcined m-$NaFePO_4$ before making electrodes with Super C65 and PTFE. The ball-milled refers to the as-synthesized m-$NaFePO_4$, which was ball-milled for 12 h with acetone to reduce its particle size. The re-calcined m-$NaFePO_4$ refers re-heating of the ball-milled m-NaFePO4 at 873 K for 12 h under Ar atmosphere. The morphology of the as-synthesized m-$NaFePO_4$ and the two fabricated samples were observed by field-emission scanning electron microscopy (FE-SEM, Hitachi SU-8020).

Electrochemical properties were measured with 2032 coin-type cells at 298 and 363 K. Na metal (Aldrich, purity 99.95%) cut into a disk (16 mm in diameter) and fixed on Al plate current collector was used as a negative electrode. Three different m-$NaFePO_4$ positive electrodes, as shown above, were prepared (as-synthesized m-$NaFePO_4$, ball-milled m-$NaFePO_4$, and re-calcined m-$NaFePO_4$).

The working electrode was prepared by mixing m-$NaFePO_4$, Super C65, and PTFE (75:20:5 wt%) and pressing the mixture on Al mesh as a positive electrode approximately 4 mg cm^{-2}. The salts, Na[FSA] (Mitsubishi Materials Electronic Chemicals purity >99%) and [C_2C_1im][FSA] (Kanto Chemical, purity >99.9%), were dried under vacuum for 24 h at 353 K. The 30 mol% Na[FSA]-[C_2C_1im][FSA] ionic liquid was used as the electrolyte. Glass microfiber filter (Whatman GF/A) was impregnated with the electrolyte at 333 K under vacuum for 1 day prior to the test.

Electrochemical measurements were measured by an HJ1001SD8 charge-discharge test device (Hokuto Denko). All the measurements were conducted at least 3 h after temperature adjustment in an ESPEC Environmental Test Chamber. The m-$NaFePO_4$ (as-synthesized, ball-milled, and re-calcined) symmetric cells for EIS were prepared using 2032 coin-type cells, and the measurements were performed with a VSP potentiostat (Bio-Logic) at 298, 323, 343, and 363 Kover a frequency range from 500 kHz to 1 mHz with a perturbation amplitude of 10 mV..

Ex-situ XRD measurements were performed using an airtight XRD sample holder by the Rigaku Smart Lab. After electrochemical measurements, cells were disassembled in an Ar-filled glovebox, and the m-$NaFePO_4$ electrodes were washed three times with dehydrated tetrahydrofuran (Wako Pure Chemical Industries, water content ≤ 10 ppm) in the glovebox. Each dried electrode was loaded onto the airtight XRD sample holder for the measurement.

X-ray absorption fine structure (XAFS) spectra were measured by Beam at SR center at Ritsumeikan University. After charging or discharging, the cells were disassembled in the glovebox, and the electrodes were washed with dehydrated tetrahydrofuran for several times. The washed electrodes were dried at 333K under vacuum. The electrode material was torn off from the Al current collector, mixed with boron nitride powder, and was pressed into the pellet for samples of XAFS measurement.

4.3 Results and Discussion

Figures 4-1 and 4-2 show XRD patterns and SEM images of the as-synthesized, the ball-milled, and the re-calcined m-$NaFePO_4$ samples. The XRD pattern of the as-synthesized m-$NaFePO_4$ (Figure 4-1a) was analyzed by a Rietveld refinement in our previous study [34], which showed that the as-synthesized $NaFePO_4$ is a pure phase of m-$NaFePO_4$ belonging to the *Pnma* space group. The XRD pattern of the ball-milled m-$NaFePO_4$ (Figure 4-1b) confirmed a pure maricite phase, but peak broadening was observed by reduction of the crystallite size, which was also confirmed in the SEM images in Figure 4-2b. The SEM images of the as-synthesized m-

$NaFePO_4$ (Figure 4-2a) indicates the crystallite size ranges from 100 and 200 nm. The crystallite size was reduced to 50~100 nm after the ball-milling treatment (Figure 4-2b). The XRD patterns of the re-calcined m-$NaFePO_4$ were recovered to the same level as the as-prepared m-$NaFePO_4$ because of the increase in crystallinity (Figure 4-1c). After the re-calcination, secondary particles grow more tightly than those in the original state (Figures 4-2a and 4-2c), which affects poor charge-discharge performance, as shown below.

Figure 4-3 exhibits the results of galvanostatic charge-discharge tests at C/10 (1C = 155 mA g^{-1}) under the Cut-off voltage of 2.0-4.0 V. The as-synthesized m-$NaFePO_4$ electrode exhibited a very limited reversible capacity of 10 mAh g^{-1} at 298 K (Figure 4-3a). The result corresponds to the previous recognition of m-$NaFePO_4$ as an inactive positive electrode material at room temperature [13, 14, 16-19]. Although a reversible capacity of the as-synthesized m-$NaFePO_4$ was doubled by elevating the operating temperature to 363 K, the capacity is limited to 20 mAh g^{-1} (Figure 4-3b), which means that elevating operating temperature somehow improves Na^+ diffusion in m-$NaFePO_4$, but there are still large hinders for the diffusion. The ball-milled m-$NaFePO_4$ exhibited a reversible capacity of 23 mAh g^{-1} at 298 K (Figure 4-3c) and 107 mAh g^{-1}at 363 K (Figure 4-3d), indicating that the reversible capacity of m-$NaFePO_4$ was dramatically improved by the combination of elevated operating temperature and the ball-milling treatment. The Coulombic efficiency of the initial cycle was 140.7% at 363 K, suggesting partial oxidation of the pristine electrode material (see XAFS analysis below), and reached 98.1% from the second cycle. The ball-milling treatment in acetone efficiently reduced crystallite size, which shortened Na^+ diffusion paths in the solid-state and increased surface area of m-$NaFePO_4$. Elevation of operating temperature also contributes to the improvement of Na^+ diffusion in the solid-state and in the electrolyte. Prolonged ball-milling (24 h) did not significantly improve the reversible capacity of m-$NaFePO_4$ (104 mAh g^{-1} at 0.1C and 113 mAh g^{-1} at 0.05C at 363 K in Figure 4-4. After re-calcination of the ball-milled m-$NaFePO_4$, the particles strongly aggregated, which made the material inactive again and limited the reversible capacity to 6.9 mAh g^{-1} at 298 and 14.2 mAh g^{-1} at 363 K (Figures 4-3e and 4-3f).

The discharge rate and cycling performances of the ball-milled $NaFePO_4$ at 363 K are shown in Figs. 4-5 and 4-6, respectively. The cell was charged to 4.0 V at a constant current density of 0.05 C and were discharged to 2.0 V at 0.05 to 10 C. The discharge capacity monotonously decreased with increasing discharging current rate. Although the electrode reaction is constrained at high discharge rates because of the high activation energy for Na^+ diffusion, discharge capacities are still 89.1 mAh g^{-1} at 0.5 C, 73.2 mAh g^{-1} at 1C, and 56.2 mAh g^{-1} at 2C (Figure 4-5). Cycling performance of the ball-milled m-$NaFePO_4$ was evaluated at 1 C with a Cut-off voltage of 2.0 and 4.0 V. The cell was stabilized, and the Coulombic efficiency reached 99% at the 10th cycle, and the Coulombic efficiency exceeds 99.8% after the 50th cycle. The capacity retention of the ball-milled m-$NaFePO_4$ was 67.2% after the 100th cycle. (Figure 4-6)

To reveal the reasons for the capacity enhancement by ball-milling and elevation of operating temperature, EIS was obtained at 298, 323, 343, and 363 K with m-$NaFePO_4$ symmetric cells for the as-synthesized, the ball-milled, and the re-calcined m-$NaFePO_4$. The cells were assembled, as shown in Figure 2-6, under a dry Ar atmosphere. Each impedance plot is composed of two semi-circles. The small semi-circle at the higher frequency region is related to the resistance of the composite material and is also observed in a cell without active materials (only acetylene black and PTFE). Another semi-circle at the lower frequency region originates from the interfacial resistance of the active material (R_{in}). The size of R_{in} for the as-synthesized m-$NaFePO_4$ is considerably large at 298 K and seems to be straight (Figure 4-7a). As increasing temperature, the size of R_{in} decreased, corresponding to the doubled capacity at 363 K from the one at 298 K. The same tendency was shown in the ball-milled and the re-calcined m-$NaFePO_4$ in Figures 4-7b and 4-7c); as temperature increased, R_{in} of the ball-milled and the re-calcined m-$NaFePO_4$ also decreased. A comparison between the R_{in} values for as-prepared and ball-milled m-$NaFePO_4$ revealed that R_{in} dramatically decreased with decreasing particle size. After re-calcination, R_{in} increased again (Figure 4-7c) to the level even larger than R_{in} for the as-prepared m-$NaFePO_4$, which agrees with the lower reversible capacity of the re-calcined m-$NaFePO_4$ than that of the as-prepared m-$NaFePO_4$ (Figures 4-3a, 4-3b, 4-3e, and 4-3f). These observations clarified that both elevating temperature and ball-milling contribute to the reduction of R_{in}, the interfacial resistance of m-$NaFePO_4$, and make the material as a positive active material. Furthermore, EIS of half cells measurement exhibited the same results that the ball-milled m-$NaFePO_4$ has smaller R_{ct} than the re-calcined R_{ct} in Figure 4-8.

Ex-situ XRD data of the ball-milled m-$NaFePO_4$ suggested that the maricite phase was preserved even after 50 cycles, and there seemed to be some subtle peak shifting to the higher angle after charging followed by the opposite shifting after discharging in Figure 4-9. However, the XRD peaks of the ball-milled m-$NaFePO_4$ are too weak and broad to discuss whether the peak shifting originates from de-sodiation and sodiation of the maricite phase. Thus, the as-synthesized m-$NaFePO_4$ with higher crystallinity (Figure 4-1a) was used to discuss the de-sodiation and sodiation mechanisms. Structural change was monitored by obtaining XRD patterns at different states of charge (SOC) of the as-synthesized m-$NaFePO_4$. Four samples were prepared for *ex-situ* XRD (Figure 4-10).

After charge-discharge at a slow constant current rate (0.05C), long constant voltage charging was additionally applied until the cells exhibit a certain capacity. The obtained XRD patterns are shown in Figure 4-11. One of the two cells charged to 4.0 V at 0.05C and kept at 4.0 V for 10 h reached a SOC of 30%, and the other one charged to 4.0 V at 0.05C and kept charged at 4 V for 150 h reached a SOC of 67 %. Slight peak shift to the higher angle was observed after charging to SOC = 30 % and 67 % (Figures 4-11b and 4-11c), which indicated a decrease of d-spacing due to de-sodiation. The peaks return back to the original peak positions after discharging at 0.05C to 2.0 V followed by constant voltage discharging at 2.0 V for 150 h (Figure 4-11d), suggesting that sodiation occurred in the maricite phase. Figure 4-12 shows *Ex-situ* XRD of the as-synthesized m-$NaFePO_4$ at 298 K, and peak shifting was not monitored in 298 K. This result could explain that the m-$NaFePO_4$ is not an active material at room temperature because (de)sodiation barely occurs in Figure 4-3a. However, elevating temperature can change m-$NaFePO_4$ as the active material, and finally, ball-milling can improve its electrochemical performance.

X-ray absorption near edge structure (XANES) spectra of the ball-milled m-$NaFePO_4$ (pristine, charged, and discharged) are shown in Figure 4-13. The XANES analysis indicates that reversible Fe^{+2}/Fe^{3+} redox reactions upon de-sodiation/sodiation. The main edge shifts toward the higher energy by charging, which explains the oxidation from Fe^{2+} to Fe^{3+} by de-sodiation. Reversely, the main edge of the discharged to 2.0 V shifts to the lower energy by discharging, which accords with the reduction of Fe^{3+} to Fe^{2+} by sodiation. However, the main edge of the pristine discharged sample is located at the lower energy than that of the pristine sample. The reason for the energy difference between the pristine and discharged states is considered to originate from the partial oxidation of the pristine sample during long ball-milling treatment, which is reflected in the small charge capacity of the 1st cycle in Figure 4-3d.

4.4 Conclusions

The electrochemical properties of m-$NaFePO_4$ as a positive electrode material for Na secondary batteries in Na[FSA]-[C_2C_1im][FSA] IL electrolytes was demonstrated in this chapter. The charge-discharge profiles show that reversible capacities increase by ball-milling of the material and elevation of the cell operating temperature. The ball-milled m-$NaFePO_4$ delivers a reversible capacity of 107 mAh g^{-1} at C/10 at 363 K. These capacity increases agree with the results of symmetric impedance spectroscopy. The interfacial impedance is gradually reduced as the temperature rises and decreasing particle size. Finally, the peaks shifting in *ex-situ XRD* was firstly confirmed that the sodiation and de-sodiation could occur in the maricite phase at elevated temperature. From these results, the elevation of cells operating temperature using ILs can improve the performance of the electrode and change an inactive electrode material to a promising electrode material for intermediate-temperature operating Na secondary batteries.

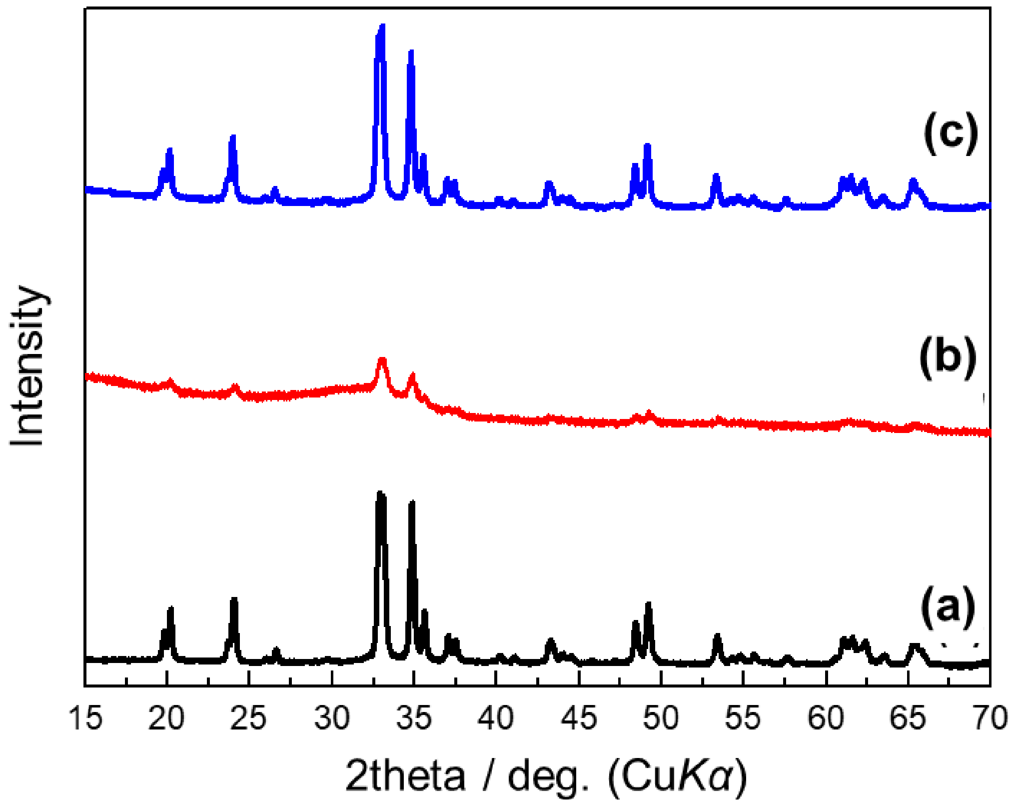

Figure 4-1 XRD of (a) as-synthesized m-$NaFePO_4$, (b) ball-milled m-$NaFePO_4$, and (c) re-calcined m-$NaFePO_4$.

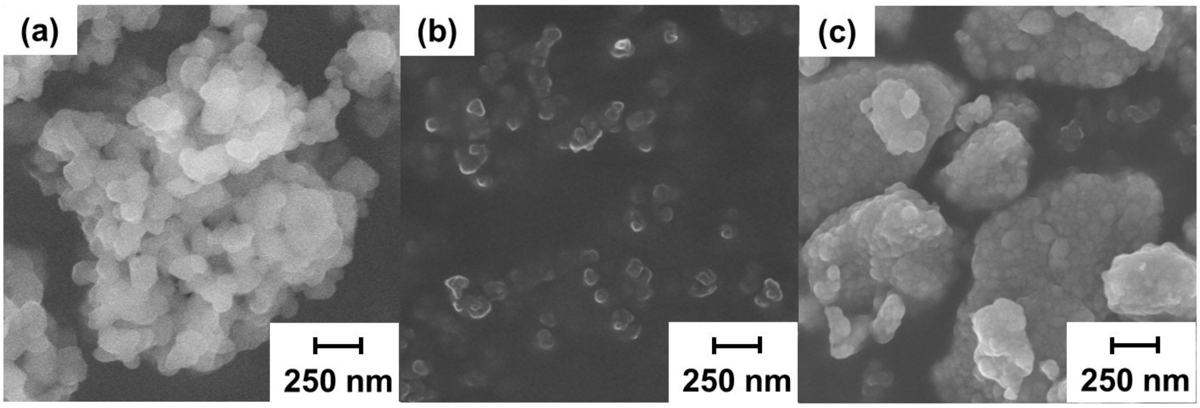

Figure 4-2 Field-emission SEM images of (a) as-synthesized m-$NaFePO_4$, (b) ball-milled m-$NaFePO_4$, and (c) re-calcined m-$NaFePO_4$.

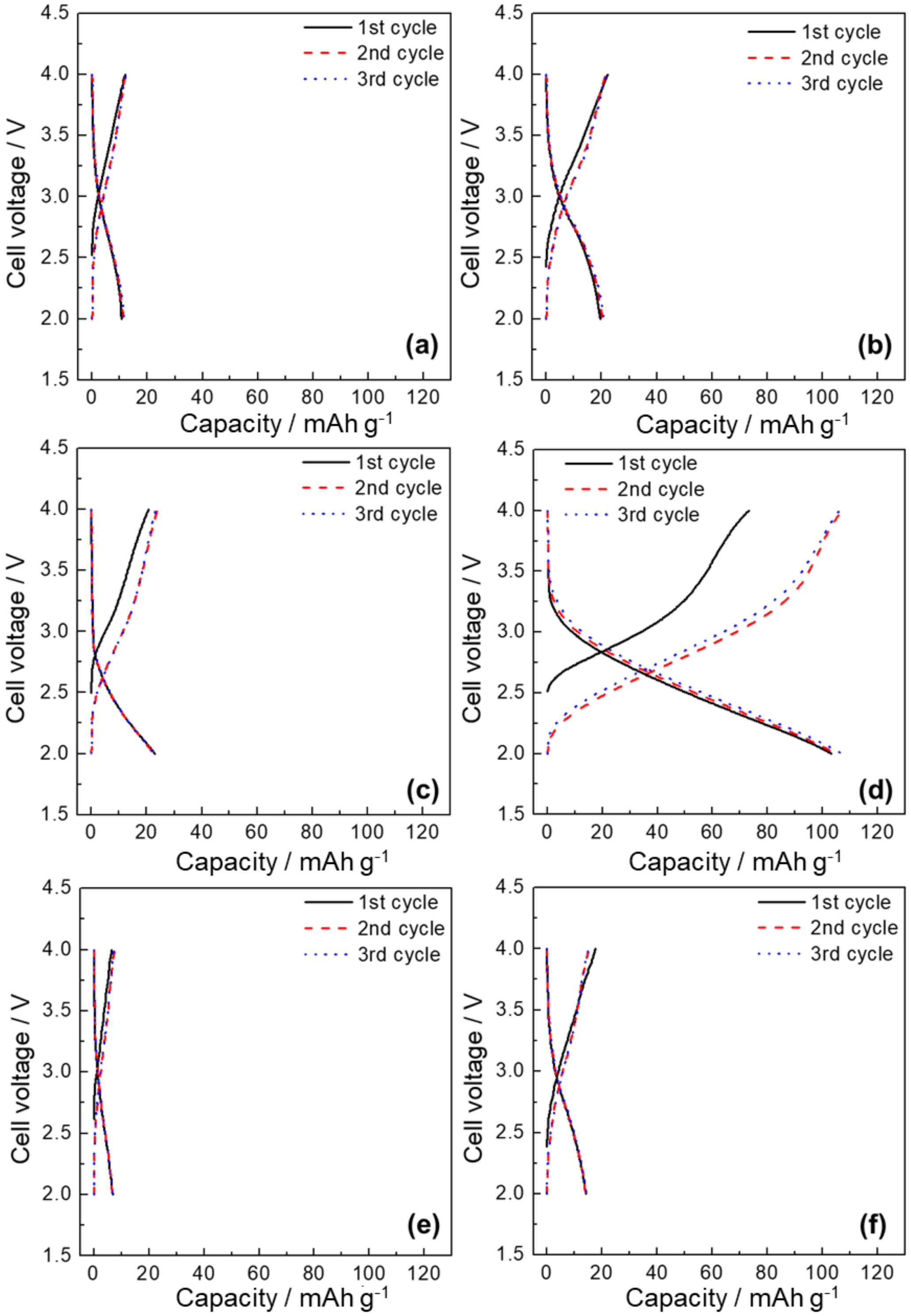

Figure 4-3 Charge-discharge curves of Na/as-synthesized m-NaFePO$_4$ cells at (a) 298 K and (b) 363 K, Na/ball-milled m-NaFePO$_4$ cells at (c) 298 K and (d) 363 K, and Na/re-calcined m-NaFePO$_4$ cells at (e) 298 K and (f) 363 K. Electrolyte: Na[FSA]-[C$_2$C$_1$im][FSA], Charge-discharge rate: C/10, and Cut-off voltage: 2.0-4.0 V.

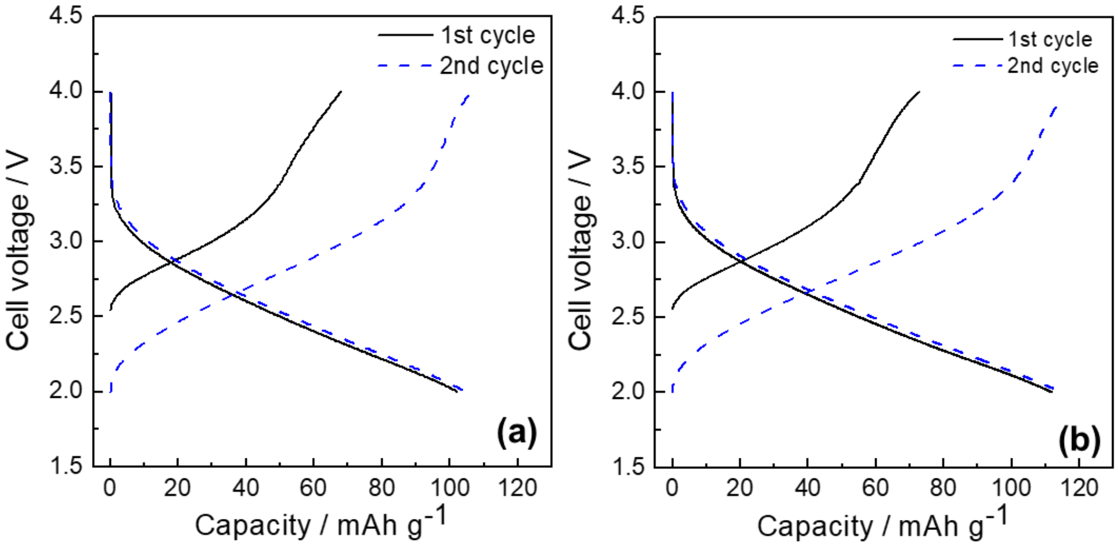

Figure 4-4 Charge-discharge curves of the Na/ ball-milled (24 h) m-NaFePO$_4$ cell at 363 K. Cut-off voltage: 2.0-4.0 V and rate: (a) 0.1 C, and (b) 0.05 C.

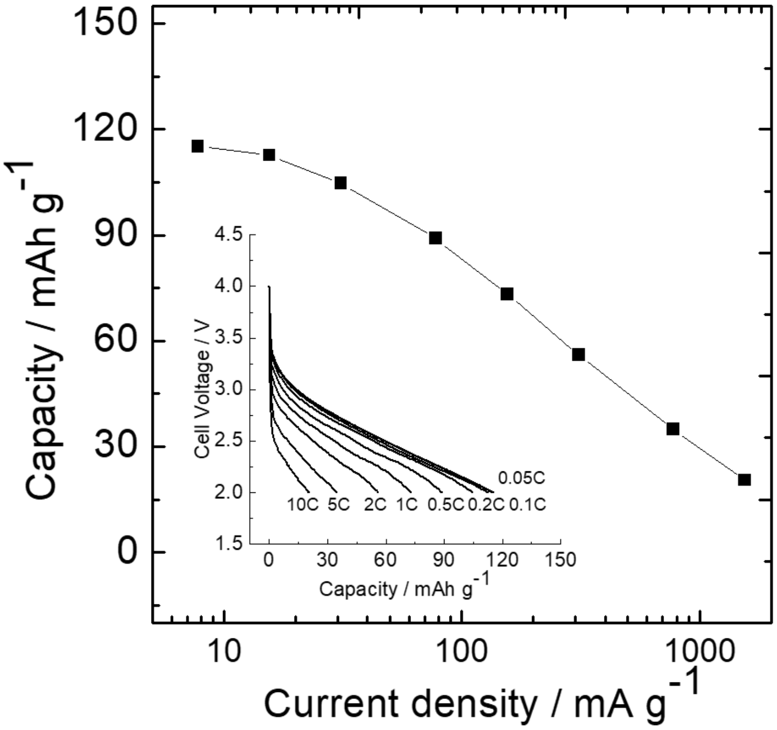

Figure 4-5 Rate capability of Na/ball-milled m-NaFePO$_4$ cell at 363 K. The charging current was C/10, and discharge currents were changed from 0.05 to 5 C. Cut-off voltage: 2.0-4.0 V.

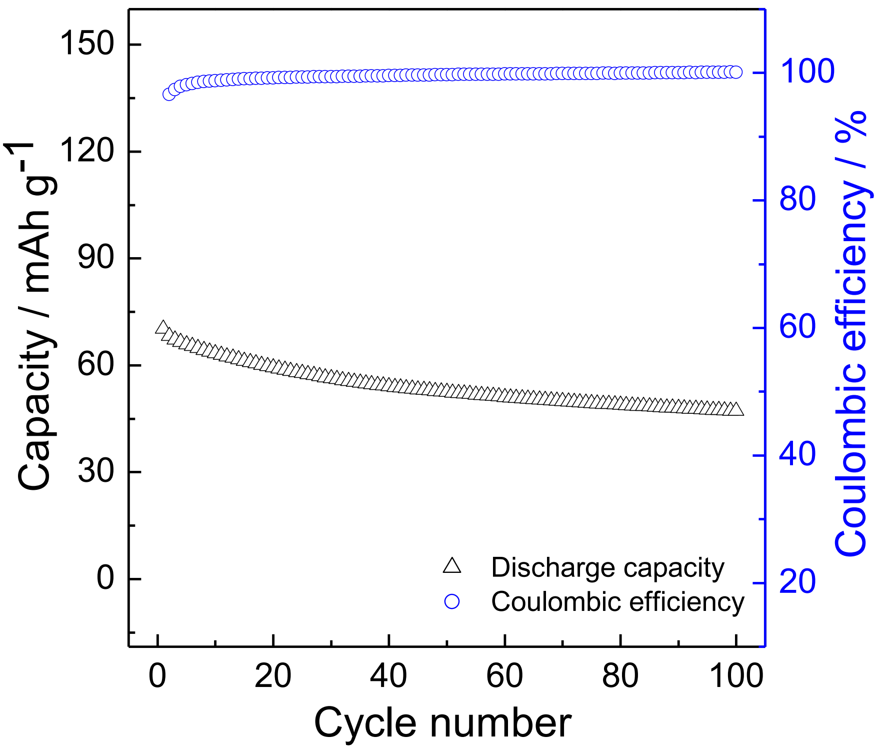

Figure 4-6 Cycleability of Na/ball-milled m-$NaFePO_4$ cell at 363 K. Black triangles indicate discharge capacity, and blue circles indicate Coulombic efficiency. Cut-off voltage: 2.0-4.0 V and rate: 1 C.

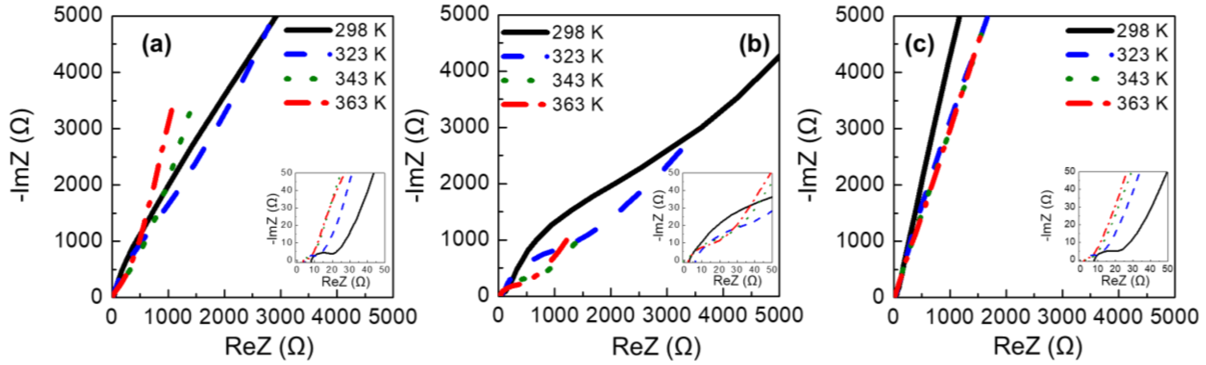

Figure 4-7 Nyquist plots for the $NaFePO_4$/Na[FSA]-[C_2C_1im][FSA]/$NaFePO_4$ symmetric cell in the temperature range between 298 and 363 K: (a) as-synthesized $NaFePO_4$ (b) ball-milled $NaFePO_4$, and (c) re-calcined $NaFePO_4$. AC perturbation: 10 mV and frequency range: 1000 kHz -10 mHz.

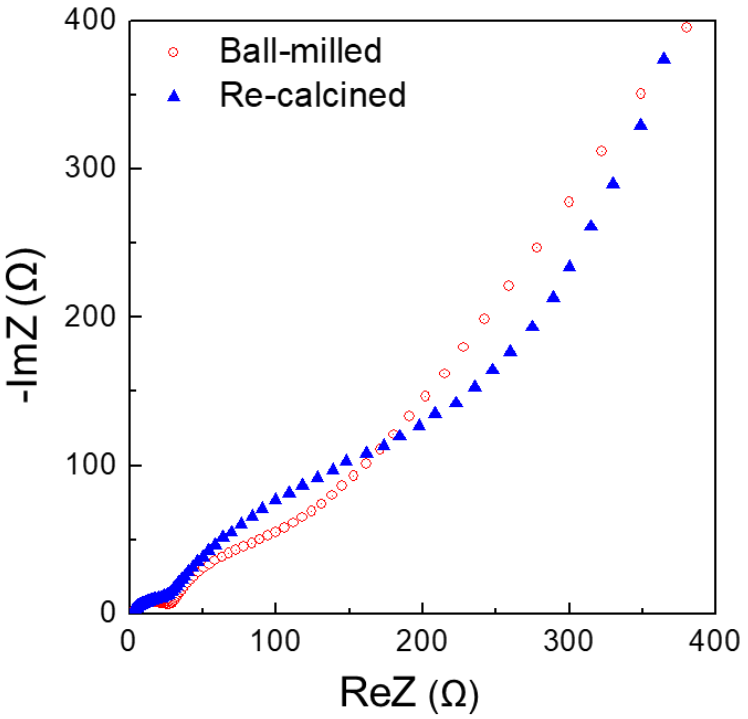

Figure 4-8 Nyquist plots of Na/m-$NaFePO_4$ half-cell. AC perturbation: 10 mV and frequency range: 1000 kHz-10 mHz.

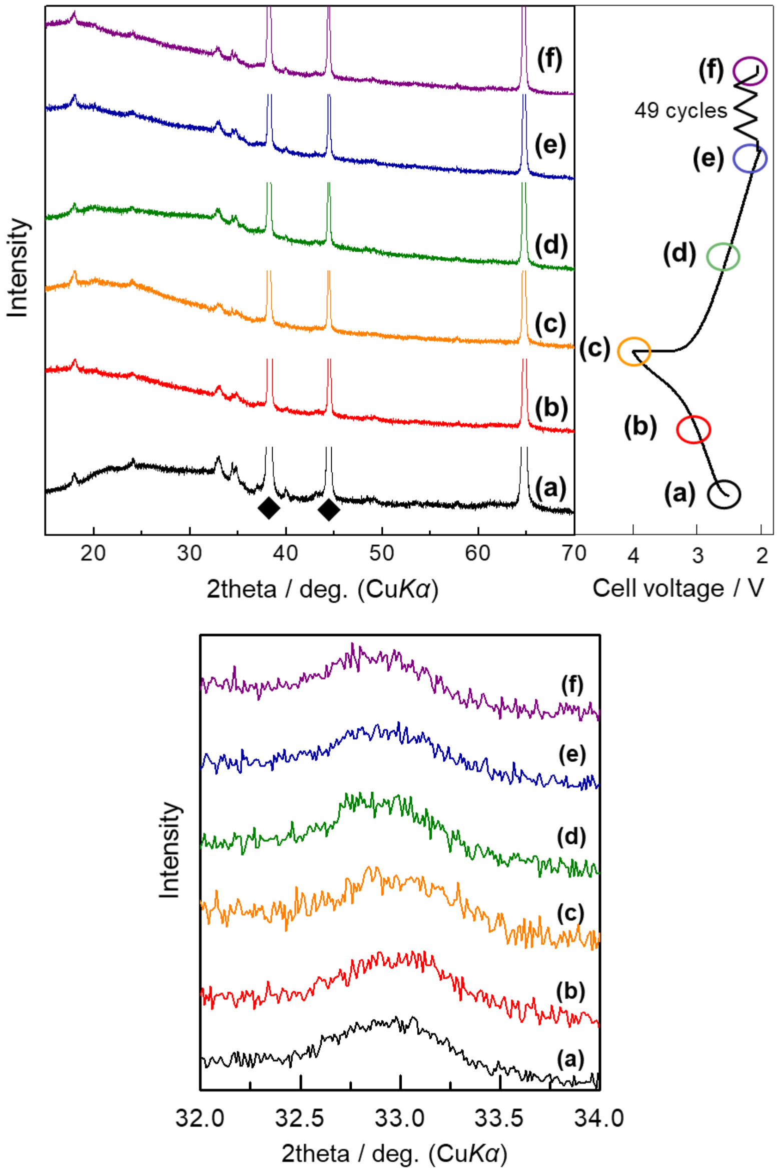

Figure 4-9 *Ex-situ* XRD patterns of the ball-milled m-$NaFePO_4$ electrode, (a) before charge-discharge test, (b) charged to 3 V, (c) charged to 4 V, (d) discharged to 2.5 V, (e) discharged to 2 V, and (f) after 50 cycles. The ♦ marks indicate the peaks of Al.

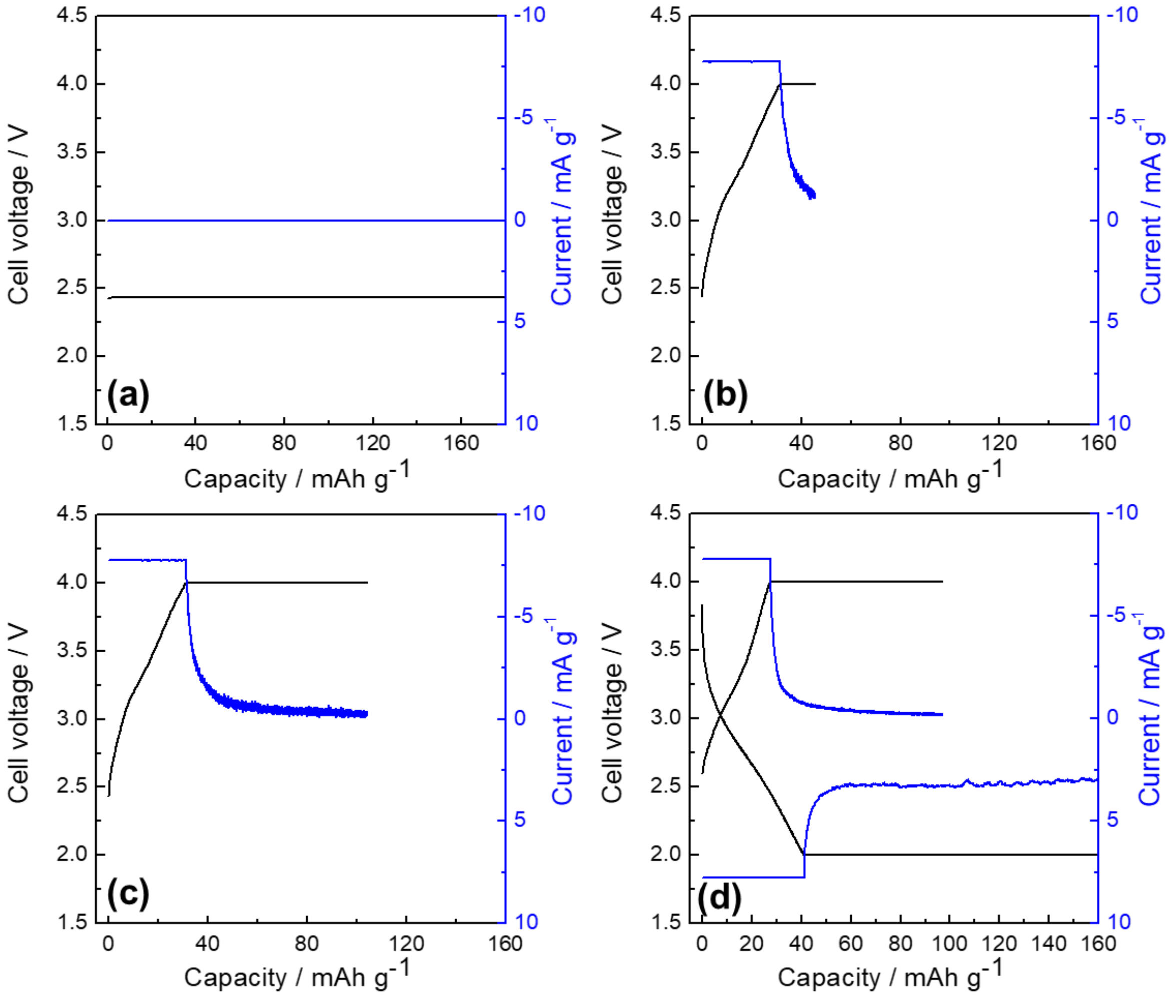

Figure 4-10 Charge-discharge profiles of the as-synthesized m-$NaFePO_4$ at 363 K to prepare the sample for *ex-situ* XRD measurement. (a) OCV 3 h at 363, (b) charged to 4 V and CCCV mode for 10 h, (c) charged to 4 V and CCCV mode for 150 h, and (d) charged to 4 V and CCCV mode for 150 h and discharged to 2 V and CCCV mode for 150 h.

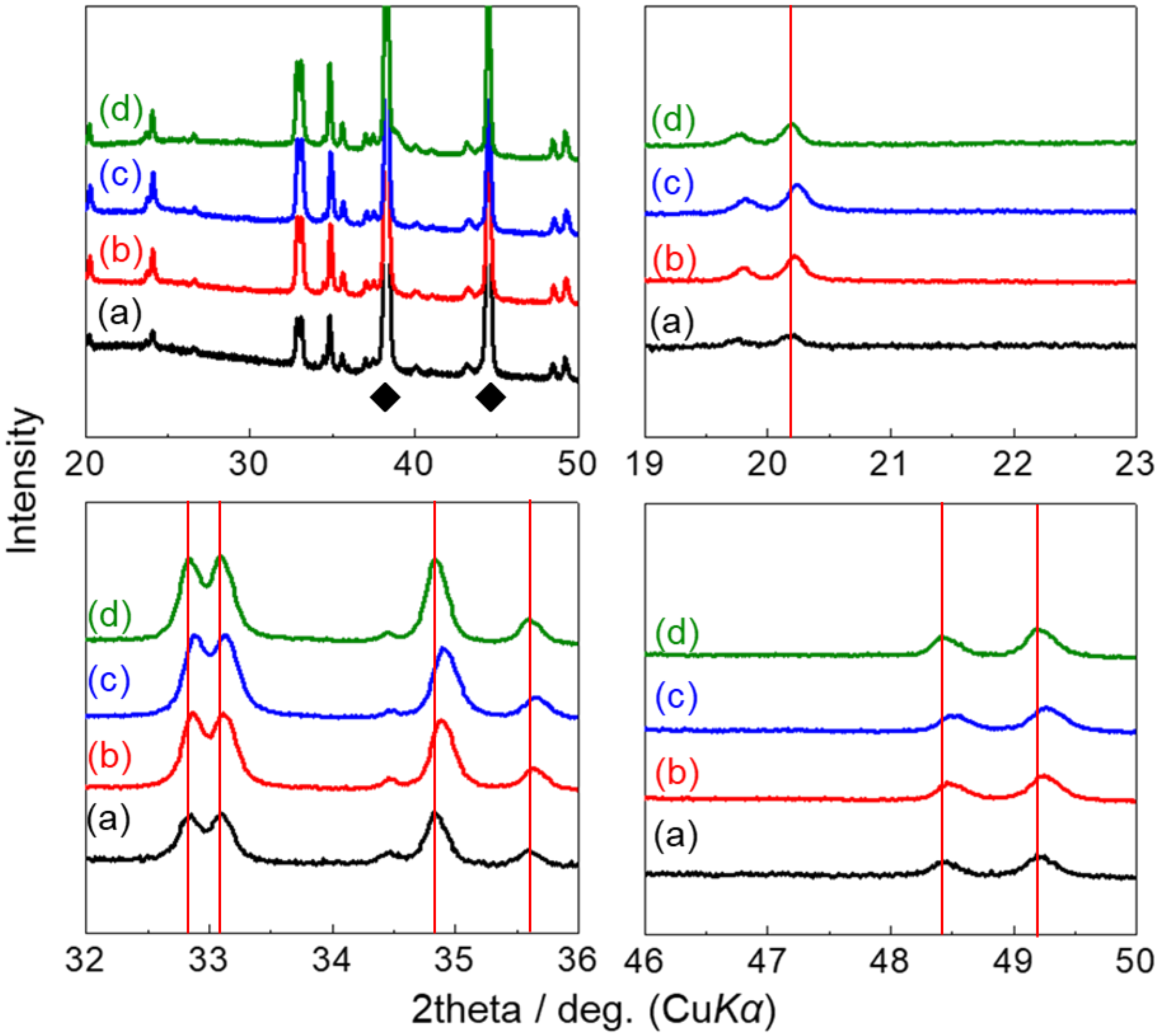

Figure 4-11 *Ex-situ* XRD patterns of the as-synthesized m-NaFePO4 electrode (a) before charge-discharge test, (b) charged to 4 V at 0.05 C and CCCV mode for 10 h, (c) charged to 4 V at 0.05 C and CCCV mode for 150 h, and (d) charged to 4 V at 0.05 C and CCCV mode for 150 h and discharged to 2 V at 0.05 C and CCCV mode for 150 h. The ♦ marks indicate the peaks of Al. The red perpendicular lines are reference lines to identify the shifting of XRD peaks clearly. The results of a charge-discharge profile to prepare *ex-situ* XRD samples are shown in Figure 4-10.

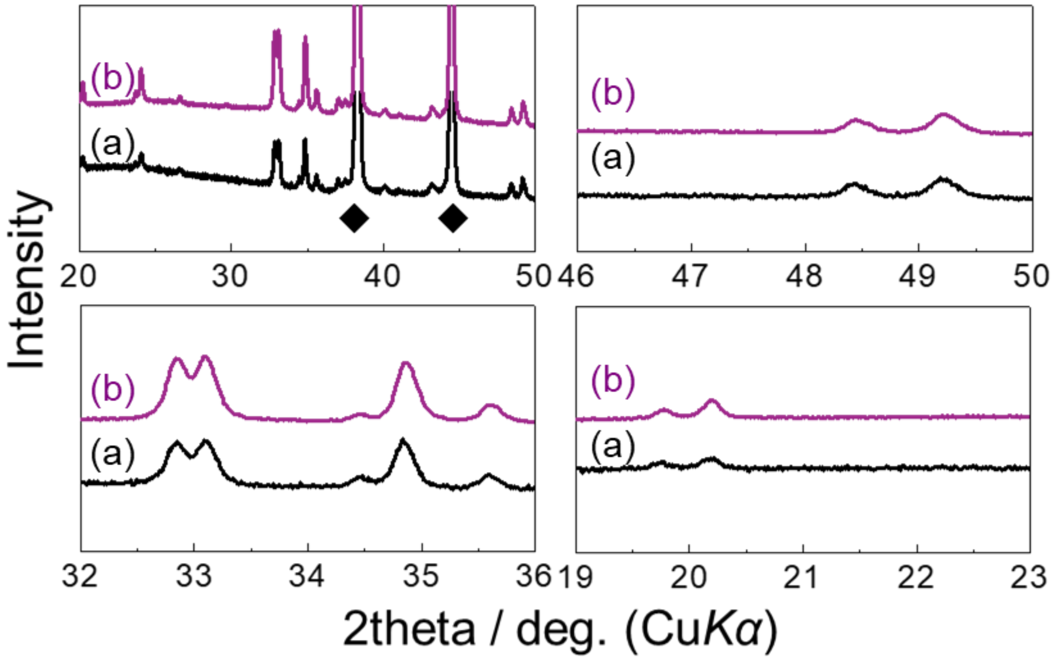

Figure 4-12 *Ex-situ* XRD patterns of the as-synthesized m-NaFePO$_4$ electrode (a) before a charge-discharge test, (b) charged to 4.5 V. The ♦ marks indicate the peaks of Al.

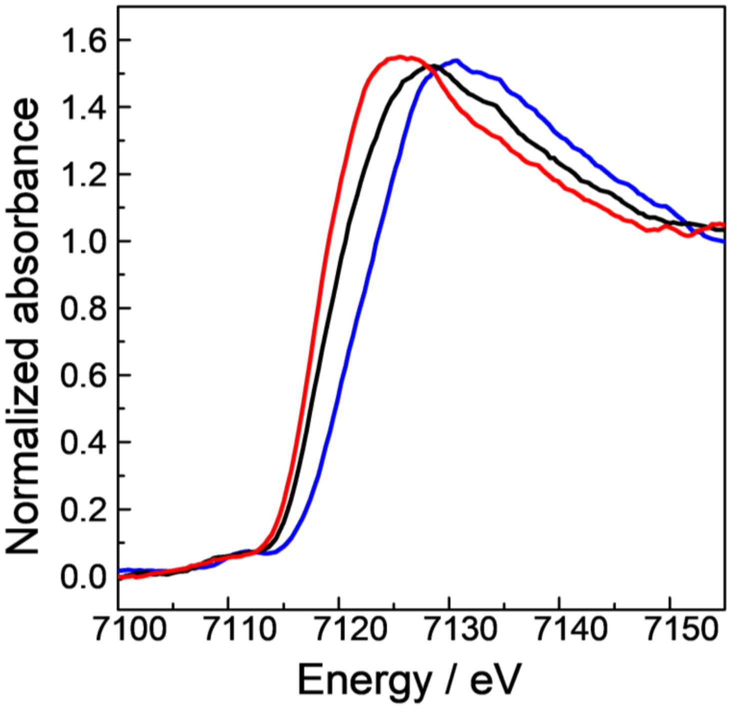

Figure 4-13 Fe *K*-edge XANES spectra of ball-milled NaFePO$_4$ electrodes (black) pristine, (blue) charged to 4.0 V, and (red) discharged to 2.0 V.

References

[1] C. Ding, T. Nohira, R. Hagiwara, K. Matsumoto, Y. Okamoto, A. Fukunaga, S. Sakai, K. Nitta, and S. Inazawa, J. Power Sources, 269 (2014) 124.

[2] C.-Y. Chen, K. Matsumoto, T. Nohira, and R. Hagiwara, J. Electrochem. Soc., 162 (2014) A176.

[3] C.-Y. Chen, K. Matsumoto, T. Nohira, C. Ding, T. Yamamoto, and R. Hagiwara, Electrochim. Acta, 133 (2014) 583.

[4] T. Yamamoto, T. Nohira, R. Hagiwara, A. Fukunaga, S. Sakai, and K. Nitta, Electrochim. Acta, 211 (2016) 234.

[5] C.-Y. Chen, T. Kiko, T. Hosokawa, K. Matsumoto, T. Nohira, and R. Hagiwara, J. Power Sources 332, (2016) 51.

[6] C.-Y. Chen, K. Matsumoto, T. Nohira, and R. Hagiwara, J. Electrochem. Soc., 162 (2015) A2093.

[7] C.Y. Chen, K. Matsumoto, T. Nohira, R. Hagiwara, Y. Orikasa, and Y. Uchimoto, J. Power Sources, 246 (2014) 783.

[8] Y. Zhu, Y. Xu, Y. Liu, C. Luo, and C. Wang, Nanoscale, 5 (2013) 780.

[9] P. Barpanda, T. Ye, S.-J. Chung, Y. Yamada, M. Okubo, H. Zhou, and A. Yamada, Electrochem. Commun., 24 (2012) 116.

[10] P. Barpanda, G. Liu, C. D. Ling, M Tamaru, M. Avdeev, S.-C. Chungm, Y. Yamada, and A. Yamada, Chem. Mater., 25 (2013) 3480.

[11] H. Kim, R.A. Shakoor, C. Park, S.Y. Kim, J.-S. Kim, Y.N. Jo, W. Cho, K. Miyasaka, R. Kahraman, Y. Jung, and J.W. Choi, Adv, Func. Mater., 23 (2013) 1147.

[12] A. Yamada, MRS Bull., 39 (2014) 423.

[13] M. Avdeev, Z. Mohamed, C. D. Ling, J. Lu, M. Tamaru, A. Yamada, and P. Barpanda, Inorg. Chem., 52 (2013) 8685.

[14] S.Oh, S.-T. Myung, J. Hassoun, B. Scrosati, and Y.-K. Sun, Electrochem. Commun., 22 (2012) 149.

[15] J. Kim, D. Seo, H. Kim, I, Park, J. Yoo, S. Jung, Y. Park, W. A. Goddard III, and K. Kang, Energy Environ. Sci., 8 (2015) 540.

[16] P. Paolo Prosini, C. Cento, A. Masci, and M. Carewska, Solid State Ionics., 263 (2014) 1.

[17] M. M. Rahman, I. Sultana, S. Mateti, J. Liu, N. Sharma, and Y. Chen, J. Mater. Chem. A, 5 (2017) 16616.

[18] R. Kapaev, A. Chekannikov, S. Novikova, S. Yaroslavtsev, T. Kulova, V. Rusakov. A. Skundin, and A. Yaroslavtsev J. Solid State Electrochem., 21 (2017) 2373.

[19] J. Hwang, K. Matsumoto, T. Nohira, and R. Hagiwara, Electrochemistry, 85 (2017) 675.

Chapter 5

Electrochemical Performance of $Na_3V_2(PO_4)_3$/C Positive Electrode

5.1 Introduction

Polyanionic compounds with tetrahedral polyanion units $(XO_4)^{n-}$ (X = P, S, Si, As, Mo, or W) can combine with MO_x (M = transition metal) polyhedral units to form structural frameworks. Phosphate-based electrode materials offer open frameworks that favor facile Na^+ ion transport [1]. Of these phosphate compounds, Na superionic conductor (NASICON)-type Na3V2(PO4)3 (NVP) is well-known for its high Na ion conductivity originated by corning sharing arrangement among polyhedral units. It has been proposed as a positive electrode material based on the V^{3+}/V^{4+} redox reaction and offers a theoretical capacity of 117.6 mAh g^{-1} ($Na_3V_2(PO_4)_3 \rightleftarrows NaV_2(PO_4)_3 + 2Na^+ + 2e^-$). Its high thermal stability enables operating across a wide temperature range. In previous studies, this material has exhibited poor cycleability and rate capabilities due to its low electrical conductivity at room temperature [2-6]. Rate capability improvements have been reported using an IL electrolyte at 353 K in a symmetrical cell (V^{3+}/V^{4+}-V^{3+}/V^{2+}) [6]; however, practical performance has not been pursued since then. Recent studies have reported that this material exhibits high cycleability and rate capability in organic electrolytes made via carbon coating [2-5, 7-11].

Figure 5-1 shows secondary battery operating temperatures required for various applications. Although batteries designed for hot environments such as rescue robots and measurement while drilling applications have been studied, academic research on the utilization of waste heat or hot environments to improve battery performance is rare [12, 13]. Hot environments are ubiquitous in our daily lives and in industrial settings. They include automobile engine compartments, heavy industrial settings that include waste heat, and waste treatment plants. The efficient use of such heat is a potential way of achieving high performance with known or unknown electrode materials. Furthermore, batteries for electric vehicle (EV), Hybrid electric vehicle (HEV), and various other applications must operate at a wide range of temperatures. Unfortunately, organic electrolytes can be used only in a limited temperature range (<333 K) due to their flammabilities and volatilities, which are the main causes of recent Li-ion battery (LIB) safety issues [14, 16].

Moreover, co-solvents and additives are required for organic electrolytes to be used at low temperatures [14, 16]. Ionic liquids (ILs) composed of only cations and anions are nonflammable as well as chemically, electrochemically, and thermally stable. In addition, they exhibit wide electrochemical windows [17-21]. Thus, they can be used as electrolytes in secondary batteries designed for use from subfreezing to intermediate temperatures. Understanding of basic physical properties was attempted for the purpose of battery applications [22-23], along with an approach to practical applications, including Na secondary batteries [15, 16]. Intermediate-temperature operating of Na secondary batteries with an FSA-based IL electrolyte was explored with a range of positive (e.g., $NaCrO_2$, $Na_2FeP_2O_7$, and $NaFePO_4$) [27-29] and negative electrode (Sn, metal-Sn alloy, and hard carbon) materials in previous studies [30-32]. FSA-based ILs are more stable than others against the reduction in both Li and Na systems with various other popular anions, and across a wide temperature range [33-37]. They are suitable for operating of Na secondary batteries at intermediate temperatures [35, 38]. Intermediate temperature operating via the use of waste heat and hot environments sometimes enhances Na^+ ion transport and electrode reactions, thus enabling increased practical capacities, as well as excellent cyclabilities and rate capability [28, 39-41].

The electrochemical properties of carbon-coated $Na_3V_2(PO_4)_3$ (NVPC) electrodes prepared via sol-gel method are tested at various temperatures using the 20-50 mol% Na[FSA]-[C_2C_1im][FSA] IL systems [42] in order to develop Na secondary batteries that operate from subfreezing to intermediate temperatures. Intermediate-temperature sodiation/desodiation mechanisms in the NVP structure are analyzed via *in-situ* XRD measurements. Finally, relationships between energy and power densities are compared to those of existing positive electrode materials ($NaCrO_2$ and $Na_2FeP_2O_7$) to confirm the effectiveness of the present system.

5.2 Experimental

Synthesis and Characterization: The powdery sample was synthesized via a sol-gel method [9]. In a typical procedure, 1.8185 g of V_2O_5 (Sigma-Aldrich Chemistry, 99.6% purity, 9.998 mmol) and 6.3036 g of oxalic acid dihydrate (Wako Pure Chemical Industries, 99.5 – 100.2% purity, 50.001 mmol) were dissolved in ion-exchange water at 353 K via continuous stirring using a magnetic bar. Oxalic acid works as both a reducing agent and a carbon source. As the mixture became a blue, homogeneous solution, 1.1999 g of NaOH (Wako Pure Chemical Industries, 97.0% purity, 30.000 mmol), 3.4510 g of $NH_4H_2PO_4$ (Wako Pure Chemical Industries, 99.0% purity, 30.002 mmol), and 1.7118 g of glucose (Wako Pure Chemical Industries, 5.001 mmol) were added to the solution and stirred for an additional 3 h. Glucose was used as a carbon source and vanadium reducing agent. The solution was dried completely at 393 K for a day and then ground using a mortar and pestle. Next, it was calcined at 623 K for 5 h under flowing Ar. After calcination, the precursor was ground using a mortar and pestle and heated at 1073 K under flowing Ar for 8 h.

NVP-SS was prepared for comparison via a conventional solid-state method. In acetone, 2.98186 g of V_2O_3 (Wako Pure Chemical Industries, > 99% purity, 19.895 mmol) and 7.166 g of NaH_2PO_4 (Wako Pure Chemical Industries, > 99% purity, 59.727 mmol) was ball-milled for 12 h at 600 rpm using a Fritsch Pulverisette 7 Premium Line. The mixture was collected and dried under vacuum for 24 hours at 393 K and then thoroughly ground using a mortar and pestle. After grinding, the precursor was pelletized (70 MPa) for 10 min. This precursor pellet was heated at 1073 K for 40 h under Ar flow and then cooled to 298 K. The $NaCrO_2$ and $Na_2FeP_2O_7$ samples were prepared as previously reported [27, 28].

XRD patterns were collected in the Bragg-Brentano geometry using a Rigaku SmartLab diffractometer with Ni-filtered Cu-$K\alpha$ radiation (40 kV and 30 mA) to confirm NVPC purity. The diffractometer was equipped with a silicon strip high-speed detector (Rigaku D/teX Ultra 250). Rietveld refinement was performed using FullProf software [43]. The NVPC morphology was observed via SEM (Hitachi SU-8020), and EDS mapping was performed using an analyzer (Horiba EMAXEvolution X-max) attached to the SEM. The surface area of the electrode materials was evaluated the BET method [44] based on the results of nitrogen adsorption analysis by Tristar II 3020 (Shimadzu Corp.).

Electrochemical Measurements: Electrochemical properties were measured using 2032 coin-type cells at 253 to 363 K. A charge-discharge rate of 0.1C was used to understand basic system behavior. Various discharge currents of 0.1C to 700C were used in rate capability tests. The Cut-off voltages were fixed to 2.4-3.8 V. Na metal (Sigma-Aldrich Chemistry, 99.95% purity) was cut into a disk (16 mm in diameter) and fixed on an Al plate current collector as a negative electrode. The positive electrode was prepared by mixing the NVPC composite, Super C65, and PTFE (80:15:5 wt%) and pressing the mixture on an Al mesh (the loading mass of the active material in the electrodes is approximately 3 mg cm^{-2}). $NaCrO_2$ and $Na_2FeP_2O_7$ electrodes were prepared in the same manner [38, 45]. The NVPC sample used for rate capability tests was washed using ion-exchange water and vacuum-dried at 363 K for 24 h prior to electrode fabrication. 20-50 mol% Na[FSA]-[C_2C_1im][FSA] ionic liquids with molar ratios of 20:80, 30:70, 40:60, and 50:50 were used as electrolytes. The salts, Na[FSA] (Mitsubishi Materials Electronic Chemicals, purity >99%) and [C_2C_1im][FSA] (Kanto Chemical, purity >99.9%), were dried under vacuum for 24 h at 353 K. The typical water content of this IL system was below 30 ppm, according to Karl-Fischer titrations (899 Coulometer, Metrohm). A glass microfiber separator was impregnated with the electrolyte at 333 K under vacuum for 1 d prior to the test. Charge-discharge properties, rate capabilities, and cycling were evaluated using an HJ1001SD8 charge-discharge test device (Hokuto Denko). All electrochemical measurements were started at least 2 h after the relevant temperature adjustments.

Cells were prepared for EIS using 2032 coin-type cells. The cells were assembled in dry Ar. Measurements were performed using a VSP potentiostat (Bio-Logic) at 298 K, 323 K, 343 K, and 363 K over a frequency range from 1 MHz to 40 mHz with a perturbation amplitude of 10 mV.

In-situ XRD Measurements: In-situ XRD measurements were performed using an air-tight cell with a Kapton® window and a temperature controller (Rigaku). The diffraction patterns were recorded at 363 K under vacuum. The electrochemical measurements were controlled using an ECAD1000 charge-discharge system (EC Frontier Inc.). The cell was continuously charged and discharged at 10 mA g^{-1} during XRD measurements performed at a scan rate of 1° s^{-1}. The cell voltage was maintained in fully charged and discharged (3.8 V and 2.4 V, respectively) states to confirm the structures in these stable states.

5.3 Results and Discussion

5.3.1 Structural Characteristics

The XRD patterns of the synthesized NVPC electrodes confirm the presence of a pure NVP phase and an amorphous carbon phase. The NVPC XRD pattern was indexed as a rhombohedral crystal system and was fitted with space group $R\overline{3}c$ via Rietveld refinement. The lattice parameters of the NVPC were determined to be a = 8.72209(12) and 21.8563(5) Å (R_{wp} = 16.0), and match crystallographic data from previous reports [9] (Figure 5-2 and Table 5-S1 in the appendix for crystallographic data). The NVPC XRD pattern matches that of NVP prepared by a solid-state method (NVP-SS) (inset of Figure 5-2), although the former exhibits slightly broader diffraction peaks.

The scanning electron microscopy (SEM) image of the NVPC powder is shown in Figure 5-3 alongside energy dispersive X-ray spectrometric (EDS) maps. The synthesized NVPC composites are composed of particles of various sizes, which produce a porous, coral-reef morphology. The magnified SEM images (Figure 5-S1) show a number of particles around 50 nm in size within the pores of the bulk NVPC particles, while NVP-SS has a particle size around 25 μm with non-porous morphology (Figure 5-S2). Surface areas obtained by Brunauer–Emmett–Teller (BET) method convinced that NVPC has 100 times larger surface area than NVP-SS. Control of morphology, together with homogeneous carbon coating is important to derive the good electrochemical performance of NVPC because the numbers of active sites and diffusion paths, are highly related to the electrode reaction. EDS mapping results match the composition of NVPC, with all the elements distributed over the particles. The actual carbon content in NVPC was determined to be 10.8 wt% via elemental analysis.

5.3.2 Electrochemical Characterization

Figure 5-4 shows galvanostatic charge-discharge curves of the Na/NVP-SS and Na/NVPC cells at 0.1C using the 50 % Na[FSA]-[C_2C_1im][FSA] IL electrolyte. The NVP-SS cell exhibits a first-discharge reversible capacity of only 44.3 mAh g^{-1} at 298 K. This reversible capacity degrades rapidly, reaching 34.0 mAh g^{-1} on the fifth cycle (Figure 5-4a). As the temperature increases, the NVP-SS cell exhibits a slightly larger first discharge capacity of 50.6 mAh g^{-1} at 363 K. However, the capacity degrades rapidly under these conditions as well as 298 K, reaching 38.7 mAh g^{-1} on the fifth cycle (Figure 5-4b). The limited performance described here occurs due to the characteristic low electrical conductivity of NVP-SS.

Charge-discharge performance improves dramatically after the carbon coating. The NVPC composite exhibits reversible capacities of 98.7 mAh g^{-1} and 104.5 mAh g^{-1} at 298 K (Figure 5-4c and 363 K (Figure 5-4d), respectively. During charging and discharging, a flat plateau is observed at approximately 3.4 V. This is associated with the V^{4+}/V^{3+} redox activity ($NaV_2(PO_4)_3/Na_3V_2(PO_4)_3$) seen in organic electrolytes [68]. Capacities of about 100 mAh g^{-1} are obtained at 298 K regardless of the Na[FSA] fraction used. Increasing the temperature increases the capacity slightly (Figures 5-S4 and 5-S5 in the appendix for charge-discharge profiles with various molar ratios).

Prior studies reported that NVP fabricated with carbonaceous materials could improve rate capabilities in organic electrolytes [7, 9, 46]. Graphene-scaffolded NVP with 1 mol dm^{-3}

$Na[ClO_4]$-EC/DEC (1:1 v/v) as the electrolyte exhibited 44 mAh g^{-1} at 50C [7]. Carbon-coated, porous NVP using a 1 mol dm^{-3} $Na[ClO_4]$-EC/PC (1:1 v/v) as the electrolyte exhibited capacity retention of 54% at 40C [46]. Another carbon-coated porous NVP using an electrolyte of 1 mol dm^{-3} $Na[ClO_4]$-PC with 2% fluorinated ethylene carbonate as the electrolyte exhibited a capacity of 75.54 mAh g^{-1} at 80C [9]. Such superior NVP rate capability was further improved upon via intermediate-temperature operating with IL electrolytes in this study.

Figure 5-5 compares the rate capabilities of the Na/NVPC cells at 298 K and 363 K. The cells shown using the Na[FSA]-$[C_2C_1im]$[FSA] system with four different Na[FSA] fractions. The cells are charged up to 3.8 V at a constant current of 0.1C and then discharged to 2.4 V at 0.1C to 40C. At both temperatures, the discharge capacity decreases as the discharge current increases, regardless of the Na[FSA] fraction in the IL. The highest capacity retention results at 20C are observed with Na[FSA] fractions of 20 mol% and 50 mol% at 298 K (40.3%) and 363 K (93.0 %), respectively. This suggests that the rate capability improves significantly at 363 K and the Na[FSA] fraction where the highest capacity retention is observed differs as a function of temperature (Figures 5-S6 and 5-S7 in the appendix for discharge curves during rate capability tests with ILs composed of various Na[FSA] fractions).

Because the Na/NVPC cells show notably high rate capabilities at elevated temperatures, further high-rate charge-discharge tests were performed using cells with high Na[FSA] contents. Figure 5-6 shows the results of super-fast rate capability tests of a Na/NVPC cell with a Na[FSA] fraction of 50% at 363 K. The cell was charged to 3.8 V at a constant current of 0.1C and then discharged to 2.4 V at currents ranging from 0.1C to 700C. A discharge rate of 700C corresponds to 813630 mA g^{-1} and a 5.1 sec discharge (Table 5-S2 in the appendix for the capacities and capacity retention values depicted in Figure 5-6). Up to a discharge rate of 100C, the cells exhibit capacity retentions of at least 80% of the values achieved at 0.1C. Moreover, capacity retentions of 48%, 35%, and 23% are obtained at 500C, 600C, and 700C, respectively. The polarization increases as the current density increases, which leads to the large capacity loss at high current densities. Thus, different lower Cut-off voltage of 0.8-2.4 V was applied to confirm a possible increase in capacity (see Figure 5-S8 and Table 5-S3). The results show that discharge capacities increase after adjusting the Cut-off voltages; capacity retentions of 69%, 58%, 36%, and 19% are obtained at 500C, 1000C, 1600C, and 2000C, respectively.

Figure 5-7 shows electrochemical impedance spectra (EIS) of the Na/NVPC half-cell (Na[FSA] fraction = 50 mol%) at a state of charge (SOC) of 0.5. EIS results reveal that the interfacial resistance, which is indicated by the high-frequency semicircle (characteristic frequencies of 60–700 Hz), decreases drastically relative to the bulk resistance as the measurement temperature increases. Regarding the charging process, the fast charge up to 3.8 V at 100C with the Na[FSA] fraction = 40 mol% at 363 K results in the charge capacity of 84.7 mAh g^{-1} (see Figure 5-S9, appendix). However, charging at 100C followed by further charging at 10C produces a charge capacity of 100.0 mAh g^{-1} in 75 sec. Charge-discharge cycles using this charging mode and a 10C discharge process exhibit stable performance over 100 cycles and the high coulombic efficiencies (average >99.9%) (Figure 5-S9, appendix).

Cycling performance was tested after the rate capability tests were performed using the same cells with four different Na[FSA] fractions were tested at 298 K and 363 K. The cells were charged and discharged at 1 C for 300 cycles. As shown in Figure 5-8, the NVPC exhibits stable cycling performance at 363 K. It achieves outstanding capacity retention of 94.8–99.0% after 300 cycles and the average Coulombic efficiency above 99.9% (Figure 5-S10 in the appendix for measurements made at 298 K). In Figure 5-8e, the long-term cycling performance of a cell-based on an IL with a Na[FSA] fraction of 40 mol% was tested at 20C. These conditions correspond to a charge-discharge cycle time of about 6 min. The cell retains its high capacity for many cycles, achieving 96.4%, 92.3%, and 89.2% capacity retention after 1000th, 3000th, and 5000th cycles, respectively. Such stable cycling performance is associated with the stable biphasic reaction of NVP and high durability of the IL against redox reactions, including Al corrosion and oxidative decomposition [47, 48].

Secondary batteries that can operate in a wide temperature range have been pursued by various manufacturers. Unfortunately, conventional organic electrolytes limit these batteries to near at room-temperature conditions. Additives and co-solvents are required for low-temperature operating, and these electrolytes have difficulty operating above 333 K because of safety issues and solid-electrolyte interphase instability.

With regard to low-temperature operating, cells with NVPC positive electrodes and IL electrolytes achieve sufficient electrochemical performance even below freezing point. Figure 5-9 shows charge-discharge measurements of samples with four different Na[FSA] fractions performed below room temperature (298 K, 263 K , 253 K, and 243 K) at 0.1C. Particular attention should be paid to the sample with Na[FSA] fraction = 20 mol%, which exhibits reversible capacities of 100.8 mAh g^{-1}, 78.1 mAh g^{-1}, and 57.6 mAh g^{-1} at 298 K, 263 K, and 253 K, respectively. Since high rate capabilities were observed with high Na[FSA] fractions at intermediate temperatures, optimization of Na[FSA] fraction may be required to match the environment in practical applications.

5.3.3 In Situ XRD Studies

Figure 5-10 shows the result of *in-situ* XRD measurement performed to investigate the structural changes in an NVPC during electrochemical cycling at 363 K. The Na/NVPC cell was charged and discharged for two cycles at 0.1C. XRD patterns were recorded in a 2θ range of 10° to 60°. For the XRD patterns recorded at 2.4 V and 3.8 V, the potential was maintained by using constant voltage mode during charging and discharging. The other patterns were recorded during charge-discharge cycles. The diffraction peak at 18.1° is assigned to PTFE, while those at 38.43° and 44.67° are assigned to the Al current collector. The measured *in-situ* XRD patterns are directly compared to the Bragg peak positions of NVP and $NaV_2(PO_4)_3$ simulated from previous structural data [49]. When charging begins, the XRD patterns match that of unaltered NVP [49]. New peaks appear, and old peaks disappear as charging proceeds, and de-sodiation from the NVP phase occurs. The XRD pattern after charging to 3.8 V matches that of $NaV_2(PO_4)_3$ prepared chemically by extracting Na^+ from NVP [49]. After the reverse process, the XRD pattern recovers to that of the original NVP via sodiation. The applicable Bragg peak position changes appear to be completely reversible for two charge-discharge cycles. The series of XRD patterns of NVPC collected for two charge-discharge cycles suggests that Na insertion/extraction occurs in a two-phase manner. The transformation from $NaV_2(PO_4)_3$ to $Na_3V_2(PO_4)_3$ and the reverse process both occur at 363 K. The process is similar to that shown in the previous study conducted at 298 K using a conventional organic electrolyte [10].

5.4.4 Comparison of Power and Energy Densities of Selected Positive Electrode Materials

Figure 5-11 shows relationships between energy and power densities for selected positive electrode materials that include FSA-based IL electrolytes ($NaCrO_2$, $NaFeP_2O_7$, and NVPC) at 298 and 363 K. The same conditions are used to determine the performance of each electrode. Power densities are calculated based on the weight of positive electrode material, assuming the use of a Na metal negative electrode. Na[FSA] fractions of 30 and 50 mol% are used at 298 K and 50 mol% at 363 K, respectively. Low and high concentrations achieve better performance at 298 K and 363 K, respectively [27, 28]. The $NaCrO_2$ positive electrode material with an average working voltage of ~3.0 V is one of the most widely investigated layered oxides for Na secondary batteries [50, 51]. It exhibits stable charge-discharge behavior at intermediate temperatures with a practical capacity of ~110 mAh g^{-1} [29, 52]. The pyrophosphate $Na_2FeP_2O_7$ possesses a theoretical capacity of 97 mA g^{-1} and has three-dimensional Na^+ diffusion paths with acceptably low activation energies [53]. This material exhibits a high rate capability at 363 K and up to 400C [28, 40]. Although electrode performance is enhanced by increasing the operating temperature, the comparison in Figure 5-11 indicates the NVPC performs considerably better than $NaCrO_2$ or $NaFeP_2O_7$. The difference between performance at 298 K and 363 K for NVPC is smaller than in the other two cases. However, the energy density delivered at a high power density is quite attractive because of the high rate capability. Such good performance of NVPC is derived from the high Na^+ ion diffusivity in the NASICON structure combined with improved electronic conductivity by carbon coating. Furthermore, the intermediate-temperature operating also enhances the interfacial process as well as the ionic and electronic conductivity, leading to the relationship between power and energy density. The higher working voltage of NVPC than those of the two other materials is also advantageous for high energy density.

5.4 Conclusions

High rate capabilities, good cycling performance, a wide range of operating temperatures, and good safety characteristics are required for practical Na secondary battery applications. In this work, the NVPC composites were prepared via sol-gel chemistry and combined with Na[FSA]-[C_2C_1im][FSA] ionic liquid electrolytes to achieve excellent electrochemical performance. The composite exhibited superior reversible charge-discharge performance across a wide temperature range of 243 K to 363 K. It also exhibited good cycling stability after over 5000 cycles and outstanding charge-discharge rates under various operating conditions. X-ray diffraction analysis revealed that the charge-discharge process proceeds in a two-phase manner at an elevated temperature (363 K), matching the mechanism previously reported at room temperature. The power and energy densities of various Na/positive electrode ($NaCrO_2$, $Na_2FeP_2O_7$, and NVPC) cells with IL electrolytes were compared, and NVPC delivered the highest energy and power densities. The results highlighted the outstanding performance of NVPC with high safety over a wide temperature range. This type of Na secondary battery has the potentials to be used in various situations such as the ones in ESS and EV, which mentioned above. Furthermore, it enables the potential for practical utilization in non-ambient conditions, particularly hot environments such as in engine compartments or near domestic boilers where the latent heat exists. Acceleration of research directed to the use of ionic liquid electrolytes at elevated temperatures is expected in future works since it provides an effective way to construct a sustainable society.

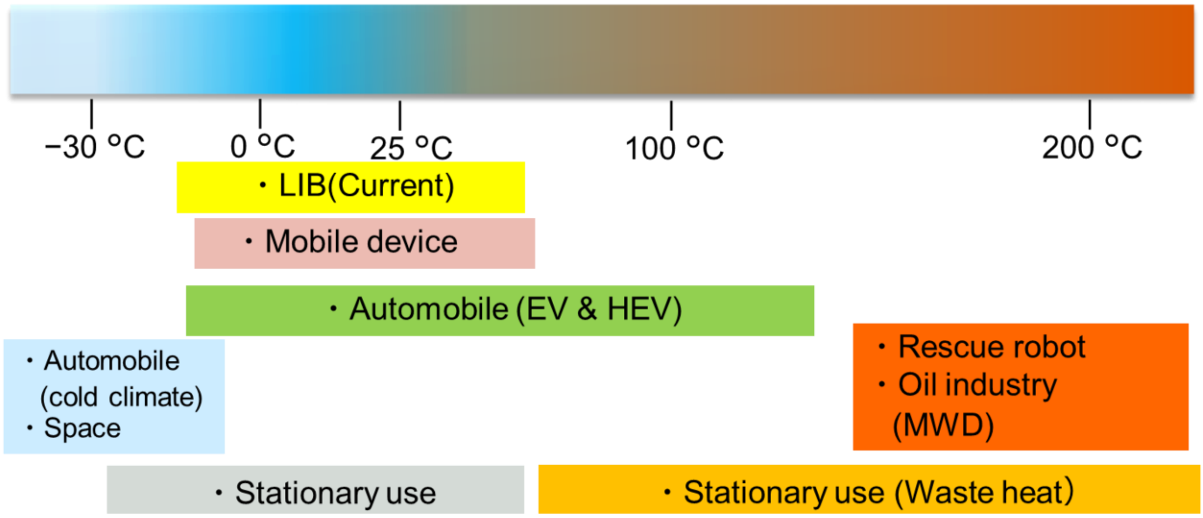

Figure 5-1 Operating temperatures of secondary batteries and temperatures required for selected applications.

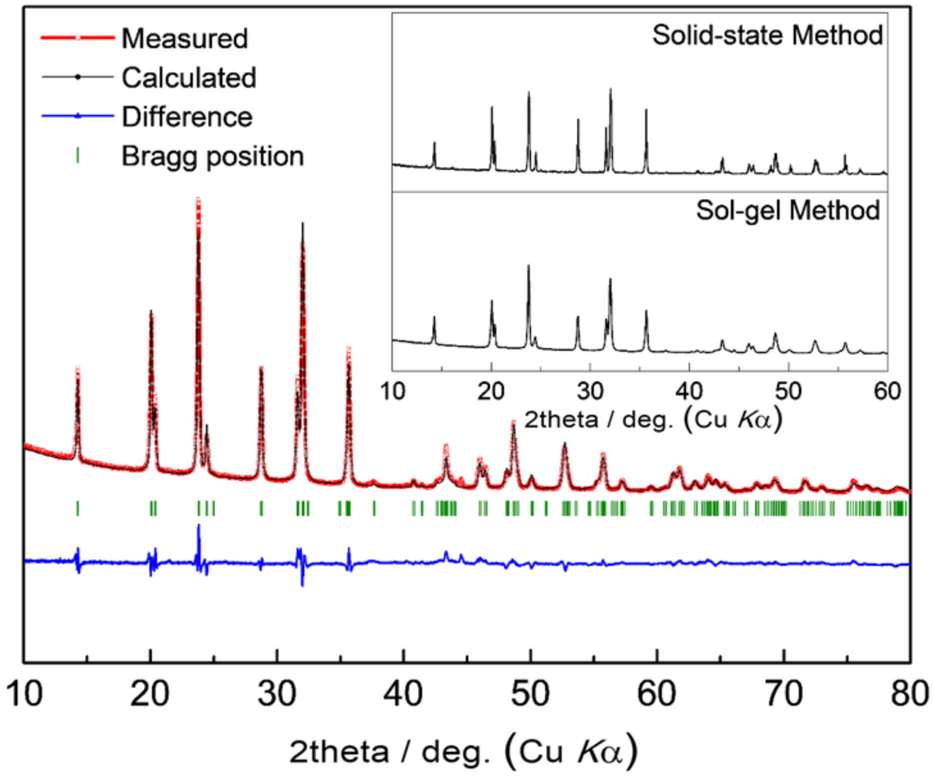

Figure 5-2 Rietveld refinement result from NVPC prepared via a sol-gel method and XRD measurement of NVP synthesized via a solid-state method (inset). See Table 5-S1 in the appendix for NVPC crystallographic details.

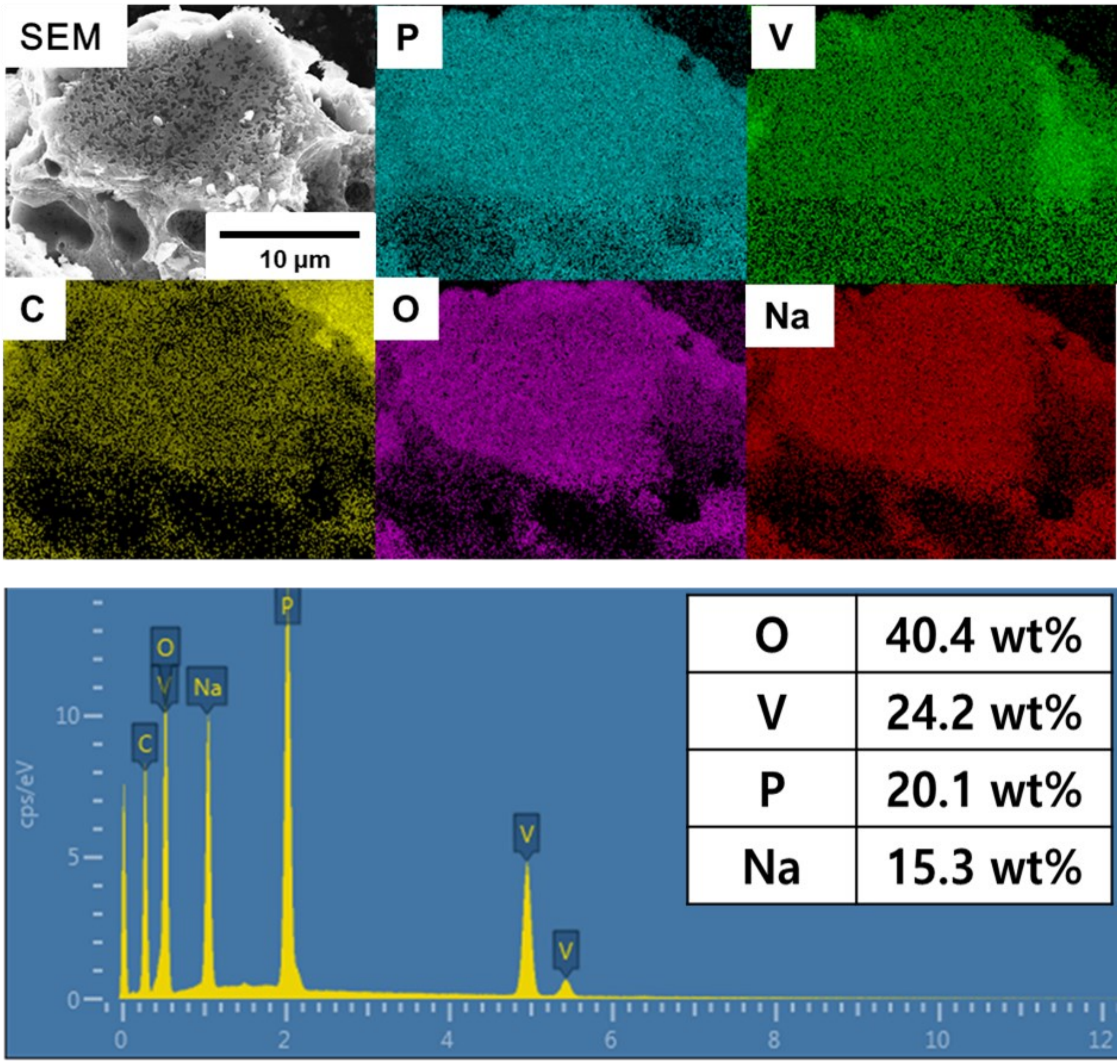

O	40.4 wt%
V	24.2 wt%
P	20.1 wt%
Na	15.3 wt%

Figure 5-3 SEM image and EDS map of elements present in the NVPC sample. The amount of carbon was omitted from the calculation of elemental composition by weight.

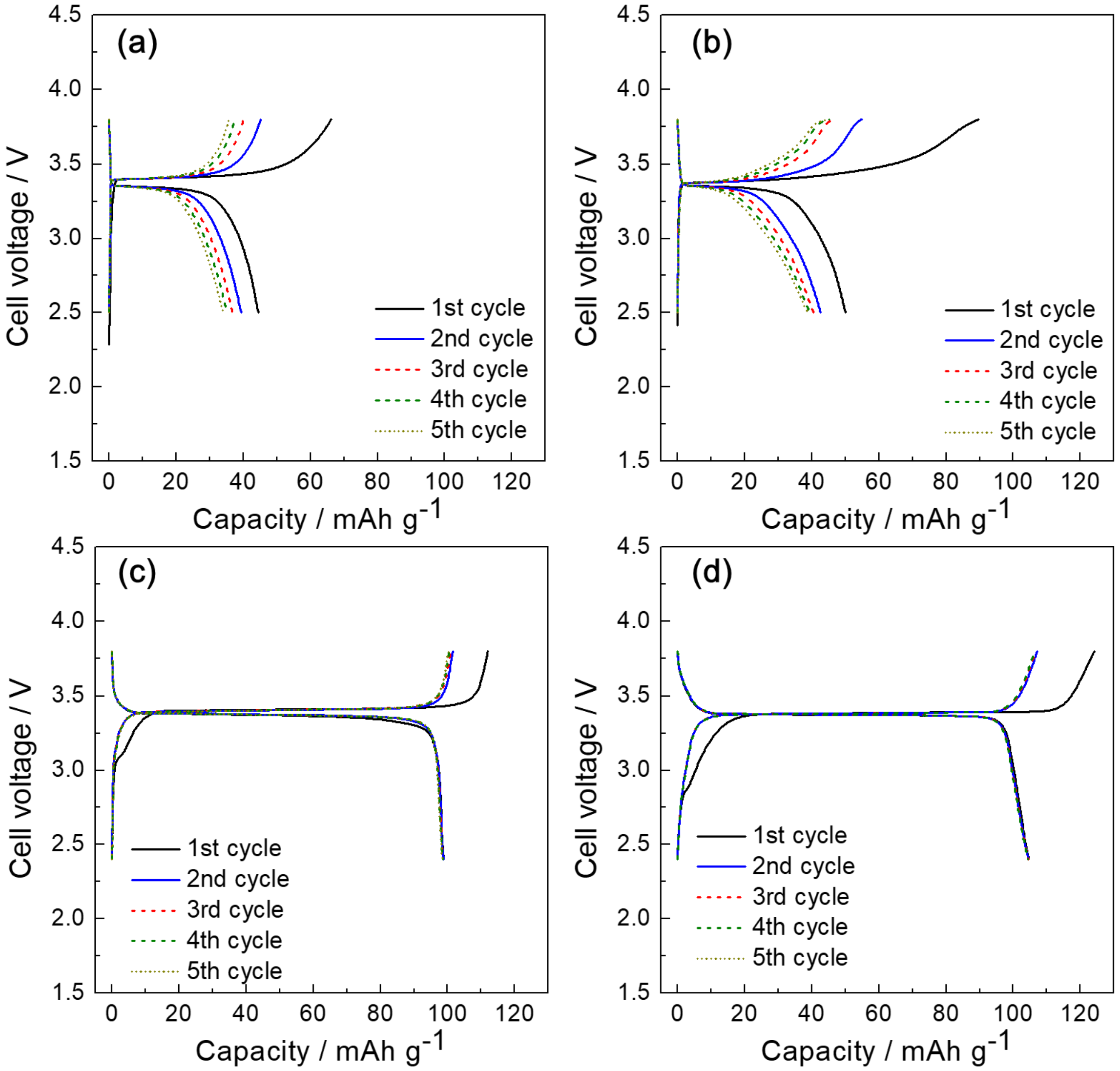

Figure 5-4 Charge-discharge curves from Na/NVP cells at (a) 298 K and (b) 363 K, as well as from Na/NVPC cells at (c) 298 K and (d) 363 K. Electrolyte: 50 mol% Na[FSA]-$[C_2C_1im][FSA]$. The charge-discharge rate and Cut-off voltages are 0.1C, and 2.4-3.8 V, respectively.

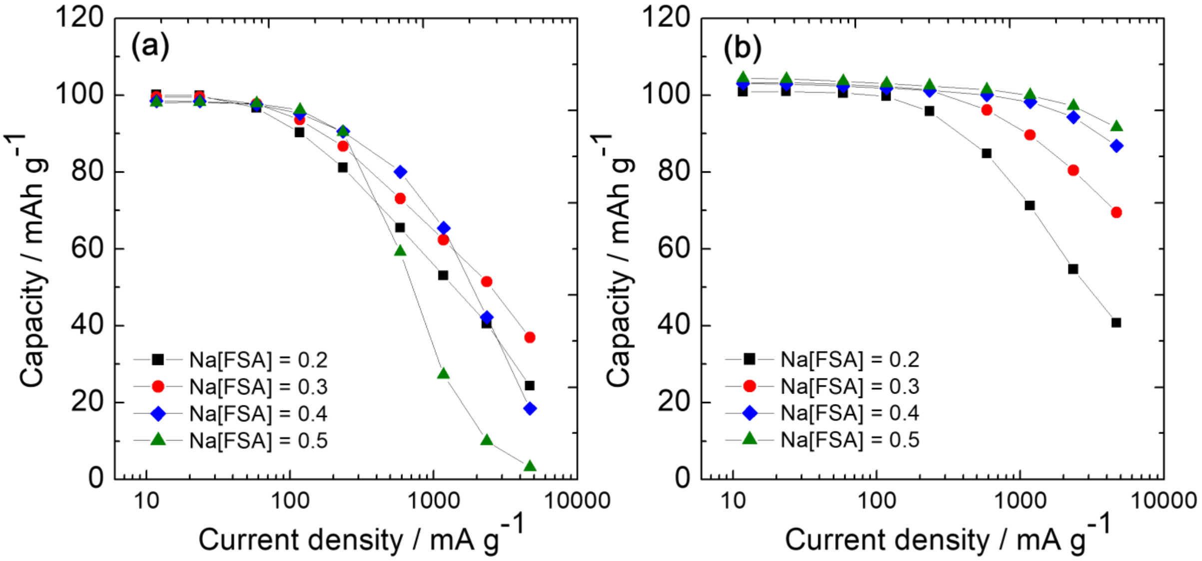

Figure 5-5 Rate capabilities of Na/NVPC cells at (a) 298 K and (b) 363 K. Electrolyte: Na[FSA]-[C_2C_1im][FSA] (Na[FSA] mol fraction = 20-50 mol%). Charge rate: 0.1C, discharge rates: 0.1C to 40C, Cut-off voltages: 2.4-3.8 V. See discharge curves in Figures 5-S6 and 5-S7 in the appendix.

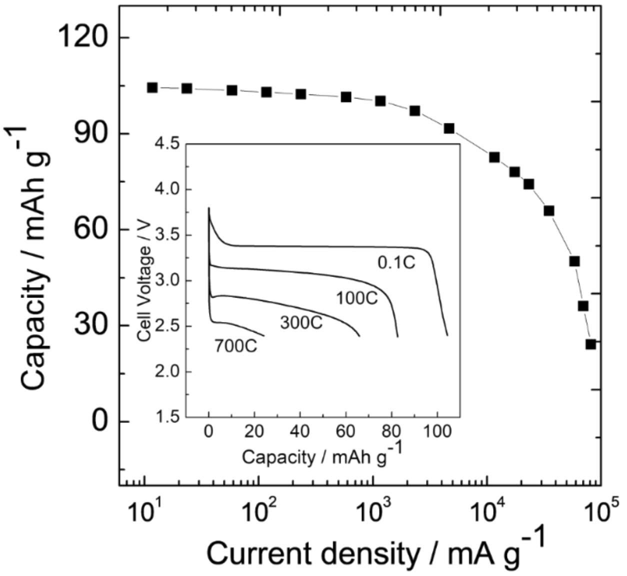

Figure 5-6 Super-fast Na/NVPC cell rate capability at 363 K. Electrolyte: 50 mol% Na[FSA]-[C_2C_1im][FSA]. Charge rate: 0.1C, discharge rates: 0.1C to 700C, Cut-off voltages: 2.4-3.8 V. See Table 5-S2 in the appendix for capacity and capacity retention details.

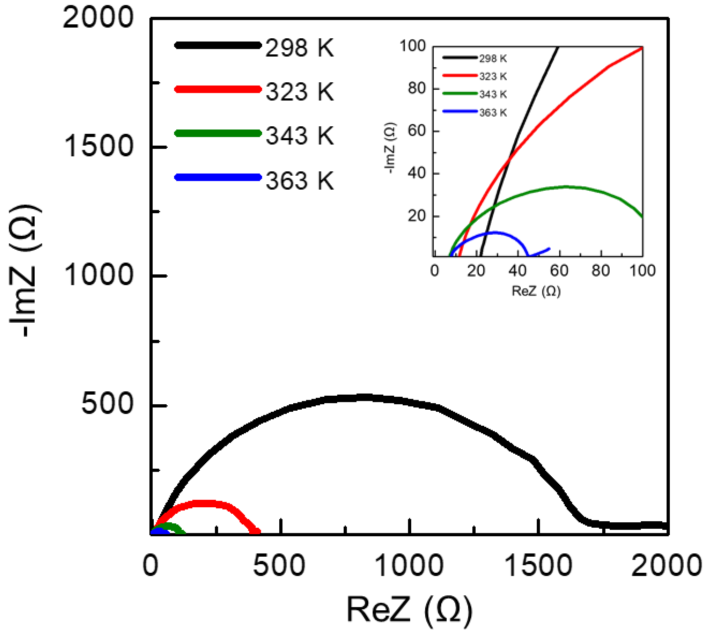

Figure 5-7 Na/NVPC cell electrochemical impedance spectra. Electrolyte: 50 mol% Na[FSA]-[C_2C_1im][FSA]. Temperature: 298−363 K, SOC = 50%, Frequency range: 40 mHz – 1000 kHz, AC amplitude: 10 mV.

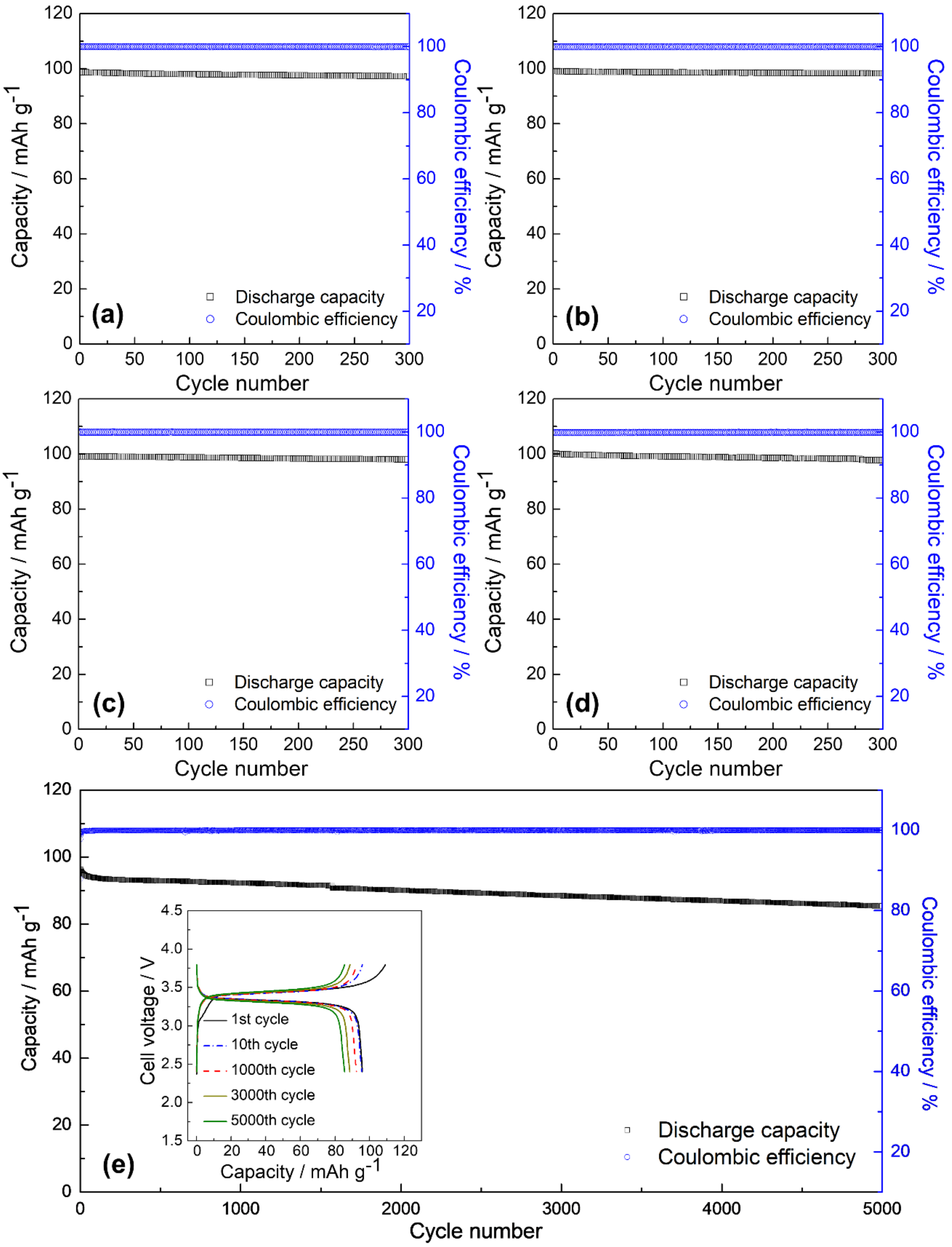

Figure 5-8 Cycling performance of the Na/NVPC cells at 363 K. Electrolyte: Na[FSA]-[C_2C_1im][FSA] with various Na[FSA] fractions. (a) Na[FSA] fraction = 20 mol%, (b) Na[FSA] fraction = 30 mol%, (c) Na[FSA] fraction = 40 mol%, and (d) Na[FSA] fraction = 50 mol%. Charge-discharge rate: 1 C for (a)–(d) and 20C for (e). Cut-off voltages: 2.4-3.8 V. See Tables S4 and S5 in the appendix for capacity and capacity retention details.

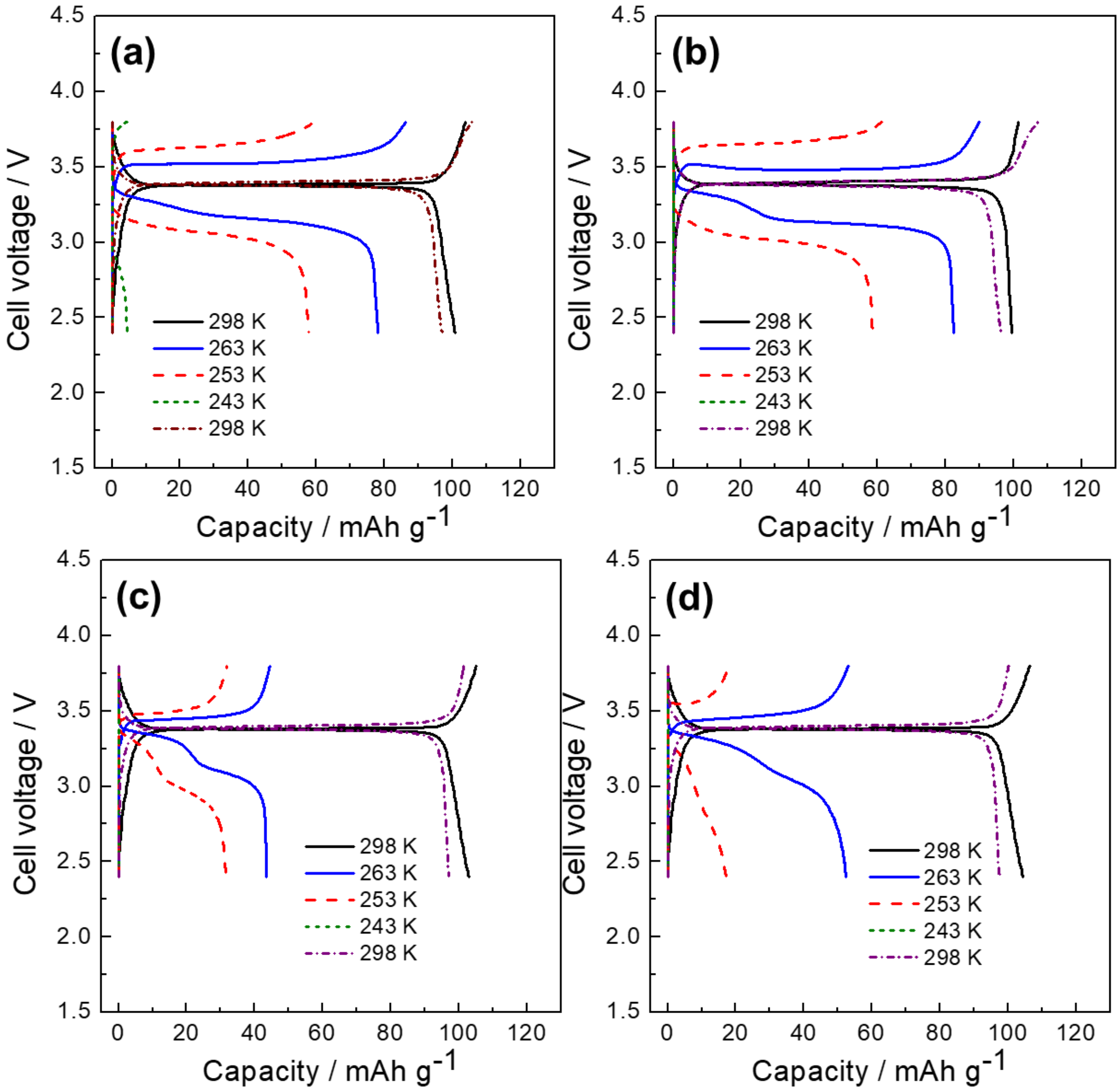

Figure 5-9 Na/NVPC cell charge-discharge tests conducted at a broad range of temperatures. Electrolytes: Na[FSA]-[C_2C_1im][FSA] with various Na[FSA] fractions. (a) Na[FSA] fraction = 20 mol%, (b) Na[FSA] fraction = 30 mol%, (c) Na[FSA] fraction = 40 mol%, and (d) Na[FSA] fraction = 50 mol%. Charge-discharge rate: 1C, temperature range: 243–298 K, Cut-off voltages: 2.4-3.8 V.

References

[1] V. Palomares, M. Casas-Cabanas, E. Castillo-Martinez, M. H. Han, and T. Rojo, Energy Environ. Sci., 6 (2013) 2312.

[2] Z. Jian, Y. S. Hu, X. Ji, and W. Chen, Adv. Mater., 29 (2017) 1601925.

[3] S. Y. Lim, H. Kim, R. A. Shakoor, Y. Jung, and J. W. Choi, J. Electrochem. Soc., 159 (2012) A1393.

[4] Q. Liu, X. Meng, Z. Wei, D. Wang, Y. Gao, Y. Wei, F. Du, and G. Chen, ACS Appl. Mater. Interfaces, 8 (2016) 31709.

[5] Q. Wang, B. Zhao, S. Zhang, X. Gao, and C. Deng, J. Mater. Chem. A, 3 (2015) 7732.

[6] L. S. Plashnitsa, E. Kobayashi, Y. Noguchi, S. Okada, and J. Yamaki, J. Electrochem. Soc., 157 (2010) A536.

[7] J. Zhang, Y. Fang, L. Xiao, J. Qian, Y. Cao, X. Ai, and H. Yang, ACS Appl. Mater. Interfaces, 9 (2017) 7177.

[8] W. Shen, H. Li, Z. Guo, C. Wang, Z. Li, Q. Xu, H. Liu, Y. Wang, and Y. Xia, ACS Appl. Mater. Interfaces, 8 (2016) 15341.

[9] H. Li, C. Wu, Y. Bai, F. Wu, and M. Wang, J. Power Sources, 326 (2016) 14.

[10] Z. L. Jian, W. Z. Han, X. Lu, H. X. Yang, Y. S. Hu, J. Zhou, Z. B. Zhou, J. Q. Li, W. Chen, D. F. Chen, and L. Q. Chen, Adv. Energy Mater., 3 (2013) 156.

[11] Y. Jiang, Z. Z. Yang, W. H. Li, L. C. Zeng, F. S. Pan, M. Wang, X. Wei, G. T. Hu, L. Gu, and Y. Yu, Adv. Energy Mat., 5 (2015) 1402104.

[12] X. Lin, M. Salari, L. M. Arava, P. M. Ajayan, and M. W. Grinstaff, Chem. Soc. Rev., 45 (2016) 5848.

[13] R. A. Guidotti, F. W. Reinhardt, and J. Odinek, J. Power Sources, 136 (2004) 257.

[14] G. G. Eshetu, S. Grugeon, S. Laruelle, S. Boyanov, A. Lecocq, J. P. Bertrand, and G. Marlair, Phys. Chem. Chem. Phys., 15 (2013) 9145.

[15] S. Wilken, P. Johansson, and P. Jacobsson, Solid State Ionics, 225 (2012) 608.

[16] J. M. Tarascon, and M. Armand, Nature, 414 (2001) 359.

[17] M. Armand, F. Endres, D. R. MacFarlane, H. Ohno, and B. Scrosati, Nat. Mater., 8 (2009) 621.

[18] L. Chancelier, A. O. Diallo, C. C. Santini, G. Marlair, T. Gutel, S. Mailley, and C. Len, Phys. Chem. Chem. Phys., 16 (2014) 1967.

[19] G. B. Appetecchi, M. Montanino, and S. Passerini, in Ionic Liquids: Science and Applications, p. 67, American Chemical Society (2012).

[20] D. R. MacFarlane, N. Tachikawa, M. Forsyth, J. M. Pringle, P. C. Howlett, G. D. Elliott, J. H. Davis, M. Watanabe, P. Simon, and C. A. Angell, Energy Environ. Sci., 7 (2014) 232.

[21] M. Watanabe, M. L. Thomas, S. Zhang, K. Ueno, T. Yasuda, and K. Dokko, Chem. Rev., 117 (2017) 71363.

[22] W. Xu, E. I. Cooper, and C. A. Angell, J. Phys. Chem. B, 107 (2003) 6170.

[23] A. Noda, K. Hayamizu, and M. Watanabe, J. Phys. Chem. B, 105 (2001) 4603.

[24] D. R. MacFarlane, M. Forsyth, E. I. Izgorodina, A. P. Abbott, G. Annat, and K. Fraser, Phys. Chem. Chem. Phys., 11 (2009) 4962.

[25] G. A. Giffin, J. Mat. Chem. A, 4 (2016) 13378.

[26] L. Otaegui, E. Goikolea, F. Aguesse, M. Armand, T. Rojo, and G. Singh, J. Power Sources, 297 (2015) 168.

[27] C. Ding, T. Nohira, R. Hagiwara, K. Matsumoto, Y. Okamoto, A. Fukunaga, S. Sakai, K. Nitta, and S. Inazawa, J. Power Sources, 269 (2014) 124.

[28] C.-Y. Chen, T. Kiko, T. Hosokawa, K. Matsumoto, T. Nohira, and R. Hagiwara, J. Power Sources, 332 (2016) 51.

[29] C. Ding, T. Nohira, K. Kuroda, R. Hagiwara, A. Fukunaga, S. Sakai, K. Nitta, and S. Inazawa, J. Power Sources, 238 (2013) 296.

[30] T. Yamamoto, T. Nohira, R. Hagiwara, A. Fukunaga, S. Sakai, and K. Nitta, Electrochim. Acta, 211 (2016) 234.

[31] A. Fukunaga, T. Nohira, R. Hagiwara, K. Numata, E. Itani, S. Sakai, K. Nitta, and S. Inazawa, J. Power Sources, 246 (2014) 387.

[32] T. Yamamoto, T. Nohira, R. Hagiwara, A. Fukunaga, S. Sakai, K. Nitta, and S. Inazawa, Electrochim. Acta, 135 (2014) 60.

[33] M. Ishikawa, T. Sugimoto, M. Kikuta, E. Ishiko, and M. Kono, J. Power Sources, 162 (2006) 658.

[34] H. Matsumoto, H. Sakaebe, K. Tatsumi, M. Kikuta, E. Ishiko, and M. Kono, J. Power Sources, 160 (2006) 1308.

[35] M. Forsyth, H. Yoon, F. Chen, H. Zhu, D. R. MacFarlane, M. Armand, and P. C. Howlett, J. Phys. Chem. C, 120 (2016) 4276.

[36] T. Hosokawa, K. Matsumoto, T. Nohira, R. Hagiwara, A. Fukunaga, S. Sakai, and K. Nitta, J. Phys. Chem. C, 120 (2016) 9628.

[37] I. A. Shkrob, T. W. Marin, Y. Zhu, and D. P. Abraham, J J. Phys. Chem. C, 118 (2014) 19661.

[38] K. Matsumoto, Y. Okamoto, T. Nohira, and R. Hagiwara, J. Phys. Chem. C, 119 (2015) 7648.

[39] C.-Y. Chen, K. Matsumoto, T. Nohira, and R. Hagiwara, J. Electrochem. Soc., 162 (2015) A2093.

[40] C.-Y. Chen, K. Matsumoto, T. Nohira, C. Ding, T. Yamamoto, and R. Hagiwara, Electrochim. Acta, 133 (2014) 583.

[41] T. Yamamoto, T. Nohira, R. Hagiwara, A. Fukunaga, S. Sakai, K. Nitta, and S. Inazawa, Electrochim. Acta, 135 (2014) 60.

[42] K. Matsumoto, T. Hosokawa, T. Nohira, R. Hagiwara, A. Fukunaga, K. Numata, E. Itani, S. Sakai, K. Nitta, and S. Inazawa, J. Power Sources, 265 (2014) 36.

[43] J. Rodríguez-Carvajal, Comm. Powder Diffr. (IUCr) Newsl., 26 (2001) 12.

[44] S. Brunauer, P. H. Emmett, and E. Teller, J. Am. Chem. Soc., 60 (1938) 309.

[45] C.-Y. Chen, K. Matsumoto, T. Nohira, R. Hagiwara, A. Fukunaga, S. Sakai, K. Nitta, and S. Inazawa, J. Power Sources, 237 (2013) 52.

[46] K. Saravanan, C. W. Mason, A. Rudola, K. H. Wong, and P. Balaya, Advanced Energy Materials, 3 (2013) 444.

[47] C. Verma, E. E. Ebenso, and M. A. Quraishi, J. Mol. Liq., 233 (2017) 403.

[48] E. Cho, J. Mun, O. B. Chae, O. M. Kwon, H. T. Kim, J. H. Ryu, Y. G. Kim, and S. M. Oh, Electrochem. Commun., 22 (2012) 1.

[49] Z. Jian, C. Yuan, W. Han, X. Lu, L. Gu, X. Xi, Y.-S. Hu, H. Li, W. Chen, D. Chen, Y. Ikuhara, and L. Chen, Adv. Funct. Mater., 24 (2014) 4265.

[50] S. Komaba, C. Takei, T. Nakayama, A. Ogata, and N. Yabuuchi, Electrochem. Commun., 12 (2010) 355.

[51] J. J. Braconnier, C. Delmas, and P. Hagenmuller, Mater. Res. Bull., 17 (1982) 993.

[52] C.-Y. Chen, K. Matsumoto, T. Nohira, R. Hagiwara, A. Fukunaga, S. Sakai, K. Nitta, and S. Inazawa, J. Power Sources, 237 (2013) 52.

[53] P. Barpanda, G. Liu, C. D. Ling, M. Tamaru, M. Avdeev, S.-C. Chung, Y. Yamada, and A. Yamada, Chem. Mater., 25 (2013) 3480.

Appendix

Table 5-S1 Crystallographic data of the prepared NVPC by Rietveld refinement.

Refinement results for $Na_3V_2(PO_4)_3$ (S.G. $R\overline{3}c$)

$R_p = 16.1$, $R_{wp} = 16.0$, $R_e = 4.21$

a/Å	c/Å
8.72209(12)	21.8563(5)

Atom	Wyckoff symbol	x	y	z	B_{iso}/Å^2	Occup.
Na1	6b	0	0	0	0.5	0.8500
Na2	18e	0.6354(5)	0	0.2500	0.5	0.7150
V	12c	0	0	0.14703(6)	0.5	1.0000
P	18e	0.287363(20)	0	0.2500	0.5	1.0000
O1	36f	0.1789(3)	0.9656(4)	0.19294(12)	0.5	1.0000
O2	36f	0.1924(3)	0.1684(3)	0.08948(15)	0.5	1.0000

Table 5-S2 Discharge capacity and capacity retention of the Na/NVPC cell at 363 K in 50 mol% Na[FSA]-[C_2C_1im][FSA]. Charge rate: 0.1C, discharge rates: 0.1C to 700C, Cut-off voltage: 2.4-3.8 V.

Current/ 1C = 117 mA g^{-1}	Capacity/ mAh g^{-1}	Capacity Retention 0.1C VS. /%
0.1C	104.4	100.0
5C	101.5	97.2
10C	100.2	96.0
40C	91.6	87.7
100C	82.7	79.2
200C	74.2	71.1
300C	65.9	63.1
500C	50.1	47.9
600C	36.1	34.6
700C	24.1	23.1

[a]Capacity retention is based on the capacity at the 1st cycle.

Table 5-S3 Discharge capacity after adjusting Cut-off voltages and energy density of the Na/NVPC cell at 363 K in 50 mol% Na[FSA]-[C_2C_1im][FSA] Charge rate: 1C, discharge rates: 1C to 200C.

C-rate	Capacity /mAh g^{-1}	Capacity Retention 0.1C VS. /%	Energy Density /Wh (kg-NVPC) $^{-1}$	Cut-off voltage /V
300	74.2	71.1	200.18	2.0-3.8
500	68.9	66.0	166.27	1.5-3.8
700	66.6	63.8	133.14	1.0-3.8
800	62.1	59.5	116.13	1.0-3.8
1000	58.2	55.7	92.83	0.8-3.8
1200	48.8	46.7	67.75	0.8-3.8
1400	38.2	36.6	47.43	0.8-3.8
1600	36.4	34.9	34.62	0.5-3.8
1800	26.9	25.8	21.96	0.5-3.8
2000	18.9	18.1	13.03	0.5-3.8

[a] Capacity retention is based on the discharge capacity of 0.1C (Table 5-S2).

Table 5-S4 Summary of cycleability for NVPC (see, Figures 5-8 and 5-S10).

Na[FSA] fraction /%	Temperature /K	Capacity retention at the 300th cycle /%	Coulombic Efficiency at the 300th cycle /%
20	298	99.6	99.8
30	298	99.8	99.8
40	298	99.8	99.8
50	298	97.1	99.8
20	363	98.7	99.9
30	363	96.3	99.9
40	363	99.0	99.9
50	363	94.8	99.9

[a] Capacity retention is calculated by dividing the capacity at the 300th cycle by that at the 1st cycle.

Table 5-S5 Long-term cycleability of NVPC (see, Figure 5-8e).

	Capacity /mAh g^{-1}	Capacity retention[a] /%
1st	95.8	
10th	95.4	99.6
1000th	92.2	96.2
2000th	363.1	94.0
3000th	88.5	92.3
4000th	86.9	363.7
5000th	85.5	89.2

[a] Capacity retention is based on the capacity at the 1st cycle.

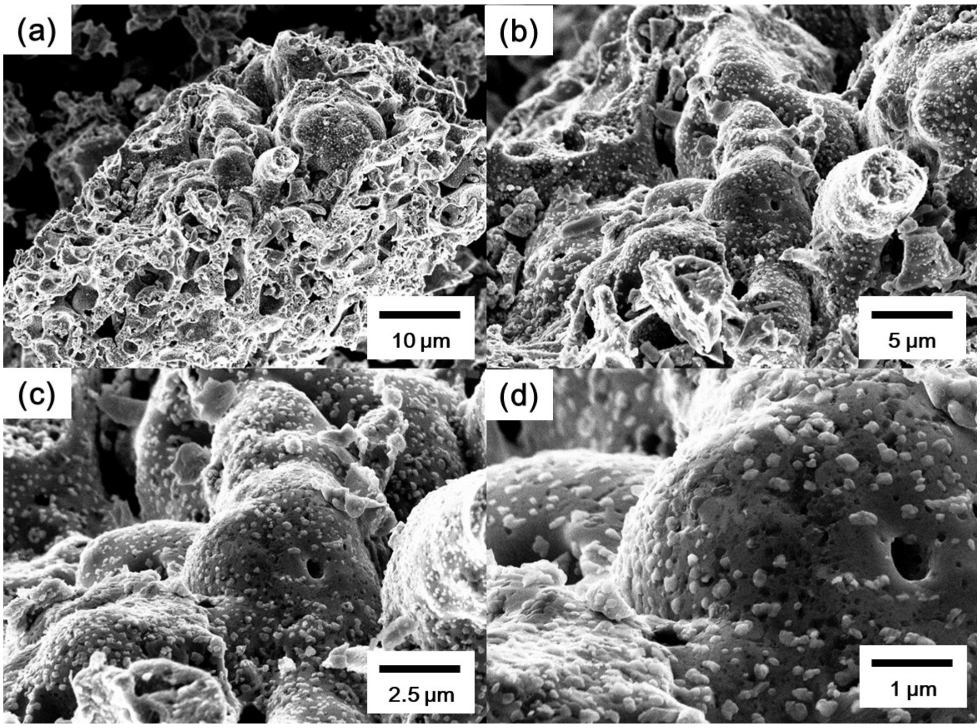

Figure 5-S1 Field-emission SEM images of NVPC prepared by a sol-gel method at different magnifications.

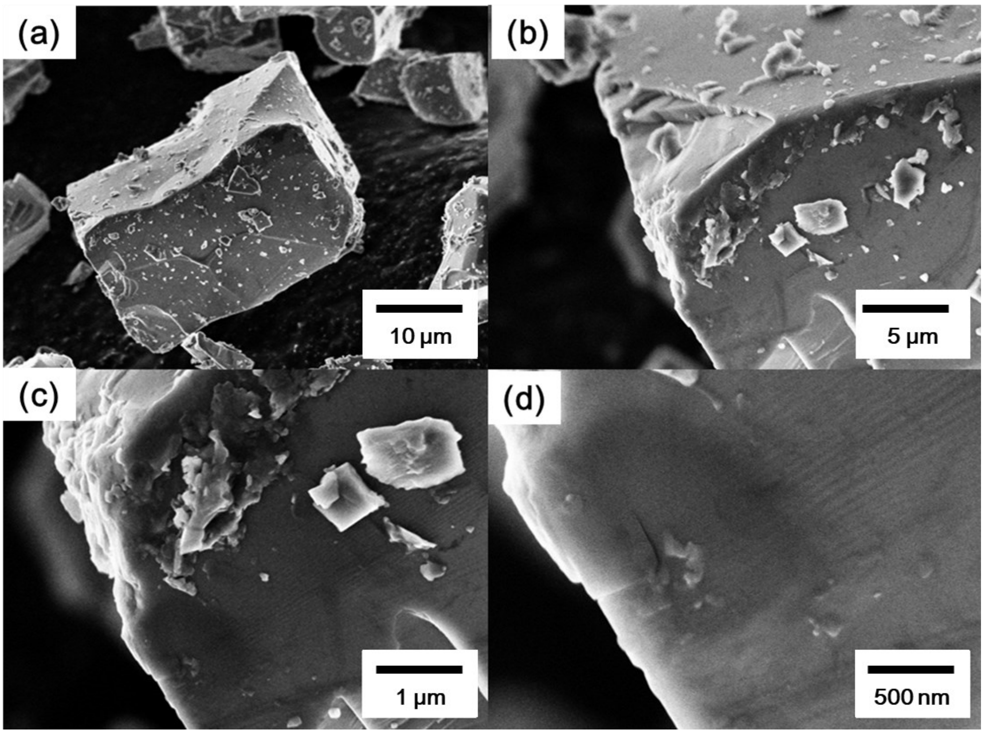

Figure 5-S2 Field-emission SEM images of NVP-SS prepared by a solid-state method at different magnifications.

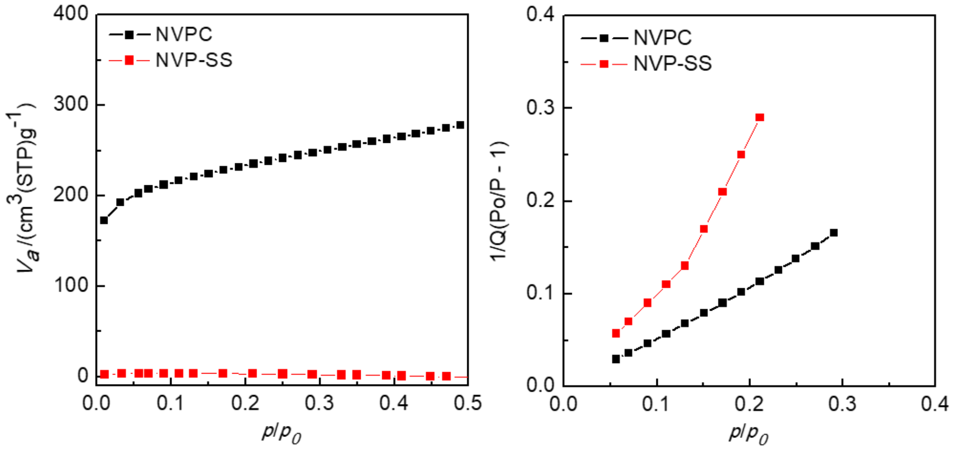

Surface Area /m^2 g^{-1}	
NVP-SS	0.0741
NVPC	7.6503

Figure 5-S3 N_2 adsorption isotherm of at 77 K, and BET surface area plots for NVPC and NVP-SS.

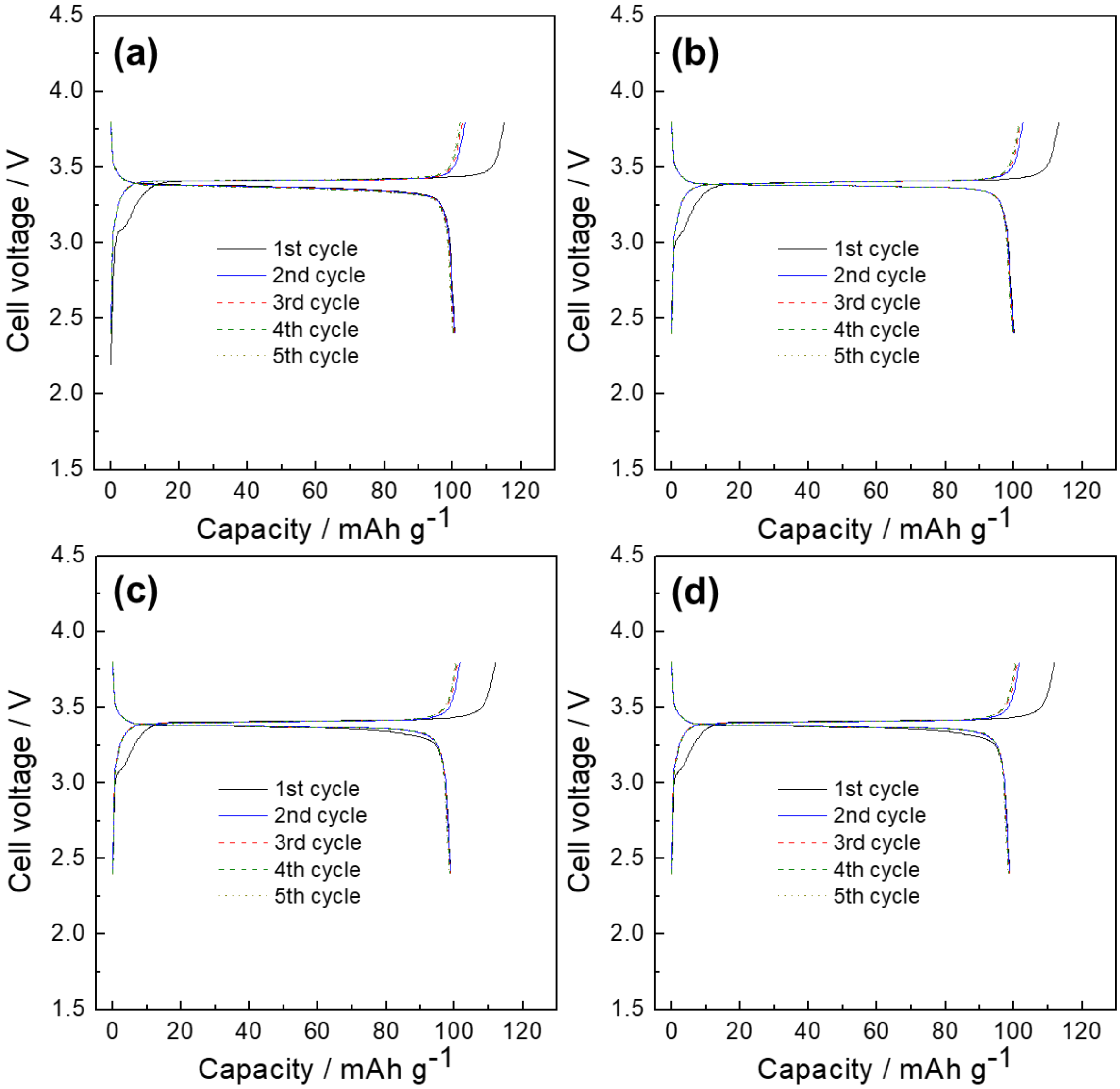

Figure 5-S4 Charge-discharge curves of the Na/NVPC cells at 298 K. Electrolyte: Na[FSA]-[C_2C_1im][FSA] (Na[FSA] faction = 20-50 mol%). (a) Na[FSA] faction = 20 mol%, (b) Na[FSA] faction = 30 mol%, (c) Na[FSA] faction = 40 mol%, and (d) Na[FSA] faction = 50 mol%. Charge-discharge rate: 0.1C, Cut-off voltage: 2.4-3.8 V.

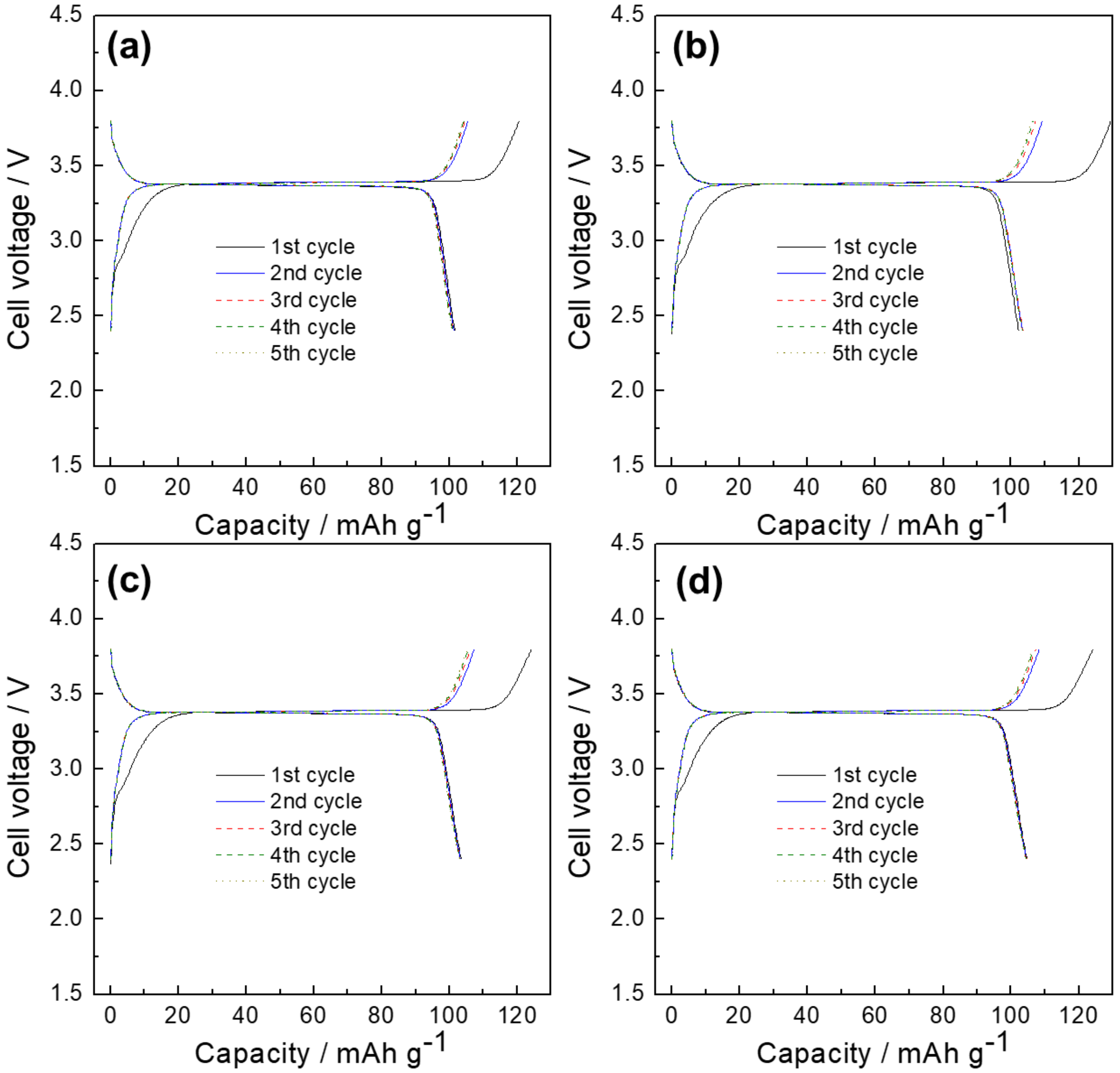

Figure 5-S5 Charge-discharge curves of the Na/NVPC cells at 363 K Electrolyte: Na[FSA]-[C$_2$C$_1$im][FSA] (Na[FSA] faction = 20-50 mol%). (a) Na[FSA] faction = 20 mol%, (b) Na[FSA] faction = 30 mol%, (c) Na[FSA] faction = 40 mol%, and (d) Na[FSA] faction = 50 mol%. Charge-discharge rate: 0.1C, Cut-off voltage: 2.4-3.8 V.

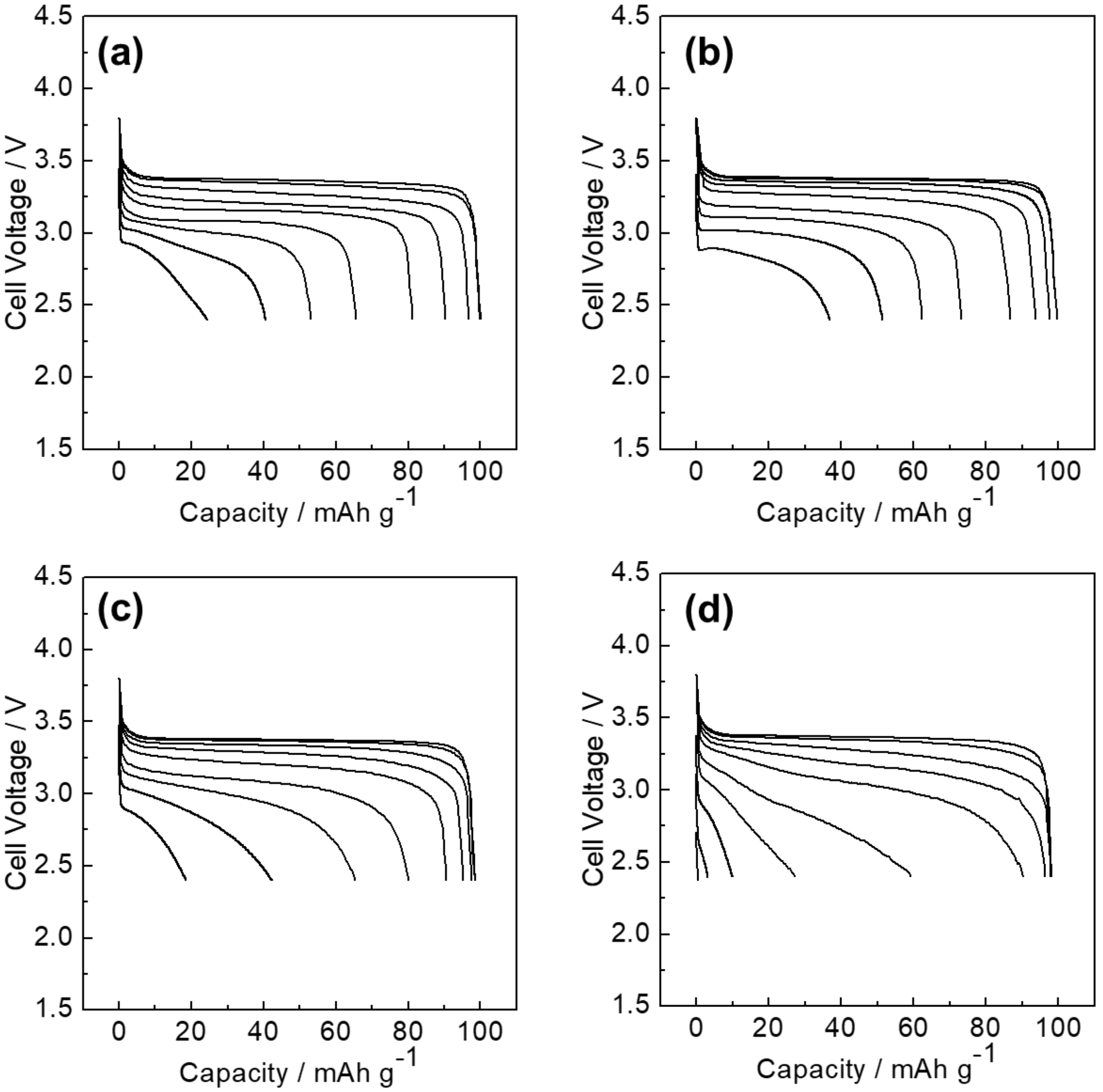

Figure 5-S6 Discharge curves of rate capability tests for the Na/NVPC cells at 298 K. Electrolyte: Na[FSA]-[C_2C_1im][FSA] (Na[FSA] faction = 20-50 mol%). (a) Na[FSA] faction = 20 mol%, (b) Na[FSA] faction = 30 mol%, (c) Na[FSA] faction = 40 mol%, and (d) Na[FSA] faction = 50 mol%. Charge rate: 0.1C, discharge rates: 0.1C to 40C, Cut-off voltage: 2.4-3.8 V.

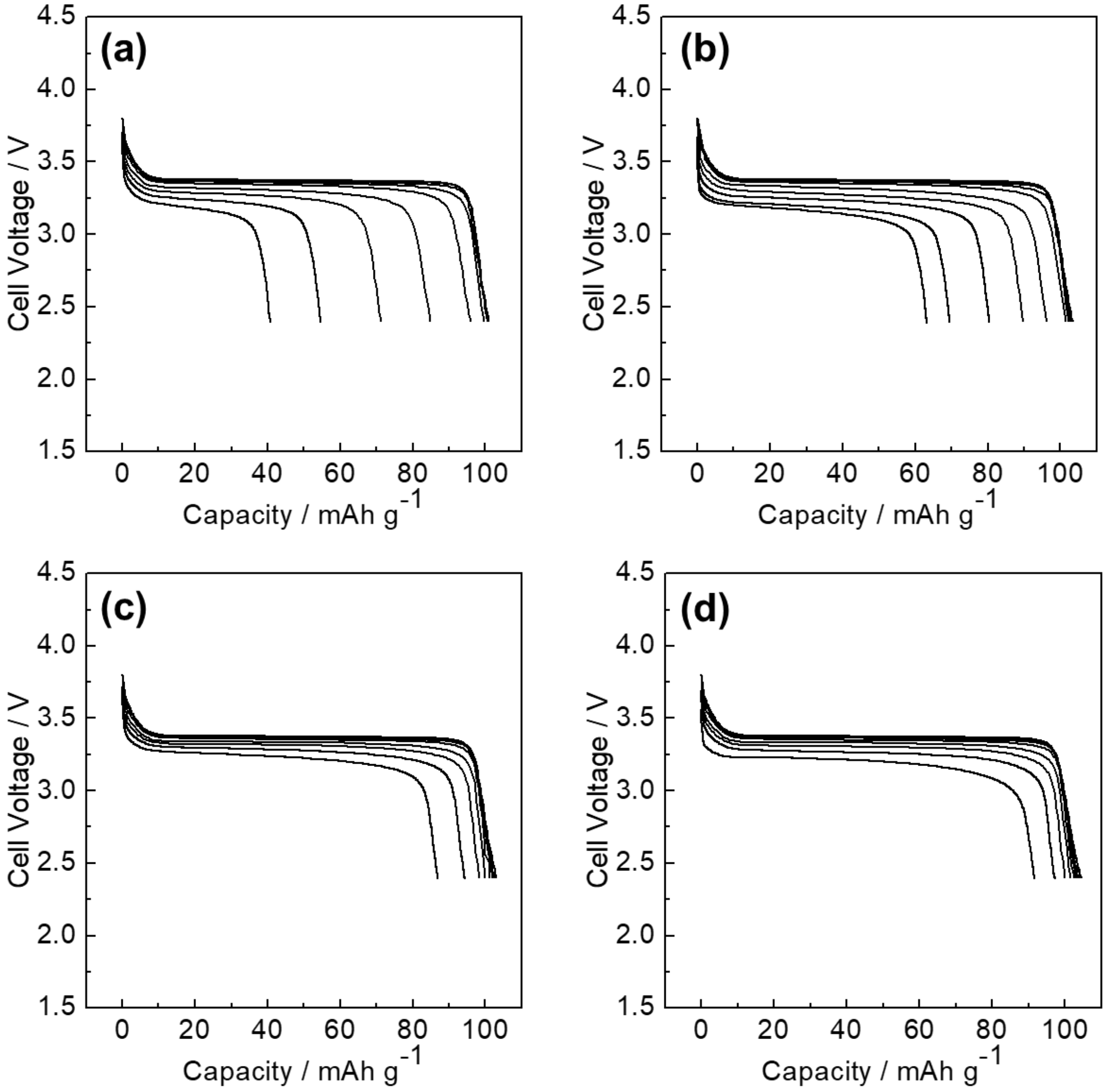

Figure 5-S7 Discharge curves of rate capability tests of the Na/NVPC cells at 363 K. Electrolyte: Na[FSA]-[C_2C_1im][FSA] (Na[FSA] faction = 20-50 mol%). (a) Na[FSA] faction = 20 mol%, (b) Na[FSA] faction = 30 mol%, (c) Na[FSA] faction = 40 mol%, and (d) Na[FSA] faction = 50 mol%. Charge rate: 0.1C, discharge rates: from 0.1C to 40C, Cut-off voltage: 2.4-3.8 V.

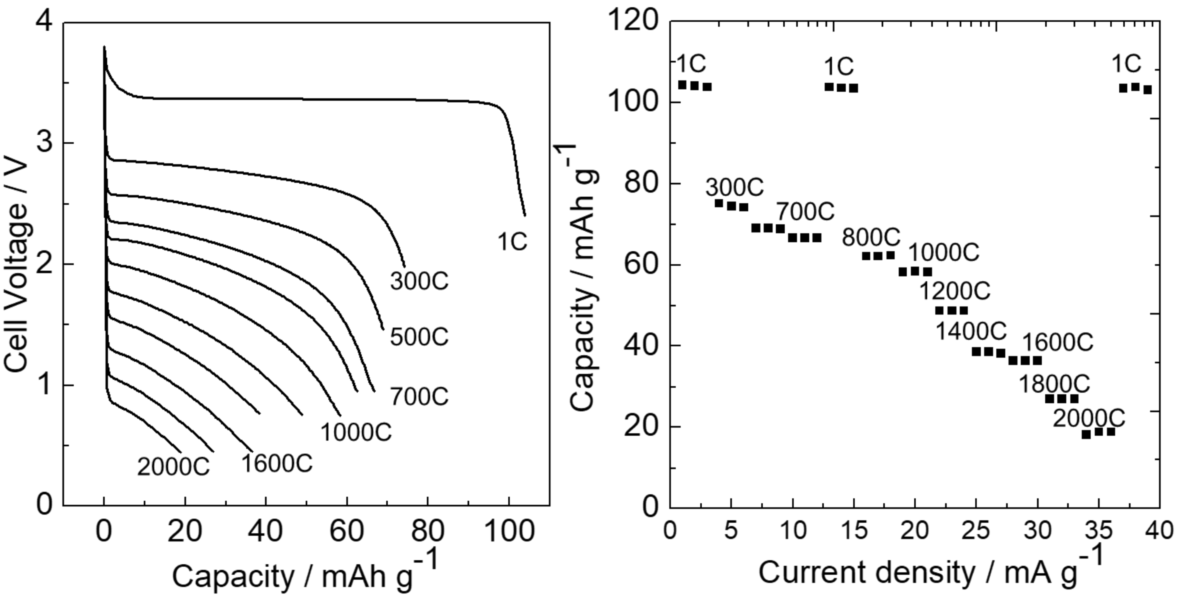

Figure 5-S8 Super-fast Na/NVPC cell rate capability at 363 K with various Cut-off voltages. Electrolyte: 50 mol% Na[FSA]-[C2C1im][FSA]. Charge rate: 1C, discharge rates: 1C to 2000C, Cut-off voltages: 0.8~2.4-3.8 V. See Table 5-S3 in the appendix for capacity and capacity retention details.

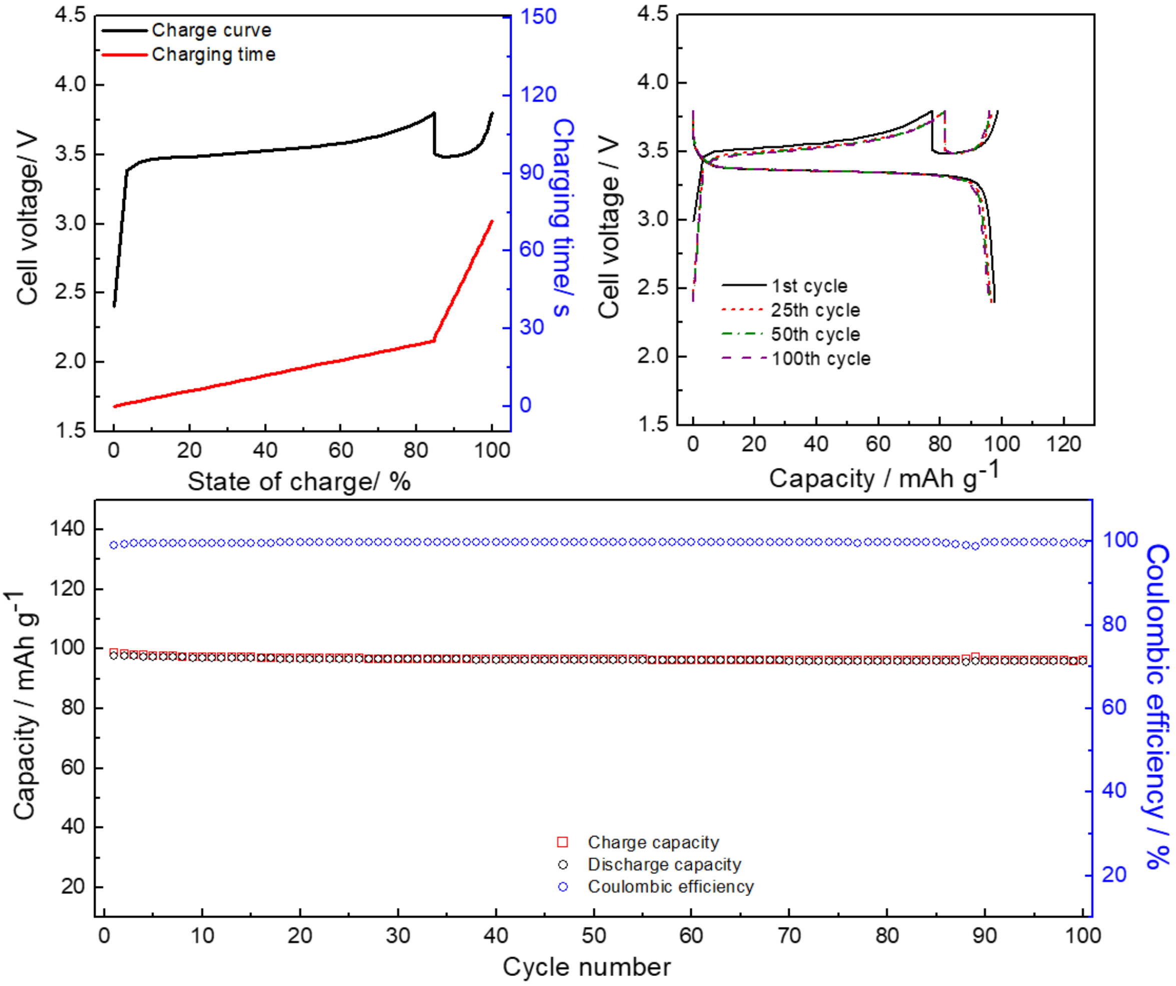

Figure 5-S9 Fast charge-discharge tests of the Na/NVPC cells at 363 K. Electrolyte: 40 mol% Na[FSA]-[C_2C_1im][FSA]. Consecutive charge rates for one charge step:100C and 10C, discharge rate: 10C, Cut-off voltage: 2.4-3.8 V.

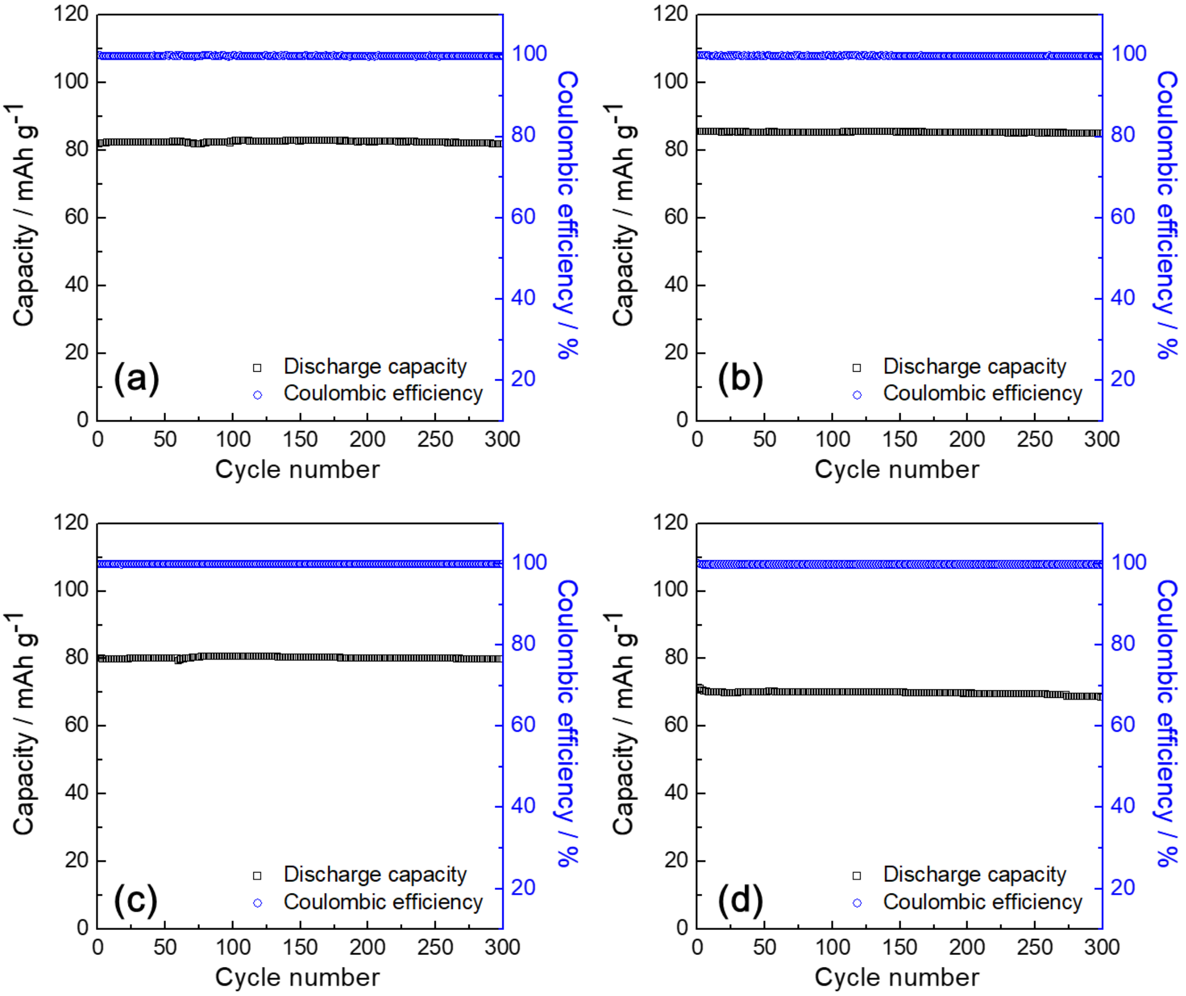

Figure 5-S10 Cycle performance of Na/NVPC cells at 298 K. Electrolyte: Na[FSA]-$[C_2C_1im]$[FSA] (Na[FSA] faction = 20-50 mol%). (a) Na[FSA] faction = 20 mol%, (b) Na[FSA] faction = 30 mol%, (c) Na[FSA] faction = 40 mol%, and (d) Na[FSA] faction = 50 mol%. Charge-discharge rate: 0.1C, Cut-off voltage: 2.4-3.8 V.

Chapter 6

High Mass Loading Test on $Na_3V_2(PO_4)_3$/C@Carbon Nanofibers Positive Electrode

6.1 Introduction

NVP acts as both positive and negative electrode materials. The former function is derived from the V^{3+}/V^{4+} redox reaction with a theoretical capacity of 117.6 mAh g^{-1} based on the two-electron reaction of $Na_3V_2(PO_4)_3 \rightleftarrows NaV_2(PO_4)_3 + 2Na^+ + 2e^-$, whereas the latter is from the V^{3+}/V^{2+} redox reaction with a theoretical capacity of 55 mAh g^{-1} based on the one-electron reaction of $Na_4V_2(PO_4)_3 \rightleftarrows Na_3V_2(PO_4)_3 + Na^+ + e^-$ [1-4]. Although previous studies have reported that NVP suffers from a low cycleability and rate capability due to its low electronic conductivity,[4-9] new strategies such as carbon coating, introducing conductive materials, and morphology control have overcome these obstacles [3, 5-16]. The previous study on a carbon-coated coral-reef morphology NVP composite (NVPC) using an ionic liquid (IL) electrolyte exhibited a superior rate capability with a capacity retention of 42.2 mAh g^{-1} at 298 K and 94.3 mAh g^{-1} at 363 K both at 20C. Moreover, only a 10.8% capacity degradation was observed after 5000 cycles [6].

Organic solvent electrolytes exhibit reliable performances in secondary batteries but have safety issues regarding volatility and flammability [17-20]. Thus, as the battery size increases, so does the risk of significant safety problems [21]. On the other hand, ionic liquid electrolytes are nonflammable, chemically, electrochemically, and thermally stable [22-28]. This is especially important when considering the room for intermediate-temperature operating of Na secondary batteries [15, 29, 30]. Although there is a concern that the high viscosity of ionic liquid electrolytes will degrade the performance compared to organic electrolytes at room temperature [17, 31, 32], this is not always true. Recent reports have revealed that ionic liquid electrolytes outperform organic electrolytes in cycleability and rate capability [15, 32, 33]. The former has been attributed to the formation of stable solid-electrolyte interphase (SEI) and electrochemical stability.

In this study, a new preparation method of NVPC@CNF is proposed (CNF = carbon nanofiber). CNFs are great materials for electronic conductive additives to enhance electron transfer and to improve the contact efficiency between particles as well as between particles and the electrolyte [34-36]. Composites are prepared via a combination of sonication and the sol-gel method. The electrochemical properties are examined using two different types of electrolytes (organic solvent electrolyte and ionic liquid electrolyte). Specifically, the electrochemical performances of high mass loading electrodes (~8.5 mg-active material cm^{-2}) are compared between 1 mol dm^{-3} $Na[PF_6]$-PC for an organic solvent electrolyte [42] and 40 mol% Na[FSA]-$[C_2C_1im]$[FSA] IL electrolyte [37] to investigate the importance of the electrode material preparation and the performance enhancement utilizing an ionic liquid electrolyte at room to intermediate temperatures.

6.2 Experimental

Volatile materials were handled in a vacuum line constructed using stainless steel, borosilicate glass, and PFA (tetrafluoroethylene-perfluoroalkylvinylether copolymer). Nonvolatile materials were handled under a dry argon atmosphere in a glove box. V_2O_5 (Sigma-Aldrich Chemistry, purity 99.6%), oxalic acid dihydrate (Wako Pure Chemical Industries, purity 99.5–

100.2%), NaOH (Wako Pure Chemical Industries, purity 97.0%), $NH_4H_2PO_4$ (Wako Pure Chemical Industries, purity 99.0%), and glucose (Wako Pure Chemical Industries) were used as received

Powdery NVPC@CNFs samples were prepared via sonication and the sol-gel method (Figure 6-1). The NVP precursor was prepared by dissolving 1.8188 g of V_2O_5 (10.000 mmol)) and 6.3035 g of oxalic acid dihydrate (5.0002 mmol) into 20 mL of ion-exchanged water at 353 K by continuously stirring using a magnetic bar. Oxalic acid works as a reducing agent for vanadium reduction. As the mixture turned into a blue homogeneous solution, 1.1991 g of NaOH (29.980 mmol), 3.4507 g of $NH_4H_2PO_4$ (29.998 mmol), and 1.7115 g of glucose (9.500 mmol) were added to the solution and stirred for an additional 3 h. Glucose was used as the carbon source and glue for the CNF frameworks and NVP particles. CNFs (0.5 g, mean diameter of 150 nm) were immersed in ion-exchanged water in a beaker at 353 K and sonicated for 30 min. Then the NVP precursor solution was added to the ion-exchanged water containing the dispersed CNFs. The mixture was vigorously stirred using a stirring magnet bar coated with PTFE at 353 K and sonicated for 30 min. The water was completely evaporated at 393 K in a day. The resulting residue was calcined at 623 K for 5 h under an Ar flow and successively baked at 1073 K under an Ar flow for 8 h. The NVPC with (carbon content 10 wt%) samples used for comparison were prepared as previously reported [15].

XRD patterns were collected in the Bragg-Brentano geometry using a Rigaku SmartLab diffractometer with Ni-filtered Cu-$K\alpha$ radiation (40 kV and 30 mA) and a silicon strip high-speed detector (Rigaku D/teX Ultra 250). Rietveld refinement was performed by the FullProf software [38]. The crystal structures were visualized using crystallographic data from the Rietveld refinement and the VESTA program [39]. The morphologies of the NVPC@CNFs were observed by scanning electron microscopy (SEM) (Hitachi SU-8020) and energy dispersive X-ray analysis (EDS) (Horiba EMAXEvolution X-max). The surface area of the electrode materials was determined by the BET method [40] based on the results of nitrogen adsorption analysis by a Tristar II 3020 (Micromeritics). Raman spectra were recorded on a Nanofinder 30 (Tokyo Instruments, Inc.) instrument using the 632.8 nm excitation line of a He–Ne laser. The Raman shift was calibrated by a single-crystal Si. The samples for Raman spectroscopy were loaded in a glass cell in the air.

Na metal (Sigma-Aldrich Chemistry, 99.95% purity) was cut into a disk (16-mm diameter) and fixed on an Al plate current collector as the negative electrode. The positive electrode was prepared by mixing the NVPC@CNFs composite, acetylene black, and PVDF (95:5:5 wt%) in *N*-methylpyrrolidone and pasting the mixture onto Al foil (the mass loading of the active material in the electrodes was approximately 8.5 mg-active material cm^{-2} after drying). For the symmetric full cell test, mass loadings of 2.0 mg cm^{-2} and 4.0 mg cm^{-2} for NVPC@CNFs were used for the positive and negative electrodes, respectively. An NVPC electrode was prepared by the NVPC composite, acetylene black, and PVDF (80:15:5 wt%). Coin cells (type-2032) were assembled in an argon-filled glove box. The specific contribution of NVP in NVPC@CNFs electrode is 74.7wt%, and NVPC electrode is 71.4wt%.

40 mol% Na[FSA]-[C_2C_1im][FSA] IL and 1 mol dm^{-3} Na[FSA]-PC (Kishida Chemical) of organic electrolyte were used as the electrolytes. The salts, Na[FSA] (Mitsubishi Materials Electronic Chemicals, purity >99%), and [C_2C_1im][FSA] (Kanto Chemical, purity >99.9%), were dried under vacuum for 24 h at 353 K. The ionic liquid electrolyte was prepared by mixing these two salts at a Na[FSA] fraction of 40 mol%. The typical water content of this IL system was below 30 ppm, according to Karl-Fischer titrations (899 Coulometer, Metrohm). A glass

microfiber separator was impregnated with an ionic liquid at 333 K under vacuum for 1 d prior to the cell assembly. In the case of an organic electrolyte, a separator was impregnated with an electrolyte just before assembling coin cells in the glove box.

The electrochemical properties were measured at 298, and 363 K. A current density of 0.1C (1C = 117 mA g^{-1}) was applied for the charge-discharge test to examine the basic electrochemical behavior. Then various discharge current rates of 0.1 to 200C were used in the rate capability tests. For all of the half-cell electrochemical measurements, the cutoff voltages were fixed at 2.4-3.8 V as the lower and upper limits, respectively. The charge-discharge properties, rate capabilities, and cycling performances were evaluated using an HJ1001SD8 charge-discharge test device (Hokuto Denko). All the electrochemical measurements were performed at least 2 h after the relevant temperature adjustments.

Cells (2032 coin-type) were prepared for the electrochemical impedance spectra (EIS) measurements. The cells were assembled under a dry Ar atmosphere. Details about the measurement method and cell preparation are in previous reports [41, 42]. Measurements were performed using a VSP potentiostat (Bio-Logic) at 298 and 363 K over a frequency range from 1 MHz to 40 mHz with a perturbation amplitude of 10 mV.

6.3 Results and Discussion

Figure 6-1 schematically illustrates the preparation of NVPC@CNFs via a combination of sonication and the sol-gel method. The CNFs are well-dispersed by sonication in ion-exchanged water at 353 K, and mixing of the dispersed CNFs with the precursor of NVPC provides CNFs embedded in the pure NVP phase.

Figure 6-2 shows the XRD patterns of the prepared NVPC@CNFs composites. All of the peaks except for the one at 26.4° are indexed as the rhombohedral crystal system and can be fitted with a pure NVP phase under the $R\overline{3}c$ space group via the Rietveld refinement (Table 6-1). The peak at 26.4° is assigned to CNFs (Figure 6-S1 in the appendix). The lattice parameters of NVP are a = 8.7294(1) and c = 21.8590(4) Å (R_{wp} = 13.2%), which agree with the crystallographic data in previous works [8, 12, 15, 43, 44]. These crystallographic data confirm that NVP is a pure phase without impurities, and CNFs do not influence the NVP crystal structure. The refined crystal structural model in Figure 6-2b contains corner-sharing with octahedral VO_6 and tetrahedral PO_4, forming an open framework of the $V_2(PO_4)_3$ units along the *c*-axis for Na ion diffusion. The constituent Na ions selectively occupy two distinct sites labeled as Na1 (occupancy of 0.781) and Na2 (occupancy of 0.727). However, a heating temperature of 1073 K is necessary to obtain the pure NVP phase; NVPC@CNFs heated at 873 K is mainly composed of amorphous NVPC@CNFs precursor according to the XRD result (Figure S1), though a small amount of the NVP phase is confirmed.

Figure 6-3 shows the morphology of NVPC@CNFs observed by SEM with the EDS mapping results. The SEM image of NVPC@CNFs shows that CNFs and additional carbon by thermal decomposition of glucose form an electronically conductive path at the surface and inside the NVP particles. The high magnification SEM images confirm a uniform CNF distribution onto the NVPC@CNFs composite (Figure 6-S2). The EDS (Na, V, P, and O) results suggest that all the elements are evenly distributed onto the NVPC@CNFs composite. These results agree reasonably well with the theoretical composition. (See Figure 6-3 caption for the observed and theoretical compositions.) In the case of carbon, the EDS image detects strong peaks corresponding to the carbon tape. Combustion elemental analysis reveals that the amount of carbon content is 17.0%.

Figure 6-4 shows the Raman spectra of two different carbon in NVPC@CNFs (carbon coating and CNF incorporation) and NVPC (carbon coating). The peaks at 1360 and 1580 cm^{-1} correspond to the D-band and G-band, which represent the disordered graphene and ordered graphene structures in NVPC@CNFs and NVPC [45]. The peak at 2684 cm^{-1} is called 2D-band or G'-band, suggesting the existence of CNFs [46-48]. The D-band is stronger than the G-band in the NVPC spectrum, indicating that the dominant carbon phase is disordered amorphous graphene. On the other hand, NVPC@CNFs exhibit a stronger G-band than a D-band. This corresponds to the addition of graphitized CNFs. The results of SEM, EDS, XRD, and Raman spectroscopy suggest that this novel method enables a uniform composite of CNFs and a carbon-coated pure NVP phase to be formed. The surface area of NVPC@CNFs was measured by the N_2 adsorption isotherm at 77 K. NVPC@CNFs have a Brunauer-Emmett-Teller (BET) surface area of 7.9 $\mathrm{m}^2\ \mathrm{g}^{-1}$, which is similar to that of NVPC (7.7 $\mathrm{m}^2\ \mathrm{g}^{-1}$). (Figure 6-S3 plots the N_2 adsorption isotherm at 77 K and the BET surface area plot for NVPC@CNFs [15]).

Figure 6-5 shows the galvanostatic charge-discharge profiles and cycling properties of the Na/IL/NVPC@CNFs cell at 298 K and a current rate of 0.1C (a) and 2C (b). The charging profiles of the first cycle differ from the other cycles. The first charge curve shows a capacity of 116 mAh g^{-1}, which contains some irreversible capacity for cathode electrolyte interphase (CEI) formation. All other subsequent cycles are highly stable and exhibit a reversible capacity of 105 mAh g^{-1} based on the two-electron desodiation/sodiation reaction accompanying the V^{4+}/V^{3+} redox activity. The flat plateaus at approximately 3.4 V in Figure 6-5a correspond to the $Na_3V_2(PO_4)_3/NaV_2(PO_4)_3$ two-phase process [15]. NVPC@CNFs exhibit a stable cycleability of over 200 cycles (Figure 6-5b). The average Coulombic efficiency during 200 cycles is over 99.9%, and 100.9% of the capacity in the first cycle is retained.

To determine the performance at intermediate temperature operations, a cycle test was carried out at 363 K. The cell exhibits a highly stable cycleability over 200 cycles at 363 K. The reversible capacity is 99.6 mAh g^{-1} at 2C with an average Coulombic efficiency of 99.1% (Figure 6-S4). These results imply that Na secondary batteries with an IL electrolyte are free from flammability safety hazards and utilize waste heat to enhance performance, as proposed in previous works [15, 49].

Many recent studies have been reported that NVP can show a high rate capability by improving the electronic conductivity originating from the phosphate group with the aid of carbon coating, morphology control, or metal ion doping.[6, 21, 24-25, 27, 54, 60-64]. However, mass loading, which significantly affects the rate performance results, is often neglected in rate capability tests. This is because mass loading is directly related to the geometric current density. Prior to the rate capability measurements of NVPC@CNFs, that of NVPC was tested at three different mass loadings: 1.5, 3.0, and 6.0 mg-active material cm^{-2} at 298 K and 363 K (Figure 6-S5). NVPC exhibits a high rate capability when the mass loading is small (1.5 mg-active material cm^{-2}; capacity retentions of 79.4% at 298 K, and 92.5% at 363 K at 40C). However, this high rate capability decreases as the mass loading increases because the Na ion diffusion paths are prolonged in the composite electrode as the mass loading increases, and is severe at room temperature (capacity retentions of 79.4%, 18.3%, and 0.6% with 1.5, 3.0, and 6.0 mg-active material cm^{-2}, respectively at 298 K at 40C). On the other hand, the rate capability is maintained at a high level at an intermediate temperature (~363 K) even for a high mass load (capacity retentions comparing at 0.1C to at 40 C of NVP 1.7 mg cm^{-2}, 3.0 mg cm^{-2}, and 6.0

mg cm^{-2} at 363 K are 92.5, 89.5, 86.6%, respectively). Furthermore, at both temperatures, there is a strong trend that the rate capability is limited by geometric current density. For example, the capacity retention of 3.0 mg cm^{-2} at 10C and 6.0 mg cm^{-2} at 5C at have the same geometric current density of 3.53 mA cm^{-2} exhibit similar capacity retention of 68.3% and 63.2%, respectively at 298 K and 96.1% and 97.3% at 363 K, respectively. The geometric current densities and details on capacity retention are provided in Table 6-S2 and 6-S3 in the supporting information.

CNF embedding improves the high rate capability of NVPC. Figures 6-6a and 6-7a show the rate capability test results for NVPC@CNFs using the IL electrolyte. For comparison, Figure 6-S7 shows the test with the organic electrolyte of 1 mol dm^{-3} Na[PF$_6$]-PC at 298 K under the same conditions. NVPC@CNFs exhibit a high rate capability at 298 K regardless of the type of electrolyte. NVPC@CNFs using IL electrolyte display 87.5 and 51.0 mAh g^{-1} at 5 and 10C, respectively. Moreover, it has a higher mass loading of 8.5 mg-active material cm^{-2} than that of NVPC with 6.0 mg-active material cm^{-2} (c.f. 63.2 and 32.6 mAh g^{-1} at 5 and 10C, respectively). The capacity of the cells after the rate capability test is promptly recovered at a low current density of 0.1C, suggesting negligible damage during the rate capability test. In the case of NVPC@CNFs using an organic electrolyte, the cell is stabilized after the fifth cycle (cf. the cell using IL electrolyte is stable from the first cycle). It exhibits 79.7 and 65.5 mAh g^{-1} at 5 and 10C, respectively. These results indicate that ILs are more favorable to form good a CEI layer and that a well-prepared positive material combined with an IL electrolyte shows almost the same electrochemical performance as those using an organic electrolyte. Despite concerns about the limited performance of IL at room temperature operating, NVPC@CNFs in IL electrolytes show higher stability with an extremely high Coulombic efficiency.

Symmetric cell EIS is a powerful method to investigate only the targeted electrode [42, 55-57]. Two identical electrodes at the same state-of-charge were used for the EIS measurement, and the EIS spectra are fitted based on an equivalent circuit (Figure 6-6b, inset). Figure 6-6b, which compares symmetric cell EIS of NVPC@CNFs/IL/NVPC@CNFs and NVPC/IL/NVPC (SOC = 50% in both cases), confirms this improvement. Table 6-S1 shows the fitted data. There are two semi-circles with characteristic frequencies of ~5000 Hz (high-frequency region denoted as R_h) and ~10 Hz (interfacial resistance denoted as R_int). R_h is often referred to as the resistance of SEI. A detailed interpretation of this resistance is still difficult, but a recent study revealed that it is strongly influenced by temperature, the electrical conductivity of an electrode, surface area, electrolyte concentration, etc., and it is intimately related to electrode performance [42]. R_h decreases by half by introducing CNFs into the NVP particles (34.5 Ω for NVPC and 13.7 Ω for NVPC@CNFs). R_int refers to the charge-transfer resistance at the electrode-electrolyte interface. The semicircle for NVPC@CNFs corresponds to R_int of 18.6 Ω, which is roughly one-fourth that of NVPC (71.3 Ω) (Table 6-S1).

The results suggest that embedded CNFs in NVPC particles improve the electronic conduction between NVP particles and the electrochemical process at the electrode/electrolyte interface [58-61]. This facilitates the insertion/desertion of Na^+ ions into the NVP framework and directly improves the rate capability. Since introducing CNFs enhances the rate capability at 298 K, the rate capability was further tested at 363 K. Despite a high mass loading of 8.5 mg-active material cm^{-2}, very stable cycles and high discharge capacities of 102.5 mAh g^{-1} at 10C, 82.3 mAh g^{-1} at 100C, and 71.7 mAh g^{-1} at 200C are observed (Figure 6-7c and 6-7d).

6.4 Conclusions

$Na_3V_2(PO_4)_3$ is a promising electrode material for sodium secondary batteries in terms of its high power and energy density. However, an efficient carbon coating and fabrication method is necessary to fabricate materials that maintain high power and energy density while simultaneously achieving a high rate performance. In this study, NVPC@CNFs composites are prepared by a combination of facile sonication and a sol-gel process. This simple method provides CNFs uniformly embedded inside NVPC particles.

With respect to practical applications, electrochemical tests with a high mass loading of 8.5 mg-active material cm^{-2} were conducted. They also exhibit a stable yet reversible charge-discharge performance and excellent cyclability across a temperature range of 298 K to 363 K. Furthermore, superior rate capabilities of 51.1 mAh g^{-1} at 10C at 298 K and 82.3 mAh g^{-1} at 100C at 363K are achieved. These improvements originate from the unique matrix structure of NVPC@CNFs because this network serves as an electron conductor between particles and facilitates the charge-transfer process on the electrode/electrolyte interface.

In summary, this study demonstrates that for the true rate performance, geometric current density has to be considered, and the present simple method efficiently improves the intrinsic electrochemical performance of NVPC@CNFs in the high mass loading electrode material comparing to NVPC. NVPC@CNFs and IL electrolytes are electrochemically, chemically, and thermodynamically stable. Consequently, they are feasible for future battery materials. This study will contribute to the realization of practical sodium secondary batteries. To this end, further studies using full cells as 18650 size batteries or pouch cells should be conducted.

Table 6-1 Crystallographic data of the NVP phase in NVPC@CNFs by Rietveld refinement.

Refinement results for the NVP phase in NVPC@CNFs (S.G. $R\bar{3}c$)

$R_p = 12.8\%$, $R_{wp} = 13.2\%$, $R_e = 2.53\%$, $a = 8.7302(2)$ Å, $c = 21.8592(2)$ Å

Atom	Wyckoff symbol	x	y	z	B_{iso}/Å^2	Occup.
Na1	6b	0	0	0	0.5	0.781(2)
Na2	18e	0.6375(4)	0	0.2500	0.5	0.727(6)
V	12c	0	0	0.1477(5)	0.5	1.000
P	18e	0.2889(2)	0	0.2500	0.5	1.000
O1	36f	0.1814(3)	0.9696(3)	0.1926(9)	0.5	1.000
O2	36f	0.1932(3)	0.1698(3)	0.0883(1)	0.5	1.000

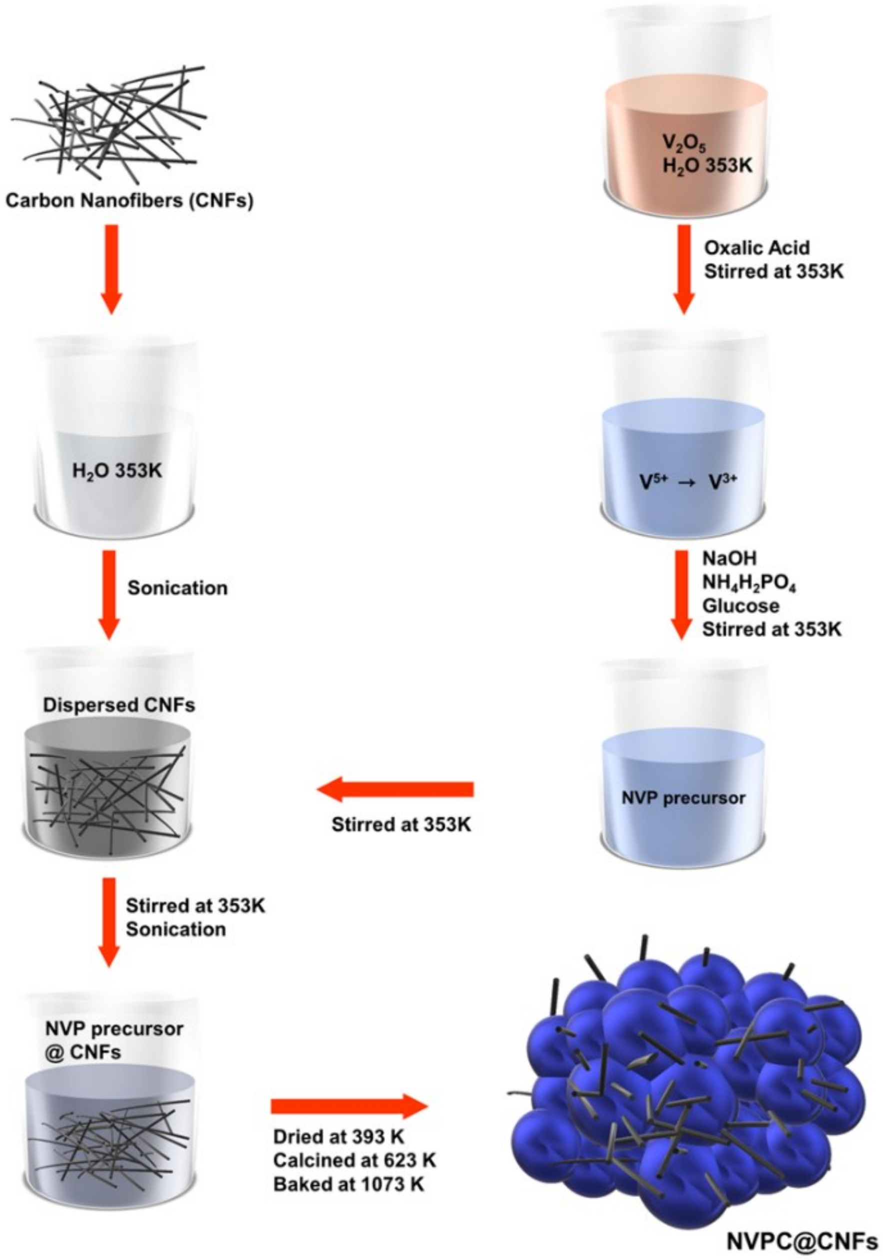

Figure 6-1 Schematic illustration of the preparation of NVPC@CNFs.

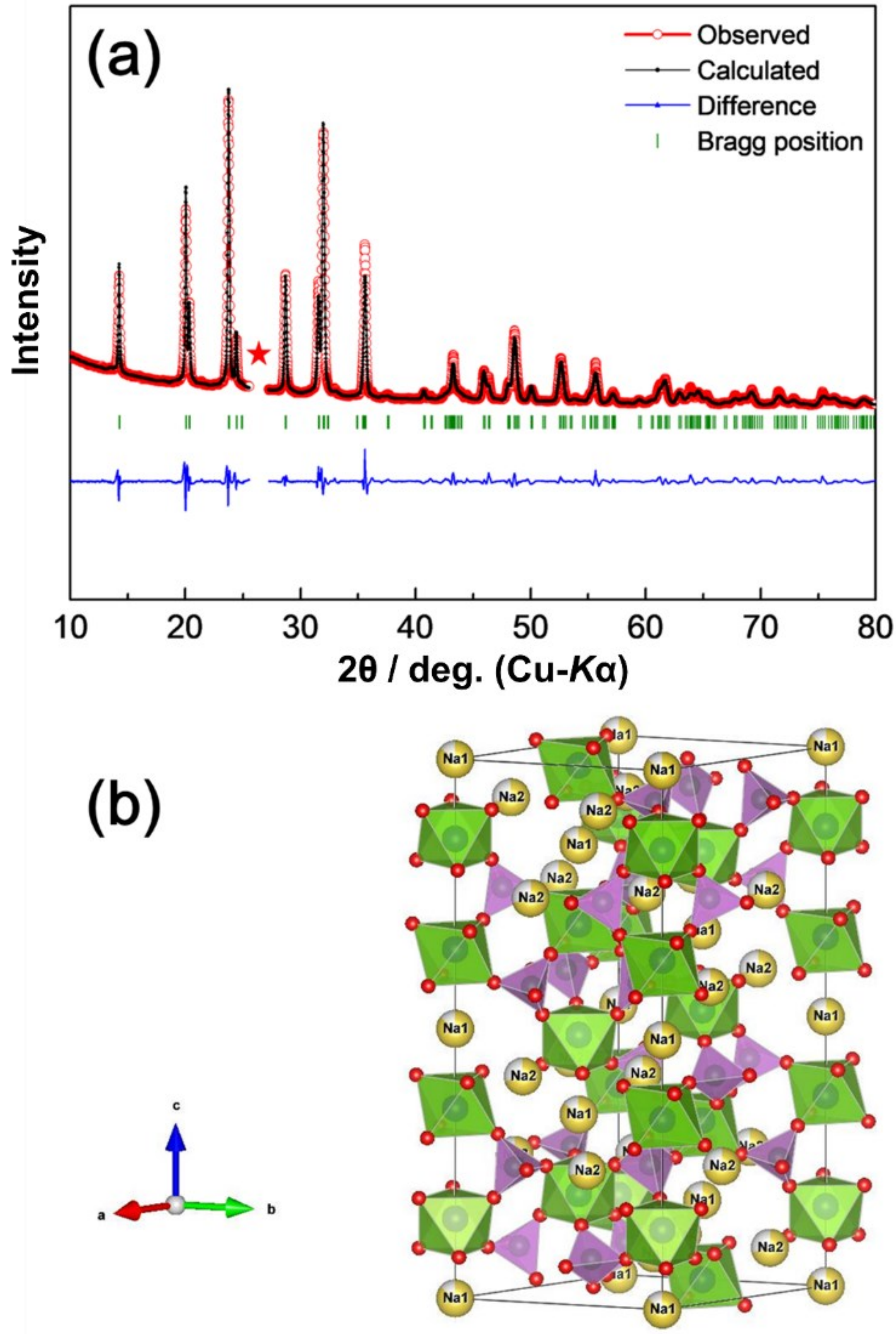

Figure 6-2 (a) Rietveld refinement results of NVPC@CNFs. The red star indicates the removed region from the patterns to avoid the strong peak of CNFs in the refinement. See Table 6-1 for the crystallographic data of the NVPC@CNFs and Figure 6-S2 in the Supporting Information for the full XRD patterns. (b) The refined NVP structural model, yellow, red, green, and purple denote sodium, oxygen, VO_6, and PO, respectively.

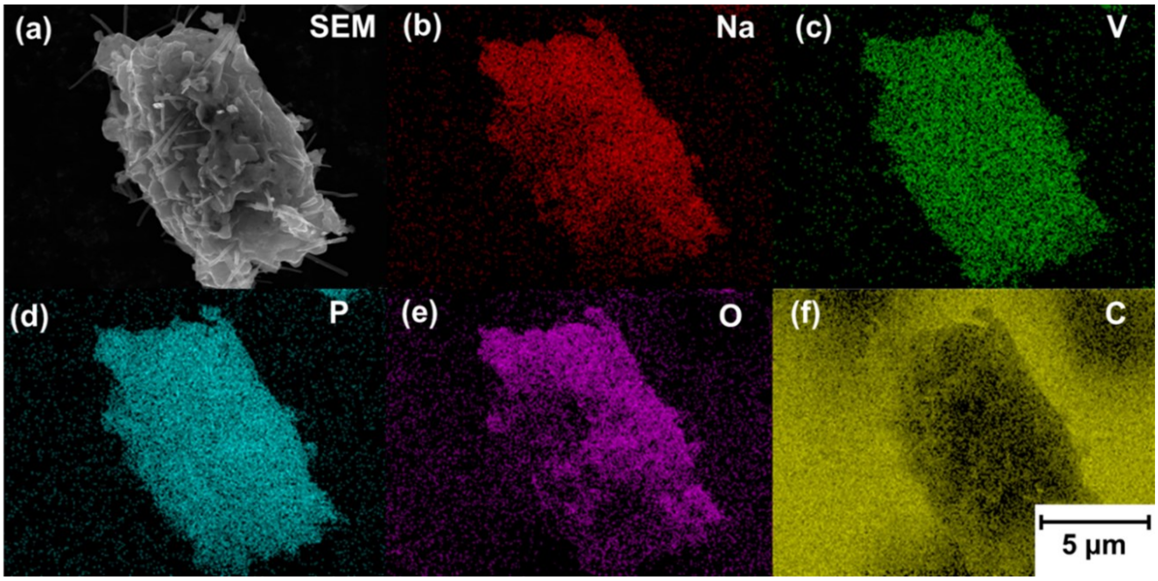

Figure 6-3 (a) SEM image and (b-f) EDX mappings of the elements in the NVPC@CNFs sample. EDX Obs: Na, 15.1; V, 22.4; P, 20.4; O, 42.1 (wt%), Calc. for NVP: Na, 13.9; V, 23.0; P, 20.4; O, 42.7 (wt%). Carbon content (17.0 wt% by combustion analysis, including 6.2 wt% contribution of CNFs) is excluded.

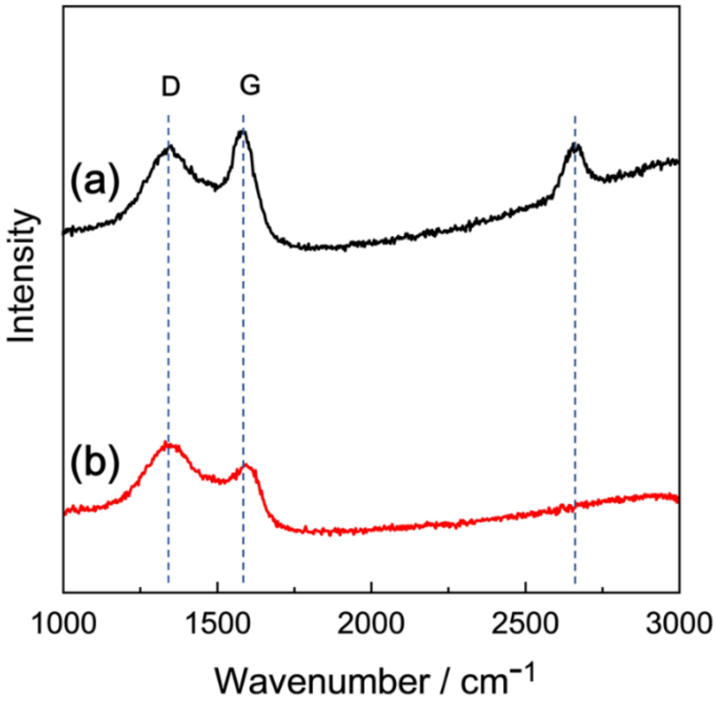

Figure 6-4 Raman spectra of (a) NVPC@CNFs and (b) NVPC. Symbols G and D denote the G-band originating from the ordered graphene structure and the D-band originating from the structural disorder in the graphene sheet, respectively.

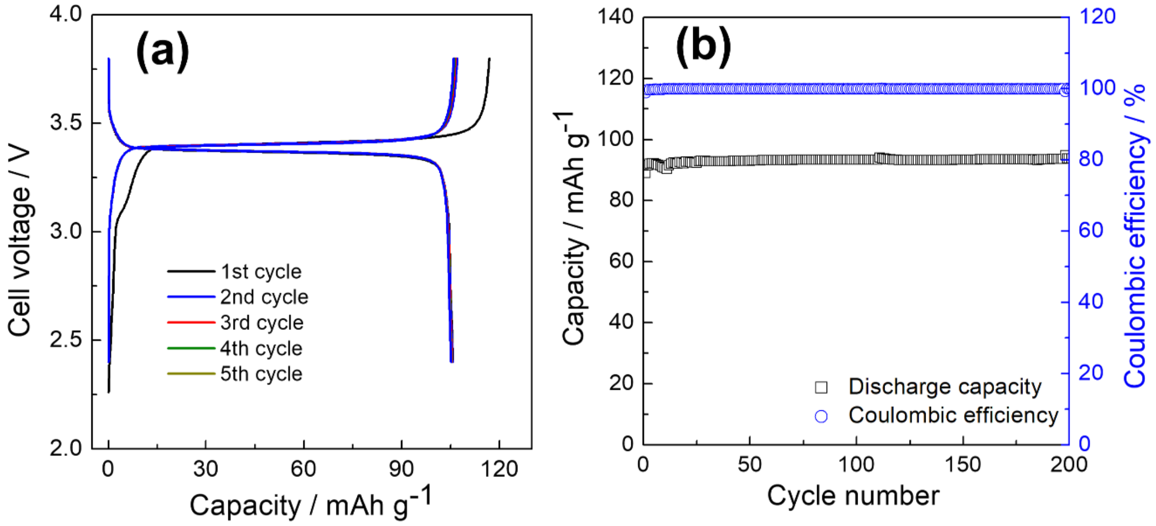

Figure 6-5 (a) Charge-discharge curves and (b) cycling properties of the Na/IL/NVPC@CNFs cell at 298 K. Current densities: (a) 0.1C and (b) 2C. Cut-off voltages: 2.4-3.8 V. Mass loading: 8.5 mg-active material cm^{-2}.

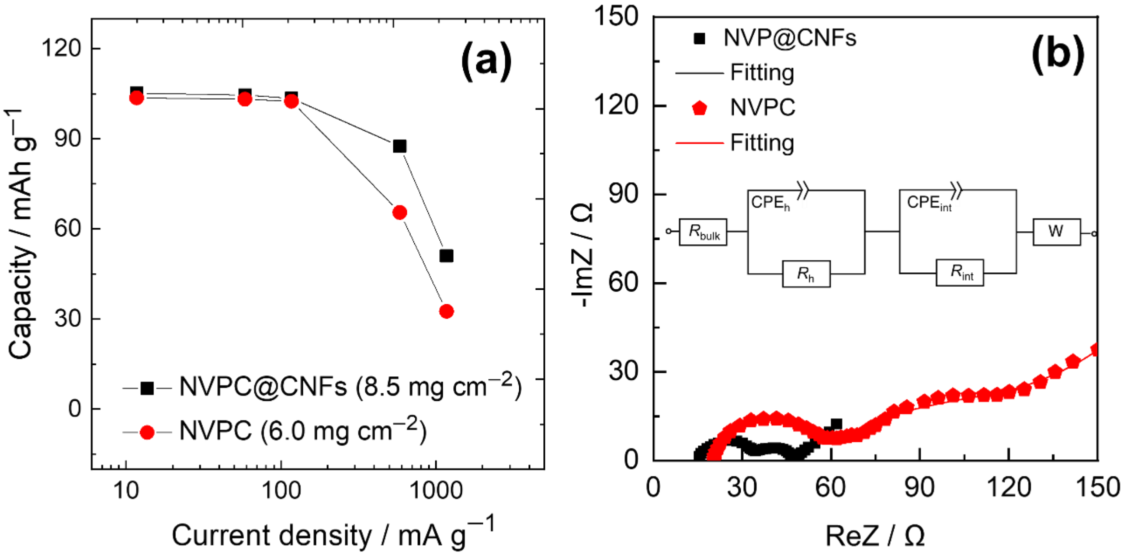

Figure 6-6 (a) Comparative rate capability plots for Na/NVPC and Na/NVPC@CNFs at 298 K. Current densities: 0.1C for charge and 0.1C to 10C for discharge with Cut-off voltages of 2.4-3.8 V. (b) NVPC@CNFs/IL/NVPC@CNFs and NVPC/IL/NVPC symmetric cell EIS. Inset shows an equivalent circuit, where CPE denotes the constant phase element, and W denotes the Warburg element at 298 K. SOC= 50%, frequency range: 40 mHz – 100 kHz, ac amplitude: 10 mV. Mass loading: 8.5 and 6.0 mg-active material cm^{-2} for NVPC@CNFs and NVPC, respectively. See Table 6-S1 in the appendix for the fitting parameters of the impedance spectra. Characteristic frequencies: R_h: ~5000 Hz and R_{int}: ~10 Hz. See Tables 6-S2 and 6-S3 in Supporting Information for details about the capacity, capacity retention, and geometric current density.

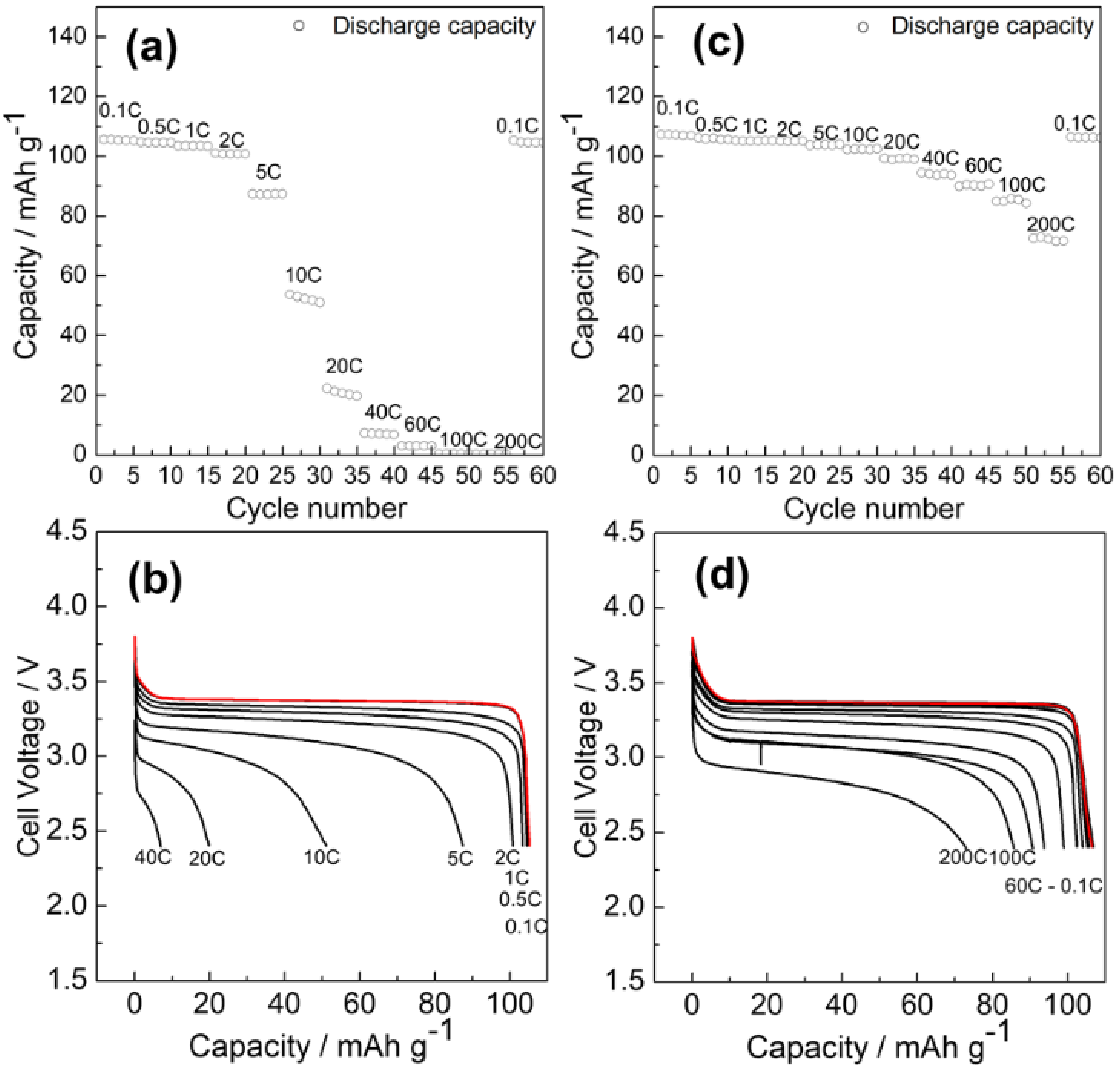

Figure 6-7 Rate capabilities of Na/IL/NVPC@CNFs cells at (a, b) 298 K and (c, d) 363 K. Red curves refer to the discharge profile at 0.1C after the rate capability test up to 200C. Current densities: 0.1C for charge and 0.1C−200C for a cycle test with Cut-off voltages of 2.4-3.8 V. Mass loading: 8.5 mg-active material cm^{-2}. See Table 6-S2-4, appendix, for details about the capacity and capacity retention and geometric current density.

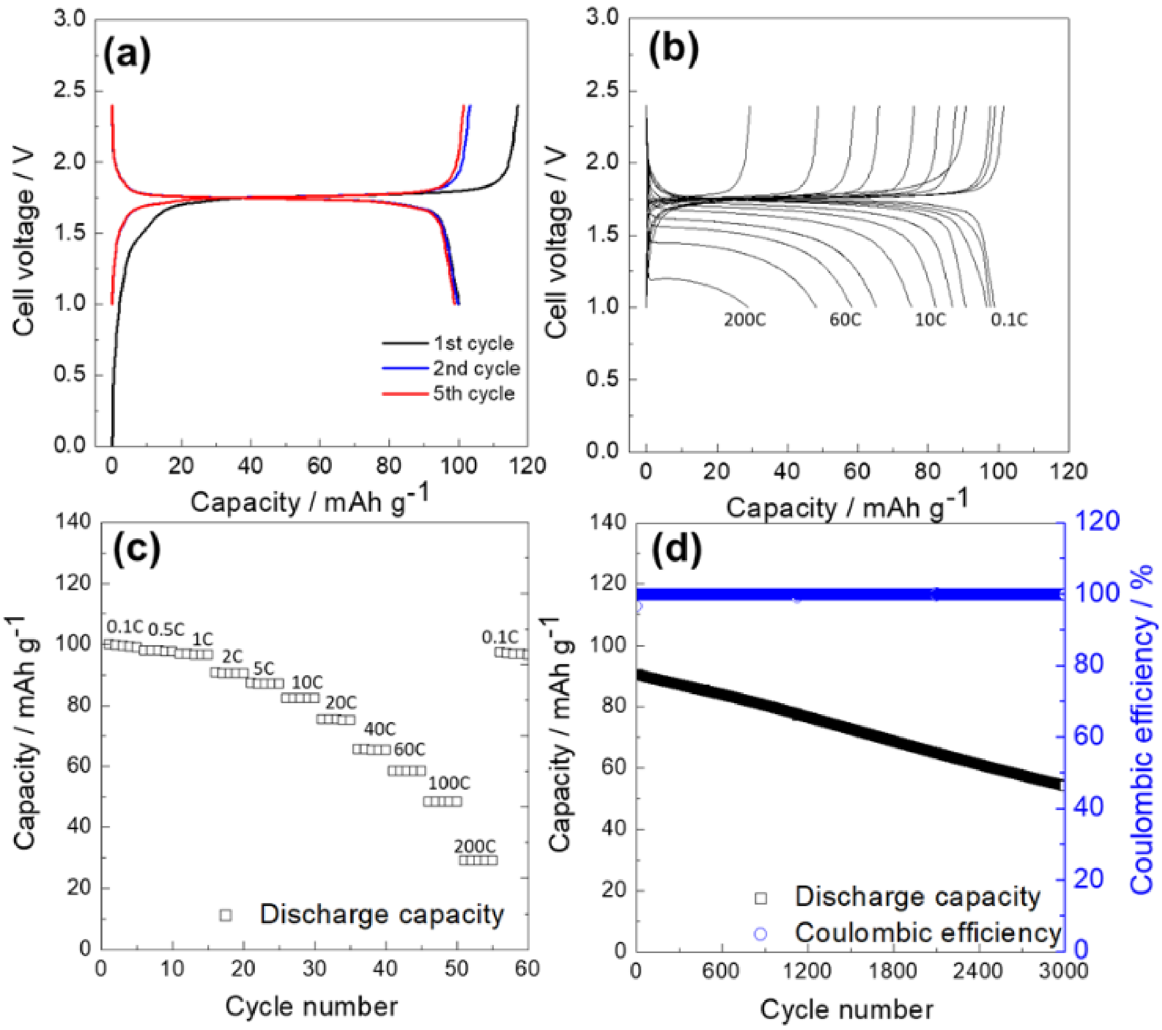

Figure 6-8 NVPC@CNFs/IL/NVPC@CNFs symmetric full cell electrochemical measurements at 298 K (a) charge-discharge curve, (b, c) rate capability and cycle test, and (d) cycle test. Current densities: 0.1C for charge-discharge test and charge for rate test, 0.1C to 200C for discharge for rate test and 2C for cycle test with Cut-off voltages of 1.0-2.4 V.

References

[1] Z. Jian, Y. Sun, and X. Ji, Chem. Commun., 51 (2015) 6381.

[2] W. C. Duan, Z. Q. Zhu, H. Li, Z. Hu, K. Zhang, F. Y. Cheng, and J. Chen, J. Mater. Chem. A, 2 (2014) 8668.

[3] C. Zhu, P. Kopold, P. A. van Aken, J. Maier, and Y. Yu, Adv. Mater., 28 (2016) 2409.

[4] L. S. Plashnitsa, E. Kobayashi, Y. Noguchi, S. Okada, and J. Yamaki, J. Electrochem. Soc., 157 (2010) A536.

[5] Z. Jian, Y. S. Hu, X. Ji, and W. Chen, Adv. Mater., 29 (2017) 1601925.

[6] S. Y. Lim, H. Kim, R. A. Shakoor, Y. Jung, and J. W. Choi, J. Electrochem. Soc., 159 (2012) A1393.

[7] Q. Liu, X. Meng, Z. Wei, D. Wang, Y. Gao, Y. Wei, F. Du, and G. Chen, ACS Appl. Mater. Interfaces, 8 (2016) 31709.

[8] Q. Wang, B. Zhao, S. Zhang, X. Gao, and C. Deng, J. Mater. Chem. A, 3 (2015) 7732.

[9] Y. Jiang, Z. Z. Yang, W. H. Li, L. C. Zeng, F. S. Pan, M. Wang, X. Wei, G. T. Hu, L. Gu, and Y. Yu, Adv. Energy Mater., 5 (2015) 1402104.

[10] J. Zhang, Y. Fang, L. Xiao, J. Qian, Y. Cao, X. Ai, and H. Yang, ACS Appl. Mater. Interfaces, 9 (2017) 7177.

[11] W. Shen, H. Li, Z. Guo, C. Wang, Z. Li, Q. Xu, H. Liu, Y. Wang, and Y. Xia, ACS Appl. Mater. Interfaces, 8 (2016) 15341.

[12] H. Li, C. Wu, Y. Bai, F. Wu, and M. Wang, J. Power Sources, 326 (2016) 14.

[13] Z. Jian, W. Han, X. Lu, H. Yang, Y.-S. Hu, J. Zhou, Z. Zhou, J. Li, W. Chen, D. Chen, and L. Chen, Adv. Energy Mater., 3 (2013) 156.

[14] L. Chen, Y. Zhao, S. Liu, and L. Zhao, ACS Appl. Mater. Interfaces, 9 (2017) 44485.

[15] J. Hwang, K. Matsumoto, and R. Hagiwara, Adv. Sustainable Syst., 2 (2018) 1700171.

[16] X. Rui, W. Sun, C. Wu, Y. Yu, and Q. Yan, Adv. Mater., 27 (2015) 6670.

[17] A. Ponrouch, D. Monti, A. Boschin, B. Steen, P. Johansson, and M. R. Palacín, J. Mater. Chem. A, 3 (2015) 22.

[18] S. Hess, M. Wohlfahrt-Mehrens, and M. Wachtler, J. Electrochem. Soc., 162 (2015) A3084.

[19] S. Wilken, P. Johansson, and P. Jacobsson, Solid State Ion., 225 (2012) 608.

[20] G. G. Eshetu, S. Grugeon, S. Laruelle, S. Boyanov, A. Lecocq, J. P. Bertrand, and G. Marlair, Phys. Chem. Chem. Phys., 15 (2013) 9145.

[21] E. Cabrera-Castillo, F. Niedermeier, and A. Jossen, J. Power Sources, 324 (2016) 509.

[22] M. Armand, F. Endres, D. R. MacFarlane, H. Ohno, and B. Scrosati, Nat. Mater., 8 (2009) 621.

[23] L. Chancelier, A. O. Diallo, C. C. Santini, G. Marlair, T. Gutel, S. Mailley, and C. Len, Phys. Chem. Chem. Phys., 16 (2014) 1967.

[24] G. B. Appetecchi, M. Montanino, and S. Passerini, in Ionic Liquids: Science and Applications, p. 67, American Chemical Society (2012).

[25] D. R. MacFarlane, N. Tachikawa, M. Forsyth, J. M. Pringle, P. C. Howlett, G. D. Elliott, J. H. Davis, M. Watanabe, P. Simon, and C. A. Angell, Energ. Environ. Sci., 7 (2014) 232.

[26] M. Watanabe, M. L. Thomas, S. Zhang, K. Ueno, T. Yasuda, and K. Dokko, Chem. Rev., 117 (2017) 7190.

[27] A. Basile, M. Hilder, F. Makhlooghiazad, C. Pozo-Gonzalo, D. R. MacFarlane, P. C. Howlett, and M. Forsyth, Adv. Energy Mater., 8 (2018) 1703491.

[28] H. Zhang, W. Feng, J. Nie, and Z. Zhou, J. Fluorine Chem., 174 (2015) 49.

[29] K. Matsumoto, Y. Okamoto, T. Nohira, and R. Hagiwara, J. Phys. Chem. C, 119 (2015) 7648.

[30] M. Forsyth, H. Yoon, F. Chen, H. Zhu, D. R. MacFarlane, M. Armand, and P. C. Howlett, J. Phys. Chem. C, 120 (2016) 4276.

[31] N. Wongittharom, C.-H. Wang, Y.-C. Wang, C.-H. Yang, and J.-K. Chang, ACS Appl. Mater. Interfaces, 6 (2014) 17564.

[32] C.-H. Wang, C.-H. Yang, and J.-K. Chang, Chem. Commun., 52 (2016) 10890.

[33] L. G. Chagas, D. Buchholz, L. Wu, B. Vortmann, and S. Passerini, J. Power Sources, 247 (2014) 377.

[34] G. Sui, S. Jana, W. H. Zhong, M. A. Fuqua, and C. A. Ulven, Acta Mater., 56 (2008) 2381.

[35] X. Fang, M. Ge, J. Rong, and C. Zhou, ACS Nano, 8 (2014) 4876.

[36] W. Li, M. Li, K. R. Adair, X. Sun, and Y. Yu, J. Mater. Chem. A, 5 (2017) 13882.

[37] K. Matsumoto, T. Hosokawa, T. Nohira, R. Hagiwara, A. Fukunaga, K. Numata, E. Itani, S. Sakai, K. Nitta, and S. Inazawa, J. Power Sources, 265 (2014) 36.

[38] J. Rodríguez-Carvajal, Phys. B, 192 (1993) 55.

[39] K. Momma, and F. Izumi, J. Appl. Crystallogr., 41 (2008) 653.

[40] S. Brunauer, P. H. Emmett, and E. Teller, J. Am. Chem. Soc., 60 (1938) 309.

[41] J. Hwang, K. Matsumoto, Y. Orikasa, M. Katayama, Y. Inada, T. Nohira, and R. Hagiwara, J. Power Sources, 377 (2018) 80.

[42] J. Hwang, K. Matsumoto, and R. Hagiwara, J. Phys. Chem. C, 122 (2018) 26857.

[43] J.-N. Chotard, G. Rousse, R. David, O. Mentré, M. Courty, and C. Masquelier, Chem. Mater., 27 (2015) 5982.

[44] Z. Jian, C. Yuan, W. Han, X. Lu, L. Gu, X. Xi, Y.-S. Hu, H. Li, W. Chen, D. Chen, Y. Ikuhara, and L. Chen, Adv. Funct. Mater., 24 (2014) 4265.

[45] A. C. Ferrari, and J. Robertson, Philos. Trans. Royal Soc. A, 362 (2004) 2477.

[46] A. C. Ferrari, J. C. Meyer, V. Scardaci, C. Casiraghi, M. Lazzeri, F. Mauri, S. Piscanec, D. Jiang, K. S. Novoselov, S. Roth, and A. K. Geim, Phys. Rev. Lett., 97 (2006) 187401.

[47] M. S. Dresselhaus, G. Dresselhaus, R. Saito, and A. Jorio, Phys. Rep., 409 (2005) 47.

[48] L. Jiao, L. Zhang, X. Wang, G. Diankov, and H. Dai, Nature, 458 (2009) 877.

[49] K. Shubham, H. Jinkwang, M. Kazuhiko, S. Yuta, and H. Rika, ChemElectroChem, 5 (2018) 1340.

[50] Z. L. Jian, W. Z. Han, X. Lu, H. X. Yang, Y. S. Hu, J. Zhou, Z. B. Zhou, J. Q. Li, W. Chen, D. F. Chen, and L. Q. Chen, Adv. Energy Mater., 3 (2013) 156.

[51] K. Saravanan, C. W. Mason, A. Rudola, K. H. Wong, and P. Balaya, Adv. Energy Mater., 3 (2013) 444.

[52] Z. L. Jian, L. Zhao, H. L. Pan, Y. S. Hu, H. Li, W. Chen, and L. Q. Chen, Electrochem. Commun., 14 (2012) 86.

[53] X. Li, Y. Huang, J. Wang, L. Miao, Y. Li, Y. Liu, Y. Qiu, C. Fang, J. Han, and Y. Huang, J. Mater. Chem. A, 6 (2018) 1390.

[54] S.-J. Lim, D.-W. Han, D.-H. Nam, K.-S. Hong, J.-Y. Eom, W.-H. Ryu, and H.-S. Kwon, J. Mater. Chem. A, 2 (2014) 19623.

[55] N. Ogihara, Y. Itou, T. Sasaki, and Y. Takeuchi, J. Phys. Chem. C, 119 (2015) 4612.

[56] C. H. Chen, J. Liu, and K. Amine, J. Power Sources, 96 (2001) 321.

[57] R. Petibon, C. P. Aiken, N. N. Sinha, J. C. Burns, H. Ye, C. M. VanElzen, G. Jain, S. Trussler, and J. R. Dahn, J. Electrochem. Soc., 160 (2013) A117.

[58] B. Kang, and G. Ceder, Nature, 458 (2009) 190.

[59] P. Bai, and M. Z. Bazant, Nat. Commun., 5 (2014) 3585.

[60] Q. Cao, H. P. Zhang, G. J. Wang, Q. Xia, Y. P. Wu, and H. Q. Wu, Electrochem. Commun., 9 (2007) 1228.

[61] J. Mao, C. Luo, T. Gao, X. Fan, and C. Wang, J. Mater. Chem. A, 3 (2015) 10378.

Appendix

Table 6-S1 EIS fitting parameters, R_{bulk}, R_{h}, R_{int}, Q_{h}, Q_{int}, W for NVPC/NVPC, and NVPC@CNFs/NVPC@CNFs symmetric cells. See Figure 6-6 (b) for the EIS.

	Resistance / Ω			CPE / F cm^2 s$^{(a-1)}$				W / Ωs$^{-1/2}$
	R_{bulk}	R_{h}	R_{int}	Q_{h}	a	Q_{int}	a	
NVPC	20.1	34.5	75.3	2.83x10^{-6}	0.87	4.36x10^{-3}	0.47	16.4
NVPC@CNFs	15.1	13.7	18.6	1.79x10^{-3}	0.69	9.78x10^{-6}	0.62	1.6

Table 6-S2. Geometric current densities and capacity retentions of the Na/IL/NVPC cell and the Na/IL/NVPC@CNFS cell at 298 K.

C-rate	Current density / mA g^{-1}	1.5 mg cm^{-2} of NVPC		3.0 mg cm^{-2} of NVPC		6.0 mg cm^{-2} of NVPC		8.5 mg cm^{-2} of NVPC@CNF	
		Geometric current density / mA cm^{-2}	Capacity retention vs 0.1C. / %	Geometric current density mA cm^{-2}	Capacity retention vs 0.1C. / %	Geometric current density mA cm^{-2}	Capacity retention vs 0.1C. / %	Geometric current density mA cm^{-2}	Capacity retention vs 0.1C. / %
0.1C	11.8	0.018	100	0.035	100	0.071	100	0.100	100
0.5C	58.8	0.088	99.6	0.176	99.6	0.353	99.61	0.500	99.4
1C	117	0.177	99.1	0.353	99.0	0.701	98.9	1.00	98.3
5C	588	0.882	97.1	1.76	90.5	3.53	63.2	5.00	83.2
10C	1180	1.76	94.9	3.53	68.3	7.06	31.4	10.0	48.5
20C	2350	3.53	89.8	7.06	38.9	14.1	13.2	20.0	18.8
40C	4700	7.06	79.5	14.1	18.3	28.2	0.577	40.0	6.66

Table 6-S2. Geometric current densities and capacity retentions of the Na/IL/NVPC cell and the Na/IL/NVPC@CNFS cell at 298 K.

C-rate	Current density / mA g^{-1}	1.5 mg cm^{-2} of NVPC		3.0 mg cm^{-2} of NVPC		6.0 mg cm^{-2} of NVPC		8.5 mg cm^{-2} of NVPC@CNF	
		Geometric current density / mA cm^{-2}	Capacity retention vs 0.1C. / %	Geometric current density mA cm^{-2}	Capacity retention vs 0.1C. / %	Geometric current density mA cm^{-2}	Capacity retention vs 0.1C. / %	Geometric current density mA cm^{-2}	Capacity retention vs 0.1C. / %
0.1C	11.8	0.018	100	0.035	100	0.071	100	0.100	100
0.5C	58.8	0.088	99.6	0.176	99.6	0.353	99.61	0.500	99.4
1C	117	0.177	99.1	0.353	99.0	0.701	98.9	1.00	98.3
5C	588	0.882	97.1	1.76	90.5	3.53	63.2	5.00	83.2
10C	1180	1.76	94.9	3.53	68.3	7.06	31.4	10.0	48.5
20C	2350	3.53	89.8	7.06	38.9	14.1	13.2	20.0	18.8
40C	4700	7.06	79.5	14.1	18.3	28.2	0.577	40.0	6.66

Table 6-S3. Geometric current densities and capacity retentions of the Na/IL/NVPC cell and the Na/IL/NVPC@CNFS cell at 363 K.

C-rate	Current density / mA g^{-1}	1.5 mg cm^{-2} of NVPC		3.0 mg cm^{-2} of NVPC		6.0 mg cm^{-2} of NVPC		8.5 mg cm^{-2} of NVPC@CNF	
		Geometric current density / mA cm^{-2}	Capacity retention vs 0.1C. / %	Geometric current density mA cm^{-2}	Capacity retention vs 0.1C. / %	Geometric current density mA cm^{-2}	Capacity retention vs 0.1C. / %	Geometric current density mA cm^{-2}	Capacity retention vs 0.1C. / %
0.1C	11.8	0.018	100	0.035	100	0.071	99.8	0.100	100
0.5C	58.8	0.088	99.9	0.176	99.3	0.353	98.9	0.500	98.8
1C	117	0.177	99.3	0.353	98.7	0.701	98.5	1.00	98.4
5C	588	0.882	97.1	1.76	97.2	3.53	97.3	5.00	97.2
10C	1180	1.76	95.5	3.53	96.1	7.06	96.4	10.0	95.8
20C	2350	3.53	94.0	7.06	94.1	14.1	93.4	20.0	92.6
40C	4700	7.06	92.5	14.1	89.5	28.2	86.6	40.0	87.7

Table 6-S4 Discharge capacity and capacity retention of the Na/IL/NVPC@CNFS cell. Charge rate: 0.1C, discharge rates: 0.1C to 200C, Cut-off voltage: 2.4-3.8 V. Electrolyte: 40 mol% Na[FSA]-[C_2C_1im][FSA].

Current/ 1C = 117 mA g^{-1}	298 K		363 K	
	Capacity / mAh g^{-1}	Capacity Retention 0.1C. / %	vs Capacity / mAh g^{-1}	Capacity Retention vs. 0.1C / %
0.1C	105.2	100.0	107.0	100.0
0.5C	104.5	99.4	105.7	98.8
1C	103.4	98.3	105.3	98.4
2C	100.8	95.8	105.2	98.3
5C	87.5	83.2	104.0	97.2
10C	51.0	48.5	102.5	95.8
20C	19.8	18.8	99.04	92.6
40C	7.0	6.7	93.8	87.7
60C	3.0	2.8	363.7	84.8
100C	0.3	0.2	82.3	76.9
200C	0.2	0.2	71.7	67.0

Capacity retention is based on the capacity at the 1st cycle.

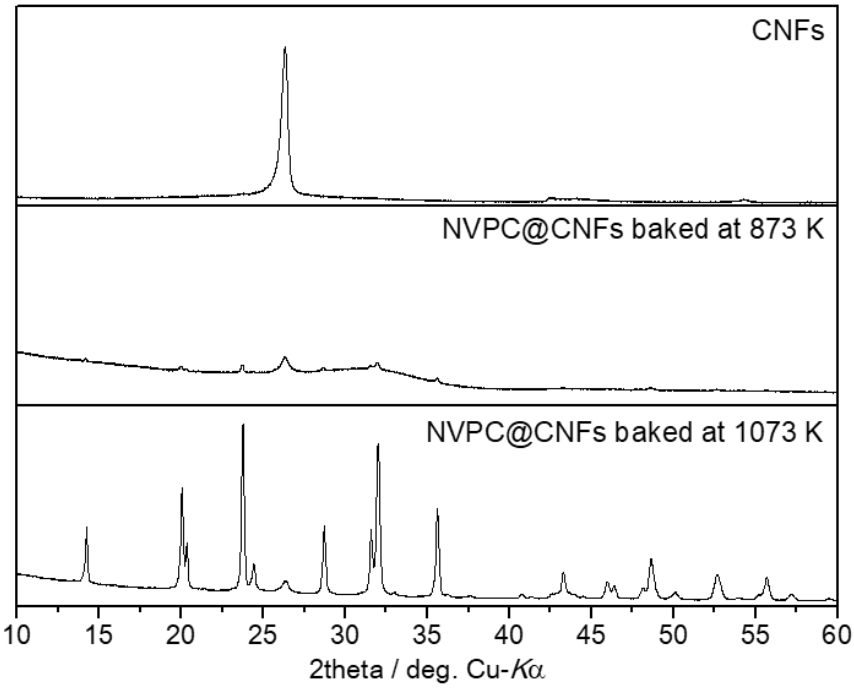

Figure 6-S1. XRD patterns of the NVPC@CNFs made via the sol-gel method baked at 873 and 1073 K and CNFs.

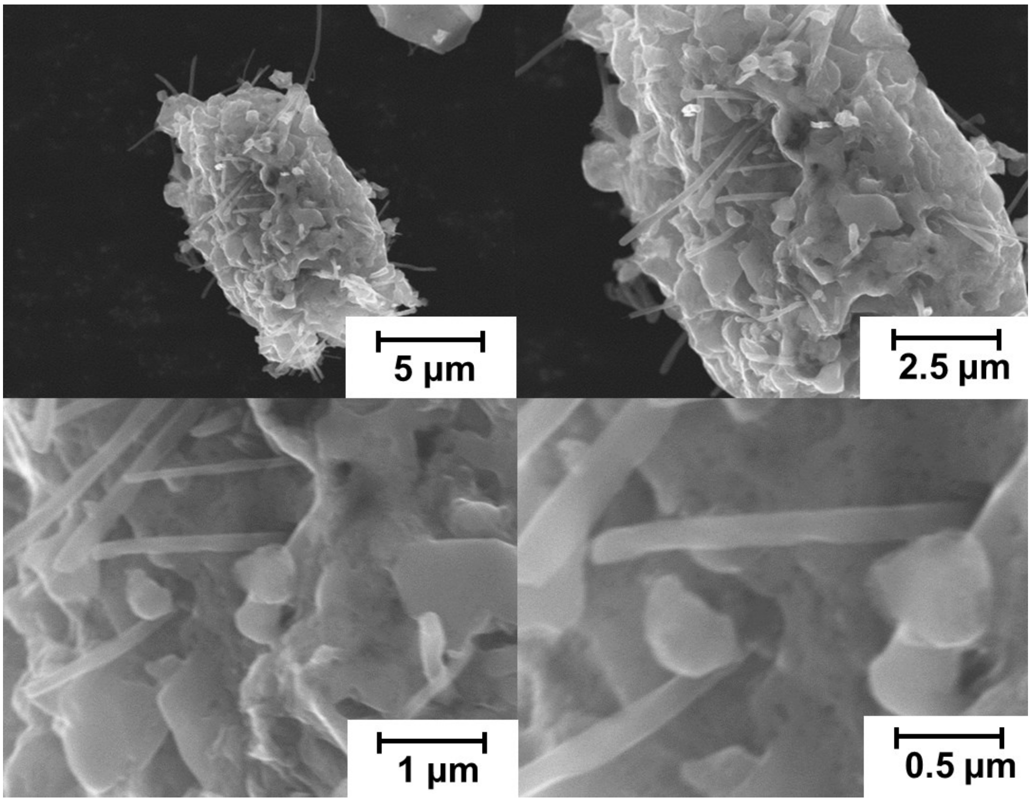

Figure 6-S2. Field-emission SEM images of NVPC@CNFs prepared by the sol-gel method and baked at 1073 K at different magnifications.

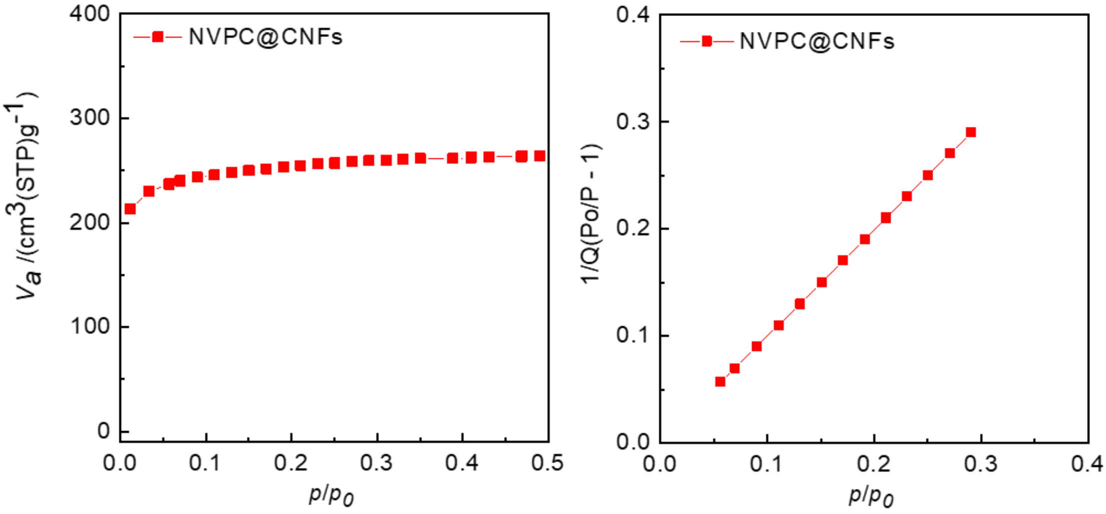

	Surface Area /m^2 g^{-1}
NVP@CNFs	7.91
NVPC	7.65

Figure 6-S3. N_2 adsorption isotherm at 77 K, and BET surface area plots for the NVPC@CNFs.

Brief comments: Surface properties of NVPC were studied in J. Hwang, K. Matsumoto, and R. Hagiwara, "$Na_3V_2(PO_4)_3$/C Positive Electrodes with High Energy and Power Densities for Na Secondary Batteries with Ionic Liquid Electrolytes That Operate across Wide Temperature Ranges", *Adv. Sustainable Syst.* **2** (2018) 1700171.

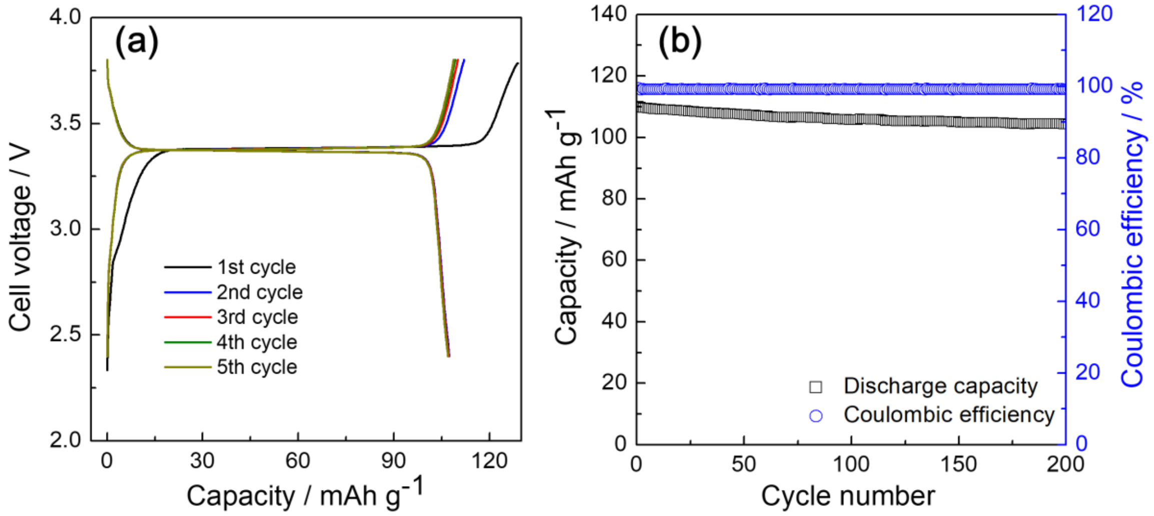

Figure 6-S4. (a) Charge-discharge curves and (b) cycle test of the Na/IL/NVPC@CNFs cell at 363 K. Current densities: 0.1C for (a) and 2C for (b) with Cut-off voltages of 2.4-3.8 V.

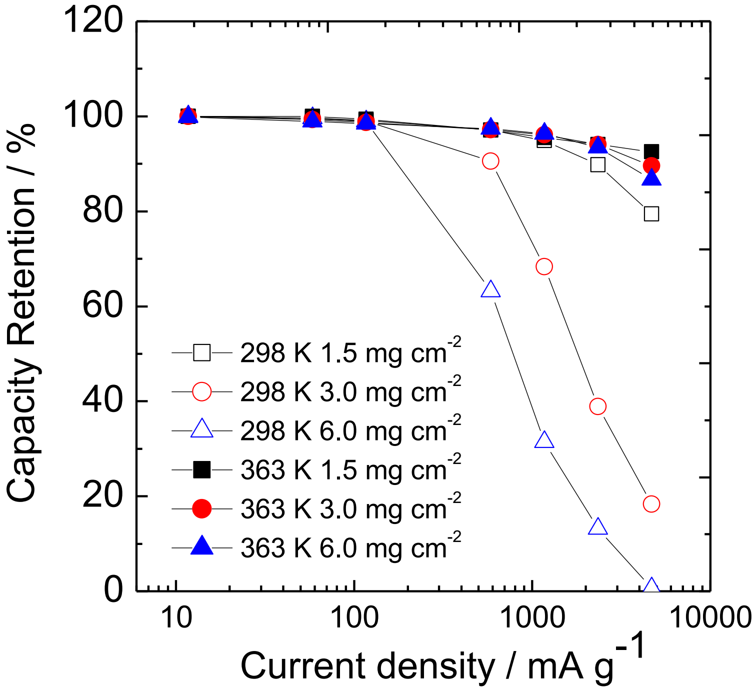

Figure 6-S5. Rate capabilities of Na/IL/NVPC cells with three different mass loading NVPC electrodes at 298 K and 363 K. Electrolyte: 40 mol% Na[FSA]-[C_2C_1im][FSA], charge rate: 0.1C, discharge rates: 0.1C to 40C, Cut-off voltages: 2.4-3.8 V.

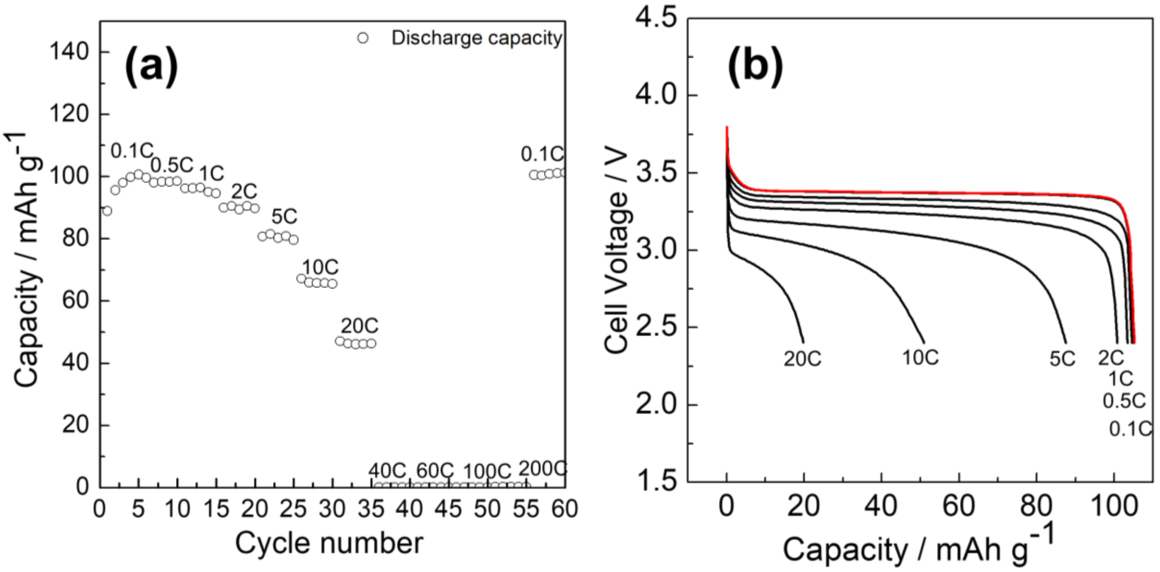

Figure 6-S7. Rate capabilities of the Na/1 mol dm^{-3} Na[PF_6]-EC/DMC/NVPC@CNFs cells at 298 K. Red curves refer to the discharge profile at 0.1C after rate capability test. Electrolyte: 1 mol dm^{-3} Na[PF_6]-EC/DMC, charge rate: 0.1C, discharge rates: 0.1C to 200C, Cut-off voltages: 2.4-3.8 V. Mass loading: 8.5 mg-active material cm^{-2}.

Chapter 7

Symmetric Cell Electrochemical Impedance Spectroscopy of $Na_2FeP_2O_7$ Positive Electrode

7.1 Introduction

Electrochemical impedance spectroscopy (EIS, which denotes electrochemical impedance spectrum hereafter) is a powerful tool that enables fast and simple analysis of the physicochemical and electrochemical characteristics of batteries [1-5]. The simplest and most effective way to obtain EIS measurements of batteries in the laboratory is to use a coin-type half-cell. The EIS results are normally interpreted by using a Nyquist or Bode plot [6-8]. Half-cell EIS provides information about both the working and counter electrodes, and separation of the information relating to these two electrodes is often difficult. This difficulty is particularly significant for Na secondary batteries with IL electrolytes because they show the very large impedance of the film on Na metal [9, 10]. On the other hand, Symmetric cell electrochemical impedance spectroscopy (SCEIS) measurements using two identical electrodes at the same state-of-charge (SOC) directly renders the data of the corresponding electrode without being adversely affected by the effects of the counter electrode. This approach is thus a preferable method to investigate electrode materials, especially for IL electrolytes, for the above-mentioned reason. However, the interpretation of SCEIS results has not been sufficiently studied, particularly for Na secondary batteries with IL electrolytes.

This chapter presents a study of the effects of the operating temperature on Na secondary batteries with IL electrolytes using SCEIS with nine different types of electrode constituents (active and additive materials), by taking the performance of the $Na_2FeP_2O_7$

electrode as an example. The pyrophosphate, $Na_2FeP_2O_7$, is one of the well-studied positive electrode materials for Na secondary batteries. The material exhibits stable charge-discharge performance using organic electrolytes and IL electrolytes, and very high rate capability was achieved using IL electrolytes at intermediate temperatures [11-14].

In this study, EIS was performed at four different temperatures (298, 323, 343, and 363 K) using the Na[FSA]-[C_2C_1im][FSA] IL system (IL_{FSA}) [15] with Na[FSA] fraction from 20 to 50 mol%. Thereby, it is aimed to obtain the fundamental information pertaining to previous results, which indicated a high rate capability for the positive and negative electrodes at elevated temperatures [13, 16-18]. Origins of the resistance appearing in the high-frequency region (R_h) are also investigated because it significantly contributes to electrode performance. The results are discussed by considering the bulk and charge-transfer resistance (R_{bulk}, R_h, and R_{ct}).

7.2 Experimental

Na metal (Sigma-Aldrich chemistry, purity 99.95%) was cut into a disk (16 mm in diameter) and fixed to an Al plate current collector as the electrode. Aluminum mesh (Nilaco Corporation) was cut into a disk (13 mm in diameter) for use as the electrode. AB (Wako Pure Chemical Industries) electrodes were prepared by mixing AB with PTFE in four different weight ratios (AB:PTFE = 95:5, 50:50, 5:95, and 100:0 wt%). Each of these combinations was mixed in a mortar and pestle, and the resulting mixtures were spread out to form a sheet. The respective sheets were pressed onto an Al mesh to obtain a loading mass of approximately 3 mg cm^{-2}. For the100% AB electrode, AB was pelletized (70 MPa) for 10 min. The electrodes of α-Al_2O_3 (Wako Pure Chemical Industries) and V_2O_5 (Sigma-Aldrich Chemistry, purity 99.6%) were prepared in the same manner as the AB/PTFE electrodes. The $Na_2FeP_2O_7$ sample was prepared in the same manner as previously reported [13, 19], and the electrodes were prepared in the same manner as the AB/PTFE electrodes. The morphologies of V_2O_5 and α-Al_2O_3 and the microstructures of the $Na_2FeP_2O_7$ electrodes were observed by field-emission scanning electron microscopy (FE-SEM, Hitachi SU-8020). (See Figure 7-S1, 7-S3, and 7-S5, respectively.) EDS mapping was performed using an analyzer (Horiba EMAXEvolution X-max) attached to the SEM. XRD patterns of V_2O_5 and α-Al_2O_3 and $Na_2FeP_2O_7$ were collected in the Bragg–Brentano geometry using a Rigaku SmartLab diffractometer with Ni-filtered Cu-*K*α radiation (40 kV and 30 mA). (See appendix for details. Figures 7-S2, 7-S4, and 7-S5, respectively)

The salts, Na[FSA] (Mitsubishi Materials Electronic Chemicals, purity > 99%) and [C_2C_1im][FSA] (Kanto Chemical, purity > 99.9%), were dried under vacuum for 24 hours at 353 K. A glass microfiber filter (Whatman GF/A) was impregnated with the electrolyte at 333 K under vacuum for 24 hours prior to the assembly of the test cell.

The charge-discharge measurements to control the SOC of the electrode materials were carried out using 2032 coin-type cells and an HJ1001SD8 charge-discharge test device (Hokuto Denko). The $Na_2FeP_2O_7$ electrodes at SOC = 50% and 0% were prepared by fully charging the cells and discharging them to SOC = 50% or 0% at 0.1C (Figure 7-1). The symmetric cells for EIS were prepared using 2032 coin-type cells using the electrodes above (at a specific SOC). The cells were assembled under dry Ar atmosphere in a glove box. The EIS measurements were performed with a VSP potentiostat (Bio-Logic) at 298, 323, 343, and 363 K over a frequency range from 1 mHz or 100 mHz to 100 kHz with an ac amplitude of 10 mV. All the measurements were performed at least 1 h after temperature adjustment in an ESPEC thermostatic chamber. The EIS parameters were fitted using EC-Lab software.

7.3 Results and Discussion

7.3.1 Symmetric Cell EIS and Nyquist Plots

Figure 7-1 shows the Nyquist plots of the Na/IL$_{FSA}$(Na[FSA] = 30 mol%)/$Na_2FeP_2O_7$ and Na/Org/$Na_2FeP_2O_7$ (Org = 1 mol dm^{-3} Na[ClO_4]-PC) half-cells at 298 K after they were fully charged and half-discharged (SOC = 0.5). The charge-discharge curves during the first two cycles are also shown. A semicircle is observed with characteristic frequencies of 398 Hz for Na/Org/$Na_2FeP_2O_7$ and 220 Hz for Na/IL$_{FSA}$(Na[FSA] = 30 mol%)/$Na_2FeP_2O_7$. The semicircle observed in the Nyquist plot of the Na/IL$_{FSA}$(Na[FSA] = 30 mol%)/$Na_2FeP_2O_7$ half-cell is significantly larger than that of the Na/Org/$Na_2FeP_2O_7$ half-cell. This large semicircle originates from the surface film between the Na metal electrode and IL electrolyte, as shown in previous work [9], and as is also confirmed by the symmetric Na metal cells described below.

Figure 7-2 displays the Nyquist plots of symmetric Na metal cells with IL$_{FSA}$ (Na/IL$_{FSA}$/Na) at 298 K to 363 K. As mentioned above, the Na/IL$_{FSA}$/Na cell exhibits a large semicircle. The characteristic frequency of this semicircle varies from 10,000 to 150 Hz, depending on the contents of Na[FSA] and the temperatures. Here, characteristic frequency indicates the corresponding frequency at the peak of semi-circles, which can help the assignment of semi-circles in Nyquist plots. Although this includes a contribution from the surface film observed at high frequencies [9], the charge-transfer resistance may also play a role, and thus, the semicircle may actually consist of two semicircles. The contribution of the surface film is considered to be larger at high temperatures and high content of Na[FSA] because the characteristic frequency increases with increasing temperature and Na[FSA] in Figure 7-2. The EIS of the Na/IL$_{FSA}$/Na cell has a dependency on temperature and Na[FSA]; the semicircle becomes small as the temperature and Na[FSA] in IL$_{FSA}$ increase. In any case, however, this resistance is significantly large and prevents the accurate estimation of the target electrodes in a half-cell configuration. This is the reason why half-cell EIS is not suitable to investigate the charge-transfer mechanism of Na secondary batteries using IL electrolytes; thus, the SCEIS measurements of the cell composed of only the target electrodes are preferable to obtain reliable impedance data [4, 20, 21].

Figure 7-3 displays a schematic drawing of the Nyquist plot for a symmetric cell with two identical positive electrode materials, as discussed below. The plot consists of two semicircles with different characteristic frequencies (high characteristic frequency of 16,000−7,000 Hz and low characteristic frequency of 200−1 Hz. All instances in which a characteristic frequency is not mentioned in the following discussion mean that the frequency is within these frequency ranges. The Nyquist plot was fitted by the equivalent circuit shown as the inset in Figure 7-3. The fitting parameters include R_{bulk}, R_{h} with CPE_{h}, and R_{ct} with CPE_{ct}. The Warburg element was omitted from the equivalent circuit because fitting this element was difficult in some cases, and it also affected the accuracy of R_{h} and R_{ct} in this study. A detailed description of each element is provided in the subsequent paragraphs.

7.3.2 High-Frequency Characteristic of Resistance

Although the semicircle in the high-frequency range is often interpreted as being either the resistance of the SEI [*c.f.* it is often referred to as the cathode-electrolyte interface (CEI) in the case of a positive electrode] or that of the film (surface layer), which is formed during cycles [1, 4, 5, 20, 22, 23], it is not fully understood yet and is often neglected. The semicircle is observed in the Nyquist plot of a symmetric cell (e.g., $Na_2FeP_2O_7/IL_{FSA}/Na_2FeP_2O_7$) even right after assembling the coin cells, indicates that the semicircle does not merely originate from the

SEI or film resistance. Herein, the resistance is named the high-frequency resistance (i.e., R_h as defined above).

Figure 7-4a–d shows the Nyquist plots of the AB/IL_{FSA}(Na[FSA] = 30 mol%)/AB symmetric cell with different PTFE amounts. AB and PTFE are a popular conductive additive and binder, respectively, for electrode fabrication. Because AB and PTFE have high and low electronic conductivities, respectively, the electronic conductivity of the entire composite electrode can be controlled by changing the ratio of AB and PTFE in the electrodes. In this measurement, four different weight ratios of AB and PTFE were used (AB:PTFE = 5:95, 50:50, 95:5, and 100:0 (pure AB pellet) wt%). According to the Nyquist plots in Figure 7-4, the high-frequency region (characteristic frequency: 5,000–1,000 Hz) only contains one semicircle, which is dependent on the temperature and electronic conductivity. An increase in the temperature causes the values of R_{bulk} and R_h to decrease in all measurements. The value of R_h becomes larger as the electronic conductivity in the electrode decreases, and the electrode with 5 wt% AB exhibits very large R_h regardless of the temperature.

Similar results were obtained using the V_2O_5 electrode (see Figure 7-S1 and 7-S2 appendix, for SEM, EDS and XRD results of V_2O_5), which has been studied for use as positive electrode material in Li and Na secondary batteries [24-28]. It should be noted that the V_2O_5 electrode has a certain electronic conductivity (10^{-2}–10^{-4} S cm^{-1} at 292 K, electrical conductivity in a single crystal of V_2O_5) [29].Figure 7-5a and b show the Nyquist plots of the V_2O_5/IL_{FSA}/V_2O_5 symmetric cell with and without AB. The V_2O_5 electrode is in a Na-free state and shows only one semicircle in the high-frequency region corresponding to R_h because R_{ct} is too large to be observed. The semicircle of the V_2O_5 electrode without AB (Figure 7-5b) is significantly larger than that with AB (Figure 7-5a). This suggests that R_h depends on the electronic conductivity of the composite electrode because V_2O_5 has a much smaller electronic conductivity than Al metal (current collector) and AB. The SCEIS results of V_2O_5 with PVDF binder (Figure 7-S7, appendix) are similar to those in Figure 7-5, indicating that the EIS results are essentially independent of the binder.

Figure 7-6 shows the Nyquist plots of the (a) Al/IL_{FSA}/Al, (b) Al_2O_3:PTFE/IL_{FSA}/Al_2O_3:PTFE, and (c) Al_2O_3:PVDF/IL_{FSA}/Al_2O_3:PVDF symmetric cells (here Al is aluminum mesh). These data are required for a comparative study to clarify the effects of the Al current collector. Although the Nyquist plot does not show a clear semicircle, a slight curvy shape appears in the high-frequency region. The curve produced by the aluminum electrode was investigated by obtaining the EIS measurements for the α-Al_2O_3 electrode symmetric cell (α-Al_2O_3/IL_{FSA}(Na[FSA] = 30 mol%)/α-Al_2O_3, where the Al_2O_3 is fixed to the Al current collector) with two different binders, PTFE and PVDF (Figure 7-6b and 7-6c). In the high-frequency region of the Nyquist plots, the Al_2O_3/IL_{FSA}(Na[FSA] = 30 mol%)/Al_2O_3 cell with PTFE exhibits a semicircle whereas Al_2O_3/IL_{FSA}(Na[FSA] = 30 mol%)/Al_2O_3 with PVDF does not. This difference arises from the degree to which the Al surface is covered with a binder; the Al current collector is not fully covered in the Al_2O_3:PTFE composite electrode, whereas it is almost fully covered in the Al_2O_3:PVDF composite electrode. These results indicate that the porous insulating material (in this case there are pores among the Al_2O_3 particles) does not contribute to the semicircle in the high-frequency region and that this porous structure itself is not the origin of R_h.

Nevertheless, the value of R_h depends on x(Na[FSA]) of IL_{FSA}. The Nyquist plots for the $Na_2FeP_2O_7$ electrode symmetric cell ($Na_2FeP_2O_7$/IL_{FSA}/$Na_2FeP_2O_7$) in the high-frequency regions (see Figure 7-8 for the entire Nyquist plot) are shown in Figure 7-S8 and indicate that R_h increases as the amount of Na[FSA] in IL_{FSA} increases. This observation suggests that R_h is also affected by the characteristics of electrolytes.

7.3.3 SOC and Charge-Transfer Resistance

The semicircle in the low-frequency range is ascribed to the charge-transfer resistance, R_{ct}, which is easily influenced by the SOC of each electrode [30, 31]. Considering a normal positive electrode with full Cut-off voltages, R_{ct} is usually very large at SOC = 100% (or above this potential) and is reduced as SOC decreases. This is because the charge-transfer at the electrode-electrolyte interface is accelerated as SOC decreases. For particular SOCs (or a certain SOC) for which small R_{ct} values are observed, R_{ct} reaches a large value at the end of the discharge curve. (For commercial secondary batteries, SOC = 100% is not defined as the fully desodiated (delithiated) state. Here, I define SOC = 100% as meaning the Na-free state (i.e., the fully desodiated state), and SOC = 0% as the fully sodiated state).

Figure 7-7a and 7-7b shows the Nyquist plots of the $Na_2FeP_2O_7$/Na[FSA]-[C_2C_1im][FSA]/$Na_2FeP_2O_7$ symmetric cells at SOC = 0 and 50 %. The size of the semicircles for R_h and R_{ct} is highly dependent on the SOC and dramatically decreases when the SOC changes from 0 to 50%. Although this dependency of the resistance on the SOC is expected from the charge-discharge curves in Figure 7-1, the large R_h at SOC = 0% compared to that at SOC = 50 % suggests that R_h is also related to the SOC of electrode materials. Table 7-1 summarizes the characteristics of R_h, as observed by SCEIS. These results suggest that R_h cannot be explained by a single factor such as the surface film, the resistance between the current collector and electrode materials, and SEI cycles [1, 4, 5, 20, 22, 23], and appears on the EIS as a combination of these complicated factors.

7.3.4 Activation Energy

As mentioned in the Introduction, the rate capability of $Na_2FeP_2O_7$ is considerably improved by intermediate-temperature operating using the Na[FSA]-[C_2C_1im][FSA] and Na[FSA]-[C_3C_1pyrr][FSA] IL electrolytes [13, 15, 18]. The activation energies of R_{ct} and R_h are discussed below in an attempt to develop an improved understanding of this phenomenon.

Figures 7-8a–d shows the Nyquist plots and EIS fitting of the $Na_2FeP_2O_7$/IL_{FSA}/$Na_2FeP_2O_7$ symmetric cells for different contents of Na[FSA] and temperatures (see Figure 7-3 for the equivalent circuit used and Table 7-S1 for the fitting parameters). Figure 7-S8 provides the magnified Nyquist plots for the $Na_2FeP_2O_7$/IL_{FSA}/$Na_2FeP_2O_7$ symmetric cells in Figure 7-8 for improved visualization of R_h. Although both R_{ct} and R_h tend to decrease as the temperature increases and content of Na[FSA] decreases, R_{ct} exhibits higher temperature dependency than R_h, leading to the relatively lower contribution of R_{ct} to the electrode kinetics at elevated temperatures.

The Arrhenius plot and activation energy derived from it provide a more quantitative measure for the kinetics of the electrochemical reaction for different values of Na[FSA] in IL_{FSA} [32-35]. The activation energies of R_{ct} can be calculated by the following equation (Eq. 7) [32, 33].

$$ln(\frac{1}{R}) =-\left(\frac{E_a}{R_g}\right)\left(\frac{1}{T}\right) + \mathrm{In}(A), \qquad (7)$$

where R, R_g, A, and T denote the resistance (R_{ct} or R_h), gas constant, frequency factor, and absolute temperature, respectively. The activation energy, E_a, corresponds to the slope of the linear fitting line multiplied by R_g for each plot.

Figure 7-9 shows the Arrhenius plots of R_h^{-1} and R_{ct}^{-1}. Table 7-2 provides the calculated activation energies for R_h^{-1} and R_{ct}^{-1}. The E_a value for R_h^{-1} is 24.9 kJ mol^{-1} at

Na[FSA] = 20 mol%, and increases as the Na[FSA] fraction increases to 36.1 kJ mol^{-1} at Na[FSA] = 50 mol%. On the other hand, E_a for R_ct^{-1} decreases slightly as the Na[FSA] fraction increases in IL_FSA, and the values of E_ct are 47.3 kJ mol^{-1} and 45.3 kJ mol^{-1} for Na[FSA] fraction = 20 and 50 mol%, respectively. Although the frequency factor of R_h^{-1} is larger than that of R_ct^{-1}, E_a for R_h^{-1} is smaller than that of R_ct^{-1}. Consequently, the contribution of R_h to the rate capability becomes more significant as the temperature increases from 298 to 363 K. Contrary to this, the contribution of R_ct shows the reverse trend in that it is more significant at 298 than at 363 K. These results indicate that the rate capability is highly dependent on R_ct at room temperature, at which R_bulk and R_h are relatively minor factors. As the temperature increases, R_ct rapidly decreases, and all three of these factors (R_bulk, R_h, and R_ct) affect the polarization of the $\mathrm{Na_2FeP_2O_7}$ electrode at intermediate temperatures.

7.4 Conclusions

SCEIS was used to examine positive electrode materials for Na secondary batteries using ILs with the aim of clarifying the factors that contribute to battery performance. In this regard, the use of SCEIS as a measurement technique provides a convenient, fast, and non-destructive method that enables the following information on R_h and R_ct to be obtained. By changing the parameters related to EIS, R_h was found to appear as a combination of the effects of temperature, Na[FSA] fraction, electronic conductivity of the composite electrode, the ionic conductivity of the electrolyte, and SOC. The activation energies of R_h and R_ct, which were obtained by linear fitting of the Arrhenius plots, provided a clear understanding of the temperature dependence of the electrochemical performance of $\mathrm{Na_2FeP_2O_7}$ in ILs. These results indicated that the improvement in the rate capability at elevated temperatures mainly resulted from the decrease in R_{ct}. At intermediate temperatures, R_{bulk}, R_h, and R_{ct} all make a certain contribution to the rate capability.

Although the present study focused on Na secondary batteries with ionic liquid electrolytes, the interpretation of the results obtained here provides useful and comprehensive information for other systems, including those based on other secondary batteries using organic electrolytes or those operating at different temperatures. The results of the EIS analysis presented in this are foreseen to facilitate the future development of new electrode and electrolyte systems.

Table 7-1 Summary of parameters affecting the semicircle in the high-frequency region.

Parameters	Condition	State of semicircle
Temperature	Increase	Size decrease
Amount of AB	Increase	Size decrease
Electrical conductivity of the composite electrode	Increase	Size decrease
Surface area	Increase	Size decrease
Al mesh	Without active material	Small but observed
α-Al_2O_3 on Al mesh with PTFE binder	Partially covered	Small but observed
α- Al_2O_3 on Al mesh with PVDF binder	Almost fully covered	Not observed
x(Na[FSA]) in electrolyte	Increase	Size increase
Electrode SOC	Change[a]	Change[a]

[a]Contribution of SOC is complicated: refer to the text.

Table 7-2 Activation energy obtained from Arrhenius plots based on the EIS fitting parameters for the $Na_2FeP_2O_7$/IL_{FSA}/$Na_2FeP_2O_7$ symmetric cells (see EIS fitted plots in Figure 7-8, EIS parameters in Table 7-S1, and Arrhenius plots in Figure 7-9).

x(Na[FSA]) / %	E_a for R_h / kJ mol^{-1}	E_a for R_{ct} / kJ mol^{-1}
0.2	24.9	47.3
0.3	25.6	46.4
0.4	30.6	46.0
0.5	36.1	45.3

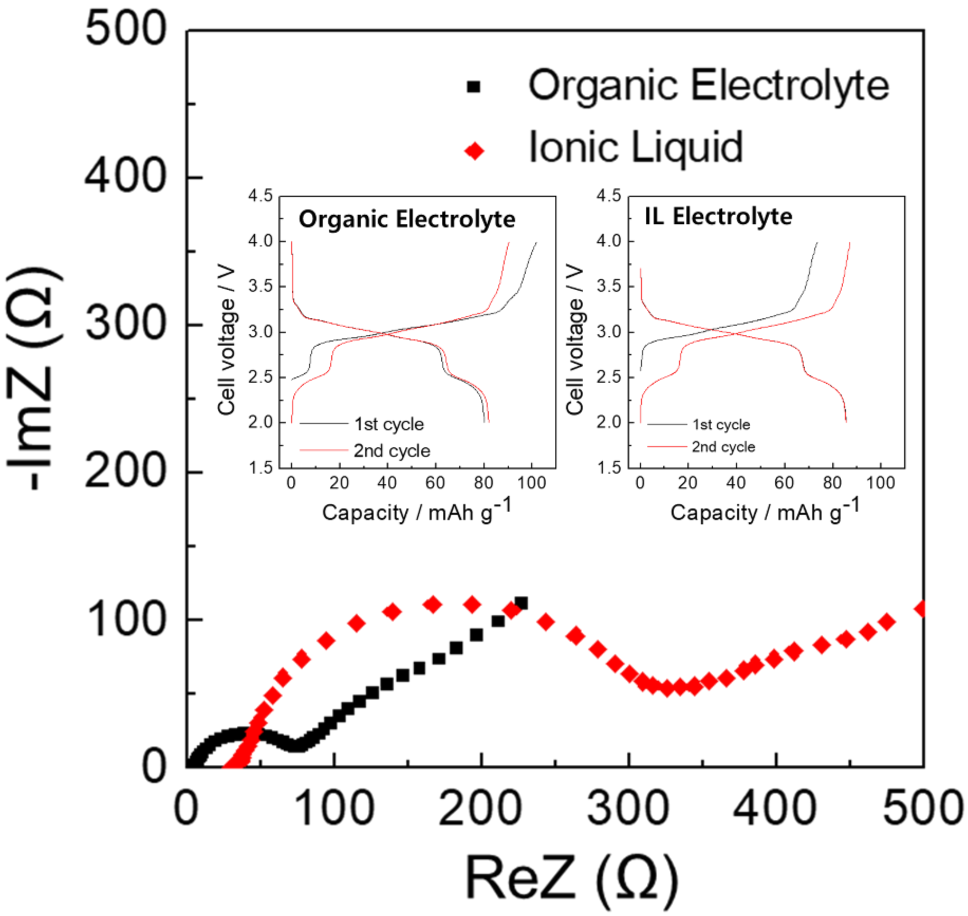

Figure 7-1 Nyquist plots of the Na/IL$_{FSA}$(x(Na[FSA])=0.3)/$Na_2FeP_2O_7$ and Na/Org/$Na_2FeP_2O_7$ half-cell (Inset: charge-discharge curves of $Na_2FeP_2O_7$ during the first two cycles at 0.1 C using the organic and IL electrolytes). Electrolytes: 30 mol% Na[FSA]-[C_2C_1im][FSA] and 1 mol dm^{-3} Na[ClO_4]-PC, temperature: 298 K, SOC = 50%, frequency range: 10 mHz – 100 kHz, ac perturbation: 10 mV.

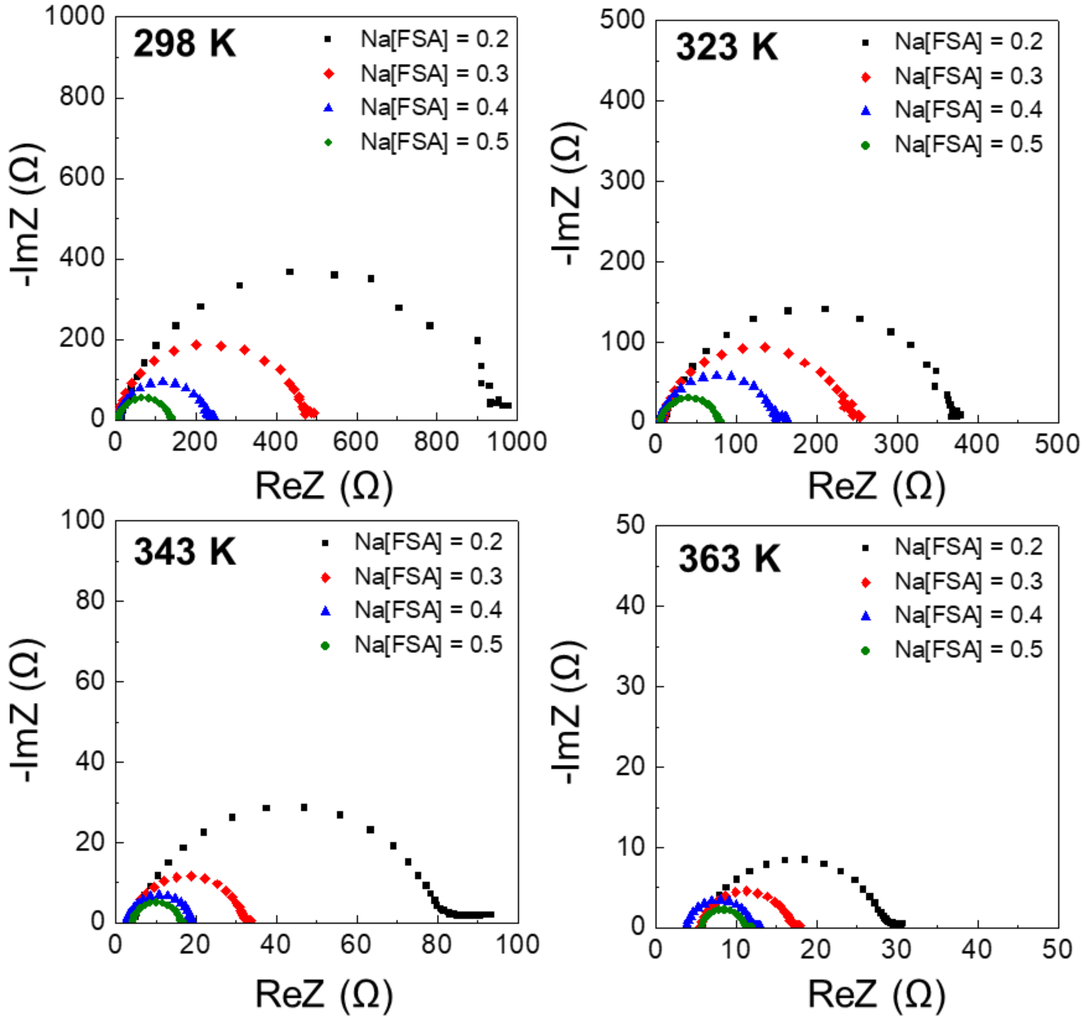

Figure 7-2 Nyquist plots of the Na/IL$_{FSA}$/Na symmetric cells in the temperature range 298–363 K. Electrolyte: Na[FSA]-[C_2C_1im][FSA] (Na[FSA] = 20-50 mol%), ac perturbation: 10 mV, frequency range: 10 mHz–100 kHz. The characteristic frequencies for the semicircles are approximately 500–150 Hz at 298 K, 1,000–350 Hz at 323 K, 5,500–1,500 Hz at 343 K, and 10,000–5,000 Hz at 363 K.

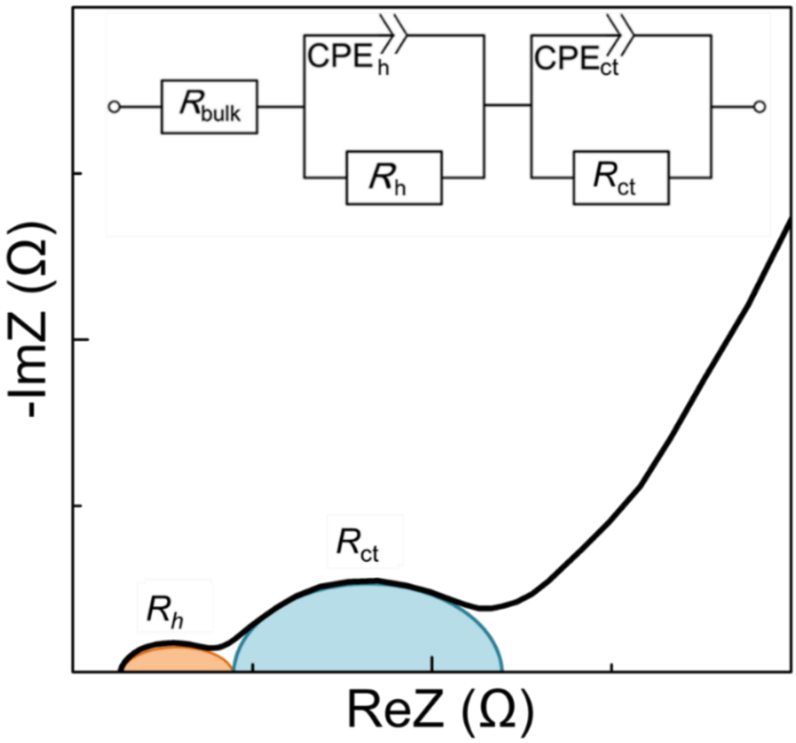

Figure 7-3 Schematic drawing of the Nyquist plot for a symmetric cell with two identical positive electrode materials and the equivalent circuit used for fitting the $Na_2FeP_2O_7$/Na[FSA]-[C_2C_1im][FSA]/$Na_2FeP_2O_7$ symmetric cells. Typical characteristic frequencies: 16,000−7,000 Hz for R_h and 200−1 Hz for R_{ct}. CPE denotes the constant phase element.

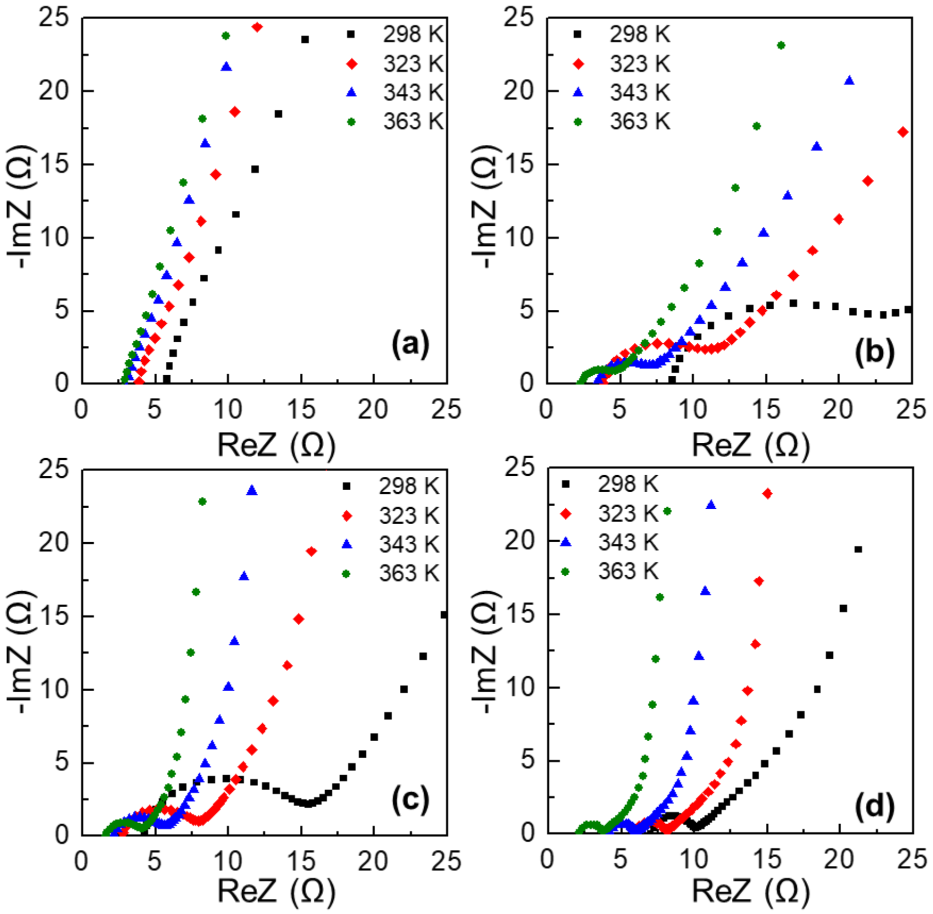

Figure 7-4 Nyquist plots for the AB/IL$_{FSA}$/AB symmetric cells in the temperature range between 298 and 363 K. (a) AB:PTFE = 5:95 wt%, (b) AB:PTFE = 50:50 wt%, (c) AB:PTFE = 95:5 wt%, and (d) pure AB pellets. Electrolyte: 30 mol% Na[FSA]-[C_2C_1im][FSA], ac perturbation: 10 mV, frequency range: 100 mHz–100 kHz.

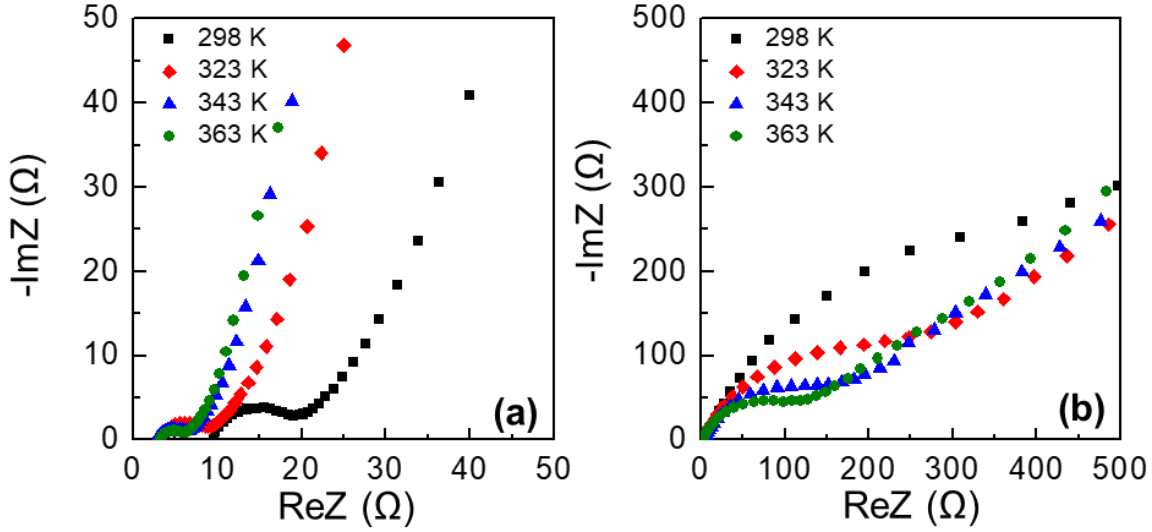

Figure 7-5 Nyquist plots for the V_2O_5/IL$_{FSA}$/V_2O_5 symmetric cells in the temperature range between 298–363 K (a) V_2O_5:AB:PTFE = 75:20:5 wt%, (b) V_2O_5:PTFE = 95:5 wt%. Electrolyte: Na[FSA]-[C_2C_1im][FSA] (x(Na[FSA] = 0.3), ac perturbation: 10 mV, frequency range: 10 mHz–100 kHz. (see Figure S6 in the Supporting Information for plots on a different scale).

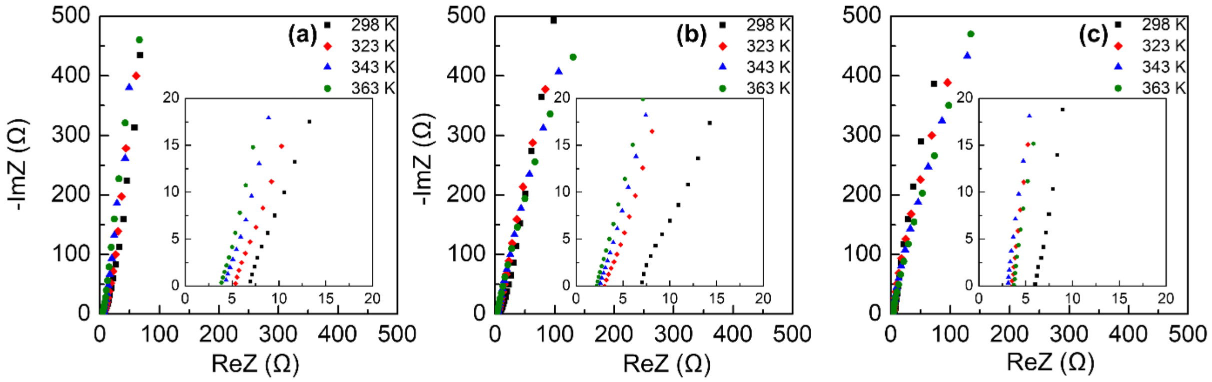

Figure 7-6 Nyquist plots for the (a) Al/IL$_{FSA}$/Al (b) Al_2O_3:PTFE/ILFSA/Al_2O_3:PTFE, and (c) Al_2O_3:PVDF/IL$_{FSA}$/Al_2O_3:PVDF symmetric cells in the temperature range between 298–363 K (the insets show the high-frequency region). Electrolyte: 30 mol% Na[FSA]-[C_2C_1im][FSA], ac perturbation: 10 mV, frequency range: 100 mHz–100 kHz.

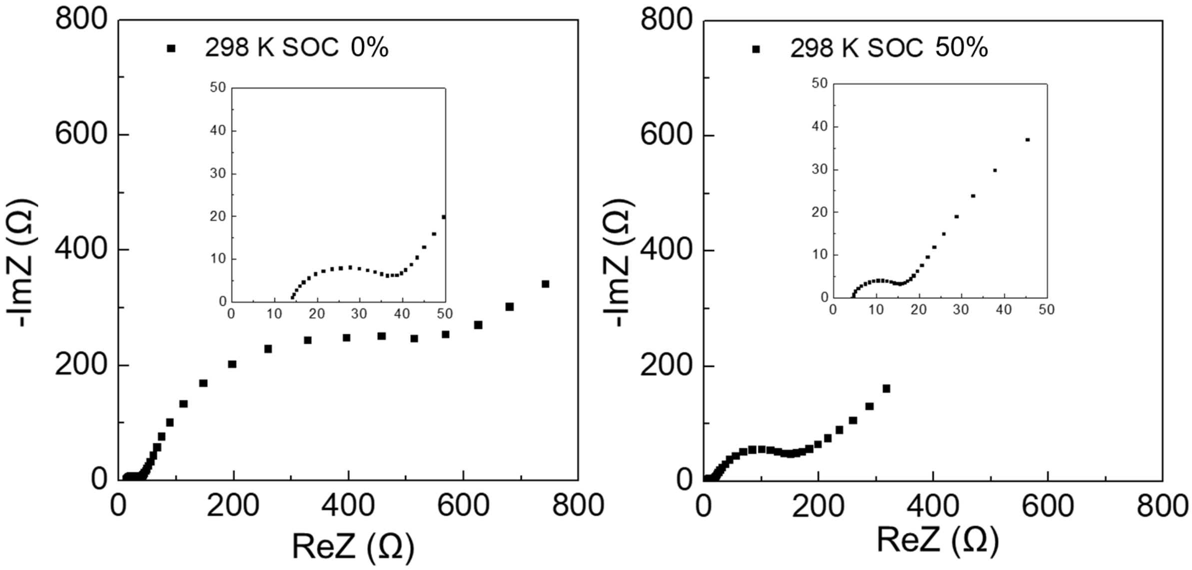

Figure 7-7 Comparative Nyquist plots of the $Na_2FeP_2O_7$/IL_{FSA}(x(Na[FSA]=0.3)/$Na_2FeP_2O_7$ symmetric cells at 298 K at (a) SOC = 0% and (b) SOC = 50%. The insets show the magnified plots at high frequencies. Electrolyte: 30 mol% Na[FSA]-[C_2C_1im][FSA], ac perturbation: 10 mV and frequency range: 10 mHz–100 kHz.

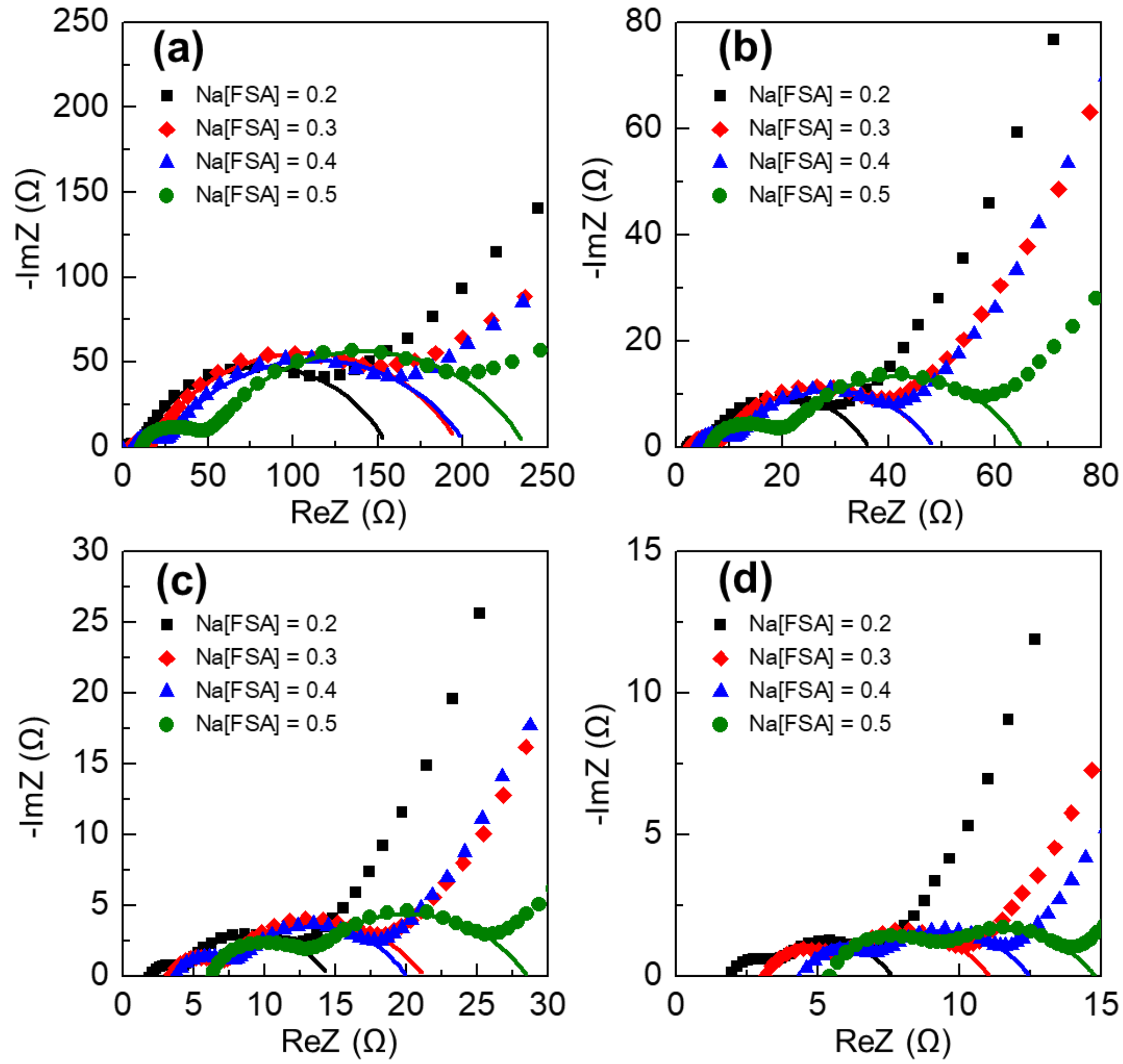

Figure 7-8 Nyquist plots and EIS fitting for the $Na_2FeP_2O_7$/IL_{FSA}/$Na_2FeP_2O_7$ symmetric cells at (a) 298 K, (b) 323 K, (c) 343 K, and (d) 363 K. Electrolyte: Na[FSA]-[C_2C_1im][FSA] (Na[FSA] = 20-50%), SOC = 50 %, ac perturbation: 10 mV, frequency range: 10 mHz–100 kHz (see Figure 7-S6, appendix, for plots at a different scale and see Figure 7-2 for the equivalent circuit, and Table 7-S1 for the EIS fitted parameters).

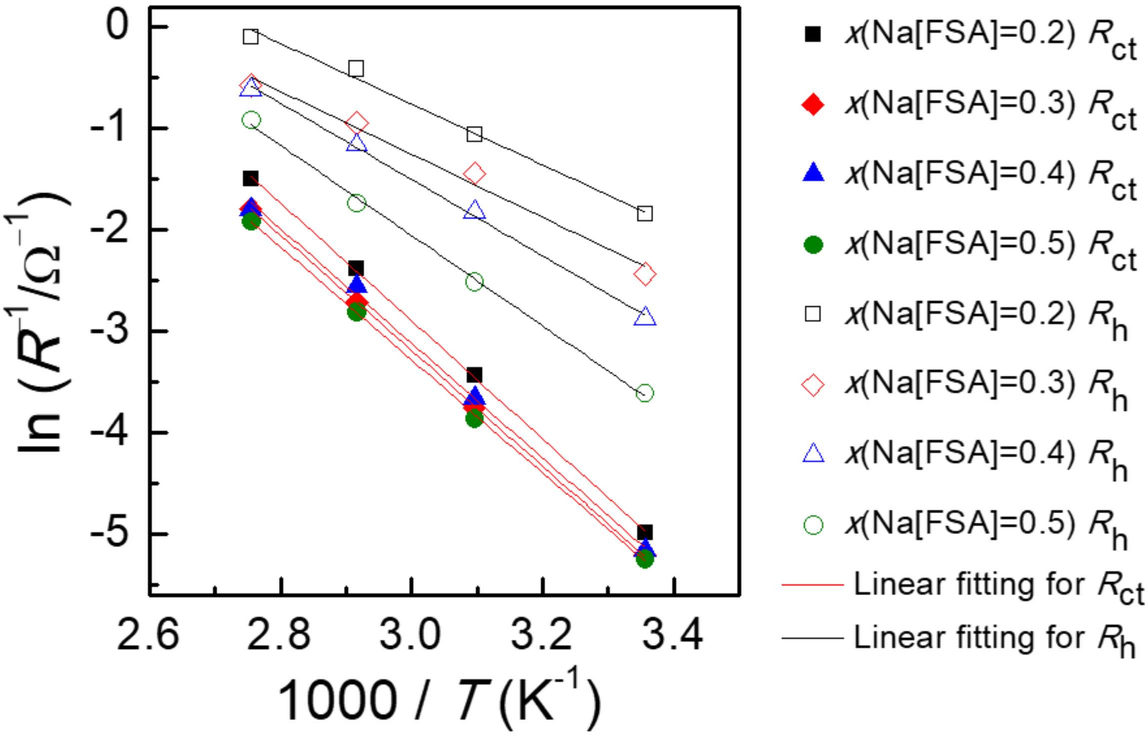

Figure 7-9 Arrhenius plots of R_h^{-1} and R_{ct}^{-1} using the EIS fitted parameters of the $Na_2FeP_2O_7$/IL_{FSA}/$Na_2FeP_2O_7$ symmetric cell.

References

[1] D. Andre, M. Meiler, K. Steiner, C. Wimmer, T. Soczka-Guth, and D. U. Sauer, J. Power Sources, 196 (2011) 5334.

[2] B.-Y. Chang, and S.-M. Park, Annu. Rev. Anal. Chem., 3 (2010) 207.

[3] J. Guo, A. Sun, X. Chen, C. Wang, and A. Manivannan, Electrochim. Acta, 56 (2011) 3981.

[4] F. Wohde, M. Balabajew, and B. Roling, J. Electrochem. Soc., 163 (2016) A714.

[5] P. Lu, C. Li, E. W. Schneider, and S. J. Harris, J. Phys. Chem. C, 118 (2014) 896.

[6] S.-M. Park, and J.-S. Yoo, Anal. Chem., 75 (2003) 455 A.

[7] M. G. S. R. Thomas, P. G. Bruce, and J. B. Goodenough, J. Electrochem. Soc., 132 (1985) 1521.

[8] S.-U. Woo, B.-C. Park, C. S. Yoon, S.-T. Myung, J. Prakash, and Y.-K. Sun, J. Electrochem. Soc., 154 (2007) A649.

[9] T. Hosokawa, K. Matsumoto, T. Nohira, R. Hagiwara, A. Fukunaga, S. Sakai, and K. Nitta, J. Phys. Chem. C, 120 (2016) 9628.

[10] C.-H. Wang, C.-H. Yang, and J.-K. Chang, Chem. Commun., 52 (2016) 10890.

[11] H. Kim, R. A. Shakoor, C. Park, S. Y. Lim, J.-S. Kim, Y. N. Jo, W. Cho, K. Miyasaka, R. Kahraman, Y. Jung, and J. W. Choi, Adv. Funct. Mater., 23 (2013) 1147.

[12] P. Barpanda, G. Liu, C. D. Ling, M. Tamaru, M. Avdeev, S.-C. Chung, Y. Yamada, and A. Yamada, Chem. Mater., 25 (2013) 3480.

[13] C.-Y. Chen, T. Kiko, T. Hosokawa, K. Matsumoto, T. Nohira, and R. Hagiwara, J. Power Sources, 332 (2016) 51.

[14] T. Honma, T. Togashi, N. Ito, and T. Komatsu, Fabrication of Na2FeP2O7 Glass-Ceramics for Sodium Ion Battery, p. 344 (2012).

[15] K. Matsumoto, T. Hosokawa, T. Nohira, R. Hagiwara, A. Fukunaga, K. Numata, E. Itani, S. Sakai, K. Nitta, and S. Inazawa, J. Power Sources, 265 (2014) 36.

[16] T. Yamamoto, T. Nohira, R. Hagiwara, A. Fukunaga, S. Sakai, and K. Nitta, Electrochim. Acta, 211 (2016) 234.

[17] J. Hwang, K. Matsumoto, Y. Orikasa, M. Katayama, Y. Inada, T. Nohira, and R. Hagiwara, J. Power Sources, 377 (2018) 80.

[18] C. Ding, T. Nohira, R. Hagiwara, K. Matsumoto, Y. Okamoto, A. Fukunaga, S. Sakai, K. Nitta, and S. Inazawa, J. Power Sources, 269 (2014) 124.

[19] C.-Y. Chen, K. Matsumoto, T. Nohira, C. Ding, T. Yamamoto, and R. Hagiwara, Electrochim. Acta, 133 (2014) 583.

[20] C. H. Chen, J. Liu, and K. Amine, J. Power Sources, 96 (2001) 321.

[21] N. Ogihara, S. Kawauchi, C. Okuda, Y. Itou, Y. Takeuchi, and Y. Ukyo, J. Electrochem. Soc., 159 (2012) A1034.

[22] R. Alcántara, M. Jaraba, P. Lavela, and J. L. Tirado, J. Electroanal. Chem., 566 (2004) 187.

[23] F. Croce, F. Nobili, A. Deptula, W. Lada, R. Tossici, A. D’Epifanio, B. Scrosati, and R. Marassi, Electrochem. Commun., 1 (1999) 605.

[24] V. Raju, J. Rains, C. Gates, W. Luo, X. Wang, W. F. Stickle, G. D. Stucky, and X. Ji, Nano Lett., 14 (2014) 4119.

[25] A.-M. Cao, J.-S. Hu, H.-P. Liang, and L.-J. Wan, Angew. Chem. Int. Ed., 44 (2005) 4391.

[26] H.-Y. Li, C.-H. Yang, C.-M. Tseng, S.-W. Lee, C.-C. Yang, T.-Y. Wu, and J.-K. Chang, J. Power Sources, 285 (2015) 418.

[27] J. Shao, X. Li, Z. Wan, L. Zhang, Y. Ding, L. Zhang, Q. Qu, and H. Zheng, ACS Appl. Mater. Interfaces, 5 (2013) 7671.

[28] X. Li, C. Liu, C. Zhang, H. Fu, X. Nan, W. Ma, Z. Li, K. Wang, H. Wu, and G. Cao, ACS Appl. Mater. Interfaces, 8 (2016) 24629.

[29] J. Bullot, O. Gallais, M. Gauthier, and J. Livage, Appl. Phys. Lett., 36 (1980) 986.

[30] C. Fleischer, W. Waag, H.-M. Heyn, and D. U. Sauer, J. Power Sources, 260 (2014) 276.

[31] J. Gomez, R. Nelson, E. E. Kalu, M. H. Weatherspoon, and J. P. Zheng, J. Power Sources, 196 (2011) 4826.

[32] T. Abe, F. Sagane, M. Ohtsuka, Y. Iriyama, and Z. Ogumi, J. Electrochem. Soc., 152 (2005) A2151.

[33] F. Sagane, T. Abe, Y. Iriyama, and Z. Ogumi, J. Power Sources, 146 (2005) 749.

[34] H. Ma, S. Zhang, W. Ji, Z. Tao, and J. Chen, J. Am. Chem. Soc., 130 (2008) 5361.

[35] H. Gao, Z. Hu, K. Zhang, F. Cheng, and J. Chen, Chem. Commun., 49 (2013) 3040.

Appendix

Table 7-S1 EIS fitting parameters, R_{bulk}, R_{h}, R_{ct}, Q_{h}, *and* Q_{ct}.

Na[FSA] / mol%	T /K	Resistance / Ω			CPE / F cm^2 s$^{(a-1)}$			
		R_{bulk}	R_{h}	R_{ct}	Q_{h}	a	Q_{ct}	a
20	298	2.91	6.34	146.0	$3.80\text{x}10^{-5}$	0.73	$1.67\text{x}10^{-3}$	0.73
	323	2.39	2.87	30.97	$1.31\text{x}10^{-5}$	0.87	$2.43\text{x}10^{-3}$	0.68
	343	2.18	1.52	10.84	$4.58\text{x}10^{-6}$	0.99	$3.50\text{x}10^{-3}$	0.63
	363	2.04	1.09	4.48	$6.47\text{x}10^{-6}$	0.99	$3.47\text{x}10^{-3}$	0.62
30	298	4.56	11.41	182.0	$1.34\text{x}10^{-5}$	0.79	$4.43\text{x}10^{-3}$	0.69
	323	2.98	4.24	42.95	$1.80\text{x}10^{-6}$	0.99	$2.58\text{x}10^{-3}$	0.61
	343	3.65	2.58	15.02	$2.71\text{x}10^{-6}$	0.99	$2.94\text{x}10^{-3}$	0.60
	363	3.32	1.78	5.96	$3.70\text{x}10^{-6}$	0.99	$2.89\text{x}10^{-3}$	0.61
40	298	6.12	17.66	174.4	$1.54\text{x}10^{-5}$	0.75	$1.43\text{x}10^{-3}$	0.68
	323	3.82	6.198	38.53	$6.84\text{x}10^{-6}$	0.87	$2.16\text{x}10^{-3}$	0.64
	343	3.95	3.20	13.85	$7.31\text{x}10^{-6}$	0.363	$2.54\text{x}10^{-3}$	0.63
	363	4.61	1.80	6.06	$3.81\text{x}10^{-6}$	0.99	$1.80\text{x}10^{-3}$	0.61
50	298	10.43	36.89	189.5	$1.86\text{x}10^{-5}$	0.71	$1.09\text{x}10^{-3}$	0.51
	323	6.49	12.33	47.16	$1.28\text{x}10^{-5}$	0.79	$1.58\text{x}10^{-3}$	0.66
	343	6.39	5.66	16.48	$7.31\text{x}10^{-6}$	0.87	$2.10\text{x}10^{-3}$	0.62
	363	5.63	2.50	6.77	$3.03\text{x}10^{-6}$	0.96	$2.63\text{x}10^{-3}$	0.57

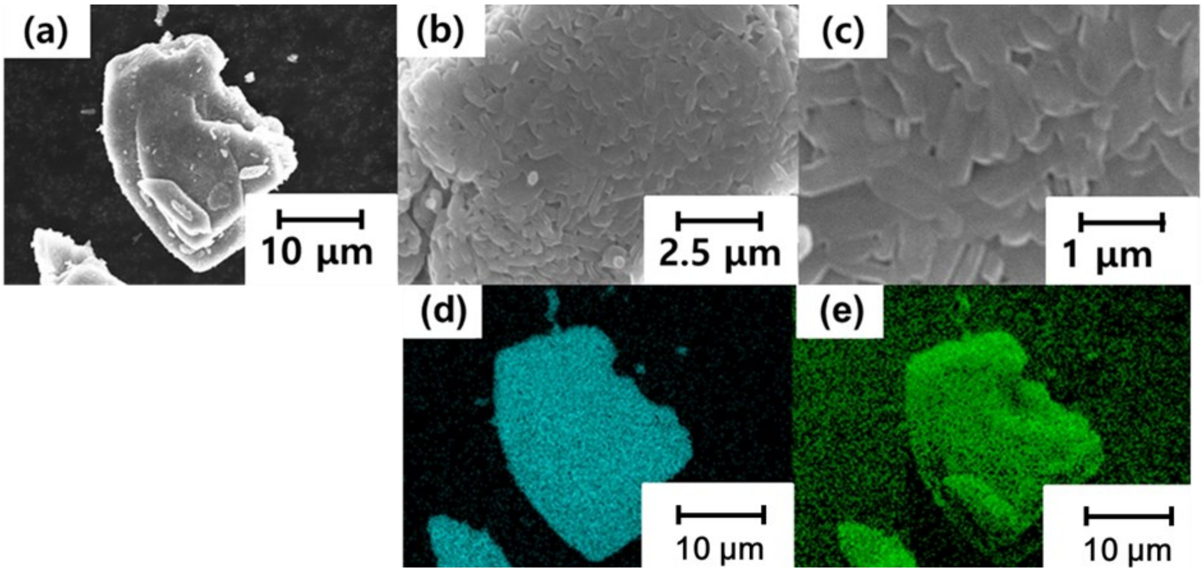

Figure 7-S1 (a-c) SEM images at different magnifications and EDS mapping of (d) vanadium and (f) oxygen for V_2O_5 used in this study.

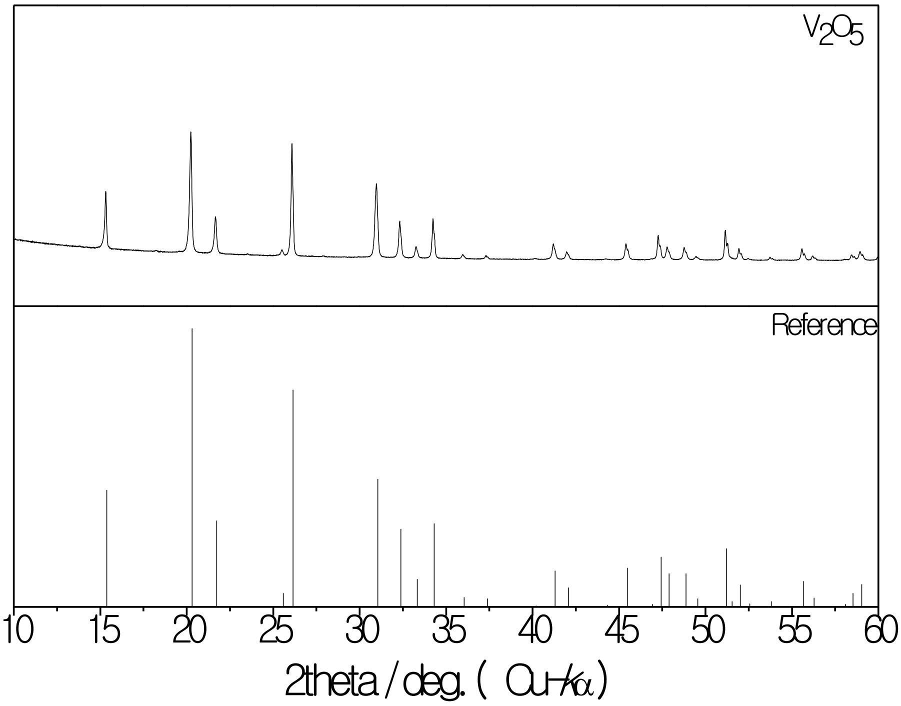

Figure 7-S2 XRD patterns of V_2O_5.

Brief comments: The V_2O_5 is indexed as an orthorhombic crystal system with space group *Pmmn* via reference.

[Reference] R. Enjalbert, J. Galy, *Acta Crystallogr. C* 42 (1986) 1467.

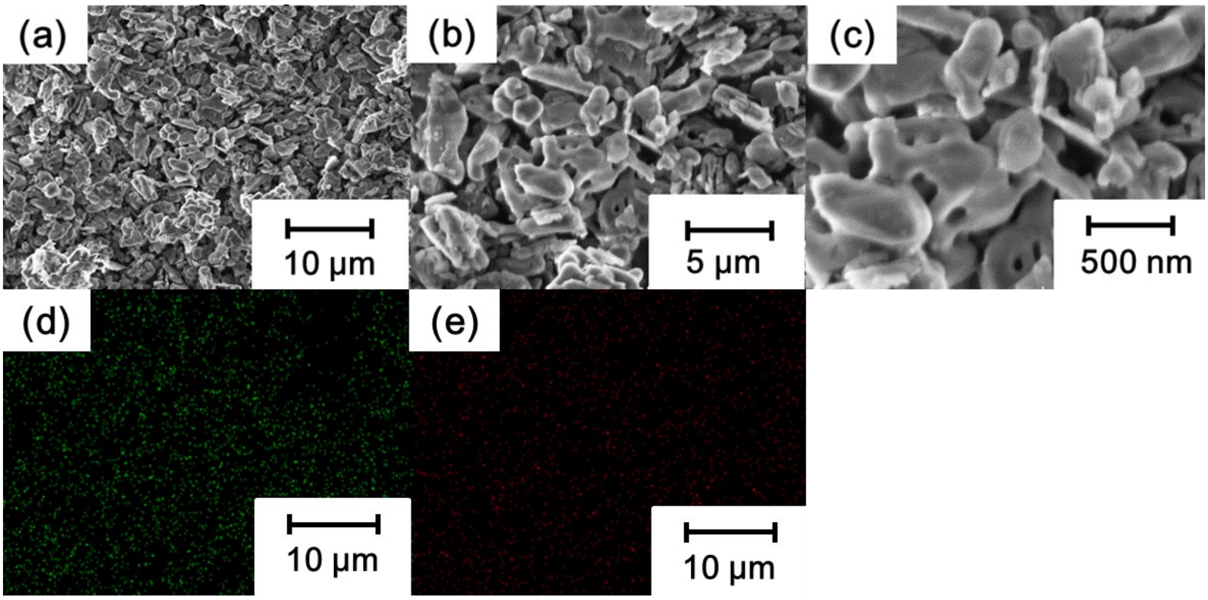

Figure 7-S3 (a-c) SEM images at different magnifications and EDS mapping of (d) oxygen and (f) aluminum for α-Al_2O_3 used in this study.

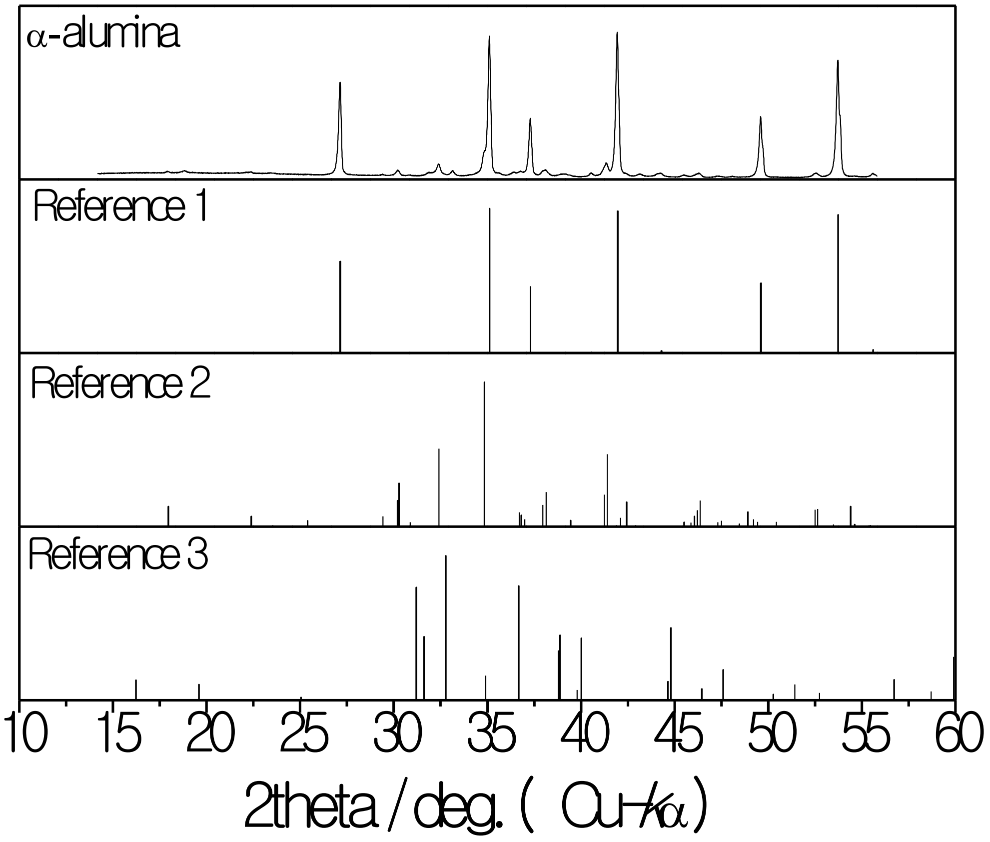

Figure 7-S4 XRD patterns of α-Al_2O_3.

Brief comments: The α-Al_2O_3 is indexed as a trigonal crystal system with space group $R\bar{3}c$. There are a small number of impurities of κ-Al_2O_3 (Orthorhombic, space group $Pna2_1$) and θ-Al_2O_3 (Monoclinic, space group $C2$/m).

[Reference 1, α-Al_2O_3] L. Lutterotti, P. Scardi, *J. Appl. Crystallogr.* **23** (1990) 246.

[Reference 2, κ-Al_2O_3] L. smrcok, V. Langer, M. Halavarsson, S. Ruppi, *Z. Kristallogr.* **216** (2001) 409.

[Reference 3, θ-Al_2O_3] E. Husson, Y. Repelin, *Eur. J. Solid State Inorg. Chem.* **33** (1996) 1223.

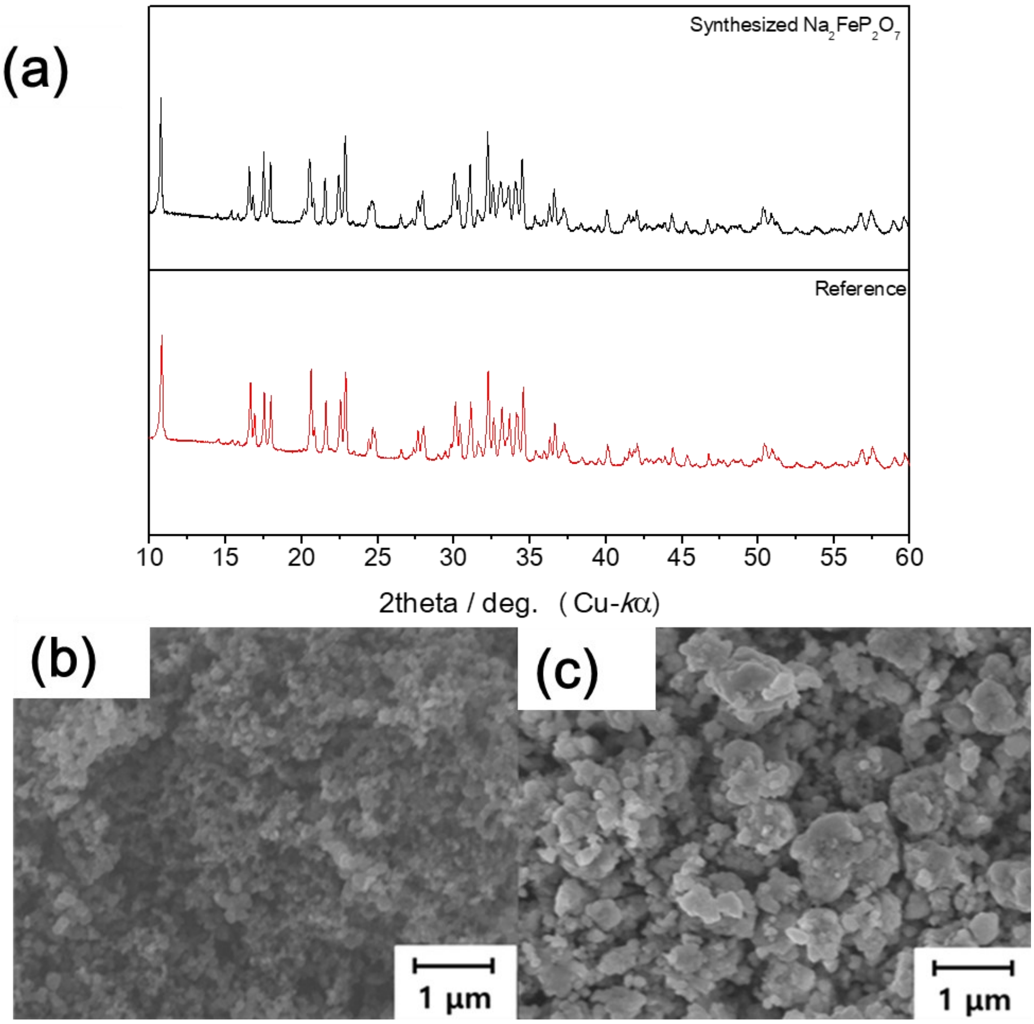

Figure 7-S5 (a) XRD patterns of $Na_2FeP_2O_7$, and SEM images of electrodes (b) AB:PTFE, and (c) $Na_2FeP_2O_7$:AB:PTFE.

Brief comments: The $Na_2FeP_2O_7$ is indexed as a triclinic crystal system with space group *P*-1, and patterns are consistent with the reference. The homogenous particle size of AB is confirmed in (b. The active material of $Na_2FeP_2O_7$ is evenly surrounded by AB with PTFE binder in (c).

[Reference] C.-Y. Chen, K. Matsumoto, T. Nohira, C. Ding, T. Yamamoto, and R. Hagiwara, *Electrochim. Acta* 133 (2014) 583.

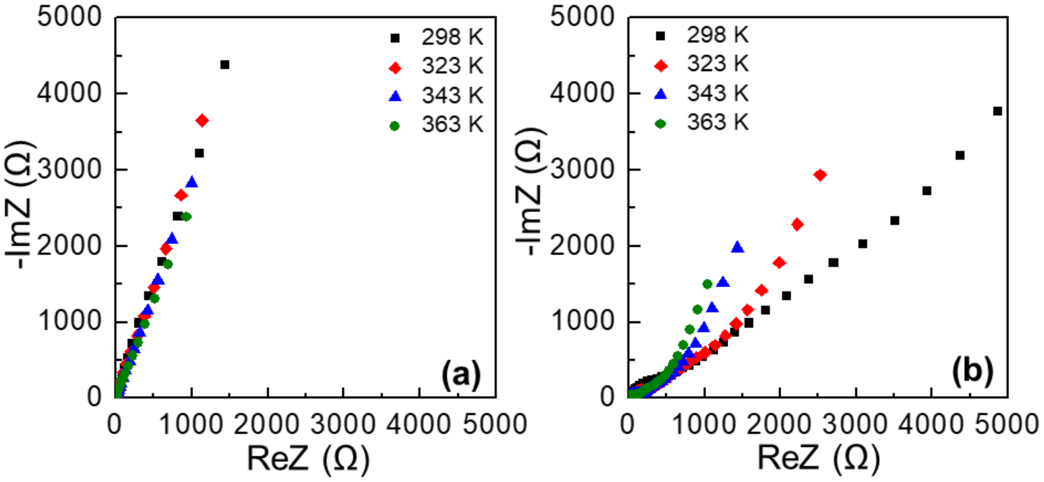

Figure 7-S6 Nyquist plots for the V_2O_5/IL$_{FSA}$/V_2O_5 symmetric cells in the temperature range between 298–363 K. (a) V_2O_5:AB:PTFE = 75:20:5 wt% and (b) V_2O_5:PTFE = 95:5 wt%. Electrolyte: 30 mol% Na[FSA]-[C_2C_1im][FSA], ac perturbation: 10 mV, frequency range: 10 mHz–100 kHz.

Brief comments: V_2O_5 (particle size: ~1μm) was selected as an electrode material at SOC 100% with a certain electronic conductivity. This is because, realistically, the fully desodiated state (SOC 100%) is difficult to establish from the electrode by starting from the discharged state (a very long constant current-constant voltage (CCCV) mode is required to extract Na^+ from the electrode). The seemingly large R_{ct} value supports the above-mentioned statement that, at SOC 100%, the Na^+ charge-transfer process does not occur.

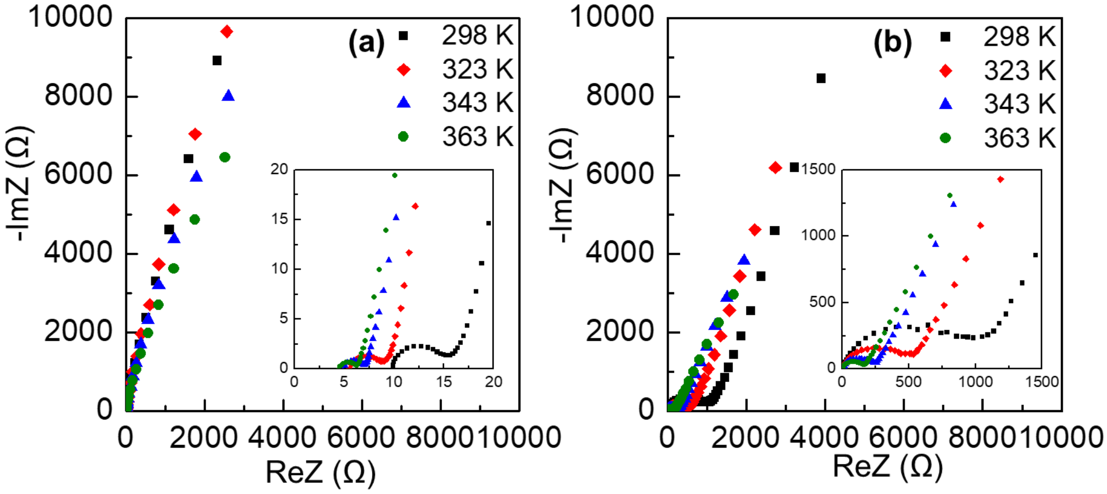

Figure 7-S7 Nyquist plots for the V_2O_5/IL$_{FSA}$/V_2O_5 symmetric cells in the temperature range between 298–363 K for t(a) V_2O_5:AB:PVDF = 75:20:5 wt% and (b) V_2O_5:PVDF = 95:5 wt% and (inset) magnified plots. Electrolyte: 30 mol% Na[FSA]-[C_2C_1im][FSA], ac perturbation: 10 mV, frequency range: 10 mHz–100 kHz.

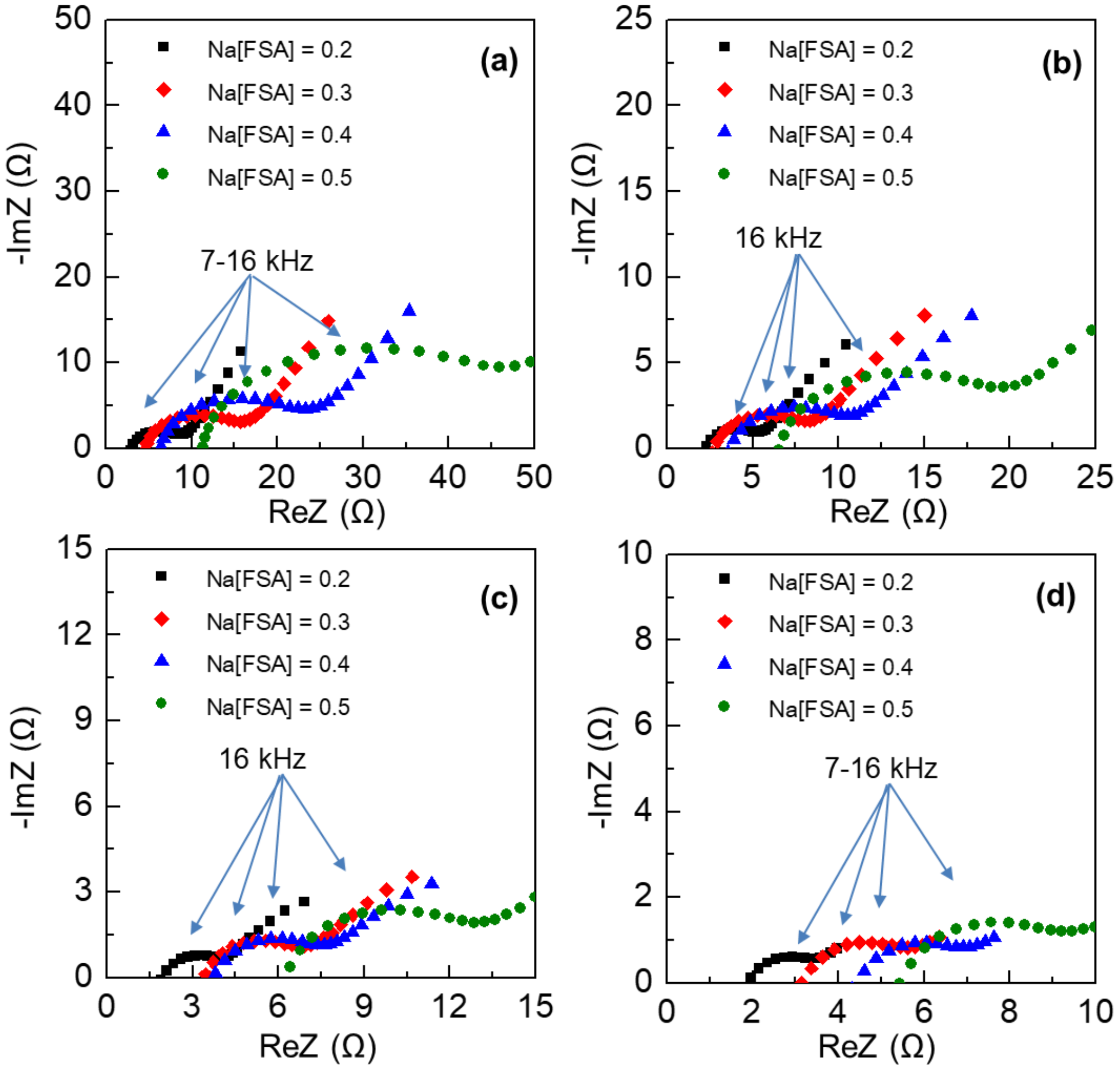

Figure 7-S8 Nyquist plots for the $Na_2FeP_2O_7$/IL_{FSA}/$Na_2FeP_2O_7$ symmetric cells at (a) 298 K, (b) 323 K, (c) 343 K, and (d) 363 K at different scales. Electrolyte: Na[FSA]-[C_2C_1im][FSA], ac perturbation: 10 mV, frequency range: 10 mHz–100 kHz.

Chapter 8

Dendrite Suppression and Improved Performance of Li Metal Negative Electrode

8.1 Introduction

There have been many attempts to use Li metal as a negative electrode in batteries based on its tenfold higher charged-state capacity than graphite (3860 vs. 340 mAh g^{-1}) [1-4]. However, Li metal has practical drawbacks because Li metal electrodes function on the basis of metal deposition/dissolution rather than ion-intercalation. Li dendrites formed in this process are converted into a dead Li layer, which limits performance by the continuous consumption of electrolyte, which leads to low Coulombic efficiency (CE), and a volumetric change causes severe safety risks due to short-circuiting [4-6]. Consequently, a graphite negative electrode is occupying the majority of the market of Li-ion batteries [3, 7]. However, the use of Li metal can meet the high energy density demands of industry and society and contributes significant advantages to conventional Li-based batteries including Li-air and Li-sulfur batteries [8-10].

Extensive studies of Li metal electrodes have been conducted to overcome the problem of dendrite formation and to increase cycling performance. Electrolytes play a crucial role in the negative electrode function by forming a stable solid electrolyte interphase (SEI) layer. Li salts including $LiClO_4$, $LiPF_6$, $LiAsF_6$, and Li[FSA] dissolved in organic solvents such as ethylene carbonate (EC), dimethyl carbonate (DMC), diethyl carbonate (DEC), 1,2-dimethoxyethane (DME), and vinyl carbonate (VC) (sometimes with additives present) have been tested to find the best conditions for creating a stable SEI layer on Li electrode surfaces

[11-15]. However, the organic electrolytes currently used in Li-ion batteries are not an optimum choice when used in conjunction with Li metal electrodes [16-18]. Dendrite formation in highly volatile and flammable organic electrolytes is not desirable from the standpoint of safety.

Artificial SEI layer formation and Li surface modification also have been pursued as a means of inhibiting dendrite growth and suppressing volumetric changes [19-21]. Recent reports indicate that ionic liquid electrolytes form an electrochemically stable SEI layer and suppress Li dendrite formation [16, 22-25].

This study reports on the suppression and mechanism of Li metal dendrite formation utilizing a nonflammable and electrochemically and thermally stable ionic liquid electrolyte of 30 mol% Li[FSA]-[C_2C_1im][FSA] (hereafter abbreviated as IL) [26]. A conventional organic carbonate electrolyte of 1 mol dm^{-3} Li[PF_6]-EC/DMC (1:1 vol/vol) (hereafter abbreviated as OE), was selected for comparison and addressed the safety and efficiency aspects of Li metal battery operation from 25 to 90 °C. Because Li metal battery operation at intermediate temperatures is more challenging than that of Li-ion batteries as safety concerns and could mean that safe operation at room temperature is guaranteed. Furthermore, a high rate capability can be achieved via enhanced electrode reaction and ion diffusion at elevated temperatures where can be a ubiquitous presence of waste heat in our daily lives and industries.

8.2 Experimental

General Procedures and reagents

The FSA salts, Li[FSA] (Kishida Chemical, water content < 20 ppm, purity > 99%) and [C_2C_1im][FSA] (Kanto Chemical, water content < 30 ppm, purity > 99%), were dried under vacuum at 90 °C for 24 h prior to use. The IL electrolyte was prepared by mixing these two salts at 30 mol% Li[FSA] [27]. The typical water content of the IL system was below 30 ppm, according to Karl–Fischer titration measurements (899 Coulometer, Metrohm).

Li_2CO_3 (Wako Pure Chemical Industries, > 99.0% purity), $FeC_2O_4 \cdot 2H_2O$ (Sigma–Aldrich, > 99% purity), and $(NH_4)_2HPO_4$ (Wako Pure Chemical Industries, > 99.0% purity) were used to prepared precursors of $Li_2FeP_2O_7$. The organic electrolyte of 1mol dm^{-3} of $Li[PF_6]$-EC/DMC (1:1 vol/vol; Kishida Chemical Co., Ltd.,), was used as supplied

Characterizations

Li metal surface was observed and analyzed by SEM, EDS, and XPS after Li deposition/dissolution tests in Figure 8-S3. The Li metal electrodes were washed with dimethyl carbonate (DMC) and dried at 60 °C under vacuum. SEM (Hitachi SU-8020, 1-15 kV), and EDS mapping was performed using an analyzer (Horiba EMAXEvolution X-max, 15 kV) attached to the SEM. SEI layer components were analyzed using XPS (JEOL, JPS-9010, Mg *K*α source). Depth profiles of Li metal electrodes were obtained by a combination with the Ar-ion etching apparatus. The accelerating voltage and current of Ar-etching were fixed at 800 V and 19.0 mA, respectively.

Electrochemical Measurements

Electrochemical properties of Li/Li symmetric cells were measured with a Bio-Logic VSP potentiostat or a charge-discharge unit (HJ1001SD8, Hokuto Denko Corp.) using glass beaker cells or 2032 coin-type cells assembled in an Ar-filled glove box. The beaker cell was prepared, as depicted in Figure 8-S1. The beaker cells were used for the observation of Li dendrite formation during cycles at 25 °C. 10 mm × 5 mm Li metal pressed on to Cu mesh current collector was used for the symmetric electrodes. The Li metal was immersed in electrolytes with a depth of 5mm (A Li metal electrode dissolution/deposition area = 5 mm × 5 mm × 2). The 2032-type coin cells were used for the prolonged cycle tests at 25- 90 °C. 13 mm Li metal discs (Sigma–Aldrich, > 99.9% purity) pressed onto Cu disk current collectors were used for the symmetric electrodes.

8.3 Results and Discussion

Symmetric Li/Li cells were prepared in a glass beaker cell (Figure 8-S1) to observe the formation of Li dendrites and the accumulation of dead Li as electrodes degraded and electrolyte consumed during the cycling test. Li metal was deposited and dissolved at two Li metal electrodes at 8.0 mA cm^{-2} for 210 min (8 min per cycle) (Figure 8-1a). Photos selected from a video recording of the cycling test show that the OE and IL cells exhibit completely different Li deposition/dissolution behaviors throughout the test (Figure 8-1a).

The OE cell shows uneven Li metal deposition at an early stage and the continual growth of Li dendrites and accumulation of dead Li, which hindered Li^+ diffusion and ultimately caused a short circuit (Figure 8-1). The overpotential of the OE cell continuously increases during cycling, owing to dead Li accumulation (Figure 8-S2a). The IL cell exhibits very stable cycling behavior and uniform Li metal deposition. Although Li nucleation is confirmed in the early stage, the increase of the amount of the deposited Li metal on the electrode in the IL cell is not visible, and the dendrite formation is suppressed at a minimum level without dead Li layer (Figure 8-1). This result accords with the invariant overpotential (Figure 8-S2b) and indicates the IL could suppress the formation of Li dendrites with uniform Li deposition and stable SEI formation [28].

Further evaluation was performed by long-term deposition/dissolution test using symmetric Li/Li cells in coin-cell configuration at current densities of 1.0 and 5.0 mA cm^{-2} for OE at 25 °C and IL at 25 and 90 °C in Figure 8-S3. The OE cell response is stable for only a limited number of cycles. The overpotential begins to increase after 25 h and reached 0.2 V after 246 h at 1.0 mA cm^{-2} and increases after only 18 min and reaches 0.3 V after 50 h at 5.0 mA cm^{-2} (Figures 8-S3a and 8-S3d). The increases in overpotential indicate severe decomposition of the electrolyte, the continual formation of Li dendrites, and dead Li accumulation in the OE cell [29]. On the other hand, the IL cells at 25 and 90 °C exhibit stable cycling performance (Figures 8-S3b, 8-S3c, 8-S3e and 8-S3f). The large overpotential during the early cycles in the IL cell at 25°C should originate from SEI formation, poor contact between the electrode and electrolyte, or kinetic limitations in the cell as previously reported [30, 31]. The profiles of the IL cell are stabilized after the 50th cycle at 25 °C and exhibit a constant overpotential of 12 mV that did not increase for 1000 h (2500 cycles) at 1.0 mA cm^{-2} (Figure 8-S3b). The overpotential becomes smaller (3 mV) at 90 °C at 1.0 mA cm^{-2} (Figure 8-S3c), which is consistent with enhanced ion diffusion in the electrolyte and more effective charge transfer at the IL/Li interface with increasing temperature. IL cells exhibited stable performance at a higher current density of 5.0 mA cm^{-2}. The overpotential of 42 mV is maintained until 1400 h and starts to gradually increase and reaches 84 mV after 2200 h at 25 °C in Figure 8-S3e. The overpotential of 16 mV is reserved until 2000 h at 90 °C in Figure 8-S3f.

The cycle efficiency ($\varepsilon_{\mathrm{cycle}}$) during Li deposition/dissolution is shown in Figure 8-S4 (See for the method of evaluating $\varepsilon_{\mathrm{cycle}}$). The value of $\varepsilon_{\mathrm{cycle}}$ is obtained to 71% in OE at 25 °C. The value increases to 92% in IL at 25 °C because IL could facilitate smooth Li deposition/dissolution, as shown in Figure 8-1, but elevating temperature triggers the consumption of Li during the cycle and shows $\varepsilon_{\mathrm{cycle}}$ value of 72%.

Electrical impedance spectroscopy (EIS) upon cycle tests are shown in Figure 8-2. The Nyquist plots of the Li/Li symmetric cells exhibit two semicircles. (See Table 8-S1 for the EIS parameters). The two semicircles are distinct at 25 °C, whereas they partially overlap each other without a definite border at 90 °C. A semicircle with the characteristic frequency range of 200 to 10 kHz corresponds to the high-frequency resistance (R_{h}) that is characteristic of the chemical or electrochemical formation of a passivation film. Semicircles at 200 to 1 Hz are characteristic of the charge transfer resistance (R_{ct}) [32, 33]. The EIS results and voltage profiles indicate that passivation films are formed on Li metal electrodes just after the electrode contact with the electrolytes during cell assembly, which reflects in the large R_{h} value and the large overpotential at initial cycles at 25 °C in OE and IL (Figures 8-2d, 8-2e and 8-S3a, 8-S3b, 8-S3d and 8-S3e). R_{h} decreases during the initial cycles, as observed in other ionic liquids [22]. This suggests that the pristine passivation layer presents a barrier to diffusion that is reduced by Li deposition/dissolution during the initial cycles to form a new SEI layer, which is more amenable to Li^+ diffusion [34]. However, a dramatical decrease of the Nyquist plot is observed in the OE cell after 25th, corresponding to the decrease in overpotential in the voltage profile after 16th cycle. This indicates a short-circuit in OE cell (Figures 8-2a and 8-2d). In IL cell at 25 °C, R_{h} decreases rapidly as the cycle proceeds while the interfacial process is slightly improved by decrease in R_{ct} from 7.65 to 6.99 Ω. (Figure 8-2e). The consecutive overpotential decrease in the voltage profile in IL at 25 °C could be related to decrease in R_h (Figures 8-2b and 8-2e). Elevating operating temperature to 90 °C decreases R_h and R_{ct} and the overpotential preserves until the end of test (Figures 8-2c and 8-2f).

The scanning electron microscope (SEM) images show apparent differences in Li morphology resulting from different Li deposition/dissolution properties of the OE and IL and of the operating temperature. The Li metal surface after cycled in OE is rough and unevenly covered by Li deposits (Figs. 3a and S5a). These images show glass fiber in the deposited layer and a rough surface, which indicates severe Li dendrite growth and dead Li accumulation in the OE cell. However, the surface of the Li electrode cycled in IL was less rough in both the SEM and optical images at 25 °C (Figs. 3b and S5b). The deposited and substrate layers are clearly distinguishable (Figure 8-3b), as confirmed by energy-dispersive X-ray spectrometry (EDS). The elemental components of the SEI layer (C, N, F, and S) are detected in the deposited Li layer, but not in the Li substrate. These results suggest the IL suppresses Li dendrite formation and facilitates Li dissolution/deposition at the electrode in Figure 8-S6. The SEM images in Figs. 3c and S5c indicate that more Li dendrite is formed in IL cell at 90 °C than at 25 °C.

X-ray photoelectron spectroscopy (XPS) was used to determine the depth profile of the SEI layer. An argon-ion beam was applied to the electrode until Li 1s peaks appeared at ~53 eV [35, 36] The electrode cycled in OE shows a Li metal peak after 1-min Ar-ion etching (Figure 8-3d), whereas the electrode cycled in IL at 25 °C shows a Li metal peak after only 5 s (Figure 8-3e). These results indicate that the OE decompose more extensively than IL in forming SEI layer and that the IL formed a stable, yet thin, SEI layer, which is favorable for Li^+ diffusion and contributes partially to the lower overpotential of the IL system in the symmetric cell test at 25 °C. The Li metal XPS peak appears after 10-min Ar-ion etching in IL at 90 °C (Figure 8-3f) because the elevated operating temperature enhances the chemical reaction between Li metal and the IL, which consumed more electrolyte and Li metal in forming a stable SEI layer. However, the thick SEI layer could not hinder Li^+ diffusion at 90 °C, because of the increase in Li^+ diffusivity with temperature.

Chemical species at the Li metal surface were further analyzed by XPS spectroscopy (Figure 8-3g) and EDS (Figure 8-S7). The formation of LiF by decomposition of the OE and IL electrolytes was confirmed by the Li 1s and F 1s XPS signals and by EDS (Figure 8-3g and S7) in agreement with previous works [22, 29, 36-38]. The major difference in the composition of the SEI layers in the IL and OE cells is the presence of N- and S-containing species in the IL cells, as the OE contains no nitrogen or sulfur. The N 1s and S $2p_{3/2}$ spectra indicate that the SEI layer of the IL cells contains $LiSO_2F$, $C–N^+$ (im), and $Li_2N_2O_2$, which arise from the decomposition of the $FSA^–$ anion and $C_2C_1im^+$ cation and contribute to the stable electrochemical performance of the IL cell. The elemental composition of the SEI layer formed in IL electrolyte seems to be effectively independent of the operating temperature, although the layer was thicker at 90 °C. The only chemical species difference between 25 and 90 °C was in the C–F composition at 25 °C. The additional details on SEI formation components are arranged in Table 8-S2.

8.4 Conclusions

Li[FSA]/$[C_2C_1im]$[FSA] IL was employed to construct a safe and wide temperature range operable Li-metal battery. The combination of Li metal and the IL presented excellent electrochemical behaviors. The IL exhibited lower polarization than corresponding cells containing OE at room temperature and showed a long life. These results accord with effective suppression of Li dendrite growth and dead Li accumulation by the IL. The cell with IL exhibited better stability and charge/discharge capacity than a cell with an organic electrolyte even at room temperature at 25 °C. These results illustrate the benefits of using IL with Li metal electrode for safe and wide temperature range operable Li-metal batteries.

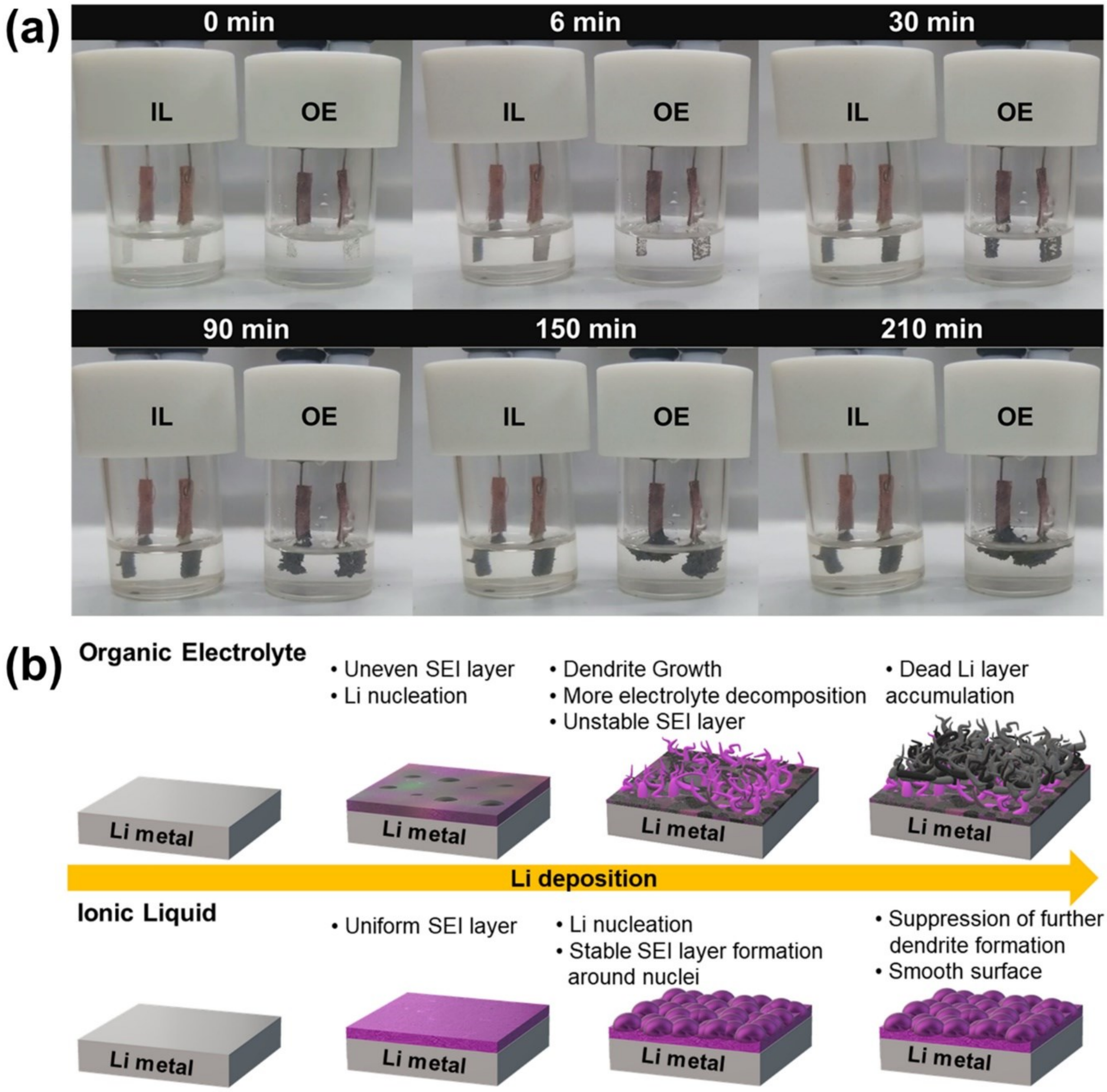

Figure 8-1 (a) Dendrite formation in symmetric Li/Li cells during cycling at 8.0 mA cm^{-2} at 25 °C. (b) Schematic comparison of Li deposition and dendrite formation with OE and IL. See Figure 8-S2 for the corresponding voltage profiles.

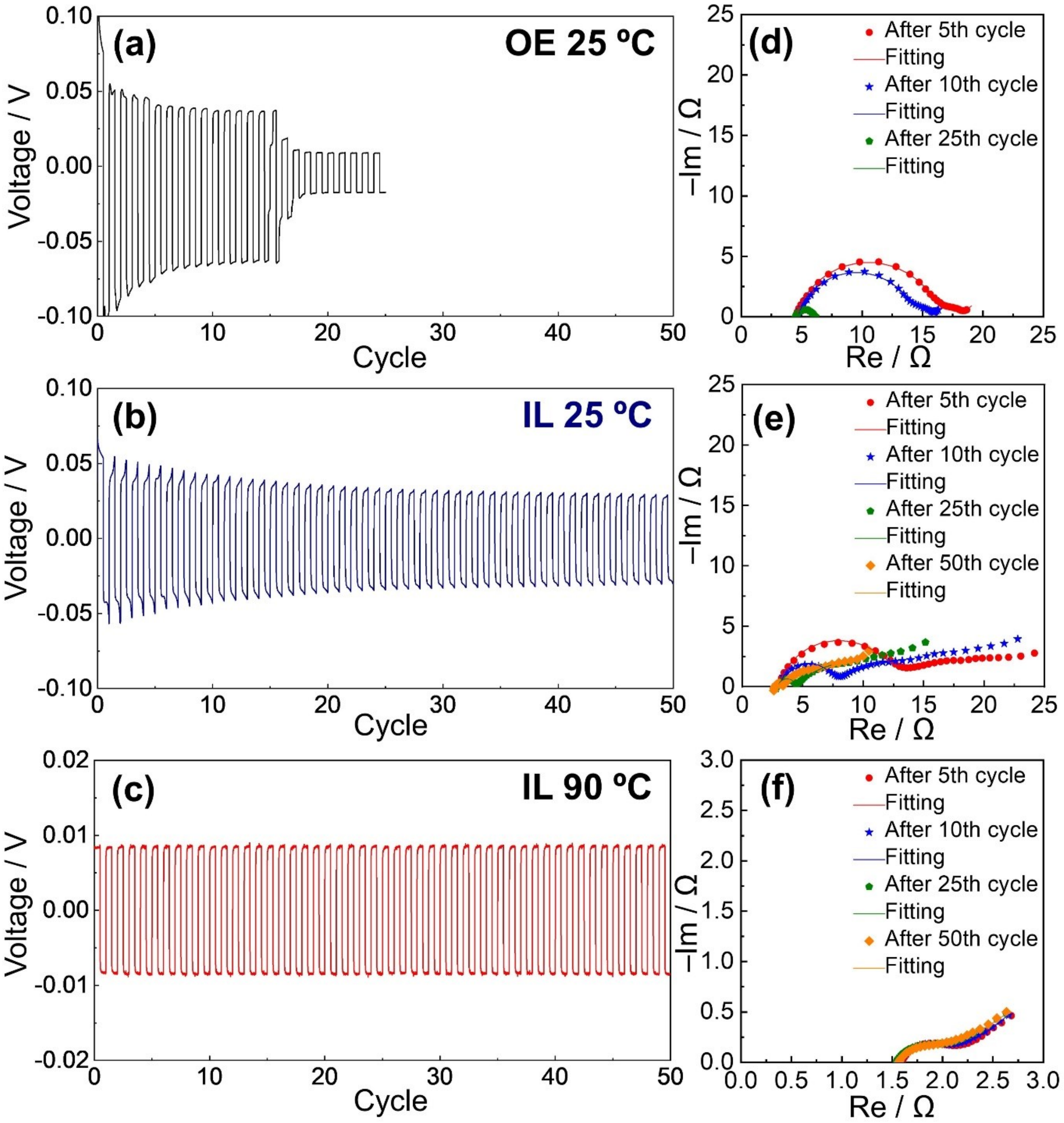

Figure 8-2 Voltage profiles of symmetric Li/Li cells cycled at 1.0 mA cm^{-2} (24 min per cycle) for (a) OE at 25 °C, (b) IL at 25 °C, and (c) IL at 90 °C. Nyquist plots upon cycles (d) OE at 25 °C, (e) IL at 25 °C, and (f) IL at 90 °C. See Figure 8-S3 for the long-term cycling tests for a Li/Li cell in coin-cell configuration and Table 8-S1 for the EIS parameters.

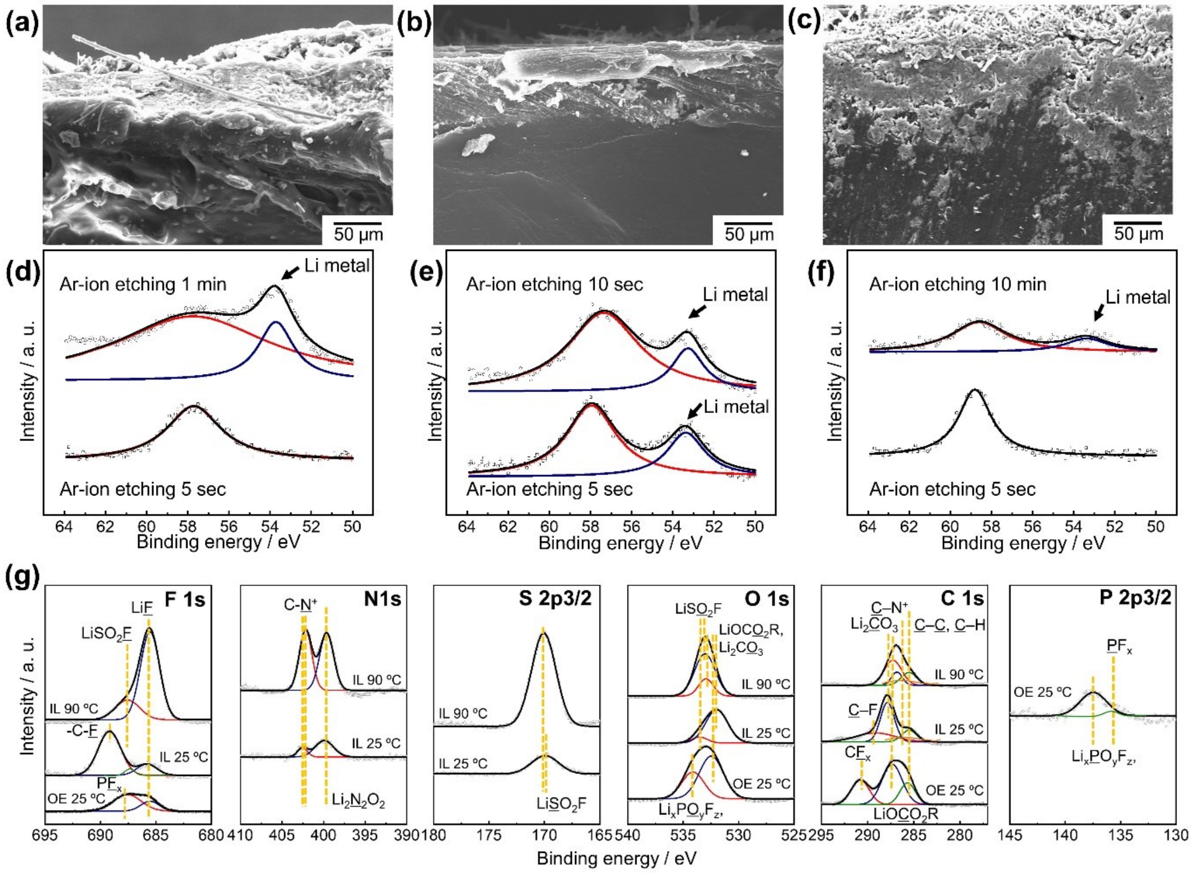

Figure 8-3 The cross-sectional SEM images of the Li metal electrodes after cycles (a) OE at 25 °C, (b) IL at 25 °C, and (c) IL at 90 °C. Li 1s XPS spectra of Li metal electrodes subjected to Ar-ion etching for (d) OE at 25 °C, (e) IL at 25 °C, and (f) IL at 90 °C. Fitting lines in (d)-(f) correspond to total (black), Li metal (blue), and LiF (red) signals. (g) XPS spectra of the Li metal electrodes after cycle test; F 1s, N 1s, S $2p_{3/2}$, O 1s, C 1s, and P $2p_{3/2}$.

References

[1] Z. Jian, Y. Sun, and X. Ji, Chem. Commun., 51 (2015) 6381.

[2] W. C. Duan, Z. Q. Zhu, H. Li, Z. Hu, K. Zhang, F. Y. Cheng, and J. Chen, J. Mater. Chem. A, 2 (2014) 8668.

[3] C. Zhu, P. Kopold, P. A. van Aken, J. Maier, and Y. Yu, Adv. Mater., 28 (2016) 2409.

[4] L. S. Plashnitsa, E. Kobayashi, Y. Noguchi, S. Okada, and J. Yamaki, J. Electrochem. Soc., 157 (2010) A536.

[5] Z. Jian, Y. S. Hu, X. Ji, and W. Chen, Adv. Mater., 29 (2017) 1601925.

[6] S. Y. Lim, H. Kim, R. A. Shakoor, Y. Jung, and J. W. Choi, J. Electrochem. Soc., 159 (2012) A1393.

[7] Q. Liu, X. Meng, Z. Wei, D. Wang, Y. Gao, Y. Wei, F. Du, and G. Chen, ACS Appl. Mater. Interfaces, 8 (2016) 31709.

[8] Q. Wang, B. Zhao, S. Zhang, X. Gao, and C. Deng, J. Mater. Chem. A, 3 (2015) 7732.

[9] Y. Jiang, Z. Z. Yang, W. H. Li, L. C. Zeng, F. S. Pan, M. Wang, X. Wei, G. T. Hu, L. Gu, and Y. Yu, Adv. Energy Mater., 5 (2015) 1402104.

[10] J. Zhang, Y. Fang, L. Xiao, J. Qian, Y. Cao, X. Ai, and H. Yang, ACS Appl. Mater. Interfaces, 9 (2017) 7177.

[11] W. Shen, H. Li, Z. Guo, C. Wang, Z. Li, Q. Xu, H. Liu, Y. Wang, and Y. Xia, ACS Appl. Mater. Interfaces, 8 (2016) 15341.

[12] H. Li, C. Wu, Y. Bai, F. Wu, and M. Wang, J. Power Sources, 326 (2016) 14.

[13] Z. Jian, W. Han, X. Lu, H. Yang, Y.-S. Hu, J. Zhou, Z. Zhou, J. Li, W. Chen, D. Chen, and L. Chen, Adv. Energy Mater., 3 (2013) 156.

[14] L. Chen, Y. Zhao, S. Liu, and L. Zhao, ACS Appl. Mater. Interfaces, 9 (2017) 44485.

[15] J. Hwang, K. Matsumoto, and R. Hagiwara, Adv. Sustainable Syst., 2 (2018) 1700171.

[16] X. Rui, W. Sun, C. Wu, Y. Yu, and Q. Yan, Adv. Mater., 27 (2015) 6670.

[17] A. Ponrouch, D. Monti, A. Boschin, B. Steen, P. Johansson, and M. R. Palacín, J. Mater. Chem. A, 3 (2015) 22.

[18] S. Hess, M. Wohlfahrt-Mehrens, and M. Wachtler, J. Electrochem. Soc., 162 (2015) A3084.

[19] S. Wilken, P. Johansson, and P. Jacobsson, Solid State Ion., 225 (2012) 608.

[20] G. G. Eshetu, S. Grugeon, S. Laruelle, S. Boyanov, A. Lecocq, J. P. Bertrand, and G. Marlair, Phys. Chem. Chem. Phys., 15 (2013) 9145.

[21] E. Cabrera-Castillo, F. Niedermeier, and A. Jossen, J. Power Sources, 324 (2016) 509.

[22] M. Armand, F. Endres, D. R. MacFarlane, H. Ohno, and B. Scrosati, Nat. Mater., 8 (2009) 621.

[23] L. Chancelier, A. O. Diallo, C. C. Santini, G. Marlair, T. Gutel, S. Mailley, and C. Len, Phys. Chem. Chem. Phys., 16 (2014) 1967.

[24] G. B. Appetecchi, M. Montanino, and S. Passerini, in Ionic Liquids: Science and Applications, p. 67, American Chemical Society (2012).

[25] D. R. MacFarlane, N. Tachikawa, M. Forsyth, J. M. Pringle, P. C. Howlett, G. D. Elliott, J. H. Davis, M. Watanabe, P. Simon, and C. A. Angell, Energ. Environ. Sci., 7 (2014) 232.

[26] M. Watanabe, M. L. Thomas, S. Zhang, K. Ueno, T. Yasuda, and K. Dokko, Chem. Rev., 117 (2017) 7190.

[27] A. Basile, M. Hilder, F. Makhlooghiazad, C. Pozo-Gonzalo, D. R. MacFarlane, P. C. Howlett, and M. Forsyth, Adv. Energy Mater., 8 (2018) 1703491.

[28] H. Zhang, W. Feng, J. Nie, and Z. Zhou, J. Fluorine Chem., 174 (2015) 49.

[29] K. Matsumoto, Y. Okamoto, T. Nohira, and R. Hagiwara, J. Phys. Chem. C, 119 (2015) 7648.

[30] M. Forsyth, H. Yoon, F. Chen, H. Zhu, D. R. MacFarlane, M. Armand, and P. C. Howlett, J. Phys. Chem. C, 120 (2016) 4276.

[31] N. Wongittharom, C.-H. Wang, Y.-C. Wang, C.-H. Yang, and J.-K. Chang, ACS Appl. Mater. Interfaces, 6 (2014) 17564.

[32] C.-H. Wang, C.-H. Yang, and J.-K. Chang, Chem. Commun., 52 (2016) 10890.

[33] L. G. Chagas, D. Buchholz, L. Wu, B. Vortmann, and S. Passerini, J. Power Sources, 247 (2014) 377.

[34] G. Sui, S. Jana, W. H. Zhong, M. A. Fuqua, and C. A. Ulven, Acta Mater., 56 (2008) 2381.

[35] X. Fang, M. Ge, J. Rong, and C. Zhou, ACS Nano, 8 (2014) 4876.

[36] W. Li, M. Li, K. R. Adair, X. Sun, and Y. Yu, J. Mater. Chem. A, 5 (2017) 13882.

[37] K. Matsumoto, T. Hosokawa, T. Nohira, R. Hagiwara, A. Fukunaga, K. Numata, E. Itani, S. Sakai, K. Nitta, and S. Inazawa, J. Power Sources, 265 (2014) 36.

[38] J. Rodríguez-Carvajal, Phys. B, 192 (1993) 55.

[39] K. Momma, and F. Izumi, J. Appl. Crystallogr., 41 (2008) 653.

[40] S. Brunauer, P. H. Emmett, and E. Teller, J. Am. Chem. Soc., 60 (1938) 309.

[41] J. Hwang, K. Matsumoto, Y. Orikasa, M. Katayama, Y. Inada, T. Nohira, and R. Hagiwara, J. Power Sources, 377 (2018) 80.

[42] J. Hwang, K. Matsumoto, and R. Hagiwara, J. Phys. Chem. C, 122 (2018) 26857.

[43] J.-N. Chotard, G. Rousse, R. David, O. Mentré, M. Courty, and C. Masquelier, Chem. Mater., 27 (2015) 5982.

[44] Z. Jian, C. Yuan, W. Han, X. Lu, L. Gu, X. Xi, Y.-S. Hu, H. Li, W. Chen, D. Chen, Y. Ikuhara, and L. Chen, Adv. Funct. Mater., 24 (2014) 4265.

[45] A. C. Ferrari, and J. Robertson, Philos. Trans. Royal Soc. A, 362 (2004) 2477.

[46] A. C. Ferrari, J. C. Meyer, V. Scardaci, C. Casiraghi, M. Lazzeri, F. Mauri, S. Piscanec, D. Jiang, K. S. Novoselov, S. Roth, and A. K. Geim, Phys. Rev. Lett., 97 (2006) 187401.

[47] M. S. Dresselhaus, G. Dresselhaus, R. Saito, and A. Jorio, Phys. Rep., 409 (2005) 47.

[48] L. Jiao, L. Zhang, X. Wang, G. Diankov, and H. Dai, Nature, 458 (2009) 877.

[49] K. Shubham, H. Jinkwang, M. Kazuhiko, S. Yuta, and H. Rika, ChemElectroChem, 5 (2018) 1340.

[50] Z. L. Jian, W. Z. Han, X. Lu, H. X. Yang, Y. S. Hu, J. Zhou, Z. B. Zhou, J. Q. Li, W. Chen, D. F. Chen, and L. Q. Chen, Adv. Energy Mater., 3 (2013) 156.

[51] K. Saravanan, C. W. Mason, A. Rudola, K. H. Wong, and P. Balaya, Adv. Energy Mater., 3 (2013) 444.

[52] Z. L. Jian, L. Zhao, H. L. Pan, Y. S. Hu, H. Li, W. Chen, and L. Q. Chen, Electrochem. Commun., 14 (2012) 86.

[53] X. Li, Y. Huang, J. Wang, L. Miao, Y. Li, Y. Liu, Y. Qiu, C. Fang, J. Han, and Y. Huang, J. Mater. Chem. A, 6 (2018) 1390.

[54] S.-J. Lim, D.-W. Han, D.-H. Nam, K.-S. Hong, J.-Y. Eom, W.-H. Ryu, and H.-S. Kwon, J. Mater. Chem. A, 2 (2014) 19623.

[55] N. Ogihara, Y. Itou, T. Sasaki, and Y. Takeuchi, J. Phys. Chem. C, 119 (2015) 4612.

[56] C. H. Chen, J. Liu, and K. Amine, J. Power Sources, 96 (2001) 321.

[57] R. Petibon, C. P. Aiken, N. N. Sinha, J. C. Burns, H. Ye, C. M. VanElzen, G. Jain, S. Trussler, and J. R. Dahn, J. Electrochem. Soc., 160 (2013) A117.

[58] B. Kang, and G. Ceder, Nature, 458 (2009) 190.

[59] P. Bai, and M. Z. Bazant, Nat. Commun., 5 (2014) 3585.

[60] Q. Cao, H. P. Zhang, G. J. Wang, Q. Xia, Y. P. Wu, and H. Q. Wu, Electrochem. Commun., 9 (2007) 1228.

[61] J. Mao, C. Luo, T. Gao, X. Fan, and C. Wang, J. Mater. Chem. A, 3 (2015) 10378.

[1] D. Andre, M. Meiler, K. Steiner, C. Wimmer, T. Soczka-Guth, and D. U. Sauer, J. Power Sources, 196 (2011) 5334.

[2] B.-Y. Chang, and S.-M. Park, Annu. Rev. Anal. Chem., 3 (2010) 207.

[3] J. Guo, A. Sun, X. Chen, C. Wang, and A. Manivannan, Electrochim. Acta, 56 (2011) 3981.

[4] F. Wohde, M. Balabajew, and B. Roling, J. Electrochem. Soc., 163 (2016) A714.

[5] P. Lu, C. Li, E. W. Schneider, and S. J. Harris, J. Phys. Chem. C, 118 (2014) 896.

[6] S.-M. Park, and J.-S. Yoo, Anal. Chem., 75 (2003) 455 A.

[7] M. G. S. R. Thomas, P. G. Bruce, and J. B. Goodenough, J. Electrochem. Soc., 132 (1985) 1521.

[8] S.-U. Woo, B.-C. Park, C. S. Yoon, S.-T. Myung, J. Prakash, and Y.-K. Sun, J. Electrochem. Soc., 154 (2007) A649.

[9] T. Hosokawa, K. Matsumoto, T. Nohira, R. Hagiwara, A. Fukunaga, S. Sakai, and K. Nitta, J. Phys. Chem. C, 120 (2016) 9628.

[10] C.-H. Wang, C.-H. Yang, and J.-K. Chang, Chem. Commun., 52 (2016) 10890.

[11] H. Kim, R. A. Shakoor, C. Park, S. Y. Lim, J.-S. Kim, Y. N. Jo, W. Cho, K. Miyasaka, R. Kahraman, Y. Jung, and J. W. Choi, Adv. Funct. Mater., 23 (2013) 1147.

[12] P. Barpanda, G. Liu, C. D. Ling, M. Tamaru, M. Avdeev, S.-C. Chung, Y. Yamada, and A. Yamada, Chem. Mater., 25 (2013) 3480.

[13] C.-Y. Chen, T. Kiko, T. Hosokawa, K. Matsumoto, T. Nohira, and R. Hagiwara, J. Power Sources, 332 (2016) 51.

[14] T. Honma, T. Togashi, N. Ito, and T. Komatsu, Fabrication of Na2FeP2O7 Glass-Ceramics for Sodium Ion Battery, p. 344 (2012).

[15] K. Matsumoto, T. Hosokawa, T. Nohira, R. Hagiwara, A. Fukunaga, K. Numata, E. Itani, S. Sakai, K. Nitta, and S. Inazawa, J. Power Sources, 265 (2014) 36.

[16] T. Yamamoto, T. Nohira, R. Hagiwara, A. Fukunaga, S. Sakai, and K. Nitta, Electrochim. Acta, 211 (2016) 234.

[17] J. Hwang, K. Matsumoto, Y. Orikasa, M. Katayama, Y. Inada, T. Nohira, and R. Hagiwara, J. Power Sources, 377 (2018) 80.

[18] C. Ding, T. Nohira, R. Hagiwara, K. Matsumoto, Y. Okamoto, A. Fukunaga, S. Sakai, K. Nitta, and S. Inazawa, J. Power Sources, 269 (2014) 124.

[19] C.-Y. Chen, K. Matsumoto, T. Nohira, C. Ding, T. Yamamoto, and R. Hagiwara, Electrochim. Acta, 133 (2014) 583.

[20] C. H. Chen, J. Liu, and K. Amine, J. Power Sources, 96 (2001) 321.

[21] N. Ogihara, S. Kawauchi, C. Okuda, Y. Itou, Y. Takeuchi, and Y. Ukyo, J. Electrochem. Soc., 159 (2012) A1034.

[22] R. Alcántara, M. Jaraba, P. Lavela, and J. L. Tirado, J. Electroanal. Chem., 566 (2004) 187.

[23] F. Croce, F. Nobili, A. Deptula, W. Lada, R. Tossici, A. D'Epifanio, B. Scrosati, and R. Marassi, Electrochem. Commun., 1 (1999) 605.

[24] V. Raju, J. Rains, C. Gates, W. Luo, X. Wang, W. F. Stickle, G. D. Stucky, and X. Ji, Nano Lett., 14 (2014) 4119.

[25] A.-M. Cao, J.-S. Hu, H.-P. Liang, and L.-J. Wan, Angew. Chem. Int. Ed., 44 (2005) 4391.

[26] H.-Y. Li, C.-H. Yang, C.-M. Tseng, S.-W. Lee, C.-C. Yang, T.-Y. Wu, and J.-K. Chang, J. Power Sources, 285 (2015) 418.

[27] J. Shao, X. Li, Z. Wan, L. Zhang, Y. Ding, L. Zhang, Q. Qu, and H. Zheng, ACS Appl. Mater. Interfaces, 5 (2013) 7671.

[28] X. Li, C. Liu, C. Zhang, H. Fu, X. Nan, W. Ma, Z. Li, K. Wang, H. Wu, and G. Cao, ACS Appl. Mater. Interfaces, 8 (2016) 24629.

[29] J. Bullot, O. Gallais, M. Gauthier, and J. Livage, Appl. Phys. Lett., 36 (1980) 986.

[30] C. Fleischer, W. Waag, H.-M. Heyn, and D. U. Sauer, J. Power Sources, 260 (2014) 276.

[31] J. Gomez, R. Nelson, E. E. Kalu, M. H. Weatherspoon, and J. P. Zheng, J. Power Sources, 196 (2011) 4826.

[32] T. Abe, F. Sagane, M. Ohtsuka, Y. Iriyama, and Z. Ogumi, J. Electrochem. Soc., 152 (2005) A2151.

[33] F. Sagane, T. Abe, Y. Iriyama, and Z. Ogumi, J. Power Sources, 146 (2005) 749.

[34] H. Ma, S. Zhang, W. Ji, Z. Tao, and J. Chen, J. Am. Chem. Soc., 130 (2008) 5361.

[35] H. Gao, Z. Hu, K. Zhang, F. Cheng, and J. Chen, Chem. Commun., 49 (2013) 3040.

[1] M. Winter, J. O. Besenhard, M. E. Spahr, and P. Novák, Adv. Mater., 10 (1998) 725.

[2] L. Li, S. Li, and Y. Lu, Chem. Commun., 54 (2018) 6648.

[3] M. Yamagata, Y. Matsui, T. Sugimoto, M. Kikuta, T. Higashizaki, M. Kono, and M. Ishikawa, J. Power Sources, 227 (2013) 60.

[4] X.-B. Cheng, R. Zhang, C.-Z. Zhao, and Q. Zhang, Chem. Rev., 117 (2017) 10403.

[5] W. Xu, J. Wang, F. Ding, X. Chen, E. Nasybulin, Y. Zhang, and J.-G. Zhang, Energy Environ. Sci., 7 (2014) 513.

[6] X.-B. Cheng, R. Zhang, C.-Z. Zhao, F. Wei, J.-G. Zhang, and Q. Zhang, Adv. Sci., 3 (2016) 1500213.

[7] B. Scrosati, J. Hassoun, and Y.-K. Sun, Energy Environ. Sci., 4 (2011) 3287.

[8] S. Xin, L. Gu, N.-H. Zhao, Y.-X. Yin, L.-J. Zhou, Y.-G. Guo, and L.-J. Wan, J. Am. Chem. Soc., 134 (2012) 18510.

[9] Z. Ma, X. Yuan, L. Li, Z.-F. Ma, D. P. Wilkinson, L. Zhang, and J. Zhang, Energy Environ. Sci., 8 (2015) 2144.

[10] D. Lin, Y. Liu, and Y. Cui, Nat. Nanotechnol., 12 (2017) 194.

[11] F. Ding, W. Xu, X. Chen, J. Zhang, M. H. Engelhard, Y. Zhang, B. R. Johnson, J. V. Crum, T. A. Blake, X. Liu, and J.-G. Zhang, J. Electrochem. Soc., 160 (2013) A1894.

[12] L. Li, S. Zhou, H. Han, H. Li, J. Nie, M. Armand, Z. Zhou, and X. Huang, J. Electrochem. Soc., 158 (2011) A74.

[13] Y. Matsuda, and M. Sekiya, J. Power Sources, 81-82 (1999) 759.

[14] H. Yue, Y. Yang, Y. Xiao, Z. Dong, S. Cheng, Y. Yin, C. Ling, W. Yang, Y. Yu, and S. Yang, J. Mater. Chem. A, 7 (2019) 594.

[15] A. M. Tripathi, W.-N. Su, and B. J. Hwang, Chem. Soc. Rev., 47 (2018) 736.

[16] H. Yoon, G. H. Lane, Y. Shekibi, P. C. Howlett, M. Forsyth, A. S. Best, and D. R. MacFarlane, Energ. Environ. Sci, 6 (2013) 979.

[17] D. Aurbach, E. Zinigrad, Y. Cohen, and H. Teller, Solid State Ionics, 148 (2002) 405.

[18] S. Hess, M. Wohlfahrt-Mehrens, and M. Wachtler, J. Electrochem. Soc., 162 (2015) A3084.

[19] Q.-C. Liu, J.-J. Xu, S. Yuan, Z.-W. Chang, D. Xu, Y.-B. Yin, L. Li, H.-X. Zhong, Y.-S. Jiang, J.-M. Yan, and X.-B. Zhang, Adv. Mater., 27 (2015) 5241.

[20] H. Lee, D. J. Lee, Y.-J. Kim, J.-K. Park, and H.-T. Kim, J. Power Sources, 284 (2015) 103.

[21] Y. Liu, D. Lin, P. Y. Yuen, K. Liu, J. Xie, R. H. Dauskardt, and Y. Cui, Adv. Mater., 29 (2017) 1605531.

[22] A. Basile, A. I. Bhatt, and A. P. O'Mullane, Nat. Commun., 7 (2016) 11794.

[23] N. Schweikert, A. Hofmann, M. Schulz, M. Scheuermann, S. T. Boles, T. Hanemann, H. Hahn, and S. Indris, J. Power Sources, 228 (2013) 237.

[24] H. Sano, M. Kitta, and H. Matsumoto, J. Electrochem. Soc., 163 (2016) D3076.

[25] F. Mizuno, T. S. Arthur, and K. Takechi, ACS Energy Lett., 1 (2016) 542.

[26] K. Matsumoto, E. Nishiwaki, T. Hosokawa, S. Tawa, T. Nohira, and R. Hagiwara, J. Phys. Chem. C, 121 (2017) 9209.

[27] K. Matsumoto, Y. Okamoto, T. Nohira, and R. Hagiwara, J. Phys. Chem. C, 119 (2015) 7648.

[28] H. Sano, H. Sakaebe, and H. Matsumoto, J. Power Sources, 196 (2011) 6663.

[29] K.-H. Chen, K. N. Wood, E. Kazyak, W. S. LePage, A. L. Davis, A. J. Sanchez, and N. P. Dasgupta, J. Mater. Chem. A, 5 (2017) 11671.

[30] A. Basile, A. F. Hollenkamp, A. I. Bhatt, and A. P. O'Mullane, Electrochem. Commun., 27 (2013) 69.

[31] G. Bieker, M. Winter, and P. Bieker, Phys. Chem. Chem. Phys., 17 (2015) 8670.

[32] J. Hwang, K. Matsumoto, and R. Hagiwara, J. Phys. Chem. C, 122 (2018) 26857.

[33] N. Ogihara, Y. Itou, T. Sasaki, and Y. Takeuchi, J. Phys. Chem. C, 119 (2015) 4612.

[34] L. Fan, S. Li, L. Liu, W. Zhang, L. Gao, Y. Fu, F. Chen, J. Li, H. L. Zhuang, and Y. Lu, Adv. Energy Mater., 8 (2018) 1802350.

[35] P. H. Citrin, G. K. Wertheim, and Y. Baer, Phys. Rev. B, 16 (1977) 4256.

[36] L. Suo, Y.-S. Hu, H. Li, M. Armand, and L. Chen, Nat. Commun., 4 (2013) 1481.

[37] S. E. Sloop, J. K. Pugh, S. Wang, J. B. Kerr, and K. Kinoshita, Electrochem. Solid-State Lett., 4 (2001) A42.

[38] M. Wang, L. Huai, G. Hu, S. Yang, F. Ren, S. Wang, Z. Zhang, Z. Chen, Z. Peng, C. Shen, and D. Wang, J. Phys. Chem. C, 122 (2018) 9825.

Appendix

Evaluation of Li deposition/dissolution efficiency ($\varepsilon_{\mathrm{cycle}}$)

Li deposition/dissolution efficiency was tested in a Li/Cu cell at a current density of 1.0 mA cm^{-2} using OE at 25 °C and IL at 25 and 90 °C in a coin cell configuration. Li metal of 1.0 C cm^{-2} was deposited on a Cu substrate, and 0.2 C cm^{-2} of Li was dissolved and deposited until the overpotential reach 0.5 V. The ε_{cycle} was calculated based on Equation (S1) [1].

$$\varepsilon_{cycle} = \frac{N_{cycle} \times Q_{cycle}}{Q_{initial} + N_{cycle} \times Q_{cycle}} \qquad \text{(S1)}$$

N_{cycle} refers to the number of cycles until the potential reaches 0.5 V. Q_{cycle} refers to the electric charge used for Li deposition/dissolution per cycle. (200 sec, 1.0 mA cm^{-2}) Q_{initial} refers to the electric charge used for the first Li deposition on a Cu substrate (1000 sec, 1.0 mA cm^{-2}).

SEI Components

LiF was confirmed by associating peak at in 57.7and 685.5 eV in OE at 25 °C and 57.8 and 685.8 eV in IL at 25, and 58.4 and 68.5 eV in IL at 90 °C, in Li 1s and F 1s, respectively. $\mathrm{LiSO_2F}$ was confirmed in IL by associating peaks at 687.5 eV at 25 °C and 687.6 eV at 90 °C in F1s, S $2p_{3/2}$ peaks at 169.9 eV at 25 °C and 170.1 eV at 90 °C and O 1s peaks at 533.6 eV at 25 °C and 533.1 eV at 90 °C in Figure 8-3g [2, 3]. Furthermore, a peak at 689.2 eV in F1s 288.9 eV in C 1s ascribed to C–F components are notably detected in IL at 25 °C. The $\mathrm{Li_2N_2O_2}$ has confirmed in IL with N 1s peaks at 399.9 eV at 25 °C and 399,7 eV at 90 °C in Figure 8-3g [2]. The existence of carbon from the $\mathrm{C_2C_1im^+}$, C–N (im), are confirmed by N 1s peaks at 402.5 eV at 25 °C and 402.2 eV at 90 °C and C 1s peaks at 286.1 eV at 25 °C and 285.7 eV at 90 °C in Figure 8-3g [3]. In the case of OE, $\mathrm{LiPF_6}$ salt formed $\mathrm{PF_x}$ and $\mathrm{CF_x}$ in Figure 8-3g. SEI formation components are arranged in Table 8-S2.

Table 8-S1 EIS fitting parameters, R_{bulk}, R_{h}, and R_{ct} for the Li/IL/Li symmetric cell (see Figure 8-S2 for the corresponding EIS tests).

T /°C	**Cycle**	**Resistance / Ω**		
		R_{bulk}	R_{h}	R_{ct}
OE 25	5	4.55	11.72	1.95
	10	4.69	9.26	2.16
	25	4.54	1.46	0.16
IL 25	5	2.96	9.11	7.65
	10	3.04	4.19	7.55
	25	2.94	1.34	7.474
	50	2.75	0.54	6.99
IL 90	5	1.56	0.57	0.35
	10	1.57	0.41	0.33
	25	1.55	0.39	0.34
	50	1.56	0.43	0.31

Table 8-S2 *ex-situ* XPS data for SEI layer components on the Li metal electrode [2, 3, 5-7].

SEI Compon.	**Binding energy / eV**						
	Li 1s	**F** 1s	**S** $2p_{3/2}$	**O** 1s	**N** 1s	**C** 1s	**P** $2p_{3/2}$
LiFSA-C_2C1im][FSA]							
LiF	57.8 (298 K) 58.4 (363 K)	685.8 (298 K) 685.5 (363 K)					
$LiSO_2F$		687.5 (298 K) 687.6 (363 K)	169.9 (298 K) 170.1 (363 K)	533.6 (298 K) 533.1 (363 K)			
C–F		689.2 (298 K)				288.9 (298 K)	
C–C, C–H						285.5 (298 K) 285.5 (363 K)	
$Li_2N_2O_2$					399.9 (298 K) 399.7 (363 K)		
C–N^+					402.5 (298 K) 402.2 (363 K)	286.1 (298 K) 285.7 (363 K)	
Li_2CO_3,				532.1 (298 K) 532.8 (363 K)		287.9 (298 K) 287.3 (363 K)	
1 mol dm^{-3} Li[PF6]-EC/DMC (1/1 v)							
LiF	57.7	685.5					
Li_2CO_3, $LiOCO_2R$,	55.0			532.4		287.4	
$Li_xPO_yF_z$,		687.6		534.1			137.5
PF_x		688.0					135.2
CF_x						2363.8	
C–C, C–H						285.7	

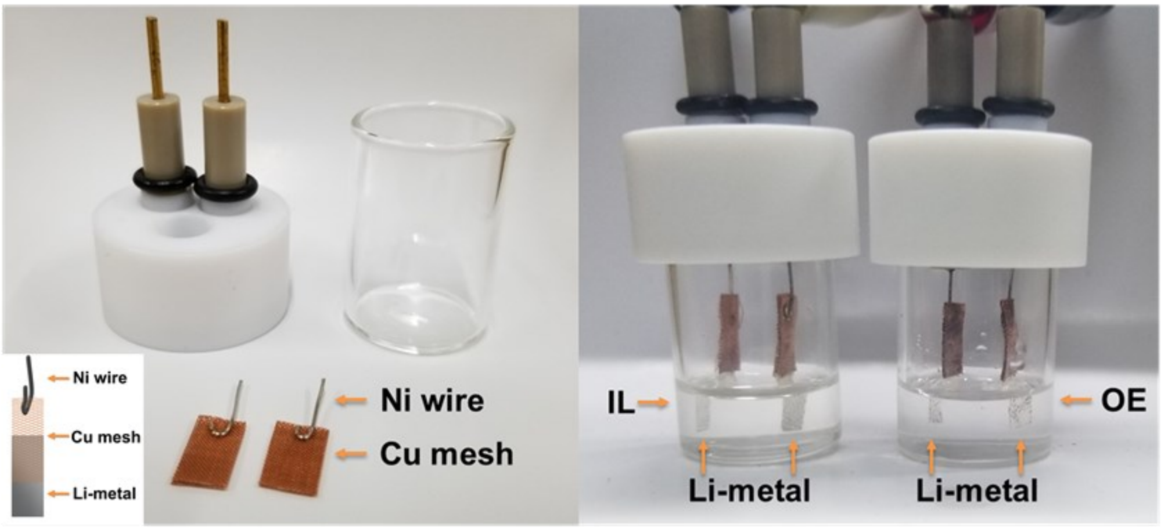

Figure 8-S1 Schematic illustration of symmetric Li/IL/Li and Li/OE/Li cells in beaker cells.

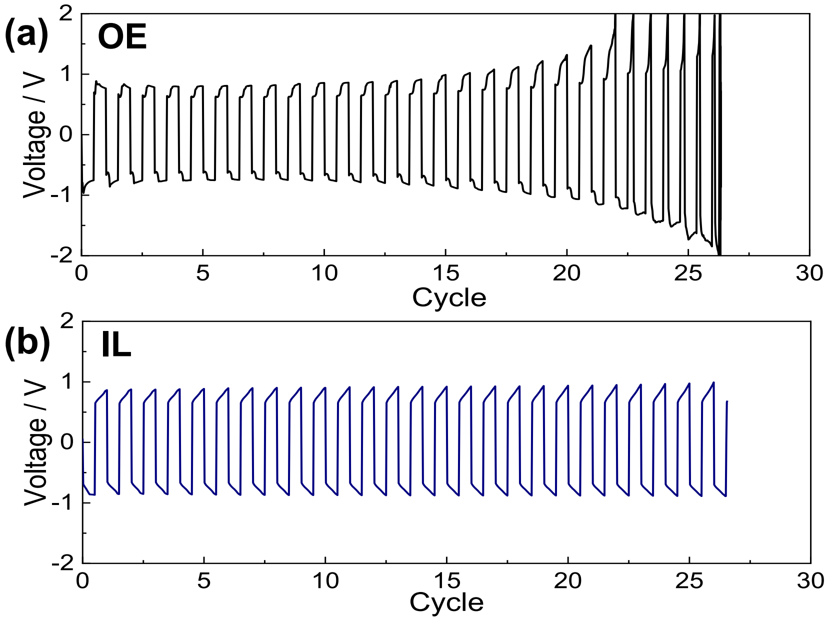

Figure 8-S2 Voltage profiles during cycle tests of the Li/Li symmetric cell at a current density of 8.0 mA cm^{-2} in the beaker cells. (a) Li/OE/Li and (b) Li/IL/Li.

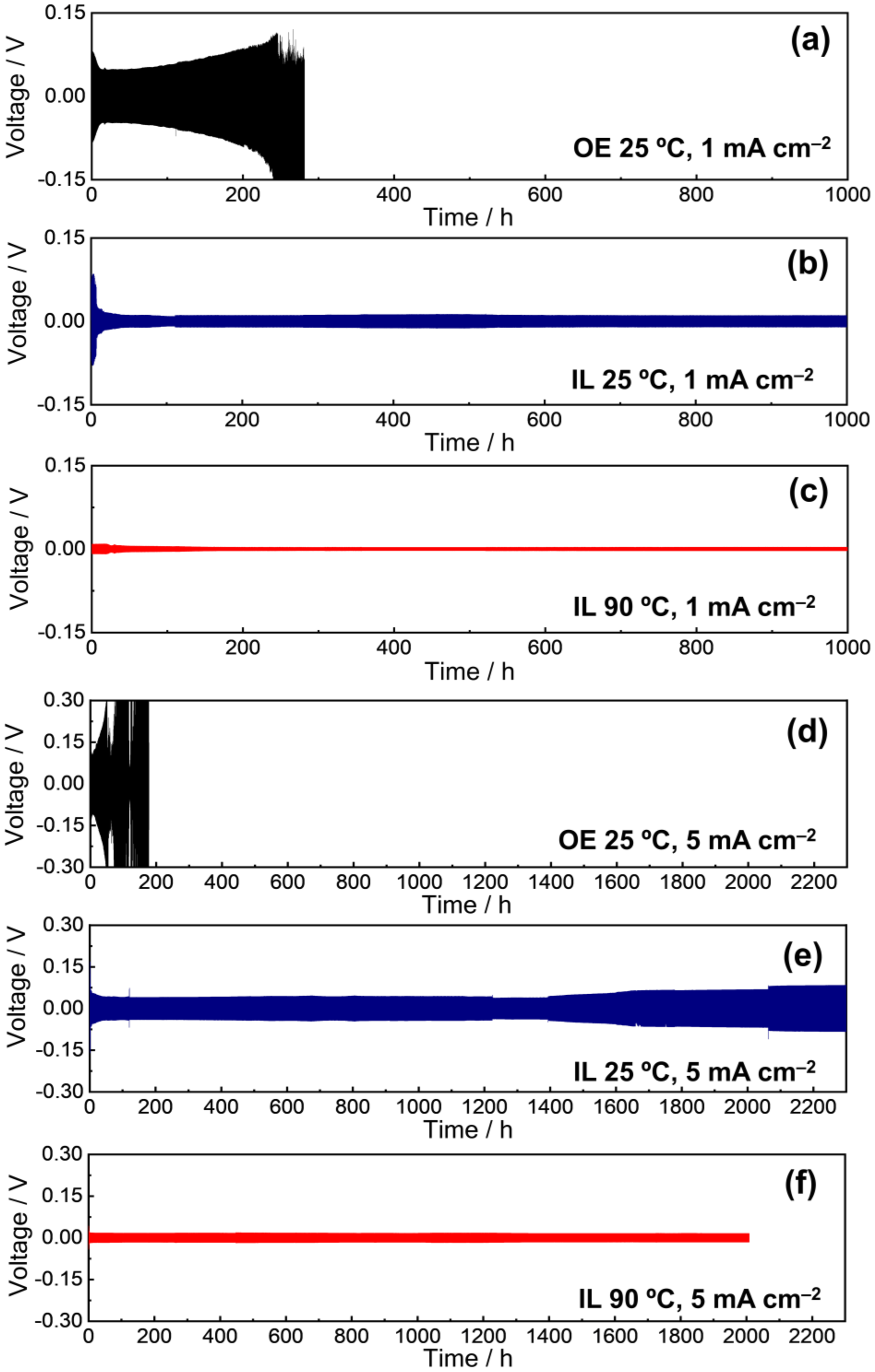

Figure 8-S3 Voltage profiles of Li/Li cells during Li deposition/dissolution of (a) OE at 25 °C, (b) IL at 25 °C, and (c) IL at 90 °C at 1.0 mA cm^{-2} and (d) OE at 25 °C, (e) IL at 25 °C, and (f) IL at 90 °C at 5.0 mA cm^{-2}. 24 min per cycle.

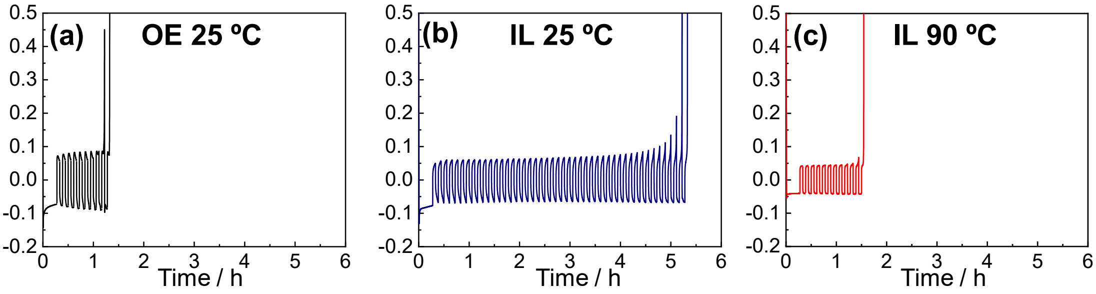

Figure 8-S4 The cycle efficiency for Li metal deposition/dissolution. (a) OE at 25 °C, (b) IL at 25°C, and (c) IL at 90 °C. 0.8 C cm^{-2} of Li was first deposited on the Cu metal substrate, and 0.2 C cm^{-2} of Li were repeatedly deposited and dissolved.

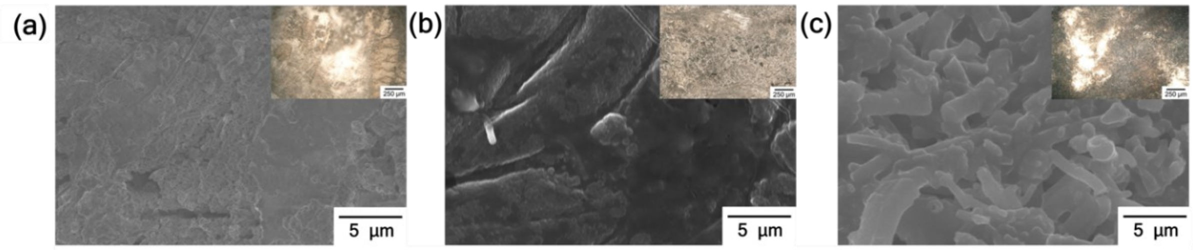

Figure 8-S5 SEM images of a Li metal electrode following Li deposition/dissolution test (a) Li/OE/Li cell at 25 °C, (b) Li/IL/Li cell at 25 °C, and (c) Li/IL/Li cell at 90 °C. The insets contain the optical microscope images of electrode surfaces after the cycling test

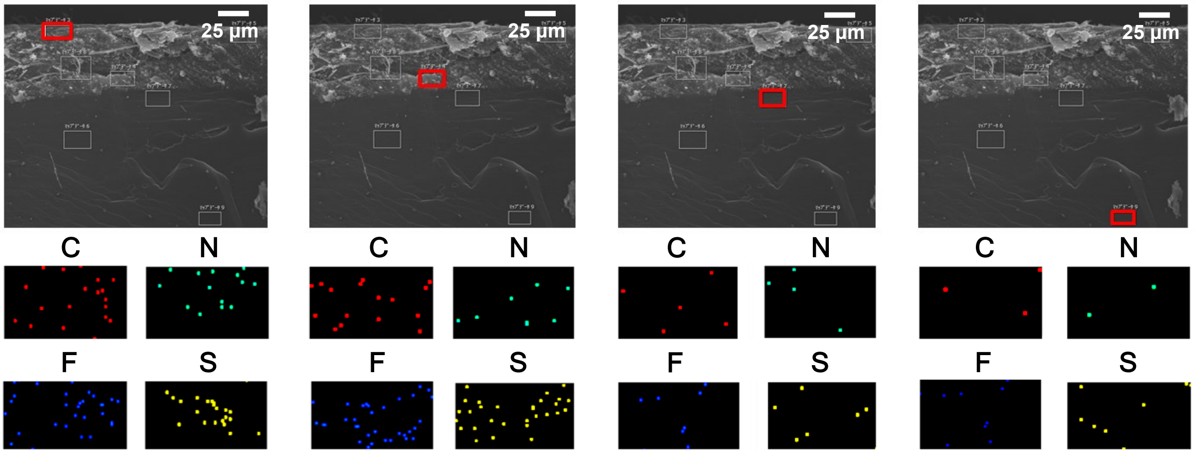

Figure 8-S6 Cross-sectional SEM images and EDS mapping in the selected region of Li metal electrode at different depth after cycle test in the IL at 25 °C.

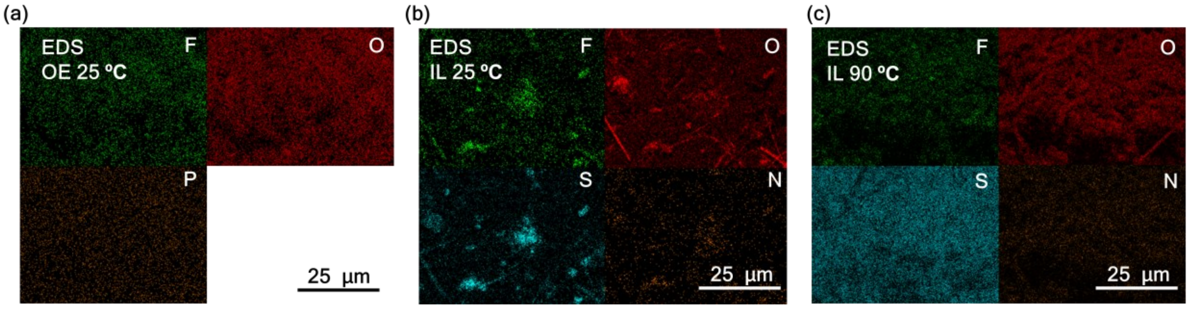

Figure 8-S7 EDS mapping of the elements on the Li metal electrodes after cycle tests in (a) the OE at 25 °C, (b) the IL at 25 °C, and (c) the IL at 90 °C. See Table S2 for XPS fitted data for the SEI components.

Appendix References

[1] K. Matsumoto, E. Nishiwaki, T. Hosokawa, S. Tawa, T. Nohira,and R. Hagiwara, J. Phys. Chem. C, 121 (2017) 9209.

[2] M. Wang, L. Huai, G. Hu, S. Yang, F. Ren, S. Wang, Z. Zhang, Z. Chen, Z. Peng, C. Shen,and D. Wang, J. Phys. Chem. C, 122 (2018) 9825.

[3] A. Basile, A. I. Bhatt,and A. P. O'Mullane, Nat. Commun., 7 (2016) 11794.

[4] M. Tamaru, S. C. Chung, D. Shimizu, S. Nishimura,and A. Yamada, Chem. Mater., 25 (2013) 2538.

[5] H. Sano, H. Sakaebe,and H. Matsumoto, J. Power Sources, 196 (2011) 6663.

[6] S. E. Sloop, J. K. Pugh, S. Wang, J. B. Kerr,and K. Kinoshita, Electrochem. Solid-State Lett., 4 (2001) A42.

[7] L. Suo, Y.-S. Hu, H. Li, M. Armand,and L. Chen, Nat. Commun., 4 (2013) 1481.

Chapter 9

General Conclusions

Li-ion secondary batteries have been well-established in the global battery market. Although there are many challenges to satisfy the demands of current battery systems, new types of Li and Na secondary batteries have indeed drawn a great deal of attention to maximize energy density and low cost, respectively. Thermally and chemically stable ionic liquid (IL) operating secondary batteries are attractive to build safer batteries, and intermediate temperature operability using ILs offers several benefits such as improving Na^+ diffusion in the electrolyte and electrode reaction. However, the practical performance of those secondary batteries has not been confirmed using IL. The author investigated electrochemical properties of positive electrode materials and Li(Na) metal to improve batteries system using IL across low to intermediate temperature range. In this study, m-$NaFePO_4$ has been investigated as a positive electrode material for intermediate-temperature operating Na secondary batteries. NASICON-type $Na_3V_2(PO_4)_3$ has been also investigated as positive electrode materials for fast charge-discharge available for Na secondary batteries. Symmetric cell electrical impedance spectroscopy (SCEIS) has been established to analyze Na secondary batteries using IL electrolyte. The Li metal dissolution and deposition properties in IL electrolyte have been investigated to establish Li metal secondary batteries in this study. The summaries of each chapter are provided below.

In Chapter 2, general experimental procedures were described. Further details on the experiments were mentioned in each chapter.

In Chapter 3, the charge-discharge behavior of m-$NaFePO_4$ ball-milled to the nano-size level was investigated in the Na[FSA]-[C_3C_1pyrr][FSA] IL electrolyte at 298 and 363 K. The charge-discharge capacity was improved by elevating the operating temperature because the Na^+ diffusion in the maricite structure and the interfacial reaction were improved. The reversible capacity increased with consecutive 120 cycles and reached 100 mAh g^{-1} with nearly 100% Coulombic efficiency in the 120th cycle at the C/2 rate at 363 K. *Ex-situ* XRD results confirmed the preservation of the maricite phase after cycling, which may indicate that the practical capacity for m-$NaFePO_4$ without amorphization.

In Chapter 4, m-$NaFePO_4$ was fabricated in two different conditions (one is ball-milled in acetone, and the other is re-calcined of the ball-milled one at 873 K). The charge-discharge test of the as-synthesized m-$NaFePO_4$, the ball-milled m-$NaFePO_4$, and the re-calcined m-$NaFePO_4$ electrodes in the Na[FSA]-[C_2C_1im][FSA] IL electrolyte at 298 and 363 K were carried out to verify temperature and crystallite size impact on electrochemical performance. The reversible charge-discharge capacities were limited in the as-synthesized m-$NaFePO_4$ and the re-calcined m-$NaFePO_4$ electrode. However, the ball-milled m-$NaFePO_4$ achieves to 107 mAh g^{-1} with almost 100 % Coulombic efficiency at C/10 rate at 363 K. The results of electrochemical impedance spectroscopy using m-$NaFePO_4$/m-$NaFePO_4$ symmetric cells visibly proposed that inactive m-$NaFePO_4$ have been changed to a positive electrode active material through the combination of the ball-milling treatment and elevating operating temperature. Moreover, the peaks of the XRD shift toward higher angles after charged to 4.0 V, and the peaks return to the original location after discharged to 2.0 V in *ex-situ* XRD measurement. These results indeed suggest that de-sodiation-sodiation process is possibly reversible in the maricite phase.

In Chapter 5, carbon-coated NASICON-type $Na_3V_2(PO_4)_3$ was prepared via the sol-gel method and investigated as a positive electrode material for Na secondary batteries operable under low-to-intermediate temperature conditions. This material fully utilizes the safety and large liquid-phase temperature range of Na[FSA]-[C_2C_1im][FSA] IL electrolytes. Electrochemical tests of the $Na_3V_2(PO_4)_3$/C composite revealed superior cycling and rate capability at 253–363 K. Cycling tests at 1 C (117 mA g^{-1}) confirmed the capacity retention of 99% and Coulombic efficiency of over 99.9% after 300 cycles at 298 K and 363 K. Even faster-current cycling at 20 C resulted in capacity retention of 89.2% after 5000 cycles at 363 K. The high rate capability at 363 K (50.1 mAh g^{-1} at 58500 mA g^{-1}) leads to excellent power and energy densities that exceed those of $NaCrO_2$ and $Na_2FeP_2O_7$ inverstigated in the same conditions.

In Chapter 6, carbon nanofibers (CNFs) are incorporated as a conductive material along with glucose for carbon coating and fixing CNF frames to NVP particles. A uniform NVP composite and CNFs network (NVPC@CNFs) are obtained by a combination of sonication and the sol-gel method. Electrochemical measurements using a high mass loading electrode around ~8.5 mg-active material cm^{-2} and Na[FSA]-[C_2C_1im][FSA] IL electrolyte. The rate capability further improved by using the NVPC@CNFs compared to NVPC, exhibit a high rate capability (at high geometric current density) of 51.1 mAh g^{-1} at 10C (10.0 mA cm^{-2}) at 298 K and 82.3 mAh g^{-1} at 100C (100 mA cm^{-2}) at 363 K (1C = 118 mA g^{-1}, 1.00 mA cm^{-2}). Furthermore, this material with the IL electrolyte exhibits superior Coulombic efficiencies over 3000 cycles of 99.9%.

In Chapter 7, SCEIS is employed to investigate the electrochemical performance of the positive electrodes of Na secondary batteries operating at temperatures ranging from room to intermediate temperatures using the IL electrolyte, Na[FSA]-[C_2C_1im][FSA]. The obtained SCEIS for Na metal, acetylene black, α-Al_2O_3, and V_2O_5 revealed that the resistance of the high-frequency region in the Nyquist plots is a combination of several factors (the Na[FSA] fraction, the ionic conductivity of the electrolyte, and electronic conductivity of the composite electrode). The activation energies obtained by the Arrhenius plots for both the high-frequency and charge-transfer resistance of $Na_2FeP_2O_7$/IL_{FSA}/$Na_2FeP_2O_7$ SCEIS showed that a significant decrease in the charge-transfer resistance contributes to the high rate capability in the intermediate temperature range.

In Chapter 8, the Li[FSA]-[C_2C_1im][FSA] IL electrolyte was investigated to be an excellent electrolyte for Li metal batteries. The IL suppresses Li dendrite growth and dead Li accumulation and shows unprecedented long life cycling performance in symmetric Li/Li cell cycling tests of more than 2000 h (>5000 cycles) at a current density of 5 mA cm^{-2}. Li metal negative electrode and this IL electrolyte demonstrate the feasibility of operating Li metal batteries from room to intermediate temperature.

This study demonstrates that operation with ILs can improve the performance of the electrode for Na secondary batteries and the possibility of establishing Li metal secondary batteries. An inactive electrode material became electrochemically available electrode material for intermediate-temperature operating Na secondary batteries using IL. Electrode fabrication methods, carbon-coating, and inserting CNF improved rate capability of Na secondary batteries using IL even at room temperature. Li and Na metal showed excellent cycle stability with IL. Finally, wide temperature operability suggests the possibility of extending the applications of secondary battery systems based on these results.

List of Publications

Chapter 3

Jinkwang Hwang, Kazuhiko Matsumoto, Toshiyuki Nohira, Rika Hagiwara

Electrochemistry, **85** (2017) 675-679.

"Electrochemical Sodiation-desodiation of Maricite $NaFePO_4$ in Ionic Liquid Electrolyte"

Chapter 4

Jinkwang Hwang, Kazuhiko Matsumoto, Yuki Orikasa, Misaki Katayama, Yasuhiro Inada, Toshiyuki Nohira, Rika Hagiwara

Journal of Power Sources, **377** (2018) 80-86.

"Crystalline Maricite $NaFePO_4$ as a Positive Electrode Material for Na Secondary Batteries Operating at Intermediate Temperature"

Chapter 5

Jinkwang Hwang, Kazuhiko Matsumoto, Rika Hagiwara

Advanced Sustainable Systems, **2** (2018) 1700171.

"$Na_3V_2(PO_4)_3$/C Positive Electrodes with High Energy and Power Densities for Na Secondary Batteries with Ionic Liquid Electrolytes That Operate across Wide Temperature Range"

Chapter 6

Jinkwang Hwang, Kazuhiko Matsumoto, Rika Hagiwara

ACS Applied Energy Materials, **2** (2019) 2818-2827.

“$Na_3V_2(PO_4)_3$@Carbon Nanofibers: High Mass Loading Electrode Approaching Practical Na Secondary Batteries Utilizing Ionic Liquid Electrolytes”

Chapter 7

Jinkwang Hwang, Kazuhiko Matsumoto, Rika Hagiwara

The Journal of Physical Chemistry C, **122** (2018) 26857-26864.

“Symmetric Cell Electrochemical Impedance Spectroscopy of $Na_2FeP_2O_7$ Positive Electrode Material in Ionic Liquid Electrolytes”

Chapter 8

Jinkwang Hwang, Haruki Okada, Shinya Tawa, Kazuhiko Matsumoto, Rika Hagiwara

Journal of Power Sources, submitted.

“Ionic Liquid Electrolyte for a Wide Operating Temperature Li Metal Battery: Dendrite Suppression and Improved Performance”

Related works not described in this thesis

Mohd Azri Ab Rani, Jinkwang Hwang, Kazuhiko Matsumoto, Rika Hagiwara

Journal of The Electrochemical Society, **164** (2017) H5031-H5035.

"Poly (vinyl chloride) Ionic Liquid Polymer Electrolyte Based on Bis (fluorosulfonyl) Amide for Sodium Secondary Batteries"

Shubham Kaushik, Jinkwang Hwang, Kazuhiko Matsumoto, Yuta Sato, Rika Hagiwara

ChemElectroChem, **5** (2018) 1340-1344.

"CuP_2/C Composite Negative Electrodes for Sodium Secondary Batteries Operating at Room-to-Intermediate Temperatures Utilizing Ionic Liquid Electrolyte"

Rika Hagiwara, Kazuhiko Matsumoto, Jinkwang Hwang, Toshiyuki Nohira

The Chemical Record, **19** (2019) 758-770.

"Sodium Ion Batteries using Ionic Liquids as Electrolytes"

Huan Yang, Jinkwang Hwang, Yushen Wang, Kazuhiko Matsumoto, Rika Hagiwara

The Journal of Physical Chemistry C, **123** (2019) 22018-22026.

"*N*-Ethyl-*N*-propylpyrrolidinium Bis(fluorosulfonyl)amide Ionic Liquid Electrolytes for Sodium Secondary Batteries: Effects of Na Ion Concentration"

Kazuhiko Matsumoto, Jinkwang Hwang, Kaushik Shubham, Chih-Yao Chen, Rika Hagiwara

Energy & Environmental Science, accepted.

"Advances in Sodium Secondary Batteries"

Jinkwang Hwang, Koki Takeuchi, Kazuhiko Matsumoto, Rika Hagiwara.

Journal of Material Chemistry A, in submitted.

"NASICON vs. Na Metal: A New Counter Electrode to Evaluate Electrodes for Na Secondary Batteries"

Acknowledgment

With all my heart, I would like to express my deepest gratitude to the following people who encouraged, inspired, supported, and sacrificed themselves to help my Ph.D. study.

Firstly, I would like to express my sincere gratitude to my supervisor Professor Rika Hagiwara. The invaluable guidance and support he gave me throughout this study have been successful. I am sincerely grateful to Professor Toshiyuki Nohira for his insightful suggestions and comments with kindness. I owe a deep sense of gratitude to Associate Professor Kazuhiko Matsumoto. Without his immeasurable amount of enlightening instructions, fruitful discussions, enthusiasm, and constant encouragement, this study would not have reached its present form. I am grateful to Assistant Professor Kouji Yasuda for his educational instructions and helpful advice.

I profusely thank all the present and former laboratory members in Energy Chemistry Laboratory. They made my time in school enjoyable and unforgettable. In particular, my sincere thanks go to Mr. Hiroki Yamamoto, Mr. Shubham Kaushik, Mr. Koki Takeuchi and Ms. Huan Yang. Special thanks are also given to Ms. Naoko Sakamoto for her various help and heedful care.

Finally, it is my privilege to thanks my wife Jihye Kim, my daughter Leah Hwang, my parents, and my brother. Their devoted love and unfailing support are the real strength behind my accomplishments.

Not all acknowledgments are described here. I am thankful to all those who are related to this study.

September 2019

Jinkwang Hwang